AN EXPERIMENTAL AND THEORETICAL ANALYSIS OF COLD WORKING AND RIVETING IN FIBER METAL LAMINATE MATERIALS

By

David S. Backman

A DISSERTATION

Submitted to
Michigan State University
In partial fulfillment of the requirements
for the degree of

DOCTOR OF PHILOSOPHY

Mechanical Engineering

2011

ABSTRACT

AN EXPERIMENTAL AND THEORETICAL ANALYSIS OF COLD WORKING AND
RIVETING IN FIBER METAL LAMINATE MATERIALS

By

David S. Backman

This research describes the results of an investigation into the behaviour of fiber metal

laminate (FML) materials after cold expansion and riveting, using both experimental and

theoretical methods with an overall aim of producing a new FML variant optimized for

these manufacturing processes. To achieve this aim three primary research objectives

have been identified including: 1. Experimentally measure the strains in fiber metal

laminates due to both hole cold expansion and riveting. 2. Develop a theoretical model

that could be used to analytically predict the strains resulting from hole cold expansion

and riveting. 3. Develop and test new variants of FML optimized with regards to cold

expansion and riveting.

Using digital image correlation techniques, full-field strains were measured on various

grades of FML after both hole cold expansion and riveting. The cold expansion results,

showed how the residual strain field was dependent on the split sleeve direction with

respect to the material orientation and that by changing the orientation of the split

sleeve one could significantly reduce the magnitude of the residual strains. The effects

of material orthotropy were also evident in the riveted coupons, but less pronounced

due to the driven and manufactured heads of the rivet obscuring the region closest to

the rivet hole. The results from this static testing suggested that designing a more

isotropic fiber metal laminate material could improve performance after cold expansion and riveting.

Two different analytical approaches were used in this research. In the first, a closed form solution for the strains resulting from cold expansion and riveting was put forward and corroborated against experimental results. In the second, a classical laminated plate approach was used to develop an analytical tool that could predict the material properties of fiber metal laminates based on the glass fiber orientation and the number of aluminum and of fiber layers. This approach was validated against experimental data and used as a design tool to predict the material properties of a variety of new fiber metal laminate (FML) variants.

Static tensile testing of the various FML variants confirmed that FML 4 with a quasi-isotropic layup had a constant elastic modulus of approximately 50 GPa, regardless of material direction. Strain measurements made after cold expansion and riveting showed that this quasi-isotropic FML 4 variant had a more uniform residual strain field, which was a significant improvement in this regard over standard FML 4 or FML 3. Fatigue testing showed that overall, cold expansion was effective in extending fatigue life. Such testing with the FML 4 variant showed that although it had a lower fatigue life than standard FML 4 in one material orientation, its overall fatigue life was fairly constant, regardless of material orientation. The results suggest that this FML 4 variant may prove to be a valuable addition to the standard grades of FML currently in use today.

This thesis is dedicated to my wife Chantal and our children.

ACKNOWLEDGEMENTS

PREFACE

This thesis is based upon research conducted from April 2006 to December 2010 at the National Research Council Canada's Institute for Aerospace Research, Ottawa, Ontario Canada.

I would like to express my sincere gratitude to my supervisor Eann Patterson. Without his advice and support this thesis would never had become a reality. I would also like to thank my supervising committee, Professor Dahsin Liu, Professor Gary Cloud, Professor Gary Burgess and Mr. Jerzy Komorowski for their guidance and advice.

I would also like to express my gratitude and appreciation to my wife Chantal, who supported me and looked after our young son Noah, during my many weekends spent in the lab poring over data and writing up the results.

David S. Backman, December 2010.

TABLE OF CONTENTS

LIST OF TABLES

LIST OF FIGURES

xxii

LIST OF ABBREVIATIONS

ARALL	ARamid ALuminum Laminate
CFRP	Carbon Fiber Reinforced Polymer
CX	Cold Expansion
DIC	Digital Image Correlation
FAA	Federal Aviation Administration
FAR	Federal Aviation Regulation
FTI	Fatigue Technologies Inc.
FML	Fiber Metal Laminate
GLARE™	GLAss REinforced
IAR	Institute for Aerospace Research
NRC	National Research Council Canada
OH	Open Hole
PAA	Phosphoric acid anodized
PE-UT	Pulse echo ultrasound
SEM	Scanning Electron Microscope
TSA	Thermoelastic Stress Analysis
UH	Unexpanded Hole

1.0   INTRODUCTION

The use of fiber metal laminate materials in aerospace is increasing as large manufacturers such as Airbus and smaller manufacturers such as Bombardier investigate and integrate fiber metal laminates (FML) into aircraft structures. These materials, especially variants based on a combination of aluminum and glass fibers, are being promoted as potential replacements for monolithic aluminum based on their lower weight and increased fatigue life.

Widespread adoption of fiber metal laminates in aerospace applications is contingent upon the material adhering to the damage tolerant philosophy required by the Federal Aviation Administration (FAA) regulations, specifically Federal Aviation Regulation (FAR) 25. As Alderliesten and Homan[1] pointed out, this requirement is currently met by manufacturers of monolithic aluminum alloys by applying fatigue crack growth reduction strategies, which translates to lowering the design allowable stress. Although the elastic modulus of FML is lower than that of aluminum, ideally, the high ultimate strength, low density and better fatigue resistance of FML-based materials should allow for the overall weight of the structure to be reduced.

Manufacturing processes such as cold expansion and riveting are more critical in FML owing to the inherent tensile residual stresses that are locked into the material during the manufacturing process. Crack nucleation and growth to a detectable level tends to occur more rapidly than is the case in monolithic aluminum alloys, but the overall

1

propagation of these cracks to failure is greatly curtailed by crack bridging from the fiber reinforced laminate layers[1,2].

Early crack nucleation in FML is a result of three factors. The first is the tensile residual stresses in the aluminum layers arising during the heating/curing process due to the difference in the coefficient of thermal expansion between the metal and the fiber reinforced thermoset layers. The second factor is that crack bridging becomes effective only when cracks have grown past the effective crack length. The effective crack length at which fiber bridging becomes effective is dependent on the laminate and is typically of the order of 0.5-1.5 mm[3]. The third factor is the difference in stiffness between the aluminum layer (75 GPa) and the glass layer (50 GPa) that results in a higher stress in the aluminum layer.

1.1   Research Objectives

Although both experimental and theoretical research has been performed on the effect of hole cold expansion and riveting in aluminum alloys, little research to date has focused on FML materials, and much of this has relied on computational modeling. By building on the current understanding of fatigue life in FML and combining this with experimental data detailing the strain field resulting from cold expansion and riveting, the aim of this thesis is the production of a new FML variant optimized for these manufacturing processes. To achieve this aim three primary research objectives have been identified:

1. *Experimentally measure the strains in fiber metal laminates due to both the cold expansion and riveting processes and establish the effect these processes have on structural performance.* Advanced full-field strain measurement techniques are used to determine the residual strains that develop as a result of both cold expansion and riveting. Standard grades of FML 3 and FML 4 are tested alongside aluminum 2024-T3 coupons. The information obtained from these experimental techniques will provide insight into how current FML formulations can be improved and could lead to the development of new FML variants that are optimized for cold expansion and riveting.

2. *Develop a theoretical model that can be used to analytically predict the strains resulting from the hole cold expansion and riveting processes.* A survey of several current closed-form solutions for cold expansion will be examined to determine whether it is possible to modify them for use with FML materials and for use in describing the riveting process. In addition, a classical laminate plate approach will be used to develop an analytical design tool that is useful for modeling the material properties of any new FML variants that are developed.

3. *Based on the above results, develop and test new variants of FML optimized with regards to standard manufacturing processes such as cold expansion and riveting.* The results garnered from the experimental measurements will be used as a starting point for designing a new FML variant, optimized for manufacturing processes such as cold expansion and riveting. A limited static and fatigue testing program will be used to

benchmark the performance of these new FML variants against currently accepted FML

types to determine if the new design(s) are successful.

2.0   BACKGROUND

This section is focused on providing background information in five critical areas. The first subject area focuses on the history and the properties of fiber metal laminate (FML) materials. The second focuses on fatigue in fiber metal laminates, while the third and fourth subject areas focus on the process specifics and mechanics of hole cold expansion and riveting respectively. The fifth and final subject area provides some background on the experimental strain measurement techniques that will be used.

2.1   Fiber Metal Laminates

The theoretical basis for fiber metal laminate (FML) materials likely originated with research done by Kaufman[4] in 1967 on the fracture toughness of multi-layered, adhesively bonded aluminum panels. Kaufman showed that the fracture toughness of multi-layer, adhesively bonded panels was higher than that of either sheet or plate of the same thickness. Kaufman's hypothesis regarding this phenomenon was that the bonding process used to adhere each layer of material served to retard fracture growth[4] due to an increase in the number of shear surfaces as each layer can crack independently. Engineers at Fokker Aerospace first started to work on the concept of combining thin sheets of aluminum with fiber reinforcement in the early 1970's with the goal of improving fatigue resistance and damage tolerance in airframes[5]. At about the same time, the department of Aerospace Engineering at the Technical University of Delft became involved with fiber metal laminate materials and began a research program to optimize these materials with respect to strength, weight and damage tolerance[6,7]. The first commercial product produced by this research group was a

combination of aluminum 7075-T61 sheet and aramid fibers; a combination termed

ARALL (ARramid ALuminum Laminate). ARALL suffered from several intrinsic

deficiencies, including:

1) Poor interface strength between the aramid fibers and the adhesive, which effectively

limited the achievable fiber volume fractions to 50% (compared to current FML with

typical fiber volume fractions of 59%) in order to achieve acceptable peel and

interlaminar shear strength[6,8].

2) Compressive failure of the aramid fibers when the material was put into compression.

When this occurred, the crack bridging mechanism that normally served to enhance

fatigue life could be compromised, which proved to be an issue in reversed fatigue

loading conditions[8].

3) Poor blunt notch behavior of ARALL compared to typical aluminum alloys, a likely

side effect of the low failure strain (~2.4%) of the aramid fibers[8].

4) An inability to produce crossed ply laminates, meaning that ARALL was more

anisotropic than current FML materials with biaxial layups[8].

The shortcomings with ARALL led researchers at the Technical University of Delft to

explore new ways to improve on the inherent design principles behind this new class of

composites, with the end result being a research program centered on replacing the

aramid fibers with high strength glass fibers. Researchers found that the adhesion

between the glass fibers and the resin was better than with the aramid fibers and that

the glass fibers were stronger when loaded in compression, improving the fatigue

resistance of the material and reducing the incidence of fiber failure during fatigue loading[8]. This new fiber metal laminate (FML) variant was termed GLARE™ (GLAss REinforced) and overall it provided higher tensile and compressive strength, better impact behavior, higher ultimate strain and higher residual strength than ARALL[6,8]. The bonding properties and the higher tensile strength of the glass fibers also made it easier to construct FML variants with multi-axial fiber layups making the material more isotropic and thus better suited to applications where biaxial loads occur[6,8]. The superior mechanical properties of FML have focused attention on how to incorporate this material into the design and construction of new airplanes, specifically as replacements for monolithic alloys used in the aircraft fuselage[8].

Production of this type of FML has become standardized with six grades being commonly produced. All grades are produced using uni-directional S2-glass fibers embedded in thermoset resin adhesive to produce a 0.127 mm (0.005 in) thick glass/resin matrix with a nominal volume fraction of 59% and different layups depending on the grade. The combination of the S2-glass pre-embedded in the thermoset resin matrix is often referred to as a prepreg. Table 1 lists the various grades of FML, showing the layup for each grade as well as providing some basic information regarding each grade[9]. For FML 1, FML 2, FML 4 and FML 5 the prepregs in the fiber layer are symmetrically stacked. In the case of FML 3, the prepreg closest to the outer aluminum layer is oriented along the rolling direction of the aluminum (0° degree). For FML 6, the prepreg closest to the outer aluminum layers is oriented in the +45° degree direction for

FML 6A and in the -45° degree direction for FML 6B. A specific laminate coding system also exists for FML and is used to precisely describe the constituent makeup of the FML grades in question. The generalized nomenclature for FML takes the form FML A – B/C – D where A represents the grade of FML (specifying the layup), B represents the number of aluminum layers, C represents the number of fiber regions and D represents the thickness of each aluminum sheet. Thus FML 3–3/2–0.3 represents an FML 3, with 3 aluminum layers, 2 fiber regions (with a fiber layup of [0/90] in each region) and utilizing 0.3 mm thick aluminum sheet.

Table 1: Standard FML grades and material properties

FML grade	Sub Grade	Metal Thickness (mm) and Alloy	Fiber Layup	Main characteristics
FML 1		0.3-0.4 7475-T761	[0/0]	Fatigue, strength, yield stress
FML 2	FML 2A	0.2-0.5 2024-T3	[0/0]	Fatigue, strength
	FML 2B	0.2-0.5 2024-T3	[90/90]	Fatigue, strength
FML 3		0.2-0.5 2024-T3	[0/90]	Fatigue, impact
FML 4	FML 4A	0.2-0.5 2024-T3	[0/90/0]	Fatigue, strength in 0° direction
	FML 4B	0.2-0.5 2024-T3	[90/0/90]	Fatigue, strength in 90° direction
FML 5		0.2-0.5 2024-T3	[0/90/90/0	Impact
FML 6	FML 6A	0.2-0.5 2024-T3	[+45/-45]	Shear, off axis properties
	FML 6B		[-45/+45]	Shear, off axis properties

The S2-glass fibers used in the construction of typical FML variants are approximately 10μm thick, with an ultimate strength of 4.0 GPa, an elastic modulus of 95 GPa and a failure strain of approximately 4.45%. The mechanical properties of the matrix within which the fibers are embedded are negligible by comparison (ultimate strength 50 MPa,

stiffness 1.7 GPa, failure strain 5-10%) however they make an important contribution to the strength of this material by determining the bond strength between the aluminum and fiber layers. The production of FML usually involves pre-treating the aluminum layers with chromic or phosphoric acid anodizing and priming them with BR-127 corrosion inhibiting bond primer. The FML is then cured in an autoclave at 120°C, resulting in such high adhesive strength that bond lines typically remain intact until cohesive adhesive failure occurs[9,10]. An exploded view of FML 4-3/2 is shown in Figure 1. Although the exact layup structure for FML 4 can be denoted as [2024-T3/90/0/90/2024-T3/0/90/0/2024-T3] the shorthand notation for the FML grades used in this research will refer only to the orientation of the fiber layers (i.e FML 4 [0/90/0]) and will assume a symmetrical laminate with one aluminum layer in the interior and two on the outside as shown in Figure 1.

Aluminum

Cross-plied glass/epoxy FM94-S2

Aluminum

Cross-plied glass/epoxy FM94-S2

Aluminum
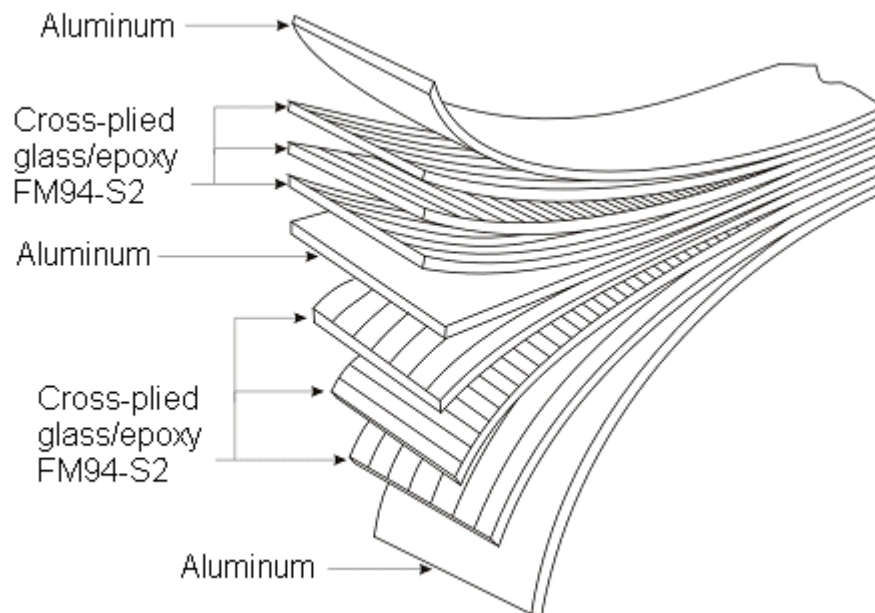
Figure 1: Exploded view of a typical layup for FML 4-3/2

9

FML 1 and FML 2 with unidirectional fibers can be strongly anisotropic with respect to yield strength, ultimate tensile strength and ultimate elongation[10]. These behaviours led to the development of FML 3 and FML 4 with cross-ply fibers which reduced the degree of anisotropy and made these materials more suitable for aerospace applications where loading is often biaxial. The unpublished results of tests performed at the National Research Council[11] are shown in Figure 2 - Figure 4, which demonstrate the variation of the elastic modulus, yield strength and ultimate strength with respect to material direction. As with standard polymeric composites, the fibers in FML reinforce the strength and modulus in the direction with which they are aligned. The ultimate failure of FML in the longitudinal direction is typically characterized by the tensile failure of the constituent fibers. Material failure occurs when the fibers reach their tensile failure strain. Most FML variants have improved ultimate tensile strength compared to monolithic aluminum sheet; however the yield strength of FML composite materials is dependant on the residual stress in the metal layers, the mechanical properties of the alloy used and the degree of strain imparted to the fibers during the curing process. The metal volume fraction approach, using the rule of mixtures, defines the fraction of load supported by the metal layer based on the proportions and modulus of the glass prepreg and metal layer respectively and can be used to predict the material properties in the principal orientations[12]. The elastic modulus of FML composites tends to be lower than that of monolithic 2024-T3 aluminum, due to the lower modulus of the glass prepreg used for reinforcement. The elastic modulus in compression is nearly equivalent to the tensile modulus since the glass fibers provide reinforcement during

compressive loading as well. Furthermore, while the compressive yield strength of FML

is slightly lower than the tensile yield strength, it is not limited to tension dominated

applications, as the S2 glass fibers are not as prone to suffering micro-buckling under

compression as are the aramid fibers in ARALL[6].
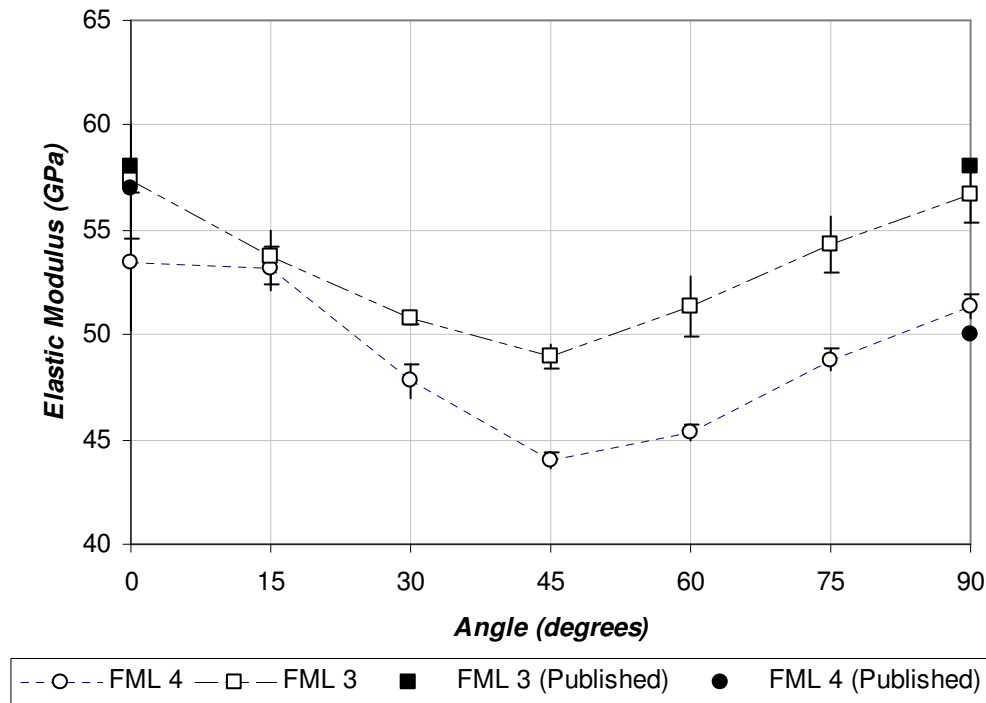
Figure 2: Variation in elastic modulus with orientation for FML 3 and FML 4 from NRC testing[11] with comparison to published values[13]
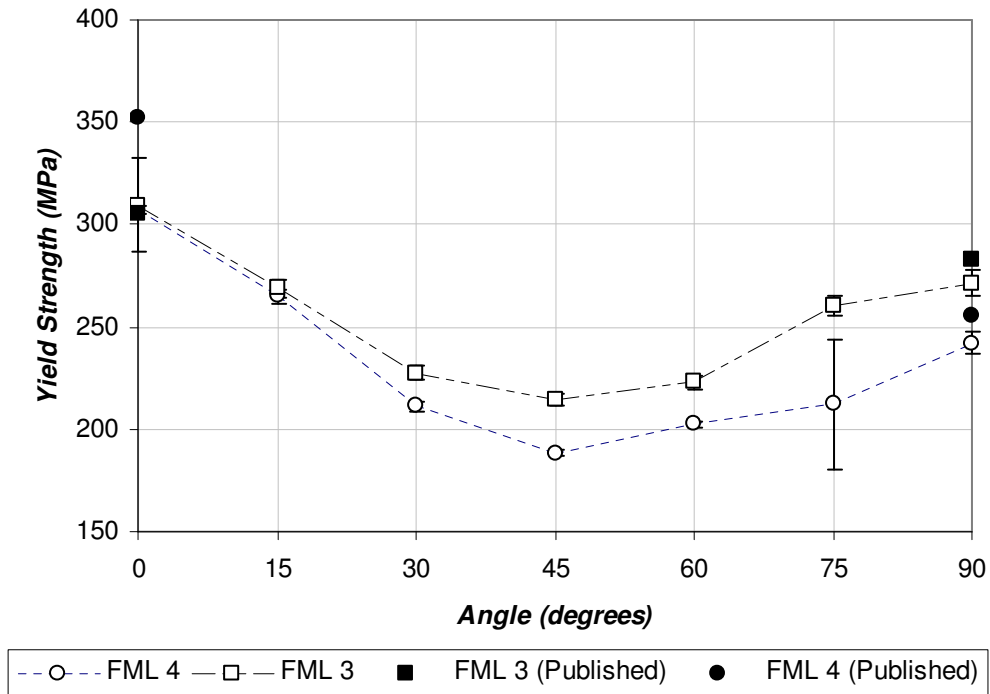
Figure 3: Variation in yield strength with orientation for FML 3 and FML 4 from NRC testing[11] with comparison to published values[13]
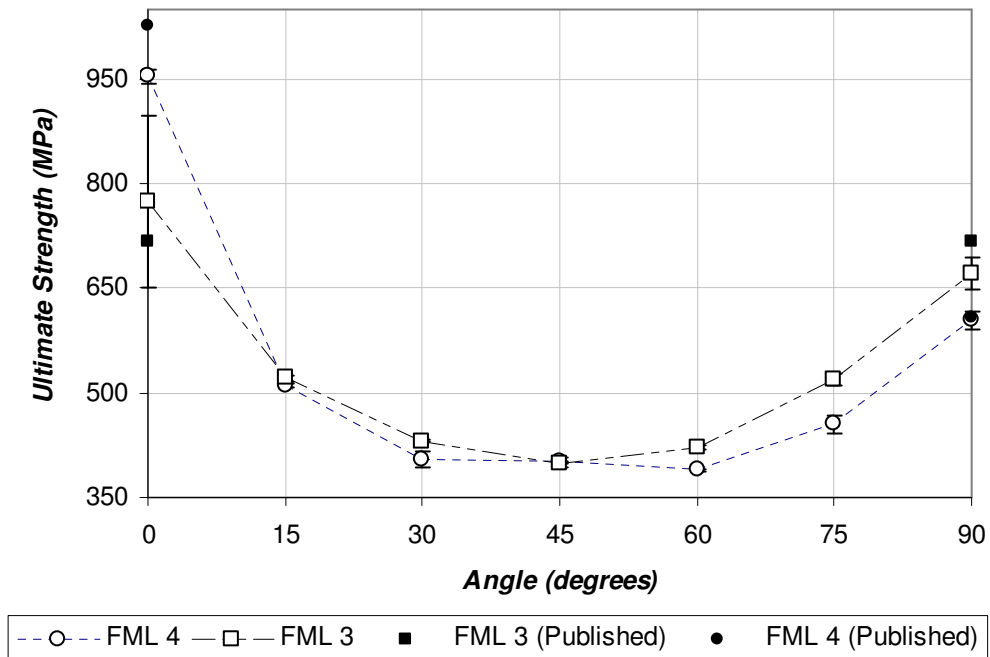
Figure 4: Variation in ultimate strength with orientation for FML 3 and FML 4 from NRC testing[11] with comparison to published values[13]

Wu and Yang[13] performed a large number of tests to determine the tensile and

compressive properties of the various standard grades of FML and a summary of some

of their tensile and compressive property data is shown in Table 2 (in addition to being

overlaid in the graphs of Figure 2 - Figure 4). The published data show a reasonable

correspondence to the test data from NRC testing[11] and also serve to highlight the

degree of anisotropy inherent in both FML 3 and FML 4.

Table 2: Longitudinal (L) and longitudinal transverse (LT) tensile and compressive properties of FML and 2024-T3 aluminum[13]

Property	FML 3-3/2	FML 4-3/2	2024-T3
Ultimate Strength, L (MPa)	717	1027	455
Ultimate Strength, LT (MPa)	716	607	448
Yield Strength, L (MPa)	305	352	359
Yield Strength, LT (MPa)	283	255	324
Elastic Modulus, E_x (GPa)	58.2	57.6	72
Elastic Modulus, E_y (GPa)	58.2	51.2	72
Compressive Yield Strength, L (MPa)	309	365	304
Compressive Yield Strength, LT (MPa)	306	285	345
Compressive Elastic Modulus, L (GPa)	60	60	74
Compressive Elastic Modulus, LT (GPa)	60	54	74
Poisson's Ratio (v_{xy})	0.288	0.289	0.33
Poisson's Ratio (v_{yx})	0.288	0.257	0.33
Shear Modulus (GPa)	23.3	23.3	28
Density (g/cm^3)	2.5	2.42	2.78

Although many advantages exist to using FML type material's, the lower modulus compared to monolithic aluminum can pose a problem in specific applications. For aerospace use, FML materials are used in conjunction with new manufacturing processes that bond internal reinforcing stringers and ribs to produce a resultant structure that can support the same load as an aluminum fuselage with riveted reinforcements. From a fatigue perspective, current FML materials must be oriented carefully to ensure that the direction of the applied load is aligned with the materials stiffest orientation, otherwise unexpectedly rapid fatigue crack growth could result.

2.2 Fatigue of Fiber Metal Laminate Materials

Although the static properties of a material are always important from an engineering design perspective, for aerospace applications another critical factor is fatigue performance. For a typical aerospace component, the number of flight loading cycles required for a fatigue crack to grow from a detectable to a critical length typically drives the required inspection interval, while the number of cycles to crack nucleation typically drives the start of the inspection regime.

It was the early work on aramid based FML materials such as ARALL that showed how the concept of adhesively combining monolithic alloy sheets with unidirectional prepregs resulted in a material with fatigue properties superior to those of the monolithic alloy[7,8,14]. This fatigue resistance was attributed to a phenomenon known as fiber or crack bridging.

2.2.1 Crack Bridging and the Fatigue Crack Growth Mechanism

Crack bridging is the term used to describe the load redistribution that occurs when cracks form in the aluminum layers of a fiber metal laminate. The fiber layers are insensitive to fatigue loading, and can transfer load over the fatigue crack, effectively restraining crack opening[9,15]. In conjunction with fiber bridging, delamination typically occurs at the interface between the aluminum and fiber layers in the wake of the crack (Figure 5). During the crack propagation phase, a large part of the applied stress is transferred over the crack in the aluminum layer by the intact fiber layer immediately adjacent to it. The mechanism for load transfer between the aluminum and the fiber are the cyclic shear stresses in the composite layer. The cyclic shear stresses in the composite layer are directly related to the fiber bridging stresses. These cyclic shear stresses cause the delamination between the aluminum and the composite layer to grow, meaning that the free length over which the fibers are elongated increases, effectively decreasing the fiber strain. A balance exists between delamination growth and the fiber bridging stress. Increasing the adhesion of the composite layer would result in better crack bridging and thus slower crack growth, however, increasing adhesion beyond a critical point would increase the fiber strain to the point where failure would occur and crack growth would increase[15]. At the beginning of the crack propagation phase the crack opening is sufficiently small such that the fibers in the prepreg layer are not fully loaded. A certain amount of crack length and crack opening displacement are needed (approximately 1 mm) before fiber bridging becomes fully effective[9]. This may play a role in limiting the ability of techniques like cold expansion to effectively retard the early onset of short cracks in FML.
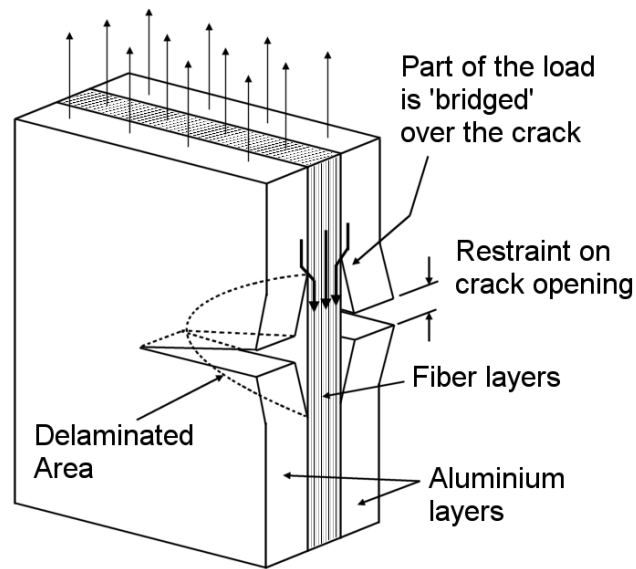
Figure 5: Crack bridging from the fiber layer and the resulting delamination from Vlot and Gunnink[9]

During the crack propagation phase, a large portion of the fatigue stresses are transferred over the cracks in the aluminum layer by the intact fiber layer (Figure 5). Load is transferred to the aluminum layers through the adhesive resin matrix surrounding the glass fibers in the prepreg, thereby inducing cyclic shear stresses in the adhesive resin matrix and thus shear deformation. These cyclic shear stresses cause delamination growth between the aluminum and the prepreg layer. The crack propagation phase in FML is typically characterised by lower stress intensities at the crack tip compared to monolithic materials which is a result of crack bridging. The lower stress intensity at the crack tip results in close to constant crack growth rates in FML[9].

It is thought that the crack opening displacement which occurs during the crack propagation phase is also due to the adhesive shear deformation and the delamination between the aluminum substrate and the prepreg. This shear deformation serves to constrain the crack opening, but cannot reduce it completely, thus resulting in a stress

16

intensity at the crack tip in the aluminum layer, albeit a smaller one than in monolithic materials[9].

2.2.2 Fatigue Crack Growth in FML

According to the definition by Schijve[16] fatigue crack growth in monolithic materials can be divided into two stages; the crack initiation period and the crack growth period. The crack initiation period is comprised of crack nucleation and micro crack growth. Since these are surface phenomena, linked to cyclic shear stresses on crystallographic slip planes[16], these mechanisms are still at work in the aluminum layers of a fiber metal laminate material.

The start of crack growth in FML materials can be treated in a similar manner as for monolithic materials if a similarity approach is used. Similar stress states in the aluminum layer of FML as in monolithic materials will produce the same result – crack nucleation. The stresses in the aluminum layers consist of both the static residual stresses and the applied stresses. Static residual stresses in FML are due to the mismatch between the coefficient of thermal expansion of the aluminum ($22\times10^{-6}/\text{ºC}$) and the glass ($2.9\times10^{-6}/\text{ºC}$) fiber layer during the curing process. Although the exact magnitude of the residual stress varies depending on the layup and the cure cycle, the autoclave curing process generally results in some degree of tensile residual stress in the aluminum layers. This explains why Young et al[17] noticed that a significant improvement (40-50%) in fatigue life was obtained by statically overloading FML specimens to 200 MPa before fatigue testing began. This static overload induced

compressive residual stresses in the aluminum layer that mitigated the tensile residual stresses from the autoclave curing process. This suggests that understanding and controlling the residual stress state in FML may have important ramifications for fatigue performance after hole cold expansion and riveting, as both processes can induce compressive residual stresses.

Vasek et al[18] focused on examining the nucleation location for fatigue cracks in FML by milling off individual layers of the laminate and examining each individual aluminum layer. From the results of his investigation, he was able to determine that fatigue cracks nucleated separately in the individual aluminum layers. Specifically, more cracks formed in the inner layer while longer cracks were forming on the surface layers.

Homan[3] and Bradshaw and Gutierrez[19] added to the work done on the fatigue properties of FML by focusing on what they referred to as "fatigue crack initiation". In both cases "fatigue crack initiation" referred to the number of cycles required for a crack of arbitrary length, in this case 1.0 mm, to propagate. Homan[3] went into more detail in his explanation of the terminology and defined the "initiation period" as including cyclic slip, crack nucleation and micro crack growth. The key point in his discussion was that "crack bridging" by the fiber layers does not come into play until the "macro crack growth" period, meaning that during fatigue testing of FML, small cracks may grow more quickly than in monolithic aluminum alloys. Homan[3] was also able to show that

classical laminate plate analysis could be useful for calculating the internal stresses as well as for estimating material properties of different FML variants.

2.3 Cold Expansion Process

Any technique that could improve the fatigue performance of fastener holes without increasing weight, would be especially valuable in extending the fatigue life of new and existing aircraft. In the 1960's Boeing engineers developed just such a process, using a split sleeve shim and an oversized mandrel that could be pulled through a fastener hole of a specific size. The insertion of this tool plastically deformed the hole in both the radial and tangential directions, and when the tool was removed the elastic material surrounding the plastically deformed region would force it to spring back so that compressive residual stresses formed in the vicinity of the hole edge. These compressive residual stresses served to reduce crack growth rates by lowering the stress intensity factor at the crack tip[20,21]. This technology is typically referred to as "split sleeve" cold expansion and has become one of the most accepted methods for performing hole cold expansion. This technique has been qualified for use in aerospace applications and as a result was the method selected for this investigation. An understanding of the cold expansion process, with an emphasis on the "split sleeve" technique is critical to understanding the results presented in this report and further details are described below.

The basic procedure for hole cold expansion begins with the drilling of a slightly undersized hole. The actual diameter of this hole is a function of the amount of cold expansion being applied, as well as the diameter of the fastener or rivet that would eventually be inserted. A hardened steel mandrel with a slightly oversized head is

19

passed through this initial hole. On the shank of the mandrel is a split sleeve shim of a specified thickness. Once the mandrel head (which is sized to pass through the pilot hole) is inserted, the split sleeve is seated in the hole. The key to the operation of the split sleeve cold expansion system, is that the diameter of the mandrel head and the thickness of the split sleeve are such that when the mandrel head is pulled through the sleeve, the combination of the two results in interference, which causes the pilot hole to be enlarged by a specified amount as a result of plastic deformation. A cross-sectional view of various stages of cold expansion are shown in Figure 6a to Figure 6d.

(a)	(b)	(c)	(d)
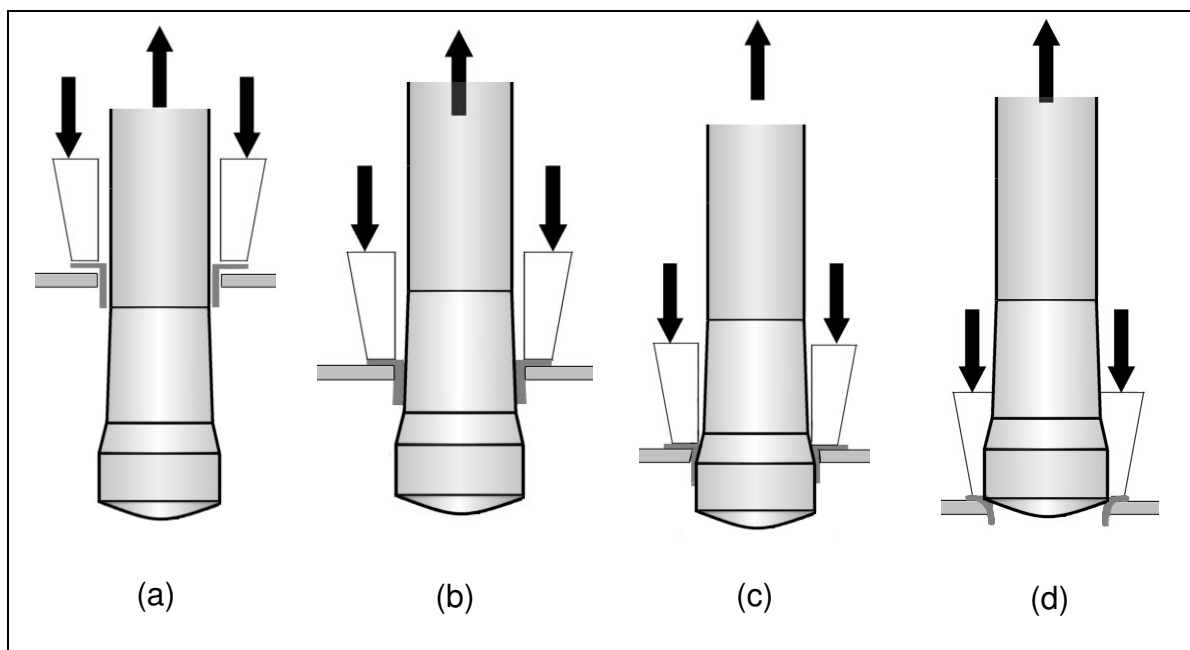
Figure 6: Basic stages of the split sleeve hole cold expansion process

The workpiece being cold expanded consists of two sides, the side with the puller unit is called the exit side, since this is the side from which the mandrel exits the workpiece. The opposite side is termed the entry side, as this is the side from which the mandrel enters the workpiece. This distinction will be important later when the surface strain fields on these two sides are compared and discussed. Another important point is that

the mandrel used in this investigation had a cylindrical segment portion of greater width than the width of the coupons being cold expanded, meaning that at one point during the process the entire width of the coupon has been expanded the maximum amount.

Another important feature of the cold expansion process is the use of a "split sleeve" shim. From a conceptual design point of view, the split sleeve shim is crucial as it allows for easy insertion onto the mandrel initially, and it allows the split sleeve shim to be easily removed after the cold expansion process is completed. The orientation of the split sleeve is given minimal mention in the manufacturers documentation (Fatigue Technology Inc), except to say that in instances where one is cold expanding close to a free edge, the split should be oriented away from the free edge[22]. Using digital image correlation methods to measure the principal strains surrounding a cold expanded hole will hopefully provide additional information regarding what if any effect the orientation of the split has on the resulting strain field.

2.4   Riveting Process

Although new methods for material joining are gaining in popularity, riveted structures are still a mainstay in the aerospace industry. A basic understanding of how a rivet works to create a tight and efficient joint is necessary for discussing the strain fields measured during the riveting process.

The riveting process can be broken down into four key stages as illustrated in Figure 7. The first stage of riveting involves drilling an oversized hole (approximately 0.1 mm larger than the rivet shank) to allow the rivet head to seat correctly (Figure 7a). As an

axial compressive load is applied to the rivet, the rivet expands radially. The diameter

of the rivet shank increases with the increase in squeeze force until the rivet diameter is

equal to that of the pilot hole. The second phase in the riveting process is characterized

by increased stress in the surrounding sheet material caused by the expanding rivet's

interference with the edge of the hole (Figure 7b). In addition, the unsupported portion

of the rivet shank begins to form the driven head. In the third stage, the area around the

rivet shank becomes plastically deformed. During this phase, the diameter of the driven

head and the hole enlargement increase until a preset protrusion height or squeeze

force is reached. The driven head typically takes on a barrel shape as a result of

contact with the sheet on one side and contact with the riveting gun on the other (Figure

7c). As the driven head makes contact with the sheet material less squeeze force is

transferred through the sheet, reducing the degree to which the rivet material is

squeezed into the hole. The final stage in the riveting process (Figure 7d) involves the

removal of the squeeze force. This stage is marked by the elastic relaxation of both the

rivet and the sheet material[23].
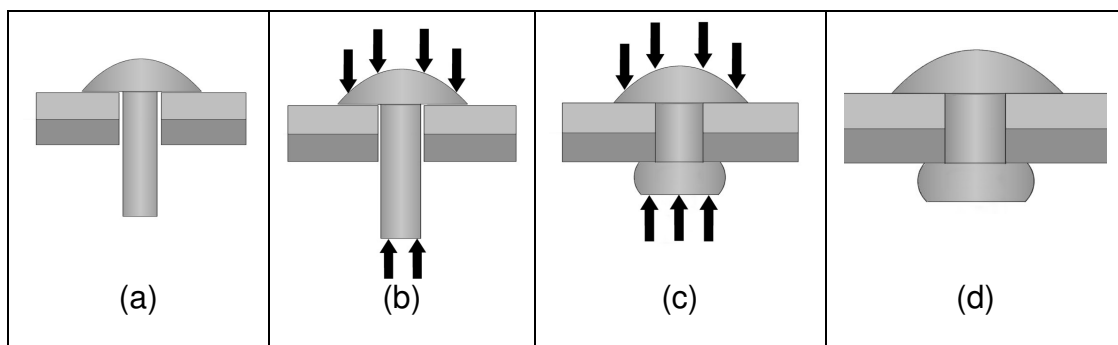
Figure 7: The four basic stages of the riveting process

2.5   Experimental Strain Measurement Techniques

Two main strain measurement techniques are used in this research program: digital

image correlation (DIC) and thermoelastic stress analysis (TSA).   Digital image

correlation provides the more comprehensive results of the two, since it presents the

full-field strain tensors in the area of interest. The results from TSA can be more difficult

to interpret since it provides results proportional to the sum of the principal stresses.

2.5.1   Thermoelastic Stress Analysis

Thermoelastic stress analysis (TSA) is a non-contacting technique for measuring full-

field stresses over the surface of a cyclically loaded specimen. The technique is based

on the measurement of the minute temperature changes that are associated with stress

changes in a solid. An elastic solid subjected to a compressive stress will register a

small increase in temperature, while a tensile stress will cause a small decrease in

temperature. From a practical standpoint, TSA entails applying a cyclic load to a test

specimen, at a frequency high enough to ensure adiabatic conditions, while monitoring

the surface temperature changes. This allows the stress changes due to the cyclic

loading to be inferred[24,25].

Until recently, the majority of all practical TSA work has involved the use of a system

called SPATE (Stress Pattern Analysis by Thermal Emission), which employed a

cadmium mercury telluride (CMT) infra-red detector, operating in a point by point

scanning mode to provide a stress contour map[26]. A major advance in TSA work has

been the introduction of indium antimonide (InSb) detector arrays which obviate the

need for point by point scanning and significantly reduce the time required to perform thermoelastic stress analysis.

The theoretical basis behind thermoelastic stress analysis was first put forward by Lord Kelvin in 1853, with his work relating temperature change and elastic deformation[27]. Lord Kelvin put forward the most generalized form of the thermoelastic equation, which relates the change in temperature of a component (ΔT) to the stress change in an elastic solid. In practical thermoelastic stress analysis, specimens are cyclically loaded at such a rate that virtually no heat conduction takes place, so one can ignore the heat input to obtain the fundamental equation behind thermoelasticity:

$$\Delta T = \frac{T}{\rho C_E} \cdot \sum_i \left(\frac{\partial \sigma_i}{\partial T} \right) \Delta \varepsilon_i \quad \text{for i,= 1,2...6} \qquad 2.5.1$$

where T is the absolute temperature of the material, C_E is the specific heat at constant strain, ρ is the density, σ_i is the contracted stress tensor, and ε_i is the contracted strain tensor.

Equation 2.5.1 is a very general form of the thermoelastic equation, useful for isotropic or anisotropic materials provided that the conditions of adiabaticity are met. To derive the more commonly used form of this equation one starts with the general relationship between stress, strain and temperature for an orthotropic material:

$$\sigma_i = \sum_{j=1}^{6} C_{ij} \cdot \left(\varepsilon_j - \alpha_j \cdot \Delta T \right) \quad \text{with i,j = 1,2...6} \qquad 2.5.2$$

where C_{ij} is the stiffness matrix and α_j are the coefficients of thermal expansion[26]. As an aside, if one were to expand Equation 2.5.2, one would notice that the shear term has no temperature term associated with it because shear deformations are volume independent and do not result in temperature increases. Equation 2.5.2 can also be inverted to provide an explicit expression for the strain:

$$\varepsilon_i = \sum_{i=1}^{6} S_{ij} \cdot \sigma_i + \alpha_i \Delta T \quad \text{with i,j=1...6} \qquad 2.5.3$$

If one assumes that both the modulus (E) and the Poisson's ratio (v) are constant, then it is possible to evaluate the differential of stress with respect to temperature in Equation 2.5.1 to obtain:

$$\frac{\partial \sigma_i}{\partial T} = -\sum_{j=1}^{6} C_{ij} \cdot \alpha_j \quad \text{for i,j=1...6} \qquad 2.5.4$$

Equation 2.5.3 and Equation 2.5.4 can be substituted into Equation 2.5.1 along with the established relationship between the specific heat at constant strain (C_E) and the specific heat at constant pressure (C_p)[26]:

$$C_p - C_E = \frac{T}{\rho} \cdot \sum_{i,j} C_{ij} \cdot \alpha_j^2 \quad \text{with i,j=1....6} \qquad 2.5.5$$

The final equation then reduces to the general form:

$$\Delta T = -\frac{T}{\rho C_p} \sum_i \alpha_i \cdot \Delta \sigma_i \quad \text{with i=1....6} \qquad 2.5.6$$

Equation 2.5.6 can then be applied to either isotropic materials:

$$\Delta T = \frac{-T}{\rho C_p} \cdot \alpha \cdot \Delta (\sigma_{11} + \sigma_{22}) \qquad 2.5.7$$

Or it can be applied to orthotropic materials:

$$\Delta T = \frac{-T}{\rho C_p} \cdot \left(\alpha_{11} \Delta \sigma_{11} + \alpha_{22} \Delta \sigma_{22} \right)$$
2.5.8

The key difference between Equation 2.5.7 and Equation 2.5.8 is that for an orthotropic

material the coefficients of thermal expansion in both principal directions must be

known.   For the results discussed in this research, the term TSA signal is often used

and it refers to the value of the temperature change ΔT measured in camera analog to

digital (a/d) units.

Additional insight into TSA can be realized by examining the response from the infrared

cameras from a signal processing perspective. For the sake of simplicity it can be

assumed that the material being analyzed is isotropic so that Equation 2.5.7 is

applicable. The Deltatherm system is designed to measure small variations in

temperature (ΔT) caused by cyclic loading. The infrared camera produces thermal

images using an array of InSb (indium antimonide) detectors. Images are captured at a

rate of over 400 frames/sec and processed to produce an image of the temperature

variation over the entire field of view. A simple analog electronics model can be used to

explain the fundamental signal processing being used to produce stress images. Figure

8 shows this idealized electronic model of the Deltatherm system, where S represents

the IR signal from the camera, minus any noise. One of the purposes of signal

processing is to eliminate the noise in the system and measure the amplitude of this IR

signal (S). This is done by correlating the reference signal (r) coming from the load

frame to the IR signal (S) from the camera. In order for the correlation to work, the

reference signal must be at the same frequency as the applied load, meaning that either

the load or displacement signal can typically be used. The signal conditioner digitizes

the reference signal, converting it to a square wave that oscillates between +1 and -1 at

the same frequency as the reference signal (r). Two digital reference signals are

produced from this, the first labelled "F" in Figure 8, is a conditioned cosine reference

and the second signal labelled "G" is a conditioned sine reference. When the

conditioned sine reference (F) is at the same frequency and has the same zero-

crossings as S, they are multiplied together resulting in a rectified sine wave that can

then be passed through a low pass filter to obtain a single value I_x. This operation can

be summarized mathematically with the following expression:

$$I_X = \sum (S \cdot F)$$
2.5.8
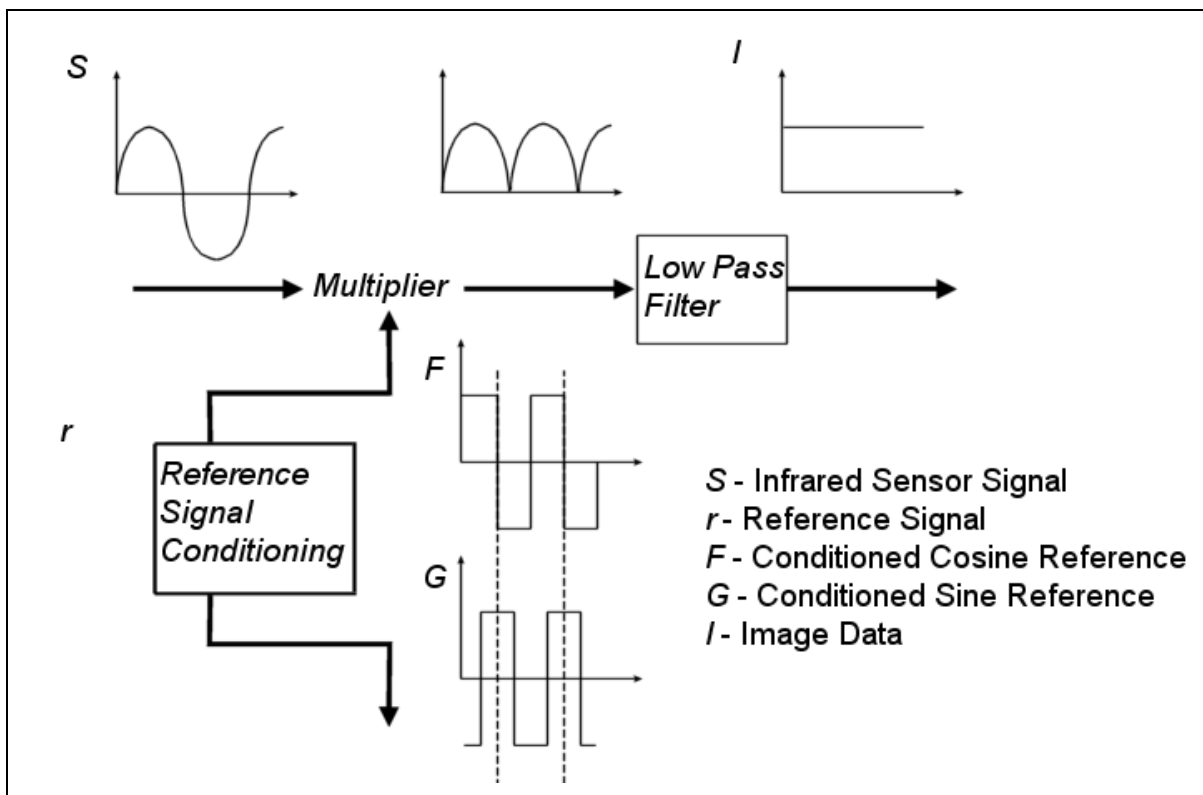
Figure 8: Simple signal processing model for the Deltatherm TSA system[28]

If the in-phase reference F is replaced with the sine reference (G) in Equation 2.5.8 then

the result is I_y. Since G is always $90°$ degrees out of phase from F, the I_y image is zero

when the I_x image is maximized. The magnitude (R) for both the I_x and I_y images is

defined as:

$$R = \sqrt{I_x^2 + I_y^2}$$ 2.5.9

The value of R remains constant regardless of the phase differences between S and F.

The phase between the digitized reference signal F and the infrared signal S can be

adjusted in software after image capture. Ideally the phase should be adjusted so that

the I_y image is as close to zero as possible. However, there may not be a phase setting

that maximizes the I_x images due to phase lag in the structure. Phase lag can be

caused by high stress gradients in the part, low cycling frequencies, or even differences

in paint thickness (thicker paint increases the amount of time it takes for heat to be

conducted to the surface and be emitted, thereby causing a phase lag)[28].

2.5.2 Digital Image Correlation (DIC)

Image correlation equipment is typically broken down into two levels of complexity: two-

dimensional and three-dimensional image correlation. Two-dimensional image

correlation is accomplished using only a single camera image of a surface under test

and a software based algorithm to calculate the strain field. This procedure is adequate

for measuring in-plane strains in specimens as long as little or no out-of-plane motion

exists. Three-dimensional image correlation is accomplished by using stereo-camera

photogrammetry, as well as the same software based algorithm employed with two-

dimensional DIC. The addition of the second camera and a photogrammetry algorithm

allow a three-dimensional DIC system to measure surface topography as well as

surface strains.

2.5.2.1 Two Dimensional Digital Image Correlation

The image correlation algorithm employed with two-dimensional DIC is common to both

the two and three-dimensional versions of this technology. The hardware used with

two-dimensional DIC consists of a single digital video camera in conjunction with

appropriate lighting.   One limitation of two-dimensional image correlation is its inability

to deal with significant out-of-plane displacement. Changes in magnification due to

small amounts of out-of-plane displacement, or changes in the depth of field, can result

in large errors in the surface strain measurement. However, this deficiency can be

overcome by using two cameras.

The basic concept behind the use of image correlation for strain measurement is that a

set of points on an undeformed object can be matched to the same set of points on the

deformed object[29-31]. For image correlation to work effectively, it is important that the

surface of the object examined has enough contrast to ensure that each subset of

points on the object is statistically different from every other subset of points. It is for

this reason that a black and white speckle pattern is often applied to the surface of the

object being tested.

The process of converting an image into digital form, represented by a matrix of pixels,

has important implications for the matching process. During the deformation of a

subset, it is entirely possible that the object centre in the undeformed image will be mapped to a location between pixels on the deformed image. In order to overcome this problem a key aspect of the image correlation process is the interpolation of pixel values in both the undeformed and deformed image. A wide variety of interpolation schemes can be used, with the most common being a bi-cubic spline fitting algorithm[30,31] and with the end result being a continuous variation in intensity patterns[31].

Assuming the subset chosen is small enough so that the displacement gradients are nearly constant, the undeformed intensity array can be related to the deformed intensity array by uniform linear mapping. This uniform linear mapping is directly related to the strain field that each individual subset undergoes. The correlation software iteratively displaces each subset looking for a match between the reference and deformed image. In addition, modern image correlation algorithms can also account for subset distortion by applying a mathematical shape function to each subset before performing the iterative search[32]. A cross-correlation function is then used to characterize the quality of the match between the reference and deformed images[30]. Once this has been completed over the entire area of interest, the displacement field obtained can be differentiated to determine the full strain tensor[30].

2.5.2.2 Three-Dimensional Digital Image Correlation (DIC)

The photogrammetric component of three-dimensional image correlation is based on a binocular vision model, similar to that used for human depth perception. By comparing the location of corresponding subsets in images taken by both cameras, the surface profile of a feature can be determined, in addition to calculating surface strains. One of the fundamental differences between two and three-dimensional image correlation is that, for the three-dimensional case, information about the orientation of the cameras is required. To obtain this information a calibration process must be carried out for the pair of cameras being used[30]. The five parameters required for modelling the imaging characteristics of the cameras, and their location relative to the sample plane, are shown in Table 3. All these parameters describe the internal workings of the camera and are camera specific values[30].

Table 3: Camera calibration parameters

Parameter	Definition
(1) Pinhole distance (phd)	distance from the imaging lens to the CCD sensor array
(2) & (3) Co-ordinates of the centre of the image (Cx,Cy)	two dimensional location of the intersection between the optical axis and the sensor plane
(4) Lens distortion factor (K)	intrinsic camera parameter
(5) Aspect ratio	two dimensional location of the intersection between the optical axis and the sensor plane

General error estimates are difficult to determine since there are many parameters that can have a direct effect on accuracy. Basic error estimates have been derived, given that the camera orientation remains within a prescribed boundary which includes: (1) Pan angle between cameras: 30-60 degrees (2) Twist and tilt angles: -5 to 5 degrees (3) Object to camera distance (Z): 0.3 m to 3 m (4) Size of region of interest (D): 10 mm to 500 mm and (5) Ratio of Z/D: Z/D > 5. When the camera orientation is within the range of values given above, the typical uncertainty for in-plane displacement is on the order of D/10 000, where D is the in-plane dimension of the object being measured. Uncertainty in the out-of-plane displacement is on the order of Z/50 000 where Z is the distance from the object to the CCD[30].

3.0   LITERATURE REVIEW

This chapter reviews the available literature regarding hole cold expansion and riveting in both aluminum and fiber metal laminate alloys. Special attention is paid to the areas of residual stress measurement, and experimental strain measurements with the goal of identifying the breadth and depth of engineering knowledge in these areas as well as knowledge gaps where additional original research contributions are required.

3.1   Cold Expansion of Aluminum Alloys

A significant body of literature has been amassed over the years pertaining to hole cold expansion and its effects on aluminum alloys. A broad overview of the different methods that can be used for cold expansion is provided by Champoux[33]. The most common hole cold expansion methods mentioned by Champoux include solid sleeve[20,34,35], ballising[36,37], split mandrel[38] as well as split sleeve cold expansion[39-48], which has been qualified for use in aerospace structures and has thus become the focus of most current research articles. Research involving hole cold expansion can be broadly categorized into three separate areas: fatigue performance after cold expansion, experimental measurements of the cold expansion process, and computer simulation of the cold expansion process; of which the first two will be of primary interest.

3.1.1   Fatigue of Aluminum Alloys as a Result of Cold Expansion

From an aerospace perspective, determining the fatigue performance of any structural modification is usually a key step in validating these modifications for use on flight articles. Petrak and Stewart[49] laid the groundwork for fatigue studies with their

research looking at the effect of several types of cold expansion and interference fit fastener systems. In their paper, several different interference fit fasters were tested, along with a new type of rivet and most importantly two different cold expansion systems: the split sleeve system developed by Boeing, as well as a solid sleeve system developed by the J.O King Company. The results showed that both split sleeve and solid sleeve cold expansion produced comparable fatigue results, which addressed the concern regarding the creation of a longitudinal ridge or "pip" that occurs during split sleeve cold expansion. In fact the results showed that compared to an open hole, any system that produced some type of interference fit would provide an improvement in fatigue life, with an apparent correlation between the degree of interference and the amount of crack growth retardation. This broad conclusion drawn by Petrak and Stewart[49] was supported by Wagner et al[50] in later studies, but did not answer some of the more detailed questions about the split sleeve cold expansion process concerning issues such as the effect of the split sleeve orientation, post cold expansion reaming, and out of plane displacement resulting from the cold expansion process. These issues were later investigated by Beaver et al[51] who looked at these three variables and their role in determining the effectiveness of split sleeve cold expansion with respect to fatigue life.   Statistical analysis of the fatigue data from a series of cold expanded 2214-aluminum alloy coupons showed that no statistically significant difference existed between test groups on the basis of split sleeve orientation, post cold expansion reaming or the removal of out of plane displacement. This proof of the robustness of the split sleeve cold expansion process was likely one of the drivers for the widespread adoption of this technique in aerospace manufacturing. Beaver et al[51] was also one of

the first to comment in the open literature on the fractographic differences between the extent of cracking on the entry and exit faces of a test coupon, an observation that was later confirmed quantitatively by Zhang and Wang[52] using replicas of the fracture surfaces to determine crack growth curves for both the mandrel entry and exit faces.

On a parallel path, other researchers took a more quantitative view of the fatigue performance of aluminum alloys after cold expansion and attempted to quantify the effect of process variables, such as the degree of cold expansion on fatigue life. In the late 1970's Chandawanich and Sharpe[20] used solid sleeve cold expansion to perform a detailed study on crack growth and the stress intensity factors on both the entry and exit faces of a fatigue test coupon. The results showed that cold expansion appeared to have little effect on "crack initiation" (defined as the number of cycles to a crack length of 0.1 mm) but that crack growth rates as well as the stress intensity factor at the crack tip were markedly reduced. A study by Chao and Xiulin[53] focused more thoroughly on "fatigue crack initiation" (defined here as the number of cycles to a crack length of 0.25 mm), with the results corroborating the findings of Chandawanich and Sharpe[20] that cracks formed first on the entry face of the coupon. However, unlike Chandawanich and Sharpe[20], Chao and Xiulin[53] found that cold expansion did play a role in increasing the number of cycles required for "fatigue crack initiation". A later study by Lacarac et al[54], looking at the role of the applied stress and the stress ratio on the effectiveness of cold expansion, found that cold expansion had only a small

influence on fatigue crack growth rates for cracks of less than 1 mm and had the largest

influence on cracks of between 1 - 2 mm. This finding was similar to that of Zhang and

Wang[52] who also showed that the benefits of cold expansion were due to the

decreased crack propagation rate of larger cracks on the order of 0.5 - 1.5 mm.

However, comparison of Lacarac et al's[54] results regarding cracks of similar length to

those of Chandawanich and Sharpe[20] or Chao and Xiulin[53] is not possible since

Lacarac et al[54] used starter notches of 0.15 mm in their coupons. Overall there

appears to be a lack of consensus regarding the ability of cold expansion to extend life

in the early stage of the fatigue process. It is possible that in the short crack regime,

immediately after crack nucleation, process variables such as the degree of cold

expansion play a larger role. What does appear clear is that cold expansion is effective

for reducing fatigue crack growth rates in aluminum alloys and is most effective after

crack nucleation and crack growth past the short crack regime.

3.1.2 Strain measurements of the Cold Expansion Process

Although fatigue experiments are useful for quantifying the life extension that can be

achieved from cold expansion, a deeper understanding of the process requires

experimental measurements of the strain fields resulting from hole cold expansion.

Some of the earliest measurements of these strain fields were made using standard foil

gauges[34,44,55]. One of the difficulties with foil gauges is that they average the strain

over their entire gauge area, making them less suitable for measuring regions with large

strain gradients such as at the edge of a hole. Also, since each individual strain gauge

measures strain in only one direction, determining hoop and radial strains requires

strain gauge rosettes or even alternating strain gauge orientations as was done by

O'Brien[44]. Another method used by several researchers for making full-field

measurements was the grid method[42,43,56]. In this method, photoresist techniques are

used to etch precisely spaced, high density grids around the area close to the hole.

Optical microscopy can then be used to determine displacements by measuring the grid

distance after cold expansion. These displacements can be differentiated with respect

to length to determine the strain fields. In some ways, grid methods can be seen as the

precursor to modern image correlation algorithms where a random dot pattern replaces

the pre-printed grid and correlation algorithms replace direct measurements of grid

spacing. Full-field strain measurements have also been successfully made by

researchers using moiré techniques[20,35,41].

Using these techniques a significant body of information has been amassed regarding

the effect of cold expansion on aluminum alloys. One of the early areas of investigation

was in regards to the location of the elastic-plastic boundary after cold expansion.

Poolsuk and Sharpe[34] used both foil strain gauges and linear variable differential

transformed (LVDT) based surface profile measurements to determine the elastic-

plastic boundary around holes which had been cold expanded using the solid sleeve

cold expansion process. The technique used by Poolsuk and Sharpe[34] was fairly

simple in practice and relied on the assumption that for an isotropic material, in the

elastic region surrounding a cold expanded hole, the magnitude of the radial and

tangential stresses would be equal. Poolsuk and Sharpe[34] used strain gauges to

determine radial and tangential strain at discrete points, but the same technique could be used with any full-field strain measurement system. Their determination of the radius of plasticity using surface thickness relied on the fact that in the plastic region, radial and tangential strains are no longer equal in magnitude and as a result of volume constancy requirements, through thickness changes must be non-zero. The results of this study showed that the radius of plasticity for solid sleeve cold expansion ranged from 6.03 mm to 7.06 mm, varying slightly depending on the degree of interference. A similar study performed by Arora et al[55] found similar results for holes expanded using a split sleeve type process. Both experimental methods agreed with one another and when compared to purely theoretical findings showed that Nadai's[57] theory worked well for plane stress situations while Rich and Impellizzeri[58] had the best theoretical results for plane strain situations.

An overview of the full-field measurements using moiré[20,35,41], grid methods[42,43,56], photoelasticity[44,59] and strain gauges[34,44,55] show very similar strain results surrounding a cold expanded hole. As expected, radial strains are compressive and tangential strains are tensile, with peak magnitudes related to the degree of cold expansion. One of the interesting results noted by several researchers is that the strains on the mandrel entry side of the coupon are consistently lower than results on the mandrel exit side of the coupon[41,43,44,47,52,60-63]. Other researchers looking at crack growth rates have confirmed that this strain differential results in faster crack

growth rates on the mandrel entry rather than on the mandrel exit faces of fatigue coupons[51-53,64]. One possible explanation for this is presented by both Zhang and Wang[52] and Forgues et al[65] is that the difference might be attributable to the level of retained expansion and to the material volume carried by the mandrel movement, while Babu et al[66] suggested that differences in the constraint conditions between the entry and exit faces might be responsible for the formation of non-uniform through-thickness residual stresses.

In conjunction with these "total" strain measurements, a significant amount of work has been done looking at the (elastic) residual strain resulting from the cold expansion process using either standard x-ray or neutron based diffraction[40,42,45,46,48,63,67-69] or Sach's type measurements[60-62,67,70]. X-ray diffraction measurements on aluminum alloys are always challenging due to the large grain size and texture in the material that typically results in high measurement inaccuracies, a fact documented by Ball and Lowry[42] who ended up using grid methods to back up their x-ray diffraction results. One of the more prolific users of x-ray diffraction technology was Stefanescu and his co-workers[45,46,48,63,69] who used a highly collimated x-ray beam as well as synchrotron radiation[47] to investigate the residual strain field around cold expanded holes and showed that the approximate difference between the entry and exit faces was on the order of 60 MPa[63]. With regards to the modified Sach's method, Ozedmir and co-

workers used this method extensively to study surface[60,62] and through thickness[61,70] residual strains resulting from hole cold expansion. A comparison between Ozedmir and Edwards[61] Sach method results and Stefanescu et al's[46] x-ray diffraction results showed very similar stress fields around a 4% cold expanded hole (Figure 9) and clearly demonstrate the difference in stress fields between the mandrel entry (inlet) and mandrel exit (outlet) faces.

(a)

(b)
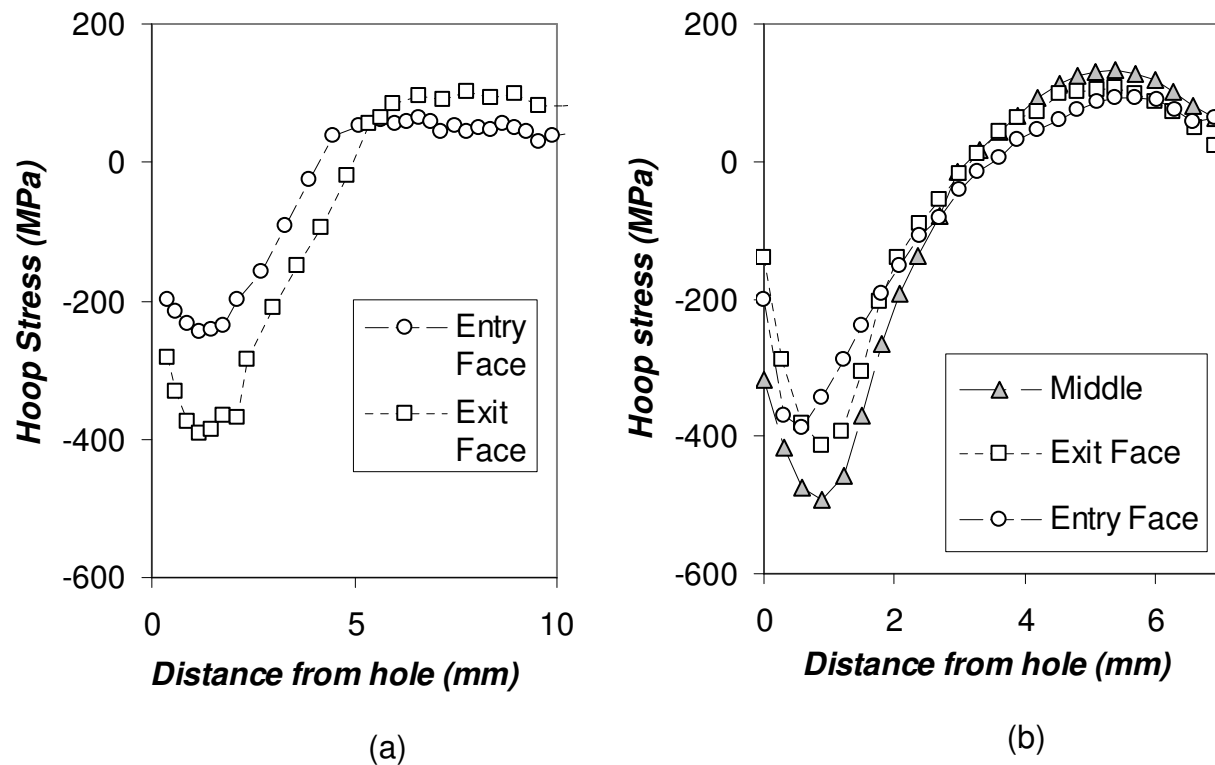
Figure 9: Residual stress measurements around a 4% cold expanded hole (a) measured using x-ray diffraction from Stephanescu et al[46] and (b) measured using a modified Sach's method from Odzemir and Edwards[61]

3.2   Riveting of Aluminium Alloys

Although the use of riveting as a joining method is not new, many of the early papers regarding riveting have dealt with the rivet material itself and/or the rivet material and process issues. From a theoretical perspective, the riveting process shares some fundamental similarities to cold expansion. In both cases, interference is created that expands the initial diameter of the hole, this means that some of the early closed form work looking at pressurization of holes could provide estimates of the residual strain resulting from riveting[57,71,72]. One of the first papers to build on the similarity between these two processes and to try and determine fatigue life differences was the work of Petrak and Stewart [49] in 1974. They compared cold expanded and riveted coupons in the zero load transfer configuration to prove their hypothesis that the degree of expansion was the main driver in improving fatigue life. The results showed that in the zero load transfer (ZLT) configuration, the rivets provided approximately the same fatigue life benefit as hole cold expansion. This result agreed with their original test hypothesis, since both treatments resulted in approximately the same degree of hole expansion. Fox and Withers[73] also noticed the similarity between cold expansion and riveting and showed, using synchrotron and neutron diffraction, that the residual stresses resulting from cold expansion and riveting were similar in magnitude and direction.   In a follow up paper Fox and Withers[74] used riveted, zero load transfer coupons to measure stress relaxation around the rivet after various numbers of fatigue cycles. The results from x-ray diffraction showed that the residual stress profile around the rivet was similar to that seen in cold expansion. Interestingly, although a relatively

high maximum applied stress (240 MPa) was used, crack nucleation was not biased towards the rivet hole, but was varied in terms of location, an indication of the effectiveness of the rivets compressive residual stress field to reinforcing the hole.

Given the difficulties making strain measurements in the region under the rivet head, the few papers that do provide experimental measurements typically relied on either x-ray diffraction[73-76] or strain gauges[23,77-79] to measure the strains resulting from the riveting process. One interesting approach to obtain results closer to the rivet hole was that of Fitzgerald and Cohen[75] who used x-ray diffraction to make residual stress measurements of the rivet head itself. Although this did not address the issue of the residual stresses beneath the manufactured head, it did provide experimental data as close to the pilot hole as possible and showed that the compressive residual stress close to the hole is a function of squeeze force. Fox and Withers[73] used the same approach, except using both synchrotron x-ray and neutron diffraction, to make both in-plane and through thickness residual strain measurements. A summary of the radial and hoop strains surrounding the 7.9 mm diameter rivet used in Fox and Withers'[73] experiment is reproduced in Figure 10, and shows compressive strains in the immediate vicinity of the rivet and tensile hoop strain as one moves away from the rivet center.
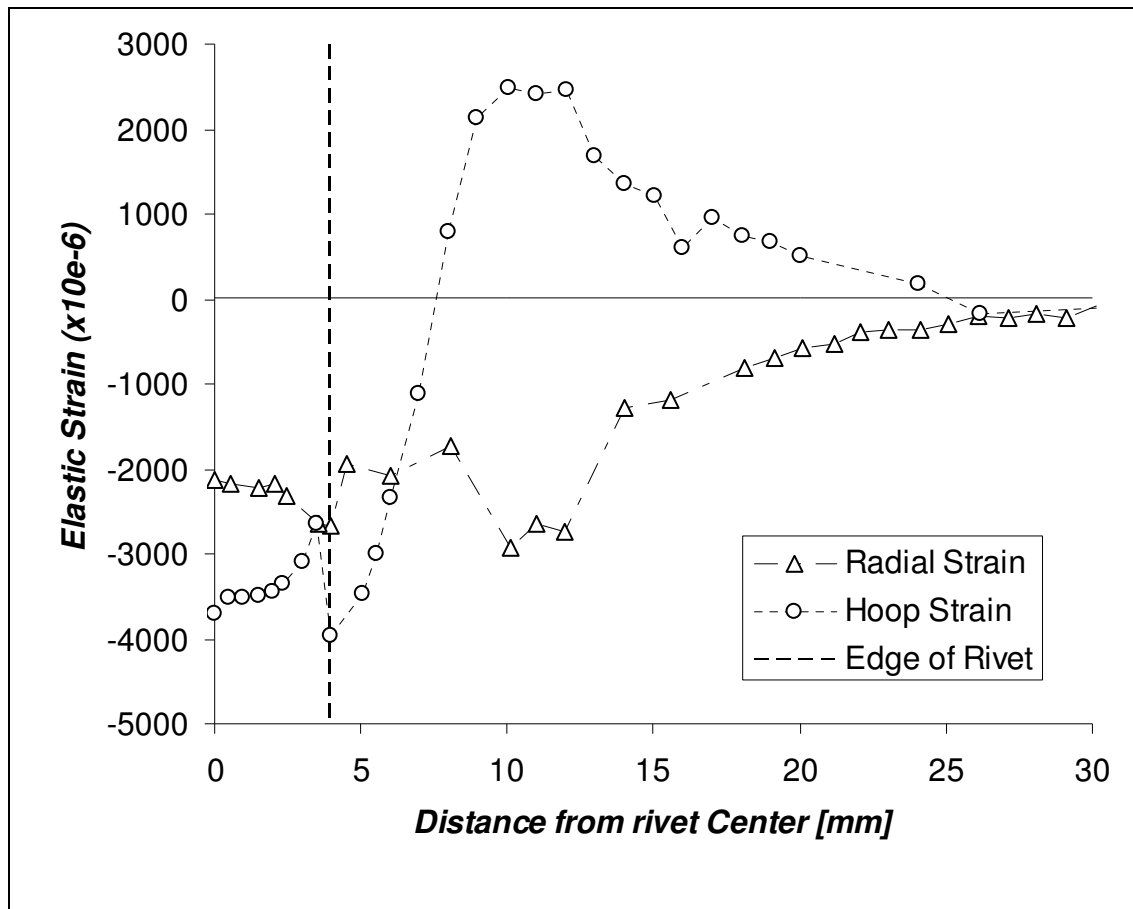
Figure 10: Radial and hoop strains due to the riveting process from Fox and Withers[73].
Vertical line denotes interface between rivet and coupon. Dashed lines are provided for
clarity only

The more common approach to estimating the strains resulting from riveting has been

to simulate the riveting process computationally using finite element software. Although

the focus of this research is experimental, a brief review of some of the analytical work

done on riveting can be helpful as it can provide some understanding of what is

happening under both the driven and manufactured head, as well as provide some

additional context for discussing the fatigue results that were obtained.

Attempts to better model the riveting process and take into account the through

thickness compression resulting from the formation of the driven head first entered the

open literature with Muller's[23] work in 1995. This work in many ways appears to be seminal publication on the effects of riveting, dealing with both experimental and analytical aspects of riveting in aluminum and fiber metal laminate materials. Muller[23] used both closed form and finite element analysis to back up the results of his fatigue tests on riveted lap joints, which demonstrated the importance of controlling riveting squeeze force and showed that the fatigue life of a riveted joint could be correlated to the squeeze force applied to the rivet.

Muller's suggestion that the clamping force played an important role in fatigue life led researchers such as Deng and Hutchinson[80] and Li and Shi[77] to work at developing better finite element models to simulate the creation of this clamping force. Li and Shi[77] developed a 2D axisymmetric model that was validated using both strain gauges and neutron diffraction and that could account for the compressive stress developed between the driven and manufactured heads and the surface of the joint. The use of strain gauges for validating various aspects of an FEA model is quite commonplace in the literature with researchers such as Langrand et al[78] and Markiewicz et al[79] using strain gauge instrumented coupons to validate the performance of their computer models. Other validation approaches have included using the force-deflection history of the rivet to validate the computer model; an approach that was used by Szolwinski and Farris[81]. Although more current papers by researchers such as Atre and Johnson[82] and Szymczyk et al[83] present 3D FEA models of the riveting process, there is little

experimental validation of the results and the results themselves are not quite comprehensive enough to support the experimental work in this research. An older, but more comprehensive research program on the residual strains induced during the riveting process was presented by Rans and Straznicky[84] who used the experimental results of Li and Shi[77] to validate their 3D FEA model. Of greatest interest from their findings was the observation that the residual stresses beneath the rivet head were primarily due to the rivet clamping force and not to the radial expansion of the rivet shank.

3.3 Riveting of Fiber Metal Laminate Materials

A review of the open literature showed that only a small body of knowledge exists focusing specifically on riveting and its effect on fiber metal laminate materials [23,85-88]. The impetus for many of these investigations was sparked by Muller[23] who performed a comprehensive series of tests as part of his doctoral dissertation looking at the fatigue behaviour of riveted lap joints in both 2024-T3 aluminum and fiber metal laminate materials. One of the key findings from his investigation was that rivet squeeze force played a key role in controlling the fatigue life of riveted joints and that higher squeeze forces could result in an order of magnitude increase in fatigue life. He also looked at direct comparisons between 2024-T3 aluminum and FML 3 riveted joints and showed that the qualitative response to riveting is similar in both materials, but that FML 3 riveted joints had a greater fatigue life with crack growth and residual strength reductions occurring more slowly. Muller[23] also noted that the location of crack nucleation tended to move away from the rivet center as the rivet squeeze force was

increased. Muller[23] inspected coupons after riveting and did not find any delamination in FML due to the riveting process. The results of an experimental test program by Lazzeri[88] on riveted FML and monolithic 2024-T3 coupons produced similar conclusions. Ryan and Monaghan[85] built on this research with a finite element based investigation looking at the potential failure modes in an unnamed grade of FML and 2024-T3 aluminum during the riveting process. They took a more basic approach to modeling FML properties in that two FEA simulations were run, one with material properties representative of the longitudinal direction and one representative of the transverse direction in the material. Although Ryan and Monaghan[85] claim to have derived material property information from actual tensile tests, the results do not conform to those for any standard grade of FML[10] with a significant difference in elastic modulus between the longitudinal direction (53.9 GPa) and the transverse directions (9.4 GPa). This fact notwithstanding, Ryan and Monaghan's[85] work suggests the potential for internal delamination of the FML plies, a suggestion that was also corroborated by Rans et al[86]. Ryan and Monaghan's[85] FEA models also showed a non-homogenous expansion of the FML due to the radial expansion of the rivet, which makes sense given the extremely orthotropic nature of the FML they used, but the magnitude of which may vary when less orthotropic FML grades are used. The finite element based study done by Rans et al[86] is the only published paper to date examining and comparing the residual stresses due to riveting in both fiber metal laminate and 2024-T3 aluminum materials. Although no direct experimental validation

was provided in this paper, the displacement of the rivet bucking bar was compared to experimental data and showed very good agreement to the FEA results. Overall, the finite element results showed that riveting in FML resulted in larger regions of plasticity with smaller gradients of residual stress. Rans et al[86] attributed this behaviour to the apparent strain hardening caused by the fiber layers. This was surmised to be because of the redistribution of load to the fiber layers once the aluminum layers started yielding. Experimental corroboration of this phenomenon will be difficult since the image correlation results are limited to the region adjacent to the manufactured or formed head of the rivet.

3.4   Cold Expansion of Fiber Metal Laminate Materials

A search of the literature regarding the effect of cold expansion on fiber metal laminates revealed only two papers. The first was a Masters thesis by van der Kuip[89] that looked at fatigue crack growth in FML 3-3/2, FML 3-5/4 and aluminum 2024-T3 coupons that had been cold expanded. Overall, van der Kuip[89] noted that crack growth rates on the entry and exit sides were noticeably different, with cold expansion extending the life in the early stage of the fatigue process on the exit side of the coupon, but not as significantly on the entry side. Mechanical removal of the individual aluminum layers showed that a typical triangular delamination pattern existed with the base of the triangle near the edge of the hole and the tip coincident with the crack tip.

The second paper was by Rans et al[90] who used computational methods to simulate the cold expansion process in FML 3-2/1. Rans et al[90] noted that expansion of the

aluminum layers in the FML occurred as a result of two mechanisms: first was radial pressure from the oversized mandrel and second was a shear-driven expansion from the elastic expansion of the prepreg layer. Although delamination between the fiber and aluminum layers was not modeled in this work, Rans et al[90] commented on the likelihood that a small amount of delamination around the cold expanded hole could be beneficial as this would extend the length over which the internal glass fibers could stretch, thus serving to better retard any cracks that form. While delamination is certainly helpful for reducing crack propagation, if delamination around the hole is confirmed, this would suggest that cold expansion may not be able to extend life in the early stage of the fatigue process. Overall Rans et al's[90] study reinforced the suitability of performing hole cold expansion process on FML.

3.5   Discussion: Identification of Knowledge Gaps

One of the main purposes for reviewing the literature regarding riveting and cold expansion in both aluminum and fiber metal laminates was to identify gaps in the current body of research that needed to be addressed. The concept behind cold expansion is not new and a substantial body of knowledge has been built up looking at both the fatigue performance as well as the strain fields generated by cold expansion. The literature clearly shows that although cold expansion does provide an increase in fatigue life, the most common method used for cold expansion, split sleeve cold expansion, produces unequal residual compressive stresses on the entry and exit faces of the coupon. The increased residual compressive stress on the exit face better serve to retard crack formation, and, thus, crack nucleation and growth tend to occur first on the entry face. This is one phenomenon that has not been deeply explored in fiber

metal laminate materials. A review of the literature shows that no full-field experimental methods have been used to measure strains in fiber metal laminate materials and that including this as part of the current research could help better understand the root cause of this phenomena in both FML as well as in 2024-T3 aluminum. Another issue that can be addressed by this research is whether cold expansion is more effective at extending fatigue life during the early stage of the fatigue process or during the crack propagation stage. This is an important question for FML materials because being able to extend fatigue life during the early stage of the fatigue process would improve one shortcoming with FML and increase the acceptance of this material in aerospace structures. Although this issue has been addressed by researchers for aluminum, there is some degree of contradiction in the conclusions. Two possible reasons for these contradictions exist, the first is that the definition of short crack length is somewhat arbitrary and is defined differently by researchers; the second is that not all researchers have recognized the difference in residual stress between the entry and exit faces and this difference can also play an important role in retarding short crack growth.

From a fatigue perspective, the riveting of aluminum and FML joints has been addressed by many researchers. Experimentally the greater focus has been on the fatigue life, while far fewer researchers have attempted to measure the strains during the riveting process in aluminum. In FML, the experimental focus has been almost entirely on the fatigue life of riveted FML coupons while only finite element models have been used to estimate full-field strains during riveting. Experimentally measuring riveting strains is difficult in general due to the fact that the rivet covers the region

closest to the hole, however the experimental methods used in this research should provide some measure of the strain field surrounding the rivet, and, when combined with analytical modeling, may provide some insight into what is occurring during the riveting process. Although zero load transfer (ZLT) coupons are less popular since they are representative of lower-load aircraft attachments, several researchers[49,91,92] have used this geometry in 2024-T3 to study fatigue life during riveting. No researchers to date have used this geometry in FML. Another area that has not been addressed is the concept of optimizing FML for improved performance in cold expansion and riveting. Ideally, the strain measurements taken both statically and during fatigue cycling will provide suggestions for new FML layups that may improve both riveting and cold expansion behaviour. Although the cold expansion and riveting of aluminum alloys are topics of some familiarity to researchers, extending this research into the realm of fiber metal laminates opens up a new avenue of original research.

4.0   RATIONAL DECISION MAKING PROCESS

For the static measurements of strain during the cold expansion and riveting process, several possible experimental mechanics techniques were available for use. To better evaluate each of these technologies in an objective manner, the rational decision methodology put forward by Olden and Patterson[93] was used. This method involves identifying essential (hard) and non-essential (soft) attributes for the technologies under consideration. The hard attributes are used to narrow down the list of potential technologies and then an expert panel is employed to rate the importance of each non-essential (soft) attribute as well as to score each technology on a scale of 1-10 in terms of its ability to fulfill each of the attributes.

4.1   Technology Selection for Measuring Strains During Cold Expansion

The essential attributes for measuring strains during cold expansion, included the ability to measure strain quantitatively (Att 1) and the ability to measure strain both during and after the cold working process (Att 2). The technique to be selected also had to be able to deal with the geometric constraints imposed by the FTI cold expansion equipment (Att 3) and had to be easily available (Att 4).   Based on these criteria a wide range of techniques were evaluated, with the results of the evaluation detailed in Table 4. A brief summary of the reason for excluding some of the techniques is presented in Table 5. The evaluation process resulted in the following techniques being chosen: digital image correlation (DIC), in-plane moiré (MI), holographic interferometry (HI), reflection photoelasticity (RP), electronic speckle pattern interferometry (ESPI) and strain gauges (SG).

Table 4: Viability of various experimental mechanics techniques for measuring strains during cold expansion

Technique	Att 1	Att 2	Att 3	Att 4	Viable
Brittle Lacqueur	N	N	N	N	N
Caustics	N	N	N	N	N
Electronic Speckle Interferometry	Y	Y	Y	Y	Y
Digital Image Correlation	Y	Y	Y	Y	Y
Moire - in plane	Y	Y	Y	Y	Y
Moire - shadow	N	N	Y	Y	N
Moire - projection	N	N	Y	Y	N
Holographic Interferometry	Y	Y	Y	Y	Y
Photoelasticity - transmission	Y	N	Y	Y	N
Strain gauges	Y	Y	Y	Y	Y
Thermoelasticity	Y	N	N	Y	N
Photoelasticity - reflection	Y	Y	Y	Y	Y

Table 5: Techniques excluded from decision making and reason for exclusion

Technique	Reason for Exclusion
Brittle Lacquer	Technique is qualitative only
Transmission Caustics	Requires a transparent specimen
Reflection Caustics	Optical access to singularity
Shadow Moiré	Measures surface deformation
Projection Moiré	Measures surface deformation
Transmission photoelasticity	Requires a transparent specimen
Thermoelasticity	Requires cyclic loading

For the techniques that were chosen, the following non-essential attributes were

selected for the next level of evaluation (Table 6):

Table 6: List of non-essential attributes for the techniques that met the essential requirements

Non-essential (soft) attributes
Insensitive to test environment
High quality data
No limitation on loading type/amount
Ease of surface preparation
Low cost per test
Real time testing
Low capital cost
Ability to measure strains near hole edge
Compatible with FTI cold expansion tools

The list of non-essential attributes was provided to each member of the expert committee and they were asked to rank the importance of each attribute on a scale of 1-5 (with 1 being the least important and 5 being the most) as well as to rank the performance rating of each technique with respect to each attribute on a scale of 1-10 (with 1 being poor performance and 10 being excellent performance). For each technique the average importance and the average performance were calculated and plotted against one another as shown in Figure 11 to Figure 13. Ideally one would want to see a technique have high performance for the most important attributes and thus a cluster of dots in the upper right hand quadrant of the graphs.
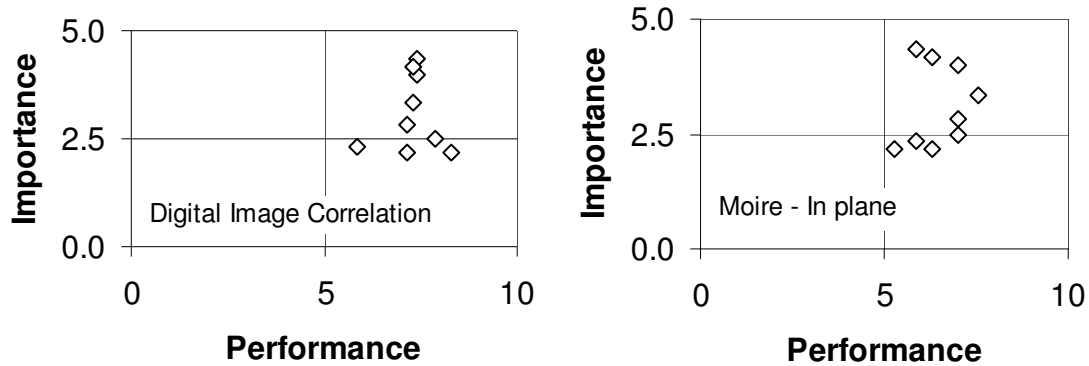
Figure 11: Plot of importance versus performance for digital image correlation and in-plane moiré
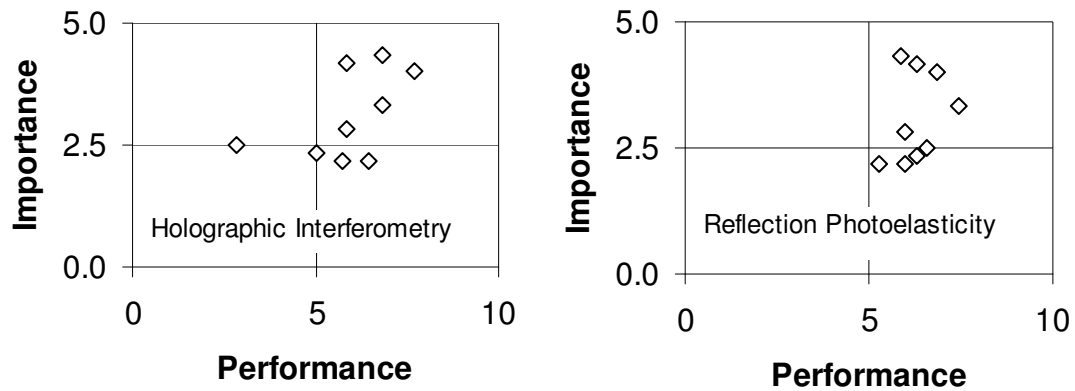
Figure 12: Plot of importance versus performance for holographic interferometry and reflection photoelasticity
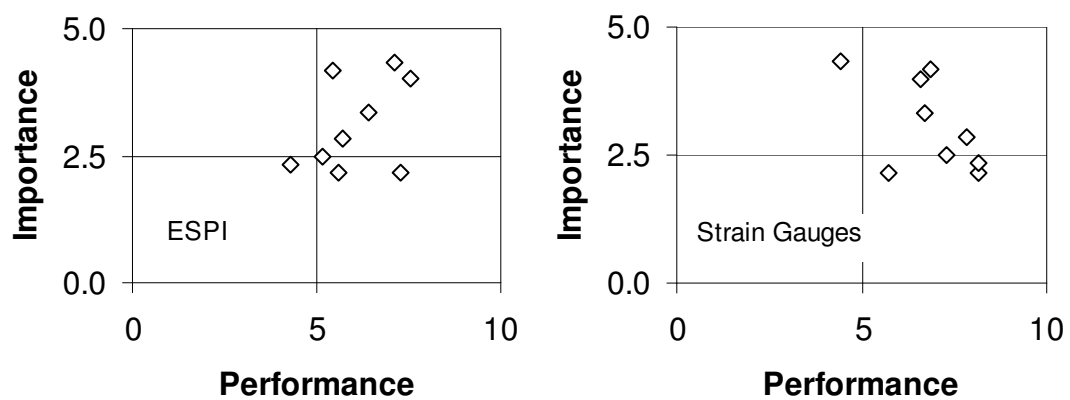
Figure 13: Plot of importance versus performance for electronic speckle pattern interferometry and strain gauges

In addition to examining the distribution of each attribute in terms of the importance and the performance, it is also useful to use a metric that can quantitatively determine the optimum technique for each situation. In this case a cumulative score for each technique was determined by multiplying the average importance of each attribute by the average score given by the expert panel and summing this up for each technique. The final cumulative scores are given in Figure 14, and show that digital image correlation is clearly the optimum technique. Holographic interferometry received the lowest scores overall, while strain gauges were second best, with the remaining three techniques all fairly close in score.
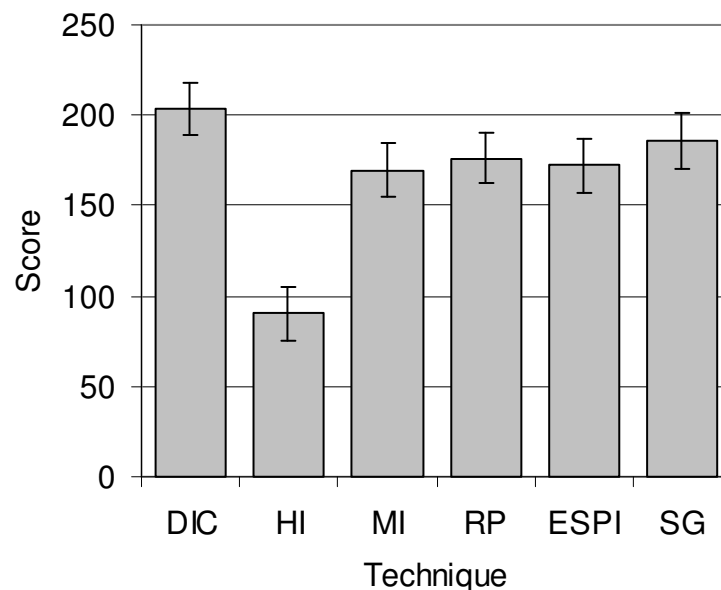
Figure 14: Cumulative scores for each technique evaluated using the rational decision making process

4.2   Technology Selection for Measuring Strains During Riveting

A second case study was performed looking at the essential attributes for measuring strains during the riveting process. These included the ability to measure strain quantitatively (Att 1), the ability to measure strains both during and after the riveting

process (Att 2) as well as ease of availability (Att 3). Based on these criteria a wide range of techniques were evaluated, with the results of the evaluation detailed in Table 7.   The evaluation process resulted in the following techniques being chosen: digital image correlation (DIC), reflection photoelasticity (RP), and strain gauges (SG).   The techniques that were excluded and the reason for their exclusion are provided in Table 8.

 The distribution for each technique in terms of importance versus performance are given in Figure 15 and Figure 16a. The final cumulative scores are given in Figure 16b, and show that digital image correlation is clearly the optimum technique. Reflection photoelasticity received the lowest scores overall, while strain gauges came in second place. The overall results are supported in the literature which showed a number of researchers who used strain gauges to corroborate their results[23,77-79] and even one researcher who used photoelasticity[72].

Table 7: Viability of various experimental mechanics techniques for measuring strains during riveting

Technique	Att 1	Att 2	Att 3	Att 4	Viable
Brittle Lacqueur	N	N	N	N	N
Caustics	N	N	N	N	N
Electronic Speckle Interferometry	Y	N	Y	Y	N
Digital Image Correlation	Y	N	Y	Y	N
Moire - in plane	Y	Y	Y	Y	Y
Moire - shadow	N	N	Y	Y	N
Moire - projection	N	N	Y	Y	N
Holographic Interferometry	Y	N	Y	Y	Y
Photoelasticity - transmission	Y	N	Y	Y	N
Strain gauges	Y	Y	Y	Y	Y
Thermoelasticity	Y	N	Y	Y	N
Photoelasticity - reflection	Y	Y	Y	Y	Y

Table 8: Techniques excluded from decision making and reason for exclusion

Technique	Reason for Exclusion
Brittle Lacquer	Technique is qualitative only
Transmission Caustics	Requires a transparent specimen
Reflection Caustics	Optical access to singularity
Shadow Moiré	Measures surface deformation
Moiré – in plane	Rivet makes grid installation difficult
Projection Moiré	Measures surface deformation
Transmission photoelasticity	Requires a transparent specimen
Thermoelasticity	Requires cyclic loading
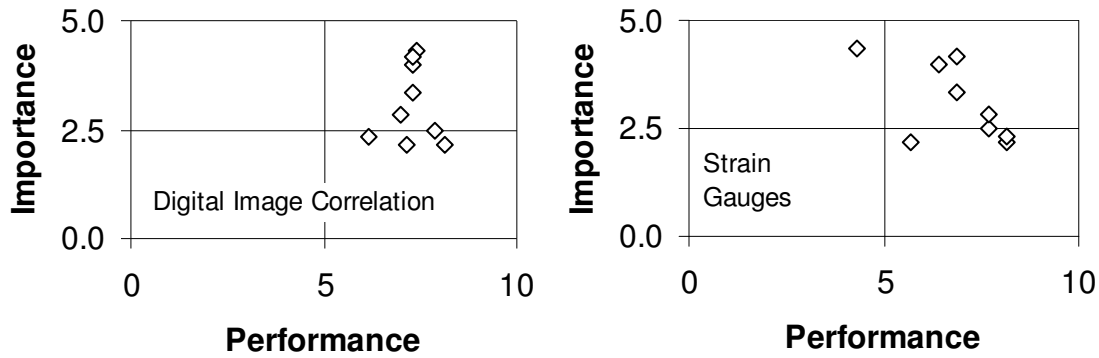
Figure 15: Plot of importance versus performance for digital image correlation and strain gauges

(a)

(b)
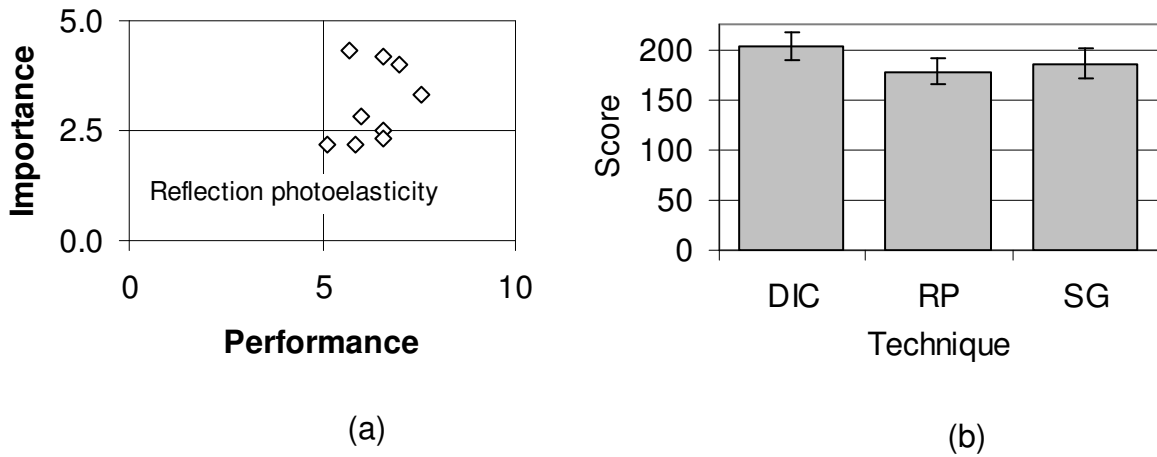
Figure 16: a) Plot of importance versus performance for reflection photoelasticity b) Cumulative scores for each technique evaluated using the rational decision making process

4.3   Discussion

The outcome from the rational decision making process suggested that digital image correlation should be explored for measuring strains during both the cold expansion and riveting process. Both strain gauges and reflection photoelasticity scored highly during both case studies, and the literature did highlight several researchers who used strain gauges for making strain measurements after cold expansion[44,55,94] and riveting[77-]

[79,95]. Reflection photoelasticity was also used to better understand the strains after

cold expansion[44,96]. The outcome from the process is dependent on the parameters

provided as constraints, and different parameters may have resulted in the inclusion or

exclusion of one or more techniques. The results of this analysis are applicable to the

static testing of the cold expanded and riveted coupons and although these results have

some relevance to the fatigue testing portion of this research, thermoelastic stress

analysis was one technique that could only be used during the application of fatigue

loads. With only one image correlation system available, thermoelastic stress analysis

was used during the fatigue portion of the testing to measure strains on the opposite

face of the coupon. The selection of thermoelastic stress analysis was mainly due to

the availability of the equipment and its compatibility with fatigue loading.

5.0 EXPERIMENTAL METHODS

The experimental methods section details the procedures involved in both the static and fatigue testing of the aluminum and fiber metal laminate coupons, including both the cold expansion and riveting procedures as well information regarding both the digital image correlation and thermoelastic stress analysis system. An overview of the production methodology for the FML panels is also provided along with residual stress measurements for each panel.

5.1 Static Test Setup

Identical test fixtures and digital image correlation (DIC) stereo camera setups were used to measure surface strains during both the hole cold expansion and the riveting process for both the aluminum and FML coupons (Figure 17). The DIC system was comprised of two digital video cameras, mounted on tripods, (Retiga 1300, Qimaging Inc, Burnaby BC) with resolutions of 1280 x 1024 pixels. For the field of view used in the static test, the effective spatial resolution was 0.052 mm/pixel and the coupon surface was illuminated using two high intensity LED light arrays (Siemens-Nerlite Inc, Nashua NH). All coupons were positioned on a custom, three-pin support fixture, to ensure consistent location of the specimens with respect to the cameras (Figure 17). The sensitivity of a particular DIC setup is a function of the speckle distribution, the image capture hardware and the correlation algorithm. The sensitivity of the DIC setup used was determined empirically after system calibration by capturing multiple reference images and processing them through the correlation algorithm. .The overall strain sensitivity in all cases was better than ±50 µε and the out of plane displacement (w) sensitivity was better than ±0.0015 mm .
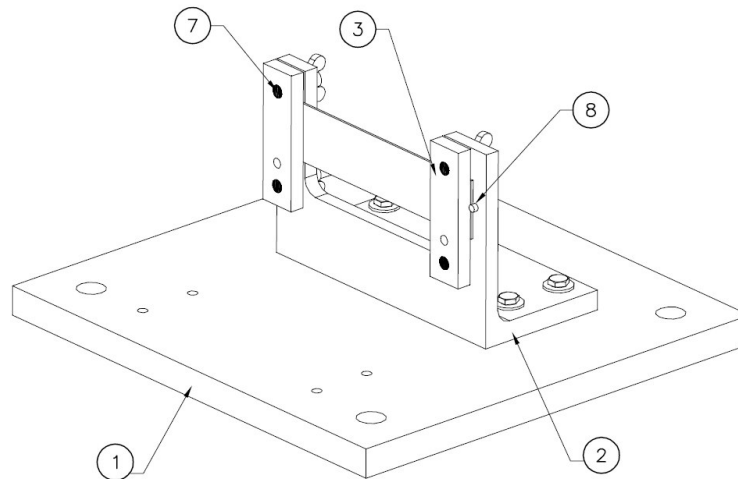
Figure 17: Isometric diagram of coupon retention fixture

5.1.1 Hole Cold Expansion Procedure

The pilot hole for all coupons was drilled on a milling machine, using a carbide drill bit.

Drill speed was approximately 500-800 rpm, with a low feed force and no cutting fluid, to

avoid contaminating the fibre layers[97]. Centre drilling was performed first, followed by a

starter drill and then a reamer to ensure consistent hole sizing.

Hole cold expansion was performed using a manual cold working tool (HP-10, FTI inc)

that was positioned behind the coupon and supported by a V block (Figure 18). This

manual cold expansion process has been used in previous research[43] and is fully

certified for aerospace use by the manufacture (Fatigue Technology Inc.). The split

sleeve was placed at the root of the mandrel and both were passed through the hole.

The mandrel was then pulled through the hole by turning the nut at the back of the

manual cold expansion tool. Images were captured at every 2 full turns until resistance

was felt as a result of the mandrel/split-sleeve contacting the hole. At that point, the

process continued with images taken every quarter turn (90º degree rotation) until the mandrel passed completely through the hole. The split sleeve and mandrel were removed from the coupon and a final image was taken.
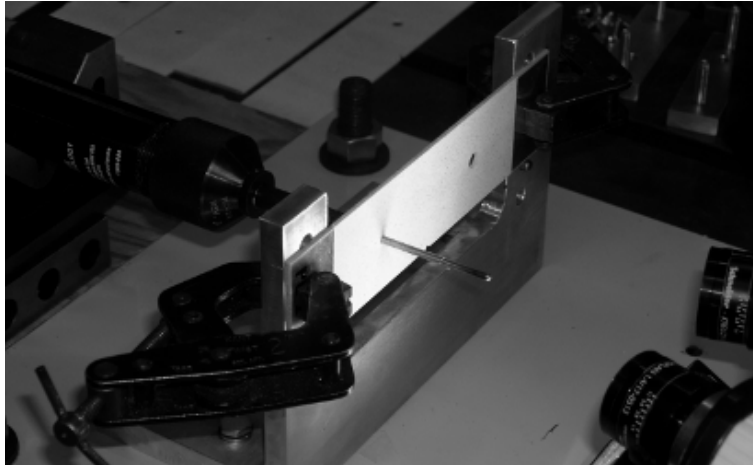
Figure 18: Initial mandrel placement for hole cold expansion process

Mandrel displacement was calculated by measuring the axial displacement of the tool caused by each rotation of the nut. Linear regression of the axial displacement versus tool rotation data (Figure 19) showed that the mandrel displaced 1.25 mm/360º degree of tool rotation and this value was used for subsequent cold expansion tests.

$y = 3.452E-03x$
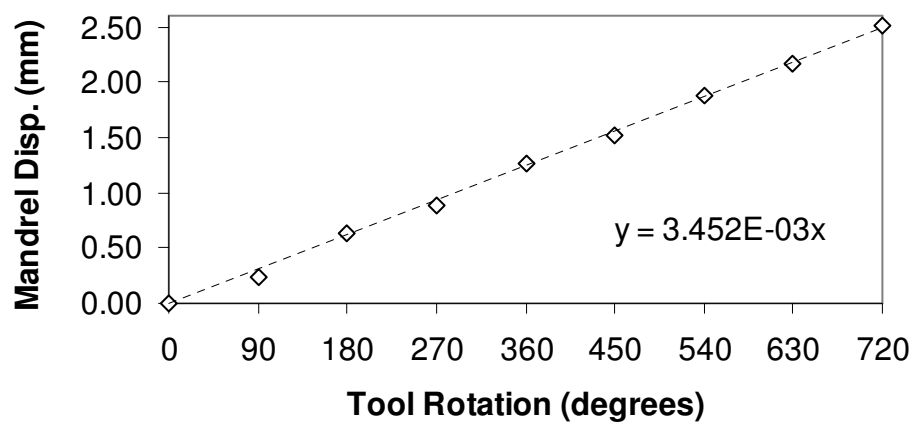
Figure 19: Mandrel displacement vs. tool rotation

Hole cold expansion was performed using a size 8-1-N split sleeve with a nominal

starting hole diameter of 6.40 mm and total interference of approximately 4.1%.

Incremental deformed images were taken from the mandrel entry side of the coupon as

the mandrel was displaced through the coupon thickness. The deformed images were

processed using Vic-3D software (Correlated Solutions Inc, Columbia SC) over an area

of interest spanning the entire height of the coupon. All images were processed with a

subset size of 17 pixels, a step size of 5 pixels and a strain window of 15 pixels.

5.1.2 Riveting procedure

The same test fixture and camera setup was used for the riveted coupons. Prior to

riveting, the coupons were painted white and speckled with black paint using a precision

spray gun. To ensure no paint adhered to the inner surface of the hole, a plug was

inserted into each hole during the painting process. A manual rivet tool was positioned

behind the coupon, supported by a V block (Figure 20). An initial image without the rivet

was used as the reference image when processing the data.

For the static testing, universal head rivets (MS20470AD-5) with a nominal diameter of

3.96 mm (0.156 inches) made from 2117 aluminum were used. These rivets were

positioned in pilot holes having a nominal diameter of 4.09 mm (0.161 inches) which left

approximately 0.12 mm of clearance around the rivet after installation. The decision to

focus on universal head rivets was made based on the difficulties other researchers had

using counter sunk rivets[86,87]. Although there is no doubt that for aerospace

applications countersunk rivets are important from an aerodynamic perspective,

producing the countersink can have negative implications if the countersink results in

the formation of a "knife-edge" at the metal/fiber laminate junction. Universal rivets

allow for a better comparison to the cold expansion results since the initial pilot hole

does not require any additional preparation and the confounding effect of the

countersink on the fatigue results is removed.
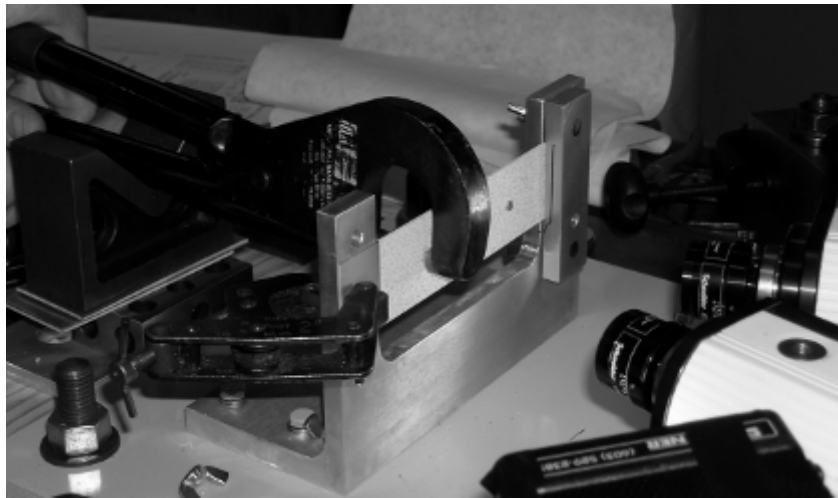
Figure 20: Manual riveting tool and coupon fixture

An initial measurement of the rivet protrusion was made before the riveting process

commenced. Riveting took place in two steps, with the first step being to use the

manual rivet press to set the rivet in the hole at which point an image was taken. Next,

the coupon was taken to a hydraulic rivet press were the final riveting was completed.

The coupon was brought back to the test frame where another image was taken and the

final rivet diameter and protrusion height were measured. If paint chips were visible,

compressed air was used to clean the coupon surface. Incremental deformed images

were taken from the driven side of the rivet as it was compressed to its final protrusion

height. The deformed images were processed using Vic-3D software (Correlated

Solutions Inc, Columbia SC) over an area of interest spanning the height of the coupon

with the rivet and rivet shadow removed, as shown in Figure 21. All rivet images were

processed with a subset size of 17 pixels, a step size of 9 pixels and a strain window of 15 pixels.

(a)   (b)

Note: For interpretation of the references to color in this and all other figures, the reader is referred to the electronic version of this dissertation
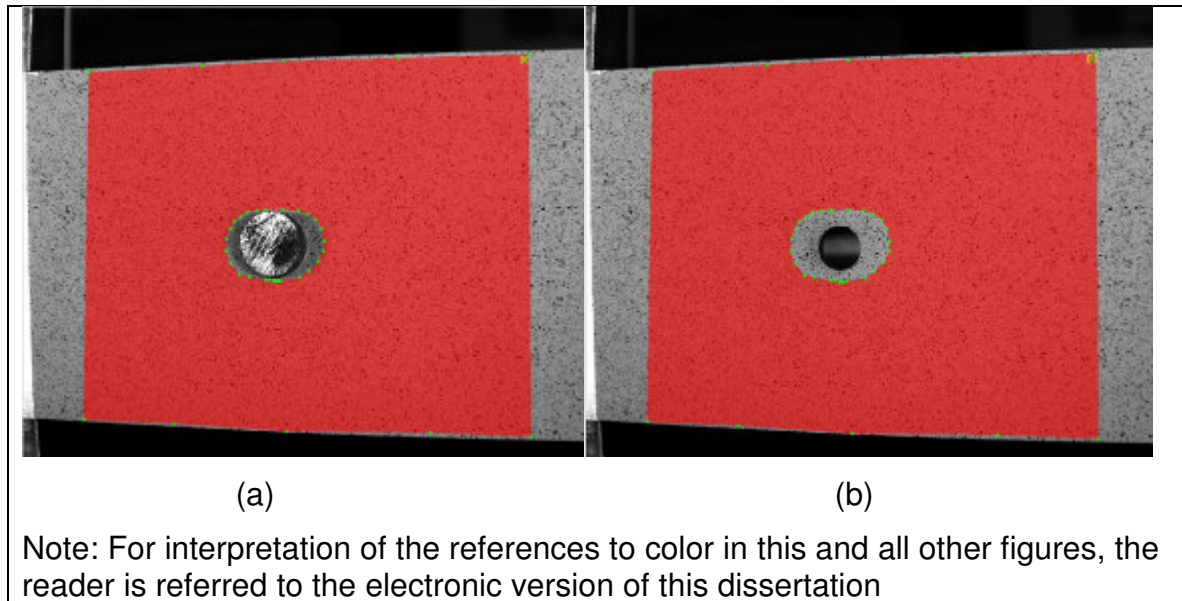
Figure 21: Chosen area of interest for rivet processing. (a) area of interest showing position of rivet and corresponding shadow and (b) actual reference image used.

5.2   Fatigue test setup

Fatigue experiments were conducted in an MTS servohydraulic frame equipped with a 90 kN load cell. Three load levels (8.3, 8.9 and 10 kN) were chosen with a load ratio of R=0.1 and a loading frequency of 10 Hz. These corresponded to net section stresses of 168, 175 and 198 MPa respectively for the unexpanded coupon and approximately 0.8% higher net section stresses for the cold-expanded coupon. Net section stress was defined as the applied load divided by the cross-sectional area (perpendicular to the load) of the specimen at the position of the hole. On the mandrel entry face of the aluminum coupons, optical images were captured using a single high resolution digital video camera (Allied Vision Technologies, Newburyport, MA) with a 1000 x 1000 pixel spatial resolution and a Canon FD zoom lens, coupled to a fiber optic based ring-light

(Olympus Highlight 3000, Center Valley, PA). The optical setup provided a resolution of approximately 15.1 µm/pixel; this combined with a light surface abrasion using 320 grit sandpaper provided sufficient contrast to eliminate the need for any type of additional speckle coating. Initial static images were captured at the maximum and minimum of the prescribed loading cycle and then images were captured at maximum load in 600-cycle increments for the unexpanded coupons and in 1200-cycle increments for the cold-expanded coupons, using a synchronization module in the image capture software (Correlated Solutions Inc, Columbia SC). Analysis of the images was performed using Vic-2D image correlation software (Correlated Solutions Inc, Columbia SC). In addition, the surface crack length was measured using Imagetool (University of Texas Health Science Center, San Antonio, TX) image processing software. On the mandrel exit face of the coupon, a thermoelastic stress analysis was used to measure strains. This technology incorporated a Deltatherm 1410 infrared camera (Stressphotonics Ltd, Madison WC) with a temperature resolution of 2 mK, an InSB detector with 256x256 pixel resolution and zoom lens providing a resolution of 74.8 µm/pixel, was used to perform thermoelastic stress analysis.

For the riveting portion of this test, individual coupons were riveted using an instrumented arbor press (Figure 22a) with a squeeze force of approximately 13.3 kN. Since the coupons were going to be used in fatigue, a special support fixture and loading platen were integrated into the arbor press (Figure 22b) to help standardize the riveting process and reduce any chance of bending the coupons. Standard 3.96 mm diameter aircraft grade rivets (MS20470AD-5) requiring a clearance hole of 4.09 mm

diameter were used and all aluminum and standard FML 4 coupons were tested at a net

stress of 263 MPa. On the driven head side of the riveted coupon the same image

correlation system as above was employed to measure strain while on the

manufactured head side of the coupon the same thermoelastic stress analysis system

was used to provide a strain map proportional to the first strain invariant.

| (a) | (b) |
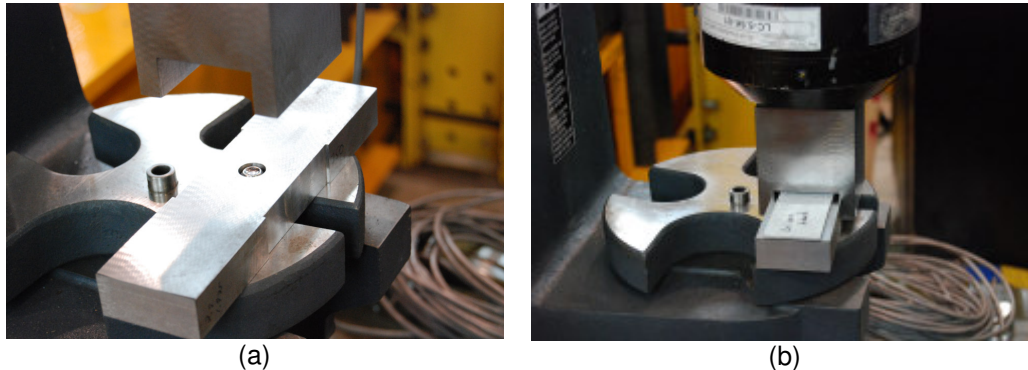
Figure 22: (a) Integral stop and support platen for the coupon during riveting with an (b) instrumented arbor press with load cell

5.3   Production of FML and 2024-T3 Aluminum Coupons

Both the FML 3 and FML 4 grades, as well as the custom FML variants used in this test,

were produced at the National Research Council composite facility[98]. All FML material

was manufactured using FM-94 film adhesive embedded with S2 glass fibers, along

with 0.3 mm thick 2024-T3 aluminum that had been phosphoric acid anodized (PAA)

and coated with BR127 primer to improve adhesion to the FM-94 film adhesive. Figure

23 shows the cure cycle used during the autoclave process for all FML sheets with a

maximum temperature of 121 ºC and a peak pressure of 517 KPa.
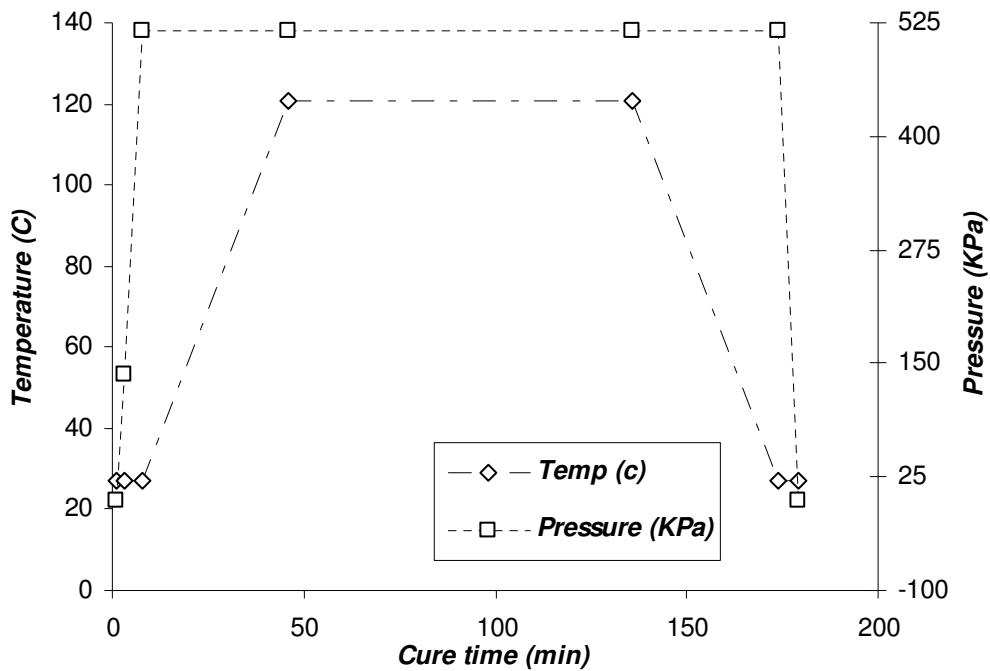
Figure 23: Standard cure cycle used for FML 3 and FML 4

5.4 Design of FML and 2024-T3 Aluminum Coupons

The design of both the static and fatigue test specimens was driven by the cost and size

constraints of the constituent materials used to produce the FML. The anodized

2024-T3 aluminum sheets used for FML production measured approximately 305 mm x

610 mm (12 inches x 24 inches) and were sheared in half to produce panels measuring

305 x 305 mm (12 inches x 12 inches) with the 0º degree orientation of the FML defined

by the rolling direction of the aluminum. Producing panels this size made the

constituent materials easier to handle while still maximizing the use of the FM-94

prepreg that measured 610 mm (24 inches) wide by approximately 200 m (656 feet).

In developing a design for the static coupons, the initial goal was to maximize the

number of coupons that could be produced from an individual panel. For the initial tests,

the coupon design was structured to provide six coupons in a given direction, with two additional coupons in an orthogonal direction (Figure 24). Additional cut plans were used to produce coupons oriented at 45° degrees to the rolling direction of the aluminum, however, this design greatly reduced the number of available coupons (Figure 25). Both the FML and aluminum coupons were cut using a waterjet cutting system, which left a relatively rough finish that required milling 3.175 mm of material on either edge of the coupons. This required that the coupons be made slightly oversized (44.45 mm) so that they could be machined down to their final width of 38.10 mm (1.50 inch). The final static coupon dimensions are shown in Figure 26.

The coupons used for fatigue testing had similar orientations and shape but were cut to 203 mm (8.0 inch) in length to allow them to be gripped in the servohydraulic load frame. To compensate for the extra length of the fatigue coupons, only one transverse coupon per sheet could be produced (Figure 27). The dimensions of the post water jet, machined coupons are provided in Figure 28. For the final phase of fatigue testing coupons were cut in the 0º, 45º and 90º degree orientation and a separate cut plan was used that allowed for only two coupons in each material orientation (Figure 29).
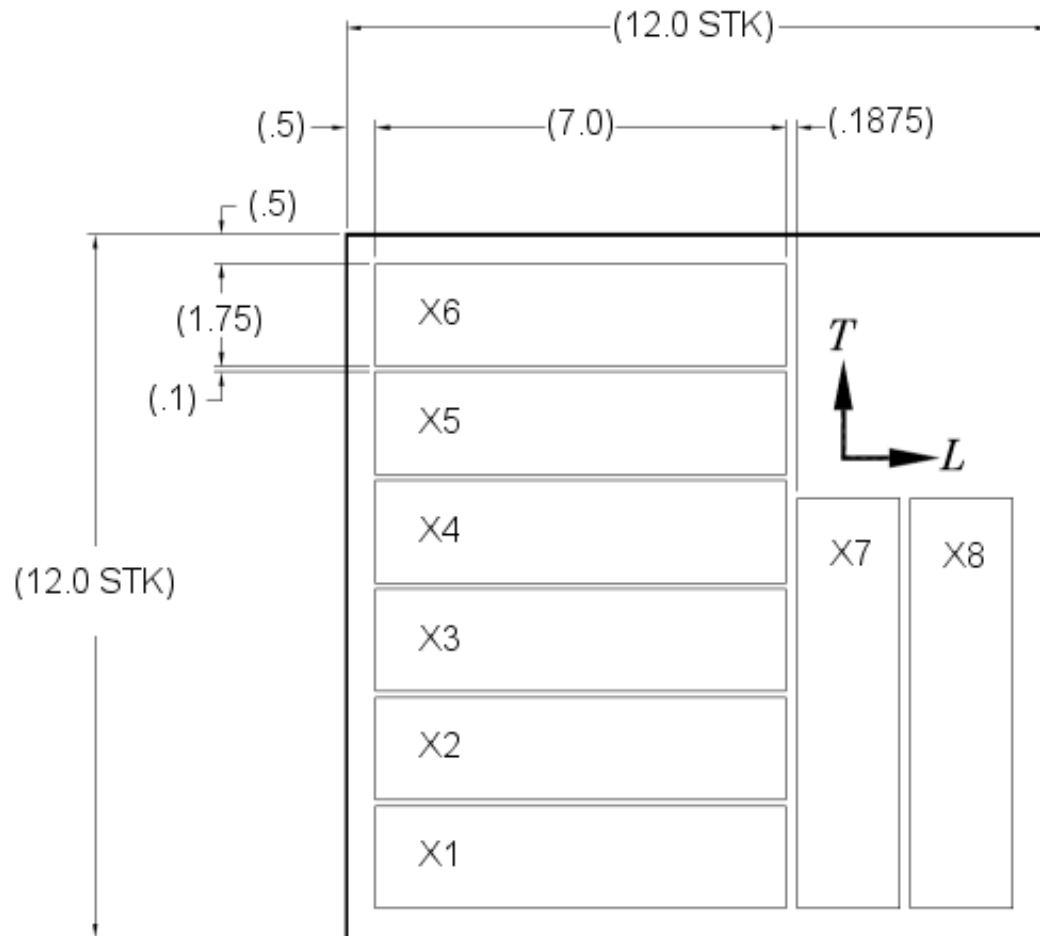
Figure 24: Layout for standard static test coupons (dimensions in inches)
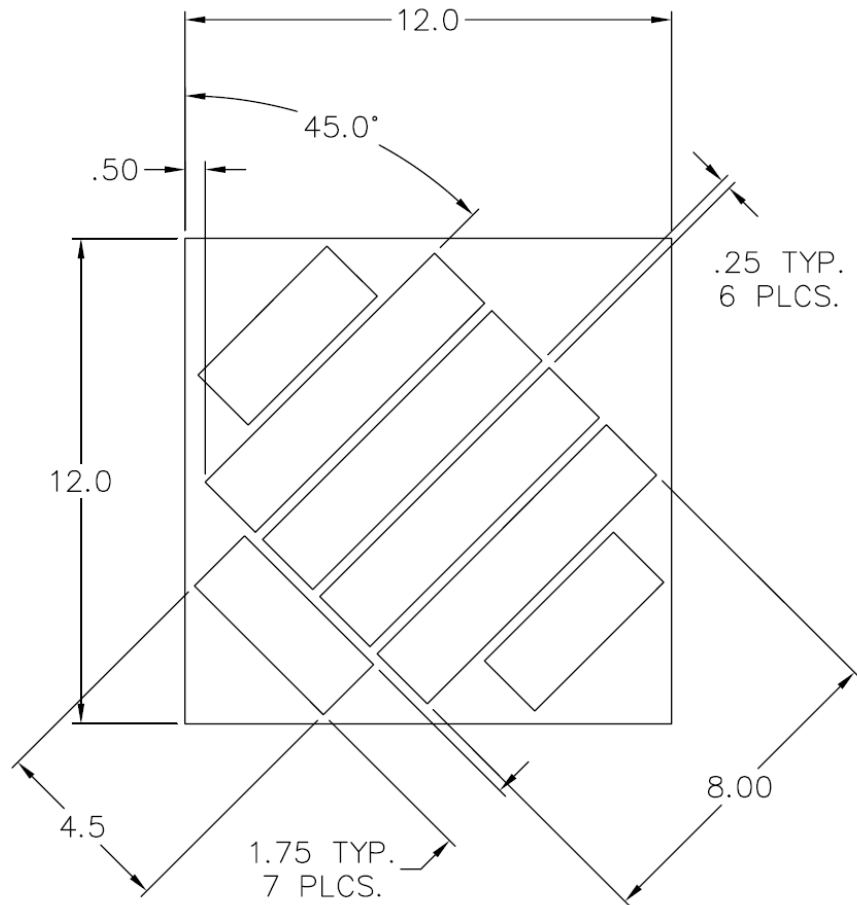
Figure 25: Layout for 45º static coupons (dimensions in inches)
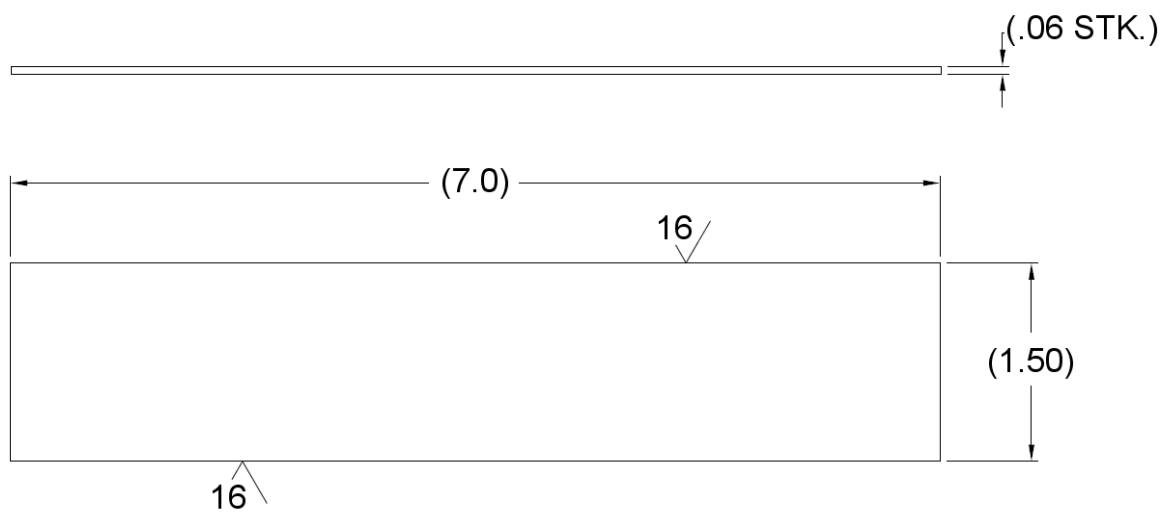
Figure 26: Dimensions of static test coupon after machining (dimensions in inches)
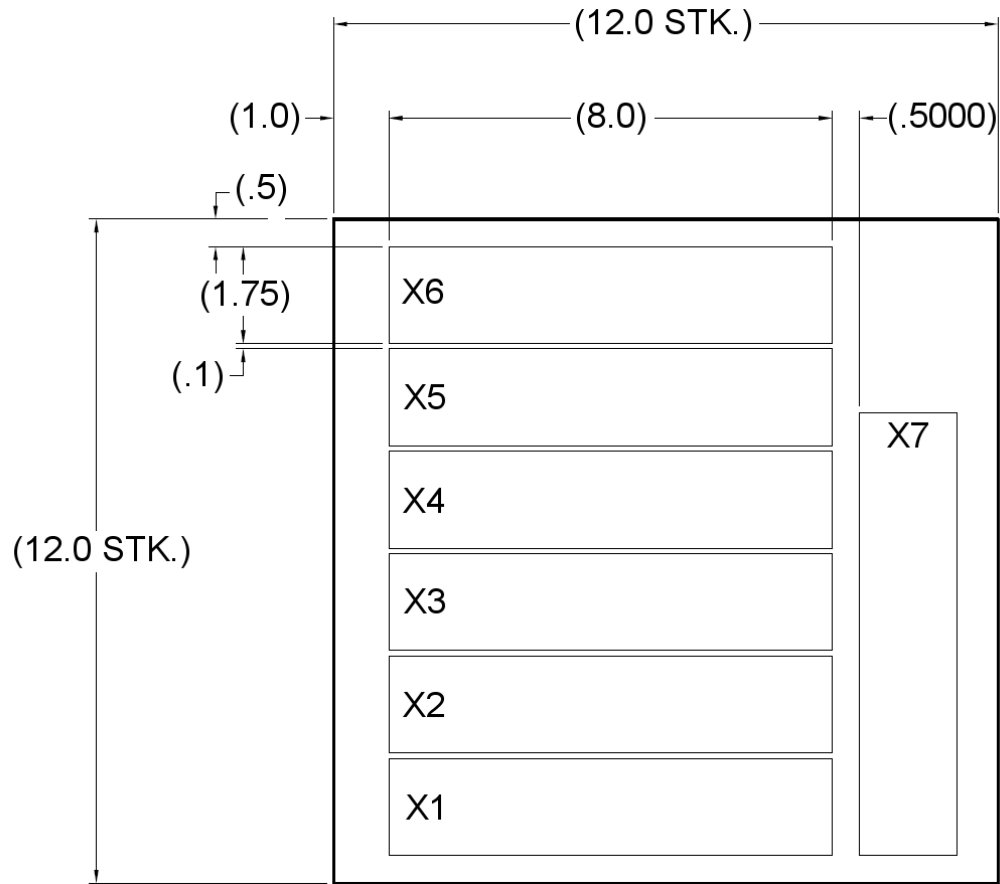
Figure 27: Layout for standard fatigue test coupons (dimensions in inches)
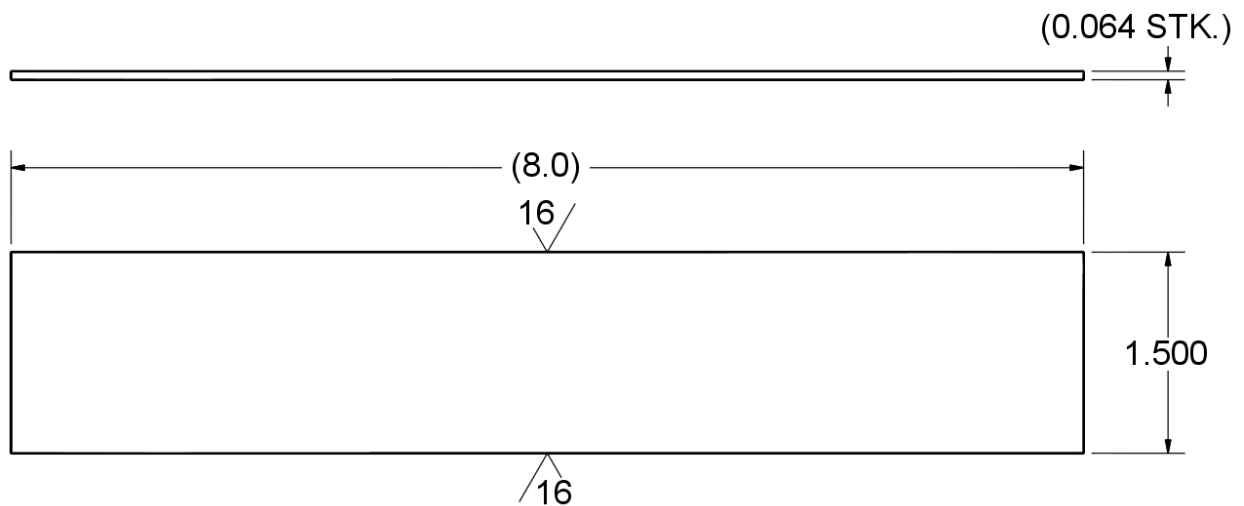
Figure 28: Dimensions of fatigue test coupon after machining (dimensions in inches)
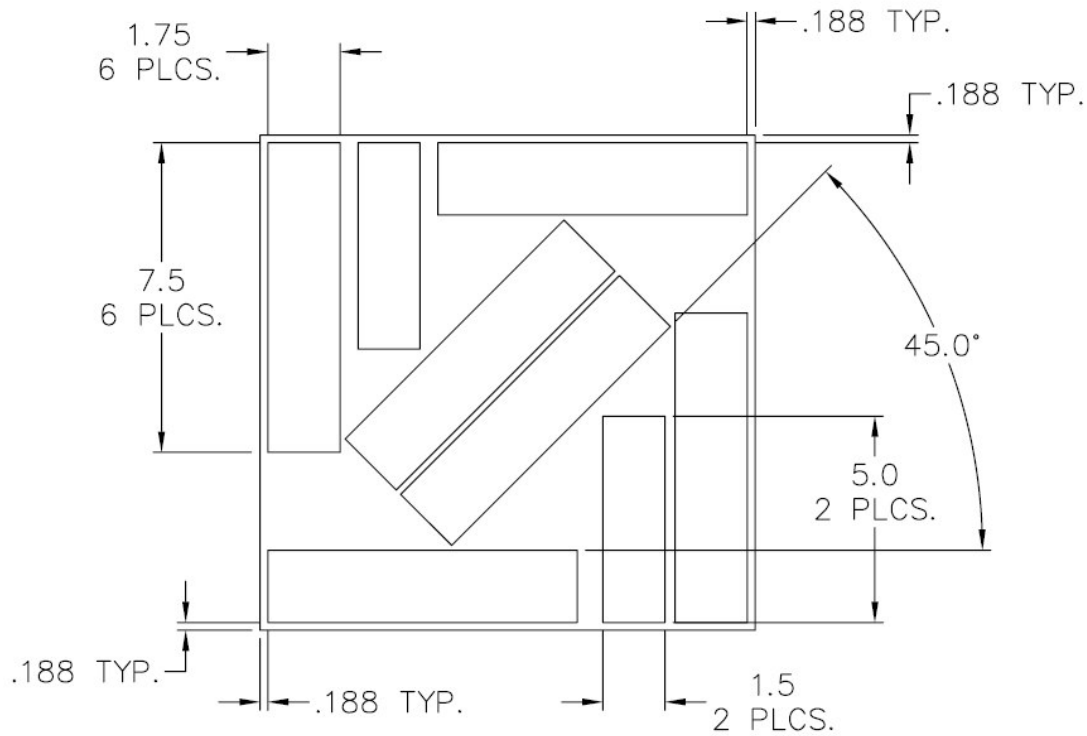
Figure 29: Layout for multi directional fatigue coupons (dimensions in inches)

5.5   Residual Stress Measurement of FML Panels

The literature on FML clearly acknowledges the effect that tensile residual stress in the

aluminum layers, caused by the manufacturing process, plays on fatigue life[1-3,99].

Measuring the residual stress experimentally is a difficult procedure that is often done

using strain gauges. For the purpose of this research program, strain gauges were not

ideal since they would have had to be mechanically removed before water jet cutting,

possibly damaging the thin aluminum layer. The non-contact nature of the DIC

technique seemed to suggest that it would be an appropriate technology for measuring

residual strains on the FML panels, however a fair number of challenges still existed. In

order to ensure the integrity of the panels, the edge of each panel was masked off after

assembly and just before autoclaving. At this point the panels were speckled. Early

73

testing with standard spray paints (Krylon Flat Industrial Acrylic Lacquer Spray Paint, Krylon Inc) showed that the heat from the autoclave caused the pattern to distort, but this was solved by moving to high temperature paints (Tremclad High Heat Enamel Flat Black, Tremclad Inc). Although the high temperature paints did not distort after autoclaving, the breather cloth placed over the panels caused the background finish to fade slightly and affected the overall contrast pre- and post-test. The eventual solution was to speckle only the panels with black paint, which provided enough contrast for the correlation algorithm to process the images. A rigid mounting frame was built to precisely locate each panel both pre- and post-autoclaving (Figure 30)

Figure 30: Experimental setup for FML panel residual strain measurement

Although the overall results were adequate, the small changes in the paint colour due to the high temperature, as well as the relatively low strain values in the FML panels resulted in more background noise, increasing the strain sensitivity to ±150 µε. As a result, strain values over the entire area of each panel were extracted and averaged out. Since the average residual strain values extracted from each panel were in the

elastic range, Hooke's law for orthotropic materials was used to perform strain to stress conversion using the material properties from Table 1 and the following equations:

$$\sigma_1 = \frac{E_1}{1 - \nu_{12}\nu_{21}} \cdot \varepsilon_1 + \frac{\nu_{12}E_2}{1 - \nu_{12}\nu_{21}} \cdot \varepsilon_2 \qquad\qquad 5.5.1$$

$$\sigma_2 = \frac{\nu_{12}E_2}{1 - \nu_{12}\nu_{21}} \cdot \varepsilon_1 + \frac{E_1}{1 - \nu_{12}\nu_{21}} \cdot \varepsilon_2 \qquad\qquad 5.5.2$$

where 1 and 2 are the principal directions, σ is the principal stress, E is the elastic modulus and ν is Poisson's ratio.

Sample maximum and minimum principal strain images are shown in Figure 31 and overall results for each panel are given in Table 9.
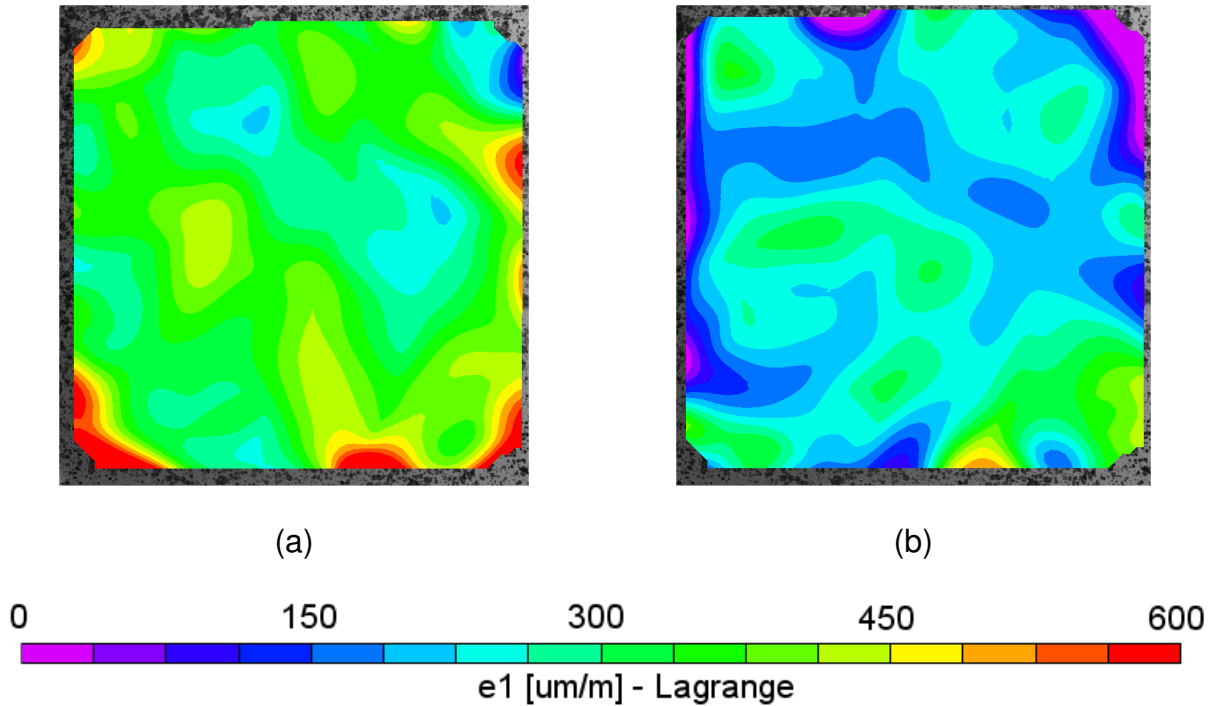
Figure 31: Sample strain results from DIC for (panel 35) FML 4 [-60/0/+60] (a) maximum principal strain and (b) minimum principal strain

Table 9: Summary residual stress results for various types of FML panels

		Residual σ	
		σ1	σ2
FML type		σ1	σ2
FML 3	Avg (MPa)	22.5	8.9
	Std Dev	3.8	5.4
FML 4	Avg (MPa)	19.6	1.4
	Std Dev	9.8	6.8
FML 4 EXP	Avg (MPa)	22.3	13.5
	Std Dev	2.5	4.1

A review of the literature on this subject shows several approaches to measuring residual stresses, including x-ray diffraction[100], neutron diffraction[101], analytical methods[102] and by measuring coupon deflection after processing[103]. Comparing these values for FML 4 to those in the literature shows a reasonable correspondence with the analytical method[102], which calculated an estimated residual stress of 20.26 MPa, and the deflection measurement, which determined an estimated residual stress of 15.1 MPa.

6.0   STATIC TEST RESULTS

All static cold expansion and riveting results were post-processed in two ways. First,

qualitative information regarding the maximum and minimum principal strains was

provided using color images of the strain fields. Secondly, quantitative information was

provided using data extracted from an annulus, centered on each cold expanded and

riveted hole, with a circle radius of 125 pixels or 6.0 mm. The decision to use an

annulus instead of a line profile was due to the asymmetry of the strain field resulting

from cold expansion. The radial co-ordinate system used to extract data from around

the cold expanded and riveted holes is shown in Figure 32.

The extracted data from each of the coupons were grouped so that specific engineering

questions could be answered with the results. For the cold expansion results, one initial

concern was determining the degree of variability inherent in the cold expansion

process. Next, differences in the strain field between the two principal material

orientations were examined, along with a comparison of the resulting strain fields in

FML and aluminum after cold expansion. Additional information was obtained by

examining the differences between FML 3 and FML 4, looking at the effect of cold

expanding coupons in the 45º degree orientation, and examining the strain differences

between the entry and exit face after cold expansion.
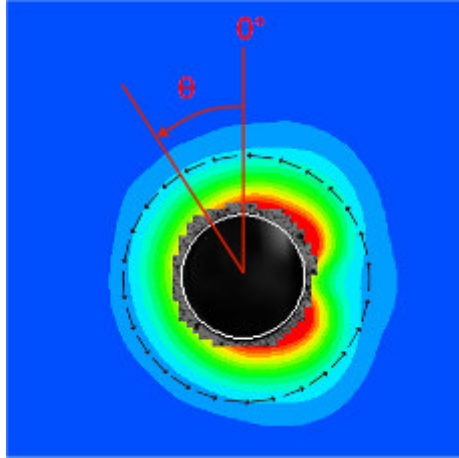
Figure 32: Radial co-ordinate system of the annular data extraction

6.1 Process Variability

The issue of process variability is important for drawing valid conclusions from the experimental data presented. The main source of variability in this stage of the experiment was assumed to be due to the cold expansion process itself. Differences in initial hole diameter, variations in mandrel size, rotation of the split sleeve and other sources of human error were among the likely contributors to any variability in the data. In order to determine the amount of variability in the data that was collected, two separate FML 3 coupons (specimen GAL1 and specimen GAL3) were selected and their strain fields compared. Looking at the plot of maximum principal strain (Figure 33) one notices that the overall pattern of the residual strains are quite similar. Both coupons exhibit the same "butterfly" pattern with the strain field from specimen GAL1 showing a slightly more prominent dip at zero degrees. The two plots of minimum principal strain (Figure 34) also look almost identical, with the compressive strains forming a slight cross shape around the cold expanded hole. Radial line profiles extracted from both sets of data highlight some of the subtle differences between the residual strain fields. The plot of maximum principal strains (Figure 35) shows how

similar the two strain fields are, with the data points overlapping except at 135° degrees where a drop of approximately 300 με is noted. The plot of minimum principal strains (Figure 35) shows greater variability, with a larger strain difference occurring at approximately 320° degrees. Close examination of Figure 34 corroborates this, as in this area the region of compressive residual strain is slightly expanded compared to specimen GAL3. Even though this difference is approximately 2500 microstrain, the relative error in this small region is only about 12% compared with the peak compressive strains seen after cold expansion. Greater variability is to be expected in this region as it is very close to the split sleeve, and the strain data could be influenced by slight variations in sleeve orientation.
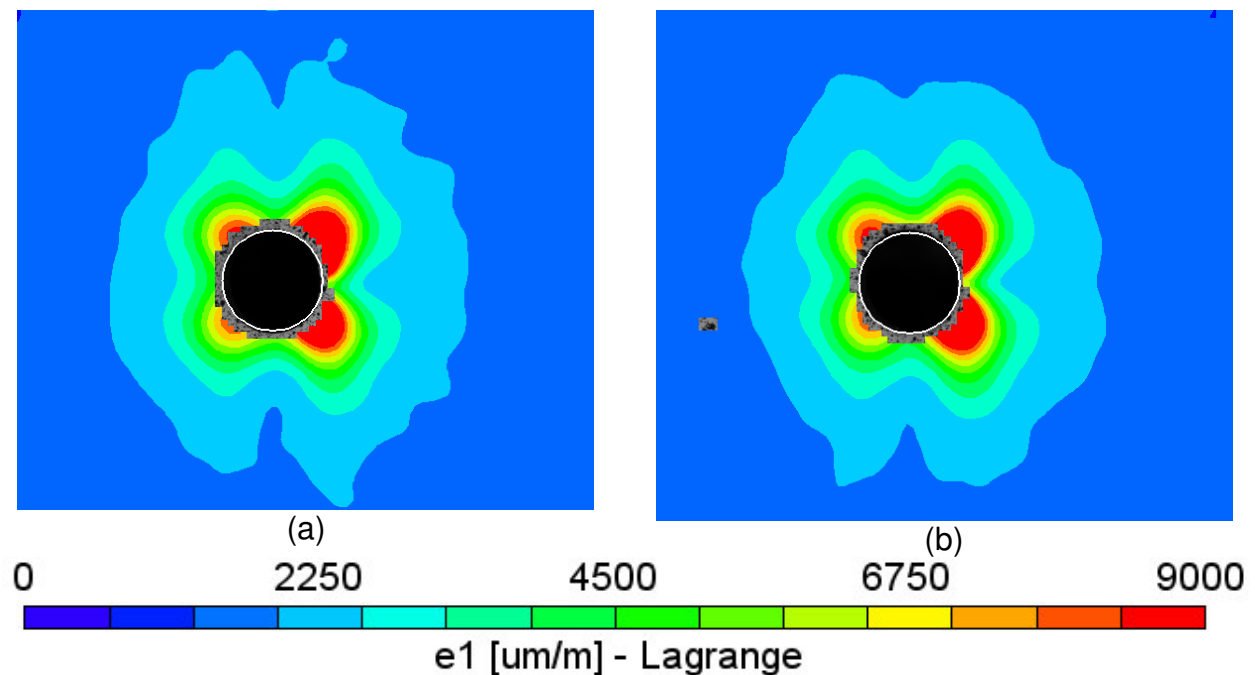
Figure 33: Plot of maximum principal strains on the entry face for two FML 3 coupons (a) specimen GAL1 and (b) specimen GAL3
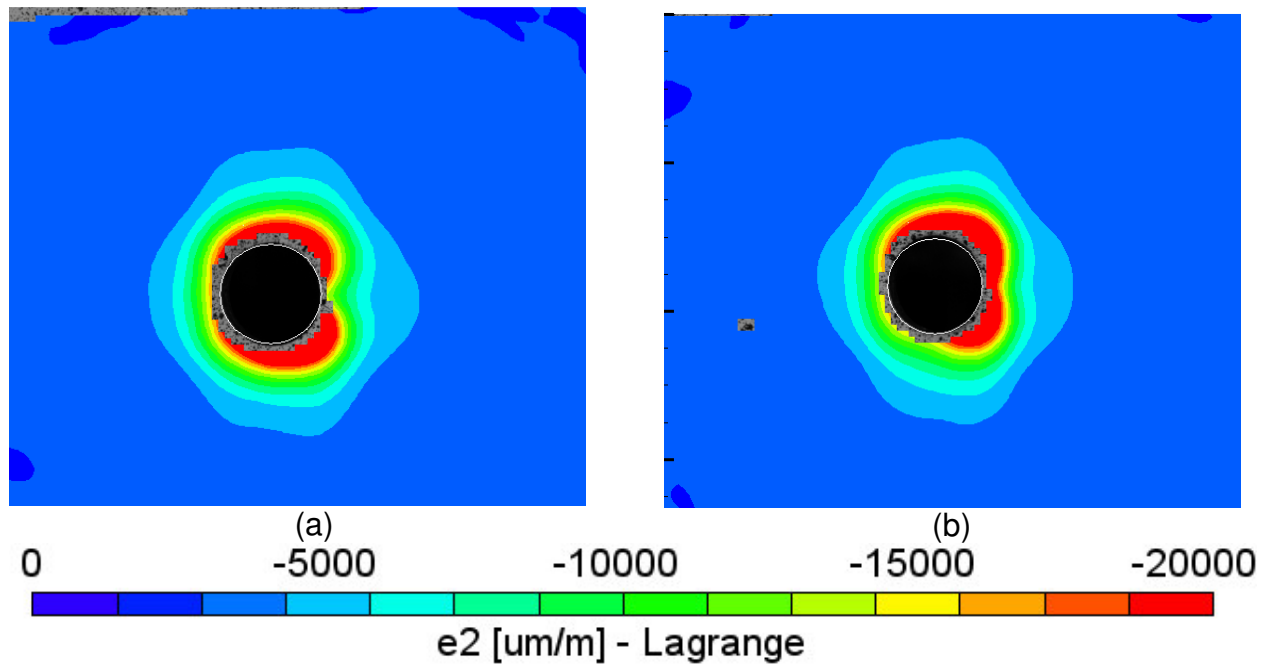
Figure 34: Plot of minimum principal strains on the entry face for two FML 3 coupons (a) specimen GAL1 and (b) specimen GAL3
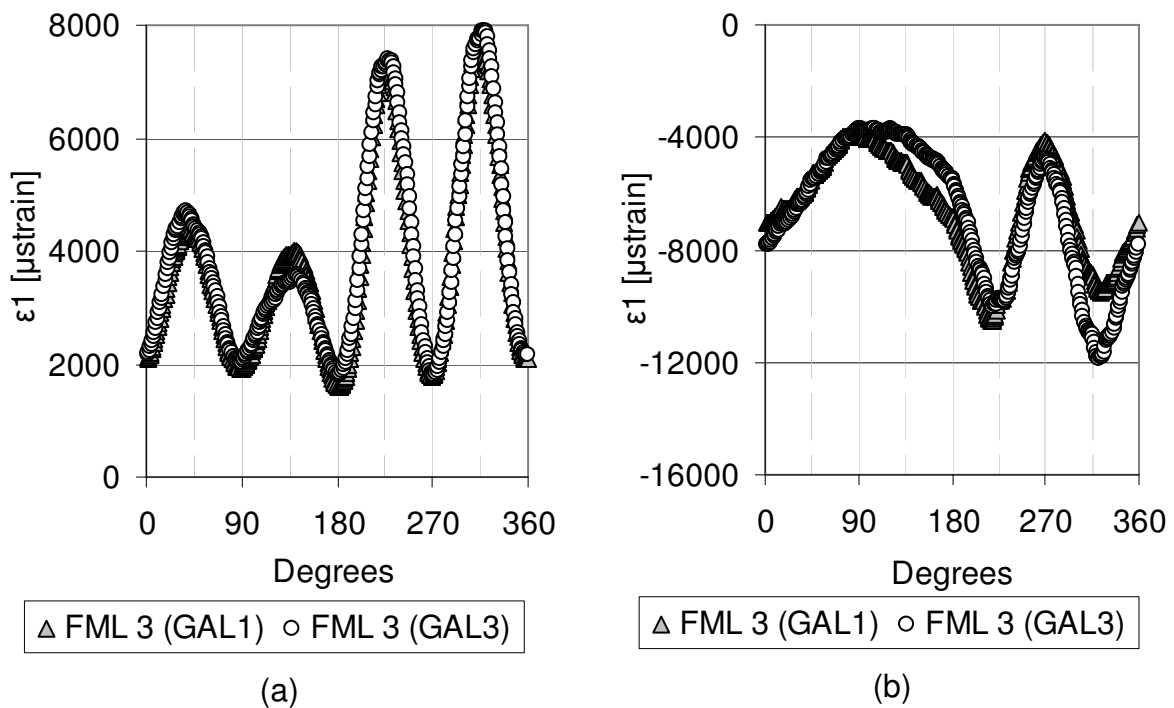
Figure 35: Plot of principal strains for two FML 3 coupons, specimen GAL1 and specimen GAL3) (a) maximum principal strain and (b) minimum principal strain

The same type of comparison was made with the 2024-T3 aluminum coupons in order to verify that the variability was material independent. Figure 36 and Figure 37 show the maximum and minimum principal strains for two aluminum coupons. The overall shape of the strain fields appears to be very comparable, with only small variations evident. The circular line extraction from the data (Figure 38) shows little difference between the strain results, with the greatest difference occurring in the plot of minimum principal strain between 225º and 315º degrees. This corresponds to the location of the split sleeve and reinforces the hypothesis that variability in this area is due to split sleeve orientation or due to the interaction between the edges of the split sleeve and the open hole.
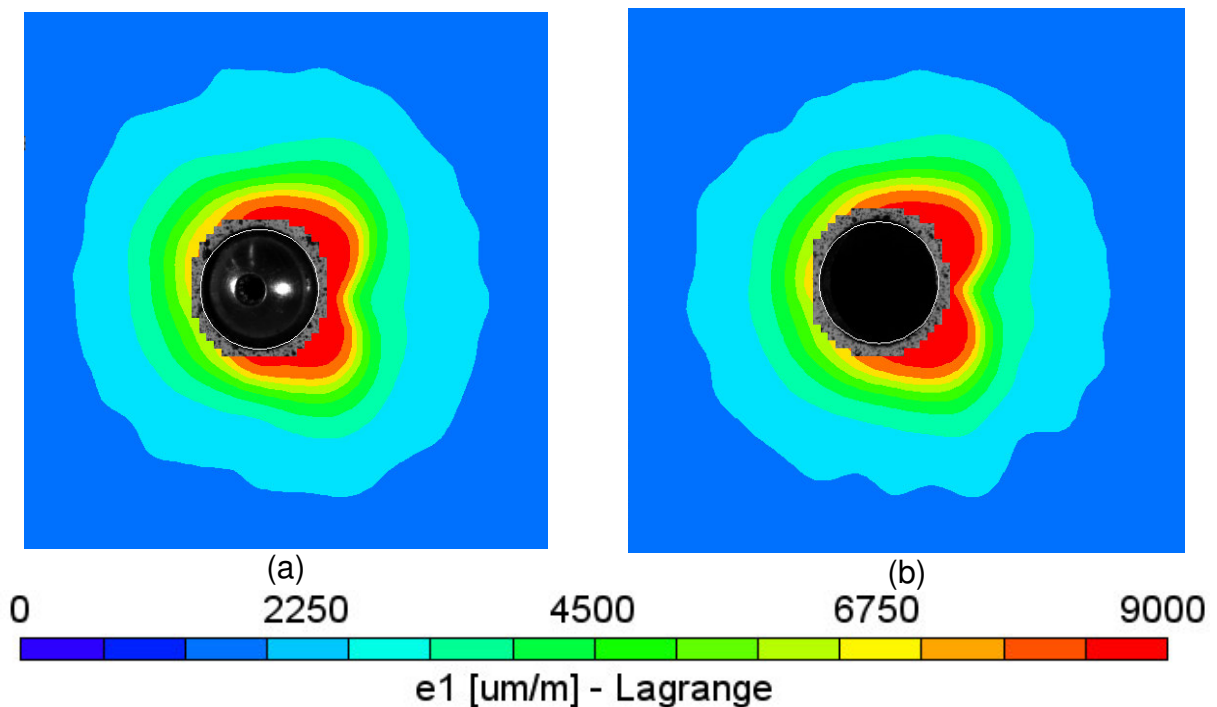
Figure 36: Plot of maximum principal strains on the entry face for two 2024-T3 aluminum coupons (a) specimen AL1 and (b) specimen BL1
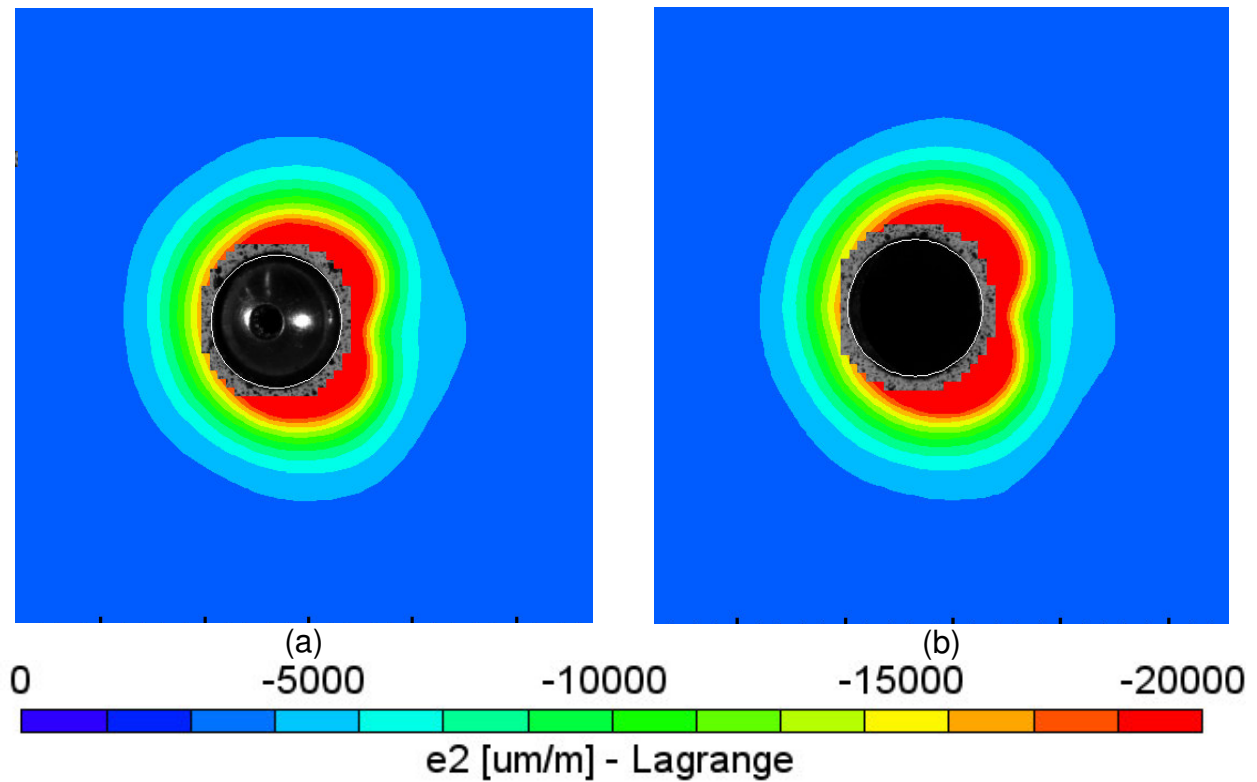
Figure 37: Plot of minimum principal strains on the entry face for 2024-T3 aluminum coupon (a) specimen AL1 and (b) specimen BL1
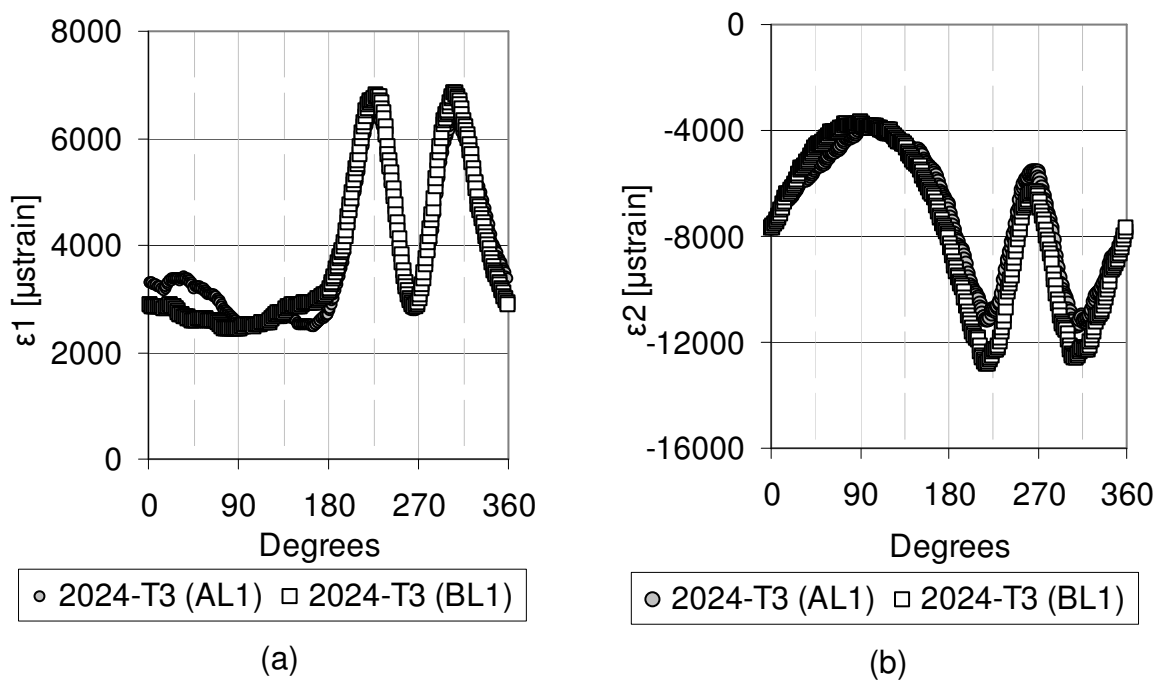
Figure 38: Plot of principal strains for two 2024-T3 aluminum coupons, specimen AL1 and specimen BL1 (a) maximum principal strain and (b) minimum principal strain

6.2 Material Orientation

To study the effect of changing material orientation with respect to the split sleeve direction, a number of FML and 2024-T3 aluminum coupons were produced with the transverse grain direction parallel to the long axis of the coupon. In these cases, the split sleeve direction remained unchanged (to the right in all images) and Figure 39 and Figure 40 show a comparison between the maximum and minimum principal strain results for these longitudinal and transversely oriented coupons.

(a)

(b)
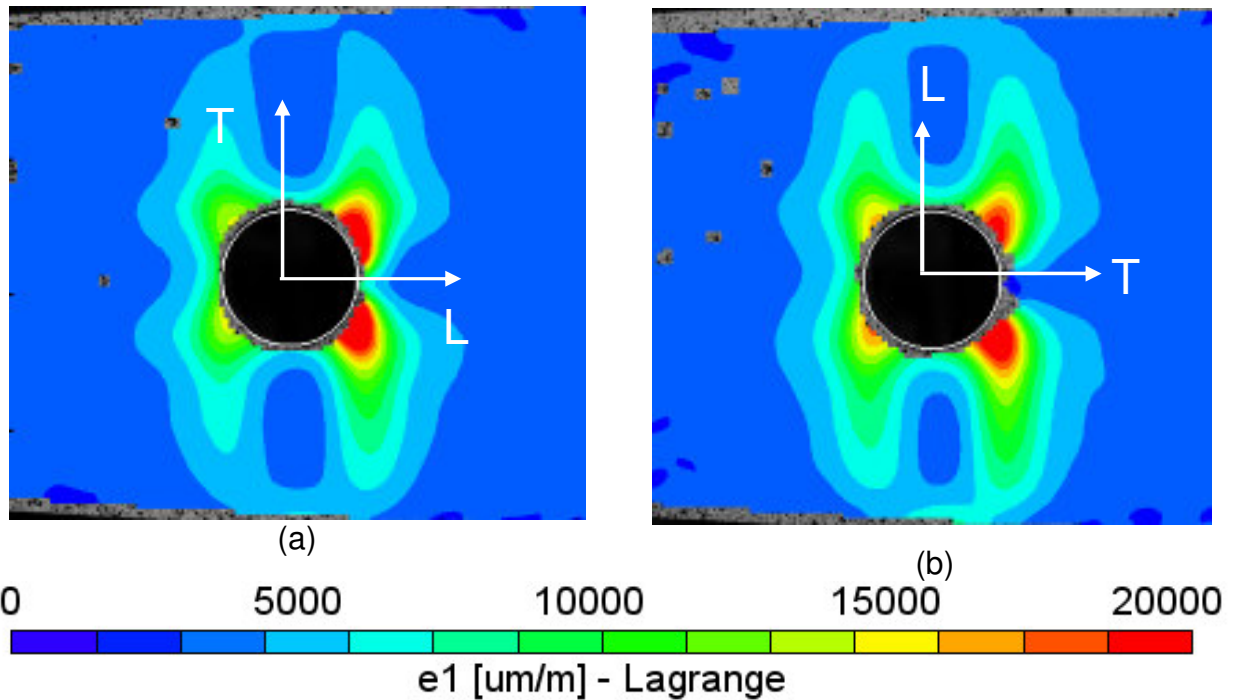
Figure 39: Maximum principal strain on the entry face for two FML 4 coupons (a) specimen GBL1 (longitudinal orientation) and (b) specimen GBT1 (transverse orientation)
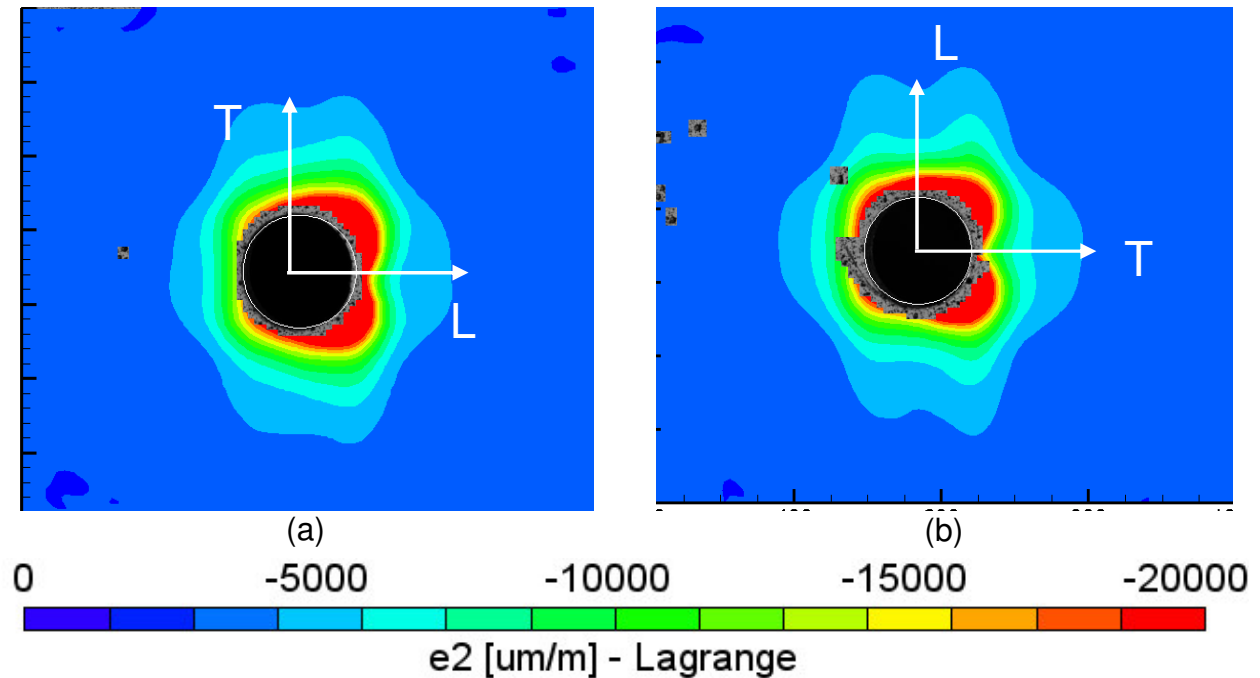
Figure 40: Minimum principal strain on the entry face for two FML 4 coupons (a) specimen GBL1 (longitudinal orientation) and (b) specimen GBT1 (transverse orientation)

Relatively little difference can be seen between the maximum and minimum principal strain patterns of both longitudinal and transverse coupons. This is likely due to the small difference (approximately 11%) in elastic modulus between the longitudinal and transverse material directions. At most this difference would result in a change of approximately 1100 µε, which is less than the difference of one color bar in the above figures, making it difficult to detect qualitatively. Figure 41 shows the results of a circular line extraction from both the longitudinal and transversely oriented coupons. The maximum principal strains are tensile and very little difference is seen between the longitudinal and transverse coupons. The strain profile is very similar to other FML specimens with a trough in the strain field located at 270° degrees. This trough corresponds to the location of the split in the split sleeve and is surrounded by two

peaks; likely from the thin, sharp edges of the split sleeve causing a strain concentration in this localized region of a magnitude just over 8000 µε.

(a)   (b)
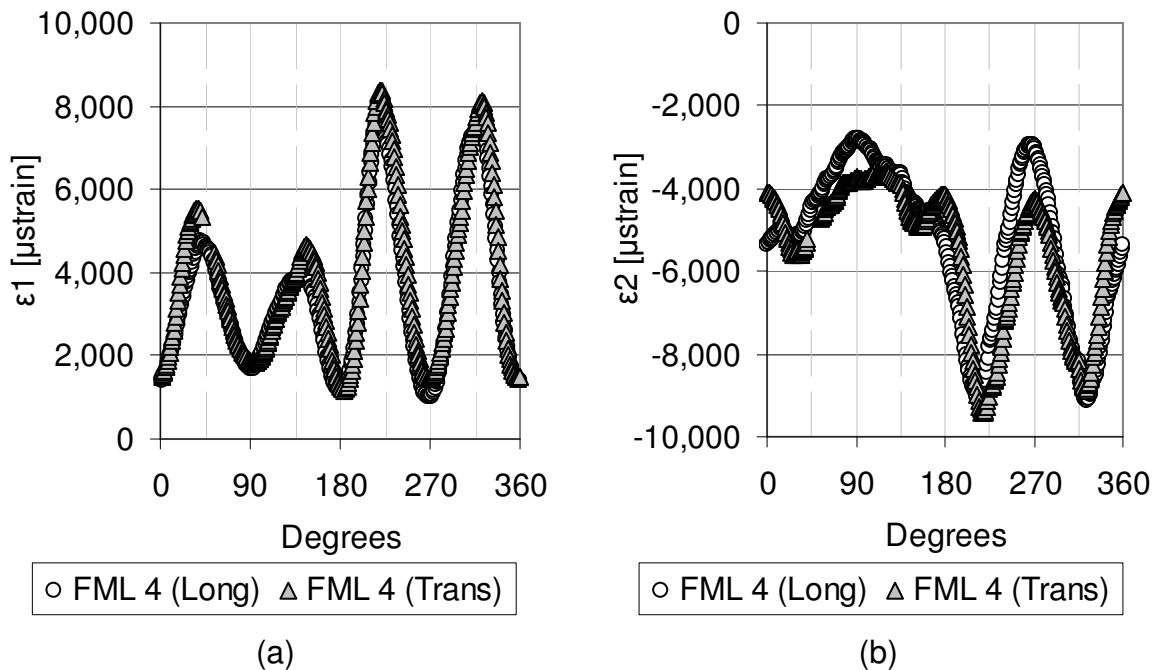
Figure 41: Plot of principal strains for two FML 4 coupons, specimen GBL1 and specimen GBT1 (a) maximum principal strain and (b) minimum principal strain

The same experiment was repeated using aluminum coupons, with the strain results shown in Figure 42 and Figure 43. Comparing the two results, one sees very little evidence of a change in the strain field as a result of varying the material orientation. An examination of the circular line extraction in Figure 44 shows even less variability between the two orientations than with the FML 4 results. The basic shape of the graph is quite representative of a cold expanded aluminum coupon, with a trough in the strain field where the split is located, surrounded by regions of higher strain on either side. The results are not unexpected when one considers that although rolled aluminum has slightly orthotropic properties, the difference in elastic modulus between the longitudinal and transverse directions is negligible compared to FML 4.
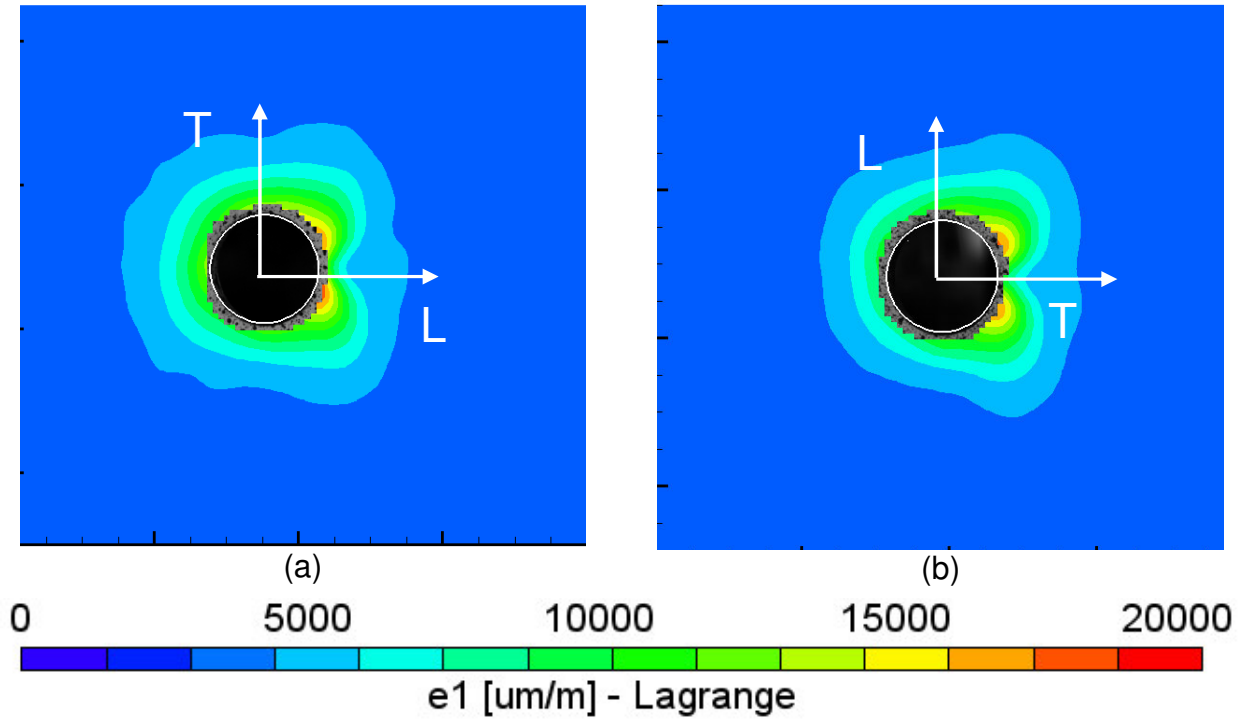
Figure 42: Maximum principal strain on the entry face for 2024-T3 aluminum coupons (a) specimen AL3 (longitudinal orientation) and (b) specimen AT3 (transverse orientation)
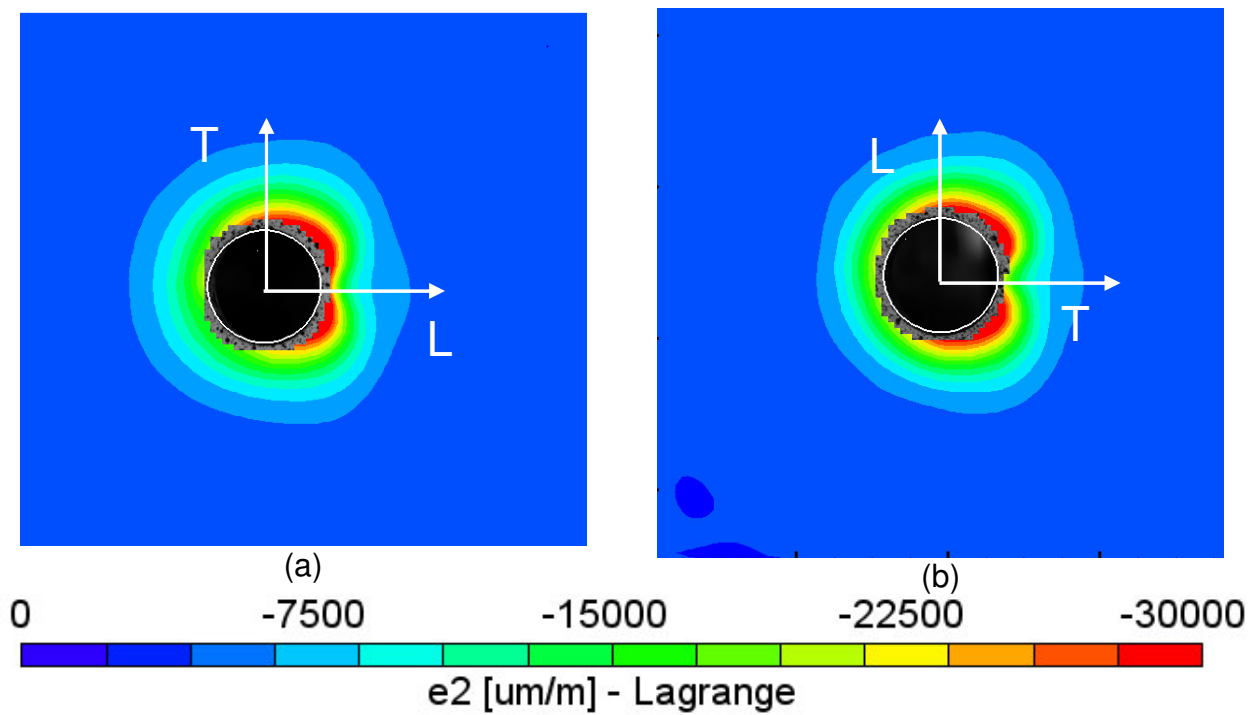
Figure 43: Minimum principal strain on the entry face for 2024-T3 aluminum coupons (a) specimen AL3 (longitudinal orientation) and (b) specimen AT3 (transverse orientation)
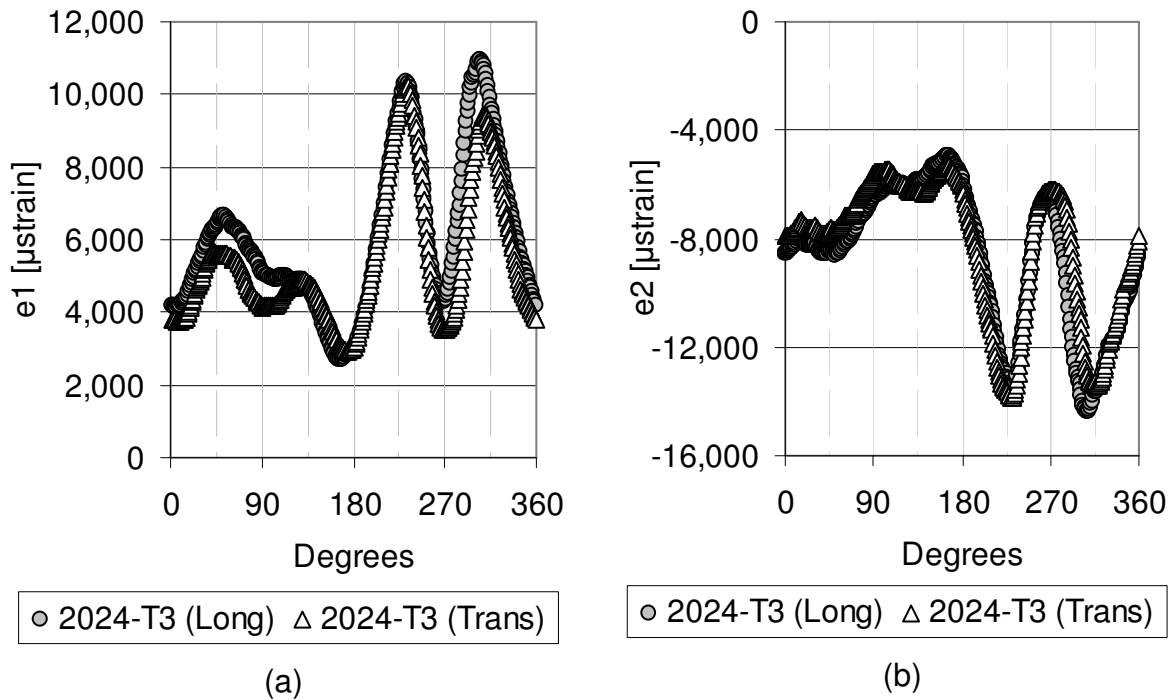
Figure 44: Plot of principal strains for 2024-T3 coupons, specimen AL6 (Longitudinal) and Specimen AT6 (Transverse) for (a) maximum principal strain and (b) minimum principal strain

6.3   Comparison Between FML 3 and FML 4

Two grades of FML, FML 3 and FML 4, were tested to determine the differences in residual strain after cold expansion. Table 1 provides the basic laminate layup of these two variants while Table 2 details their mechanical properties. From these tables it is clear that FML 4 has a higher elastic modulus and yield strength in the longitudinal (L) direction and a lower elastic modulus and yield strength in the longitudinal transverse (LT) direction. As a result of being laminate materials, both of these FML variants exhibit orthotropic behaviour, with the lowest yield strength occurring at 45° degrees to the longitudinal direction. Since FML 4 has a greater difference in elastic modulus between the L and LT direction, it would not be surprising to see a slight difference in the residual strain fields between these two FML grades. Indeed, a close examination

of Figure 45 shows that the maximum principal strain field for FML 4 is slightly

elongated in the transverse direction compared to FML 3. The same effect is evident

when examining Figure 46, which shows the minimum principal strain for both materials.
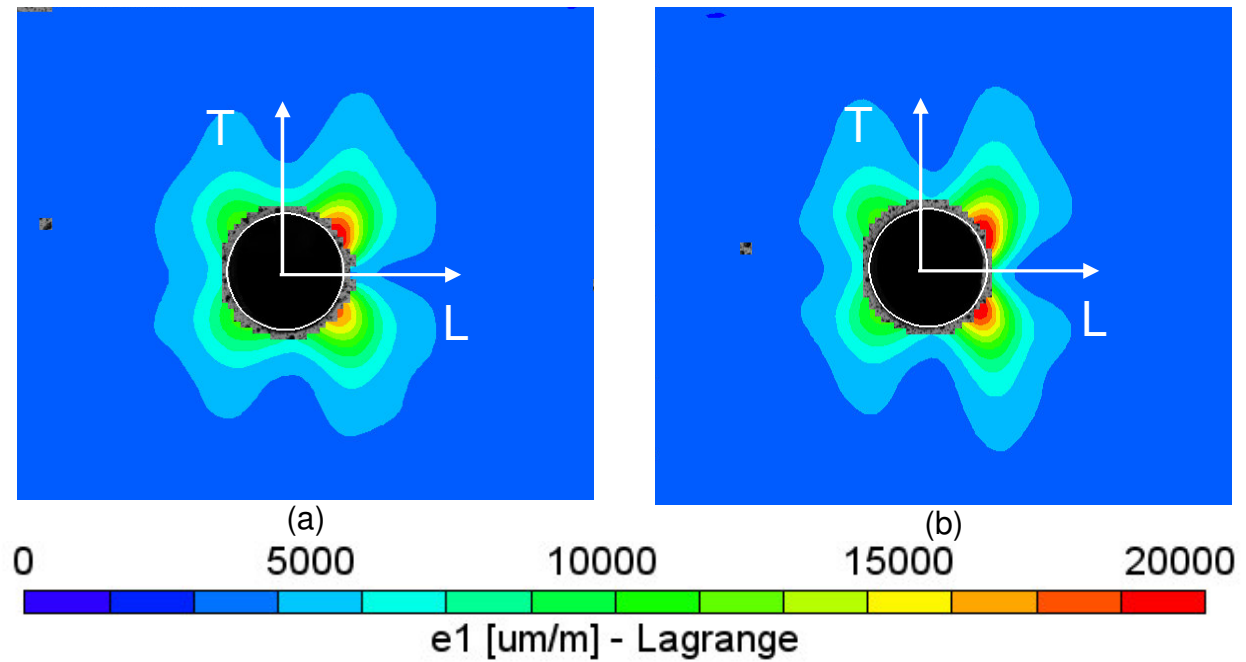
Figure 45: Maximum principal strains on the entry face for (a) FML 3 (specimen GAL2) and (b) FML 4 (specimen GBL1)
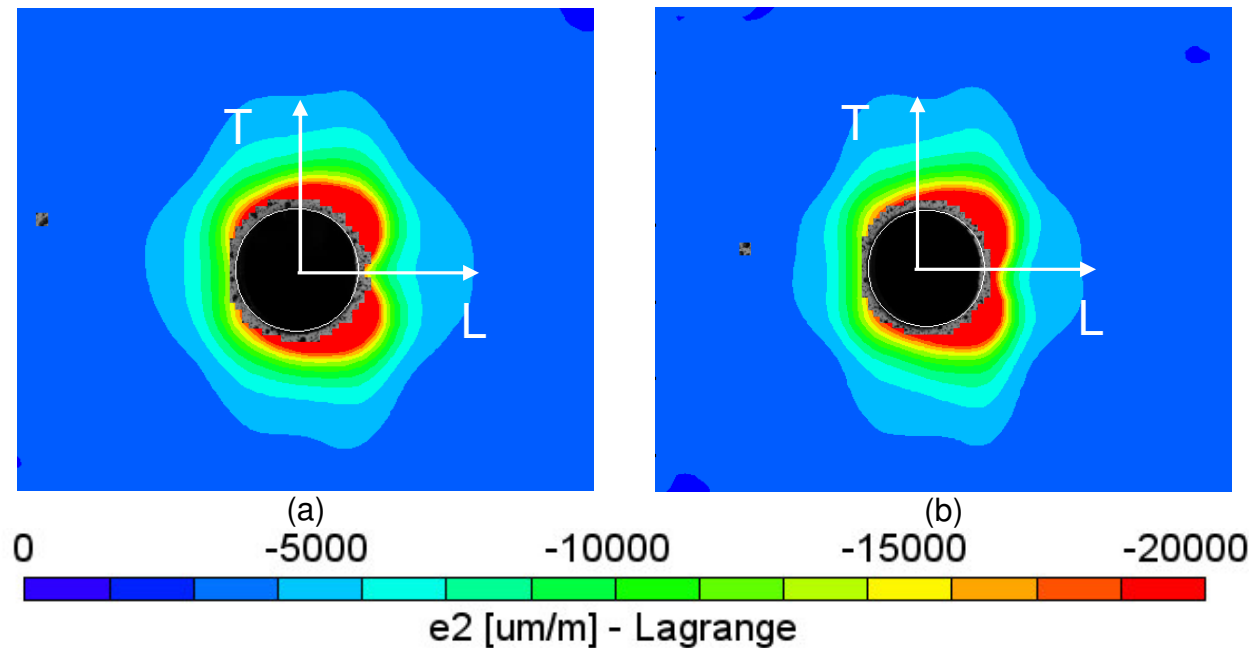
Figure 46: Minimum principal strains on the entry face for (a) FML 3 (specimen GAL2) and (b) FML 4 (specimen GBL1)

From the plot of the residual strain data extracted from around the cold expanded hole (Figure 47) it is very difficult to directly note the effect of this elongation. The effect of this elongation in the transverse direction should be most noticeable in either the 0º degree or 180º degree directions and although a very slight difference may exist, there is still enough variability in the cold expansion process to make this determination inconclusive.
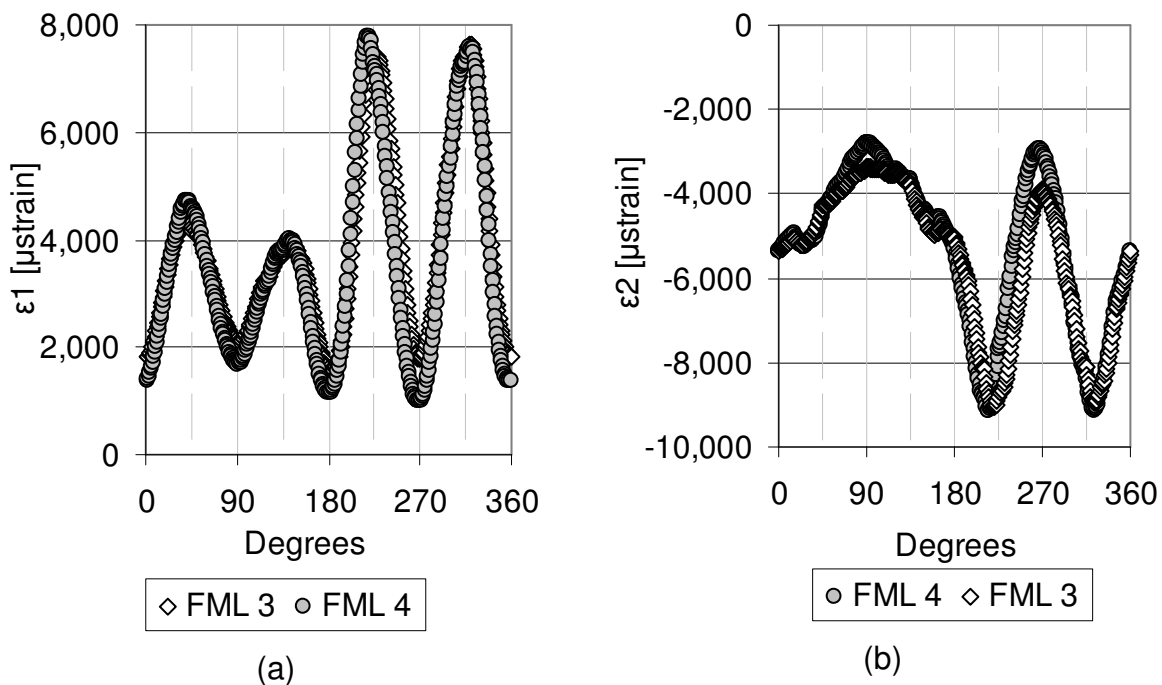
Figure 47: Plot of principal strains for FML 3 (specimen GAL2) and FML 4 (specimen GBL1) for (a) maximum principal strain and (b) minimum principal strain

6.4 FML 45º Orientation

In order to further investigate the orthotropic nature of FML and the residual strains after cold expansion, additional coupons were machined with the longitudinal direction oriented at 45° degrees to the long axis of the coupon. The split sleeve direction remained the same (to the right in the image), and Figure 48 shows the dramatic change this causes in the maximum principal strain field. From a structural point of

view, rotating the coupons' axes effectively orients the split in the split sleeve in the direction of minimum elastic modulus and minimum yield strength. The effect of this can be seen clearly in Figure 49, where the typical butterfly shape that results from the split sleeve is replaced with a more concentric annulus of compressive residual strain.
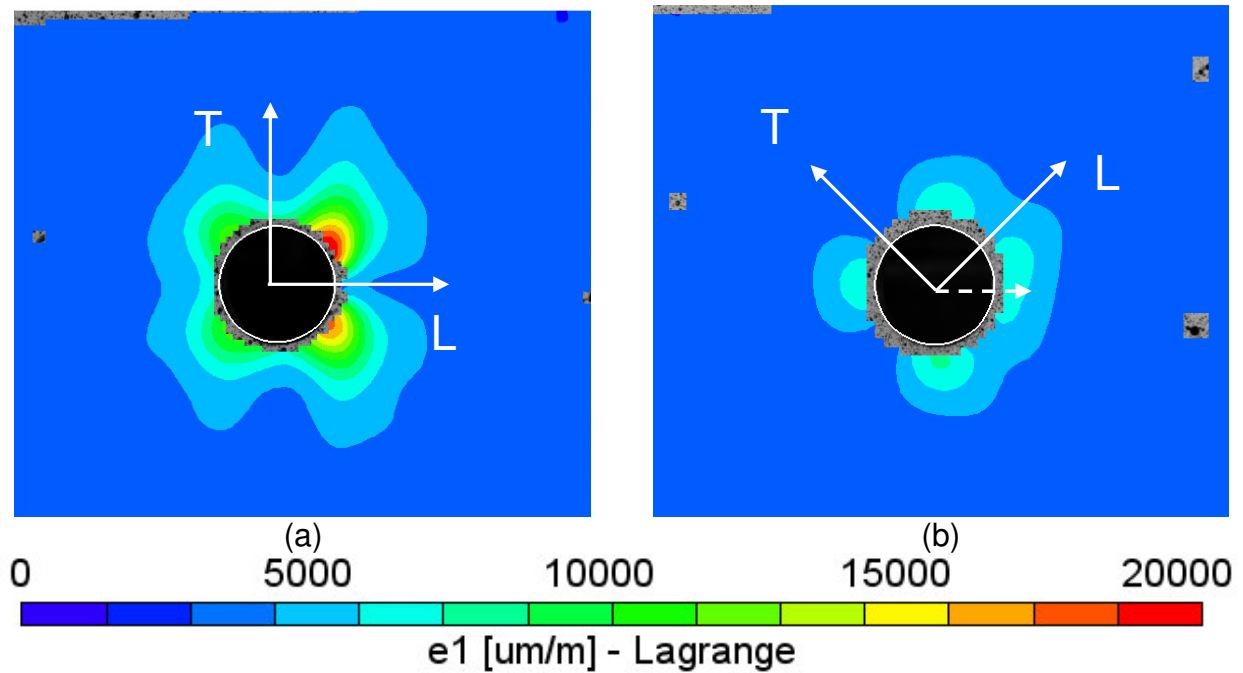
Figure 48: Maximum principal strains on entry face for FML 3 (a) specimen GAL2 (standard orientation) and (b) specimen GCF2 (45° orientation). Note: Dotted line shows orientation of split sleeve
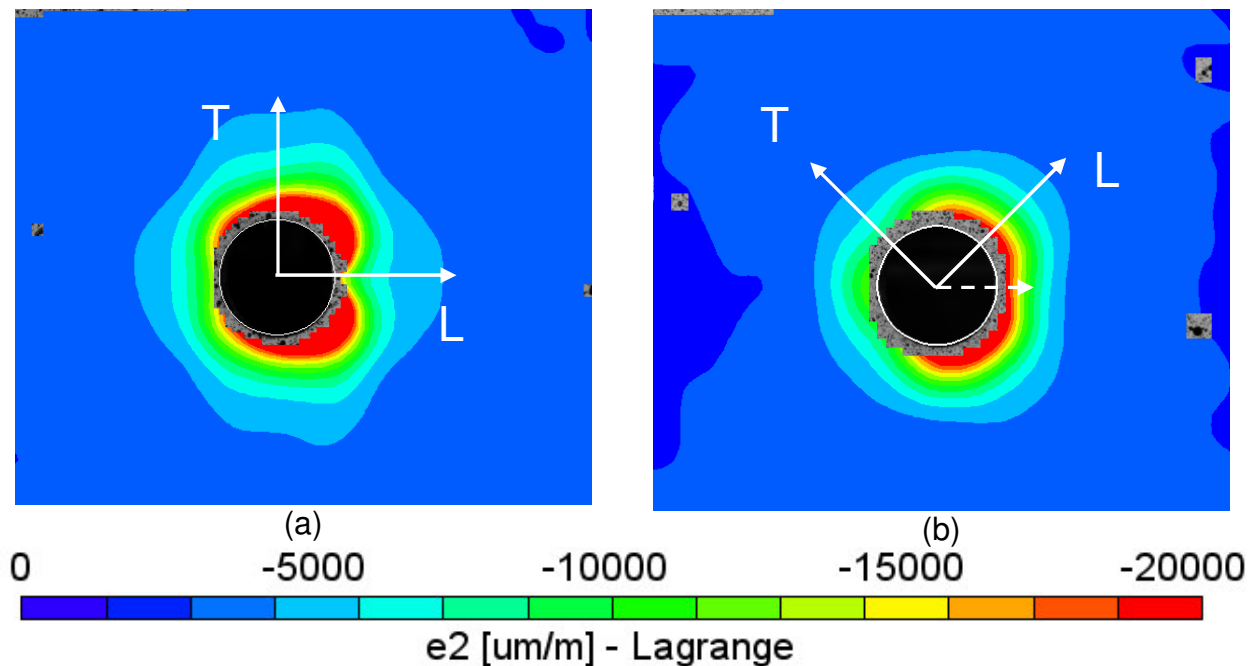
Figure 49: Minimum principal strains on entry face for FML 3 (a) specimen GAL2 (standard orientation) and (b) specimen GCF2 (45° orientation). Note: Dotted line shows orientation of split sleeve

In the plot of maximum principal strain (Figure 50a), the typical strain concentration seen between 225º - 315º degrees has almost completely disappeared. In the plot of minimum principal strain (Figure 50b), a smaller strain concentration exists in that region, but overall, the strains appear to be much more uniform than with the longitudinally or transversely oriented FML coupons.
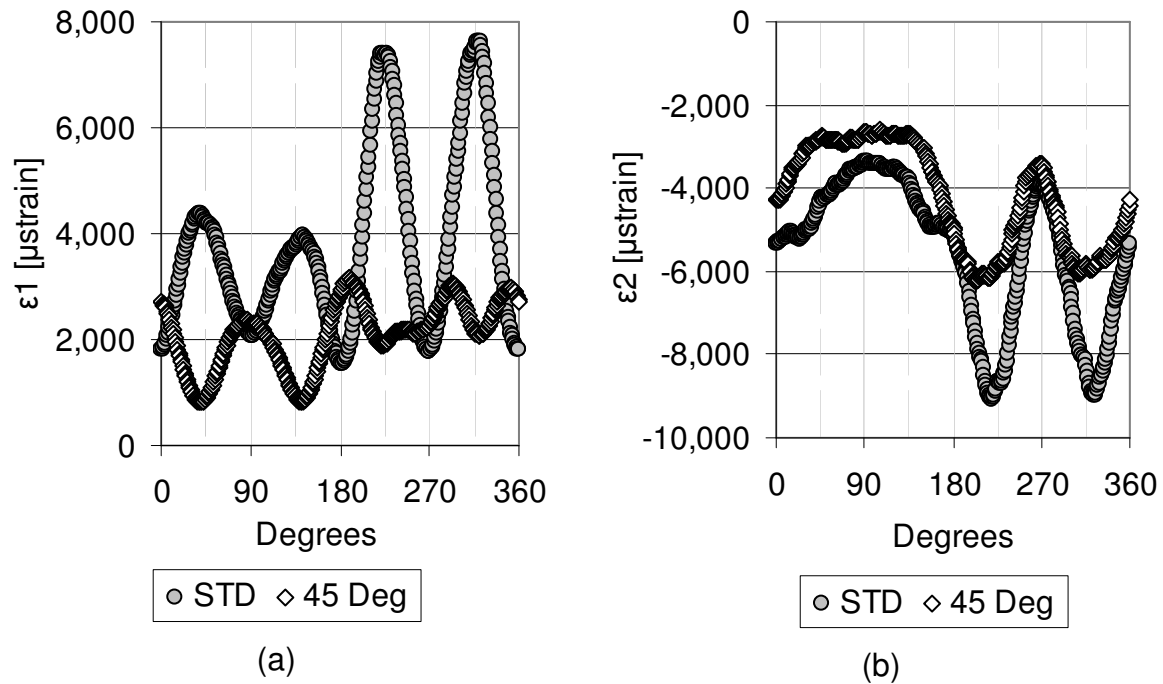
Figure 50: Plot of principal strains for FML 3 specimens GAL2 (longitudinal) and GCF2 (transverse) with (a) maximum principal strains and (b) minimum principal strains

These results reinforced the idea that the orthotropic nature of FML makes it a difficult material to cold expand predictably, at least without some forethought concerning the grade of FML and its material properties. It was this result that led to the idea of changing the material properties of FML to be more isotropic in the plane of the laminate, and to reduce the need to clearly define material direction before cold expansion.

6.5   Mandrel Entry and Exit Face Results (2024-T3 and FML)

Although a plane stress assumption would appear to be appropriate for the 1.59 mm thick material being used in this research, the open literature cites many researchers[41,43,44,47,61-63] who have demonstrated that the compressive residual strains after cold expansion are higher on the exit face than on the entry face. The implication for this, in fatigue, is that crack growth rates on the exit and entry face may

differ, a fact that has also been observed by several researchers[51-53,64]. To verify

whether this phenomenon was present for our thin (1.59 mm) FML 3 and 2024-T3

aluminum coupons, entry and exit face strains were measured and compared for both

materials. Figure 51 and Figure 52 show the maximum principal and minimum principal

strains on the entry and exit faces of an FML 3 coupon. Visual comparison of the two

faces shows very similar strain patterns, making it difficult to detect whether strains on

the exit face are indeed higher.
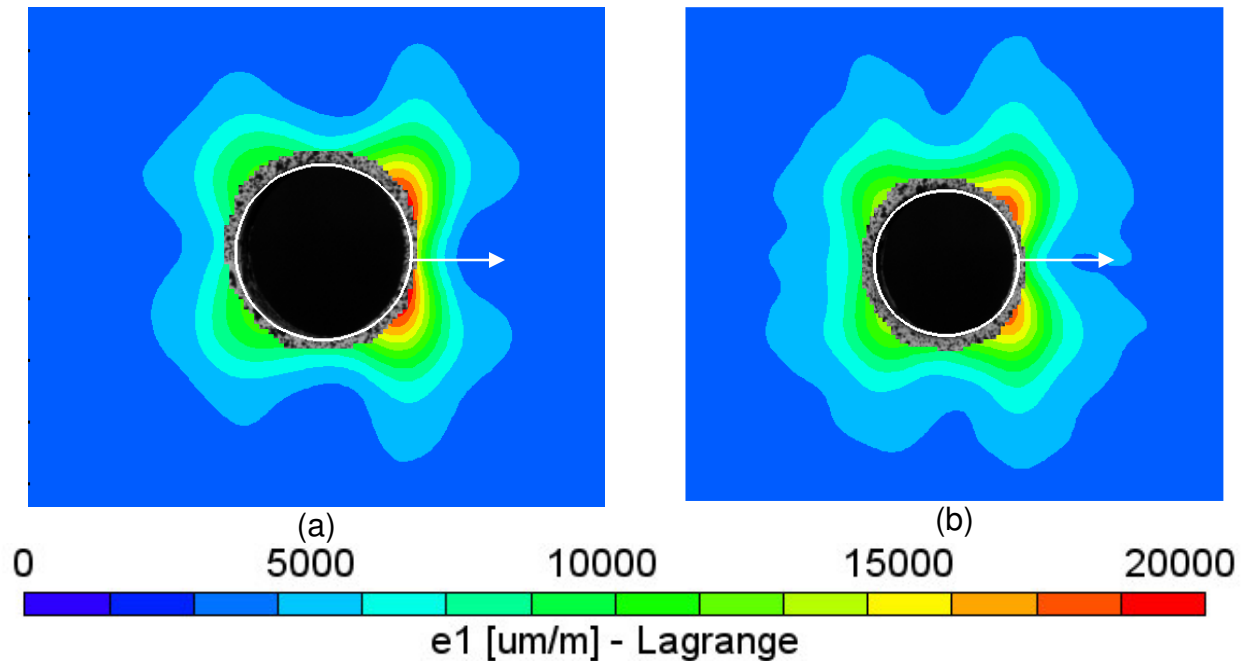
Figure 51: Maximum principal strains for (specimen 15-A-7) FML 3 coupon (a) mandrel entry face and (b) mandrel exit face
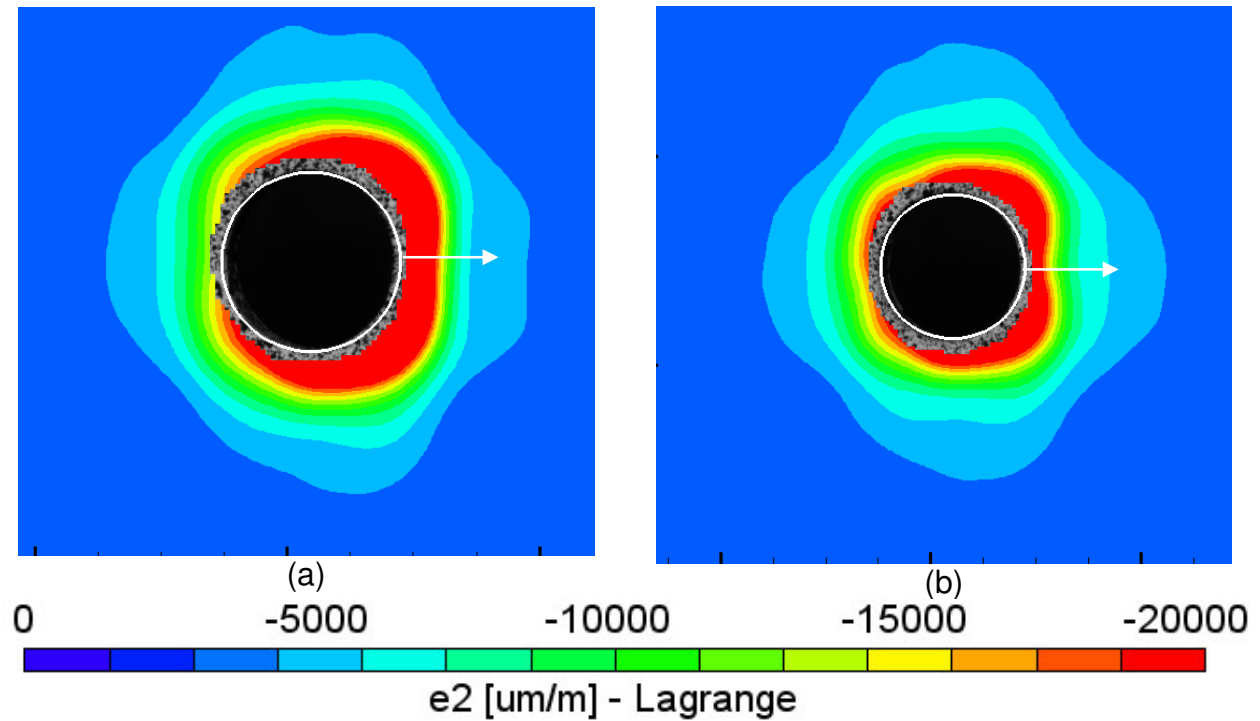
Figure 52: Minimum principal strains for (specimen 15-A-7) FML 3 coupon (a) mandrel entry face and (b) mandrel exit face

Examination of the radial extractions for FML 3 (Figure 53), shows that overall the maximum principal strains are slightly higher on the exit face, whereas for the minimum principal strains, the differences on the exit face are greatest between 0º-180º degrees. A further clarification is achieved by extracting data from a vertical line starting at 180º (in the circular co-ordinate frame) and extending to the edge of the hole. This line profile (Figure 54) shows that, immediately adjacent to the edge of the hole, both the minimum and maximum principal strains on the exit face of the coupon are of greater magnitude than those on the entry face.
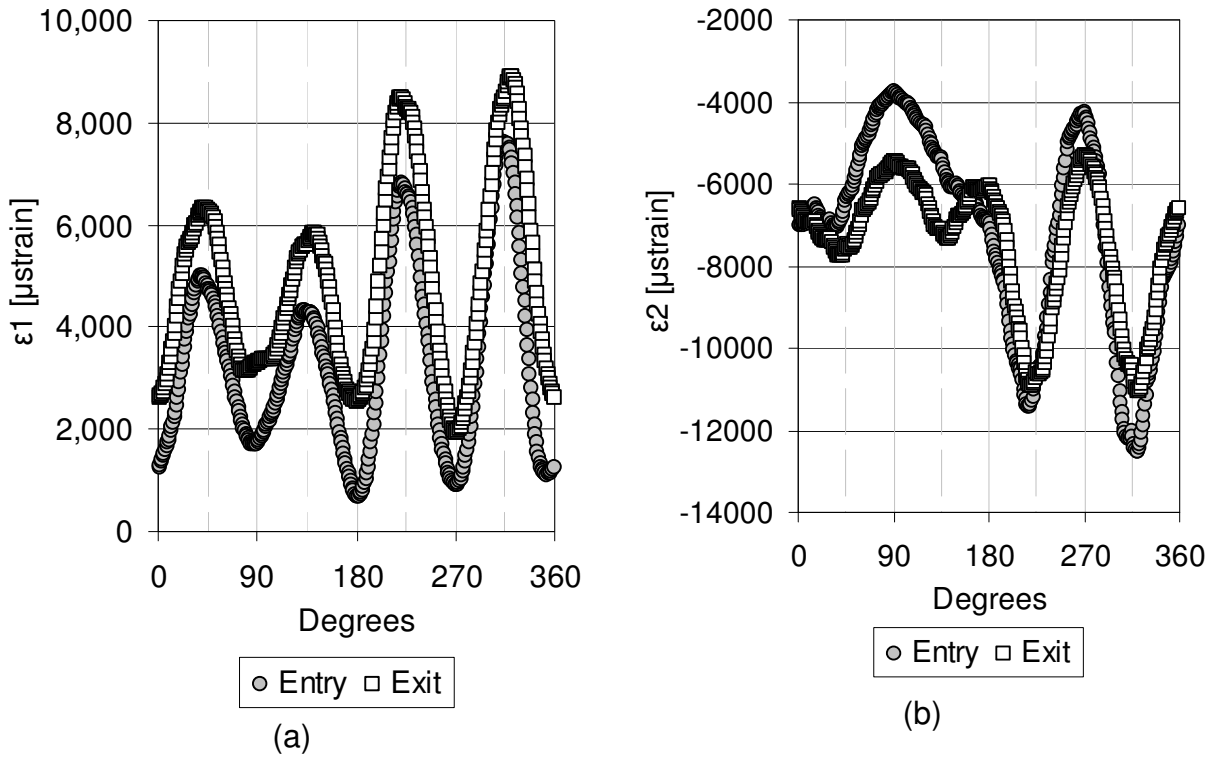
Figure 53: Plot of entry and exit face principal strains for (specimen 15-A-7) FML 3 (a) maximum principal strains and (b) minimum principal strains
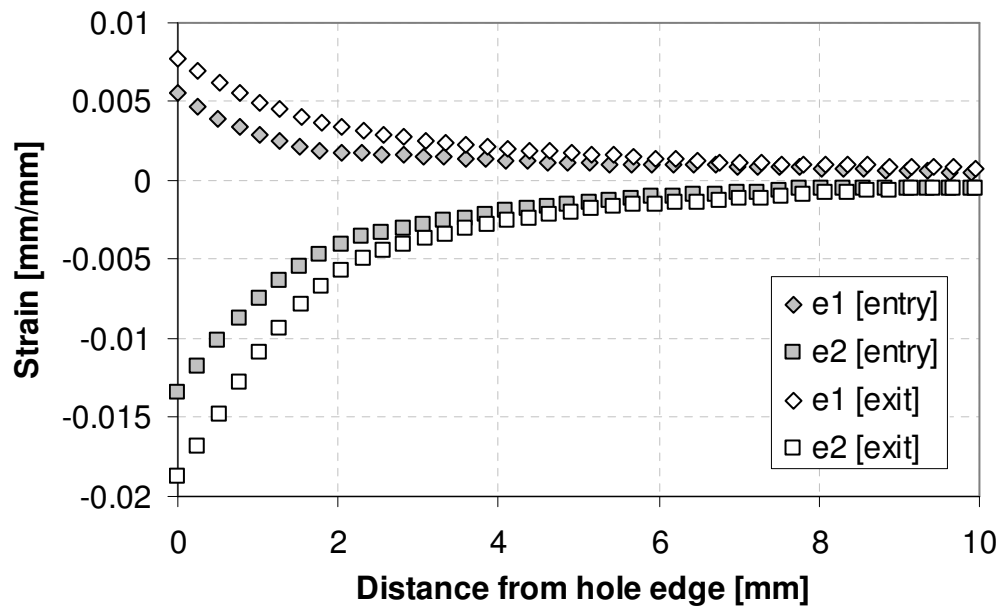
Figure 54: Vertical line profile (180º) of entry and exit principal strains for FML 3 coupon (specimen 15-A-7)

Examining the strain fields from the 2024-T3 aluminum coupons, it is apparent that the overall extent of both the maximum principal strains (Figure 55) and the minimum principal strains (Figure 56) are greatest on the exit face.
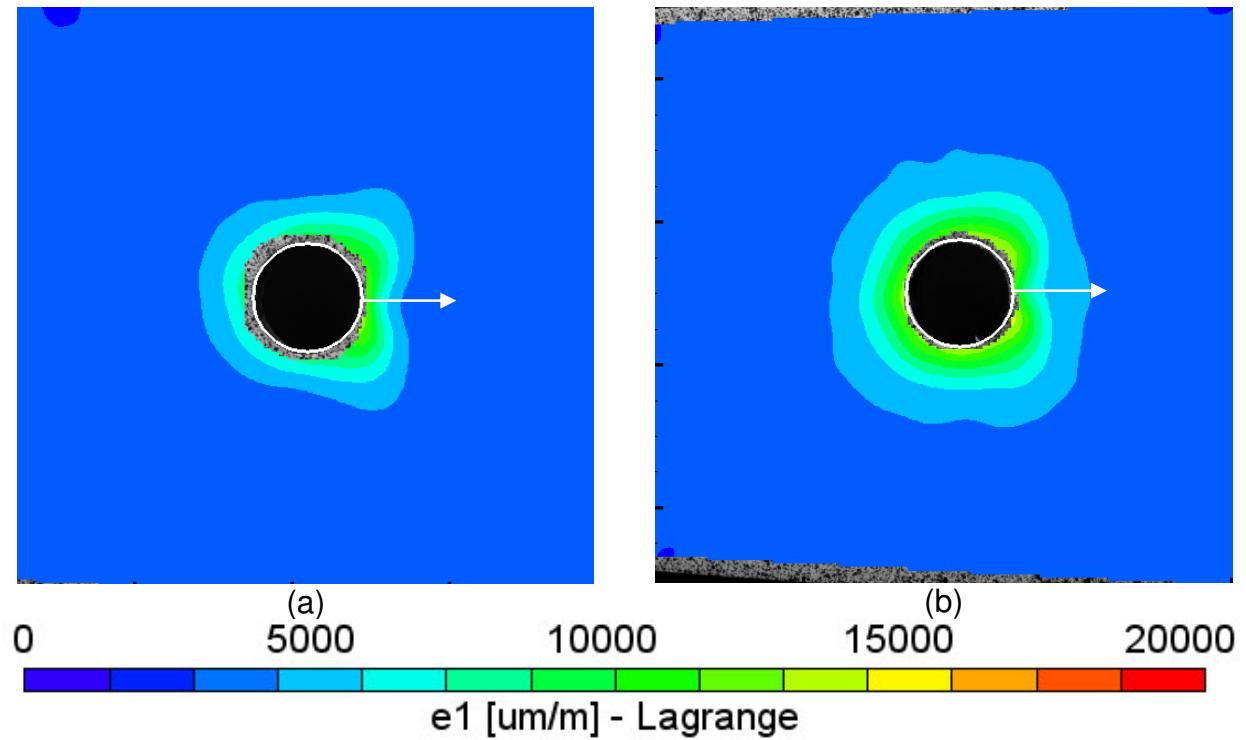
Figure 55: Maximum principal strains for (specimen AL-T-7) 2024-T3 aluminum (a) mandrel entry face and (b) mandrel exit face
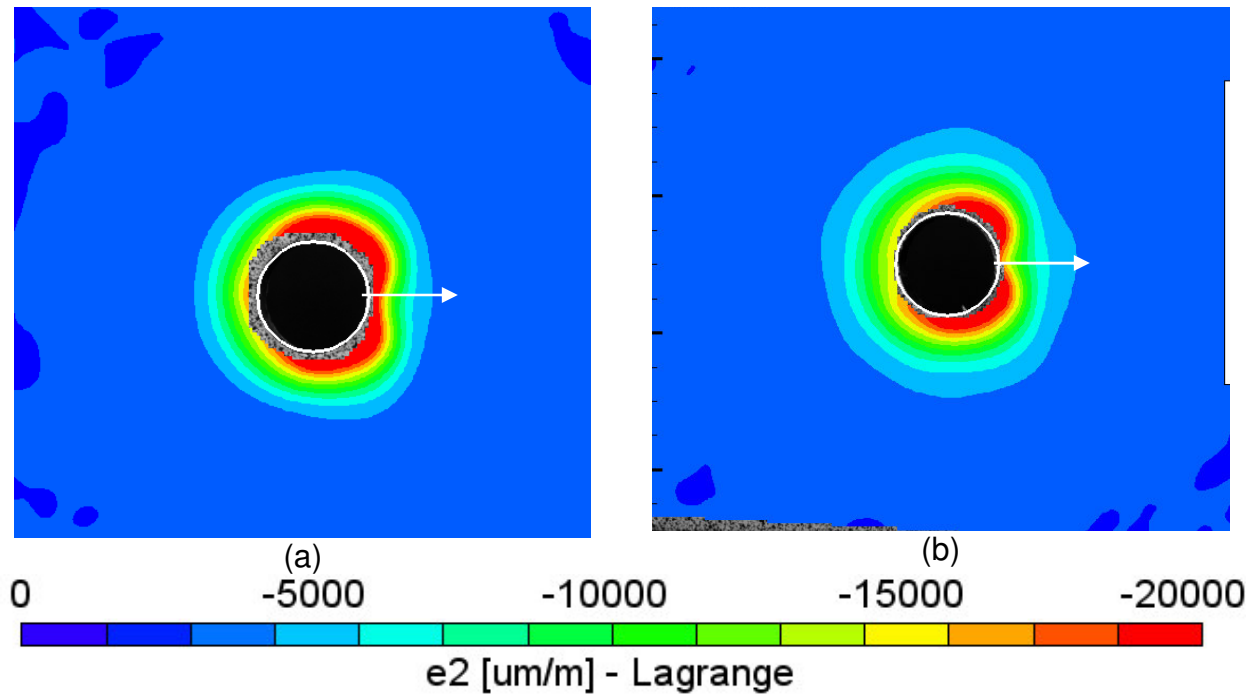
Figure 56: Minimum principal strains for (specimen AL-T-7) 2024-T3 aluminum (a) mandrel entry face and (b) mandrel exit face

From the radial strain extraction of the 2024-T3 aluminum (Figure 57), it is apparent that, overall, both the maximum and minimum principal strains are higher on the exit face.   The line profile taken from the edge of the hole (Figure 58) shows that at the point immediately adjacent to the edge, the maximum and minimum principal strains on the exit face are slightly higher than those on the entry face, in a manner similar to FML.
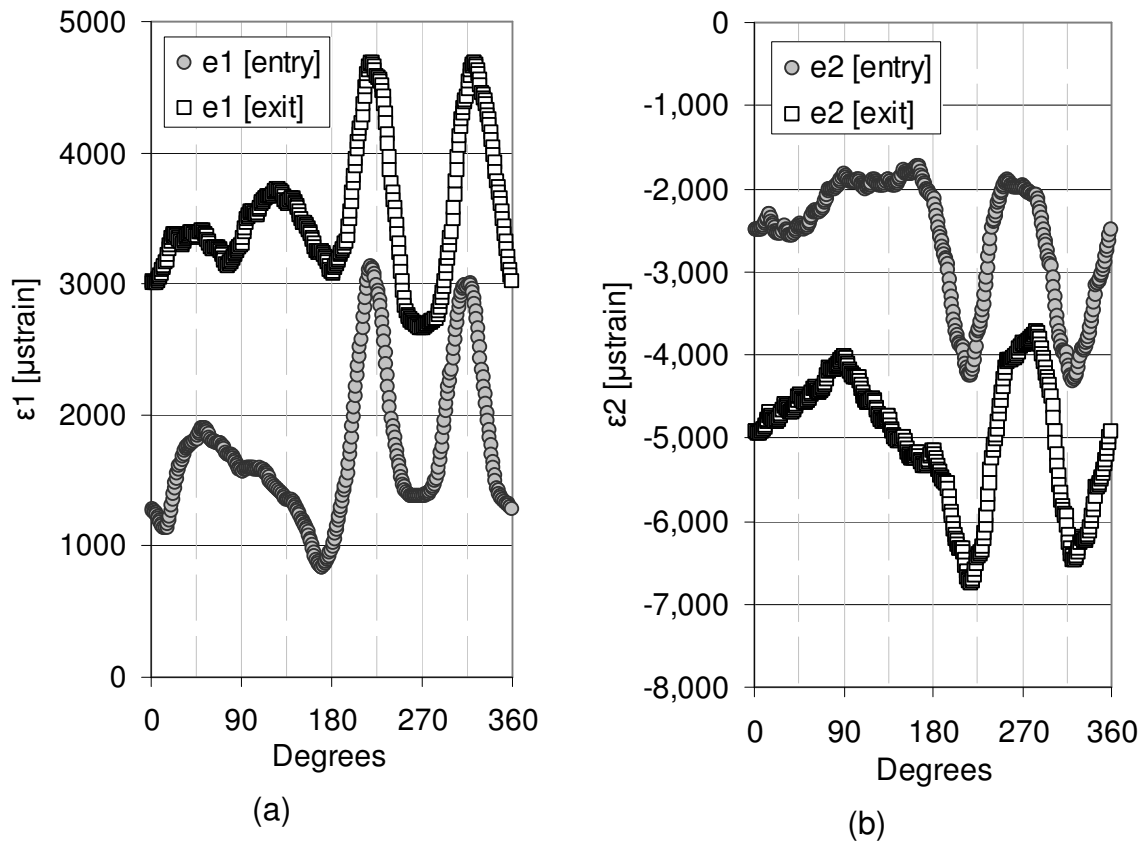
Figure 57: Plot of entry and exit face principal strains for (specimen AL-T-5) 2024-T3 aluminum (a) maximum principal strains and (b) minimum principal strains
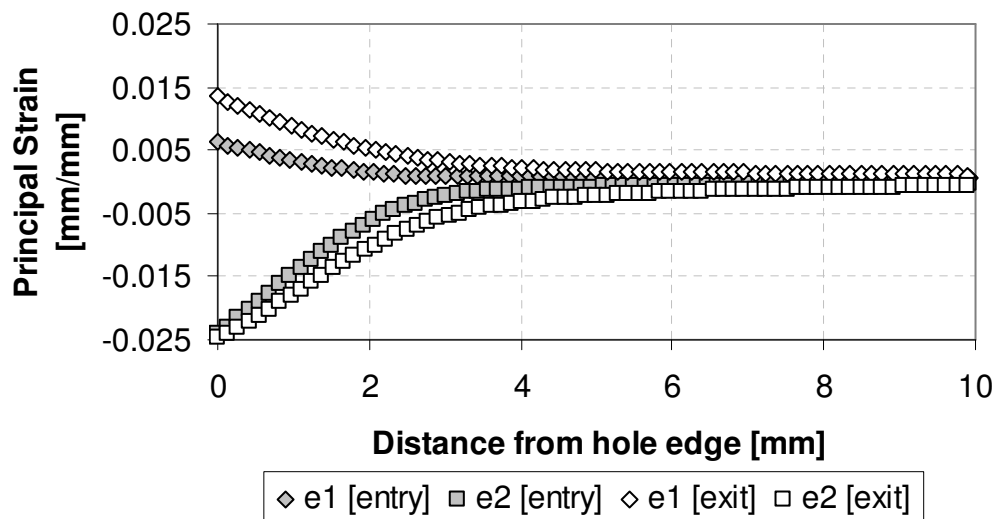
Figure 58: Plot of entry and exit principal strains for 2024-T3 aluminum coupon (specimen AL-T-5)

One ramification of this result that was not completely appreciated until during the fatigue testing was that the higher overall residual strains on the exit face was more effective at extending the life in the early stage of the fatigue process compared to the entry face.

6.5.1 Effect of Increased Edge Distance

The initial design of experiments dictated that all static and fatigue coupons should have similar widths to make comparing results more meaningful. Given a nominal cold expanded hole diameter of 6.64 mm (0.2616 inches) and a coupon width of 38.1 mm (1.50 inches) all coupons had a nominal edge ratio (defined as the ratio of edge distance to hole radius) of approximately 5.73. To determine the effect of increasing the edge distance, additional 2024-T3 aluminum and FML 3 coupons were machined with a width of 63.5 mm (2.50 inches) providing an edge ratio of 9.55.

Full-field images of the maximum principal strain surrounding the low and high edge ratio coupons are shown in Figure 59. It is clear that the change in boundary constraint provided by the difference in edge ratios has an impact on the tensile strain at the edge of the coupon. The change in edge ratio also likely has an impact on the tensile strains close to the edge of the cold expanded hole, but the full extent of this is more difficult to determine due to the different magnifications used for each coupon. This change in magnification (CL3: 0.08 mm/pixel and AL3: 0.05 mm/pixel) has an impact on strain resolution, especially in high strain gradient areas such as at the hole edge.
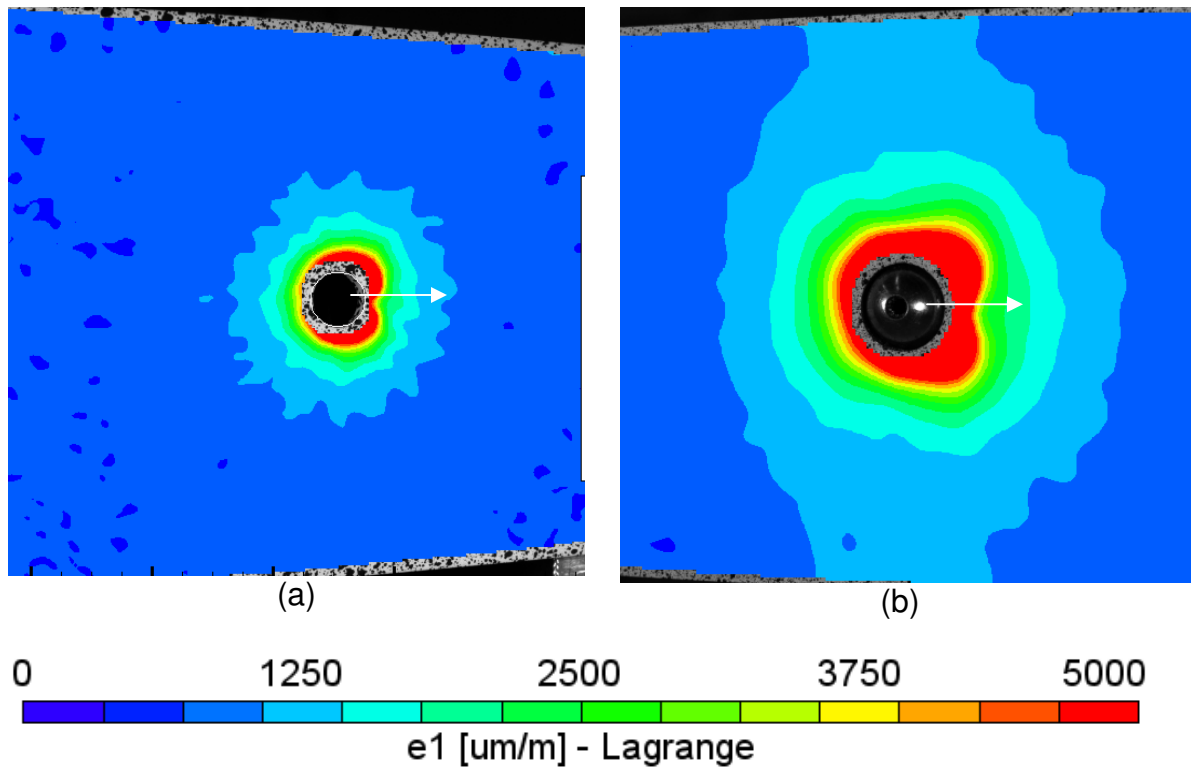
Figure 59: Plot of maximum principal strain on entry face for a) high edge ratio coupon (specimen CL3) and b) low edge ratio coupon (specimen AL1)

Vertical line profiles through the central notch of the aluminum coupons (Figure 60) show that the low edge ratio coupons have maximum principal strains approximately 500 με greater at the coupon edge than those of the high edge ratio coupons.
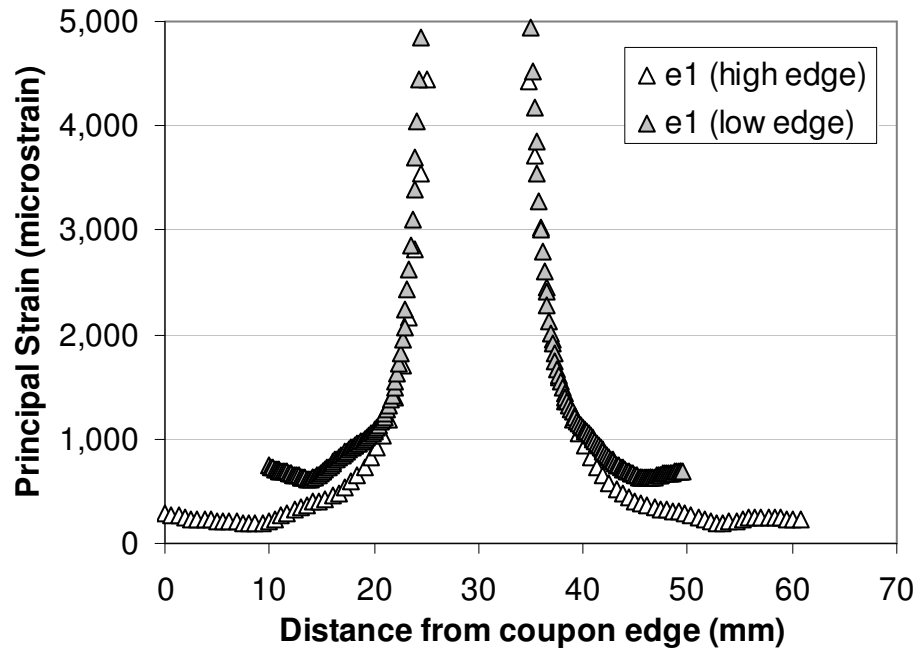
Figure 60: Vertical line profile showing variation in maximum principal strain through coupon center for both high edge ratio (specimen CL3) and low edge ratio (specimen AL1) 2024-T3 aluminum coupons

By contrast, the same line profile plotting the minimum principal strains (Figure 61)

shows that at the edge of the coupon, the minimum principal strains are more similar,

with a difference of less than approximately 300 με.
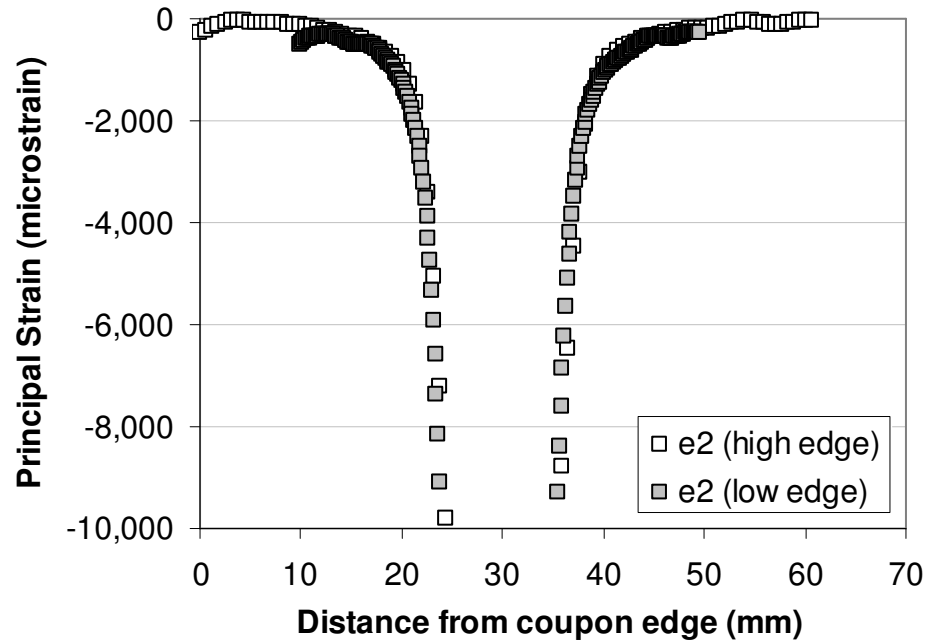
Figure 61: Vertical line profile showing variation in minimum principal strain through coupon center for both high edge ratio (specimen CL3) and low edge ratio (specimen AL1) 2024-T3 aluminum coupons

Figure 62 shows a full-field plot of the maximum principal strains in both FML 3 coupons, clearly highlighting the difference in tensile strain caused by the difference in boundary constraint. Line extractions taken from the high and low edge ratio FML 3 coupons show much the same behaviour as in the aluminum coupons. A comparison of the vertical line profile taken from both of these coupons (Figure 63) shows maximum principal strains approximately 700 µε greater at the edge of the low edge ratio coupon than at the edge of the high edge ratio coupon. The same line profile extraction for the minimum principal strains (Figure 64) shows a smaller difference, on the order of 200 µε at the coupon edge.
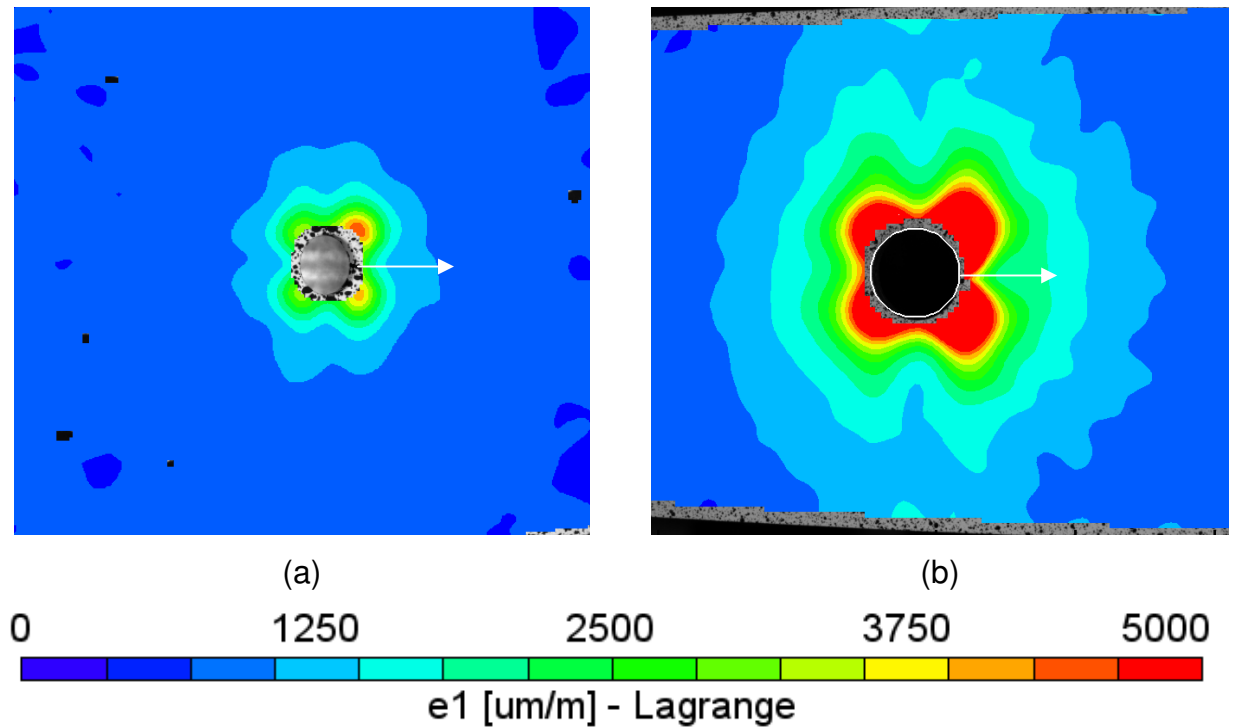
Figure 62: Plot of maximum principal strain on the entry face for FML 3 a) high edge ratio coupon (specimen GCL2) and b) low edge ratio coupon (specimen GAL1)
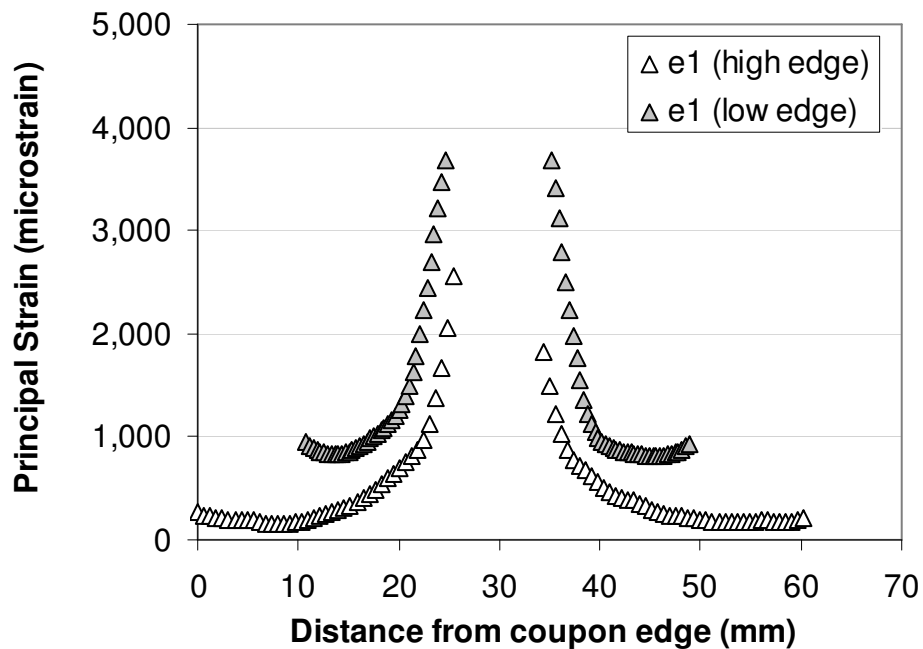
Figure 63: Vertical line profile showing variation in maximum principal strain through coupon center for both high edge ratio (specimen GAL1) and low edge ratio (specimen GCL2) FML 3 aluminum coupons
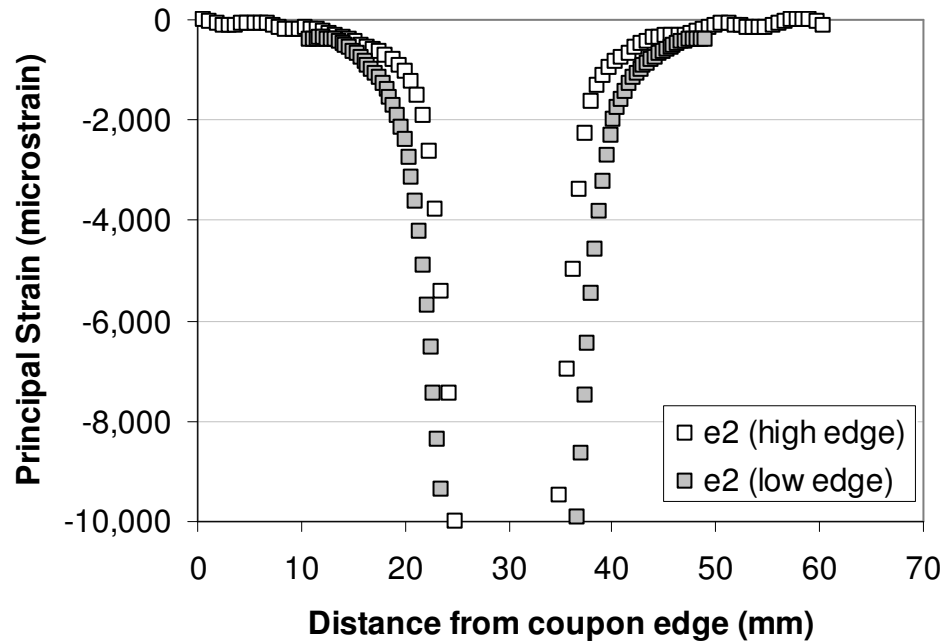
Figure 64: Vertical line profile showing variation in minimum principal strain through coupon center for both high edge ratio (specimen GAL1) and low edge ratio (specimen GCL2) FML 3 aluminum coupons

The results with FML are similar to those with 2024-T3 aluminum, in that both seem to show an increase in maximum principal strain at the coupon edge, as well as at the edge of the cold expanded hole. Although the different magnifications used for both images changed the strain resolution and makes quantification of the effect difficult at the edge of the hole, a computer simulation of this situation by Ayatollahi and Arian[104] appears to confirm both the increase in tensile strain at the edge of the coupon as well as the increase in strain at the edge of the hole and suggests that edge ratio needs to be taken into consideration during the cold expansion process as to small an edge ratio may reduced the effectiveness of the cold expansion process.

6.6 Static Riveting Results

For the static riveting results, fewer comparisons were made than for cold expansion. With the theoretically uniform nature of the riveting process, the main focus for the static riveting tests was to determine how much variability could be expected as well as to determine the resultant strain field for the different materials.

Unlike with cold expansion, the final diameter of the manufactured and driven head covered the region closest to the pilot hole and made it impossible to measure the strains in this region. It should be noted that, for clarity, some of the full-field strain results have been overlaid over the original pilot hole to provide a better sense of the relationship between the pilot hole and the measured strain field.

6.6.1 Process Variability Rivet Results

As with the cold expanded coupons, process variability was quantified by comparing two different coupons. In the rivet process, the amount of compression generated from a rivet of a specific size is related to both the height of the protruding head as well as the diameter of the protrusion created during the compression process. Although every attempt was made to use the same amount of displacement, the riveting process is very sensitive to even small changes in insertion angle which can then influence both the final rivet protrusion as well as the uniformity of the strain field.

In the case of the aluminum coupons, the overall shape of the strain field is quite similar, with the maximum principal strain field (Figure 65) appearing to be slightly larger in diameter than the minimum principal strain field (Figure 66). In both cases the strain field appears to be uniform and circular without the typical cardioid shape seen after

split sleeve cold expansion. The radial line extraction of the strain data (Figure 67) supports this conclusion, showing only small undulations in the strain fields with relatively consistent strains between the two aluminum coupons.
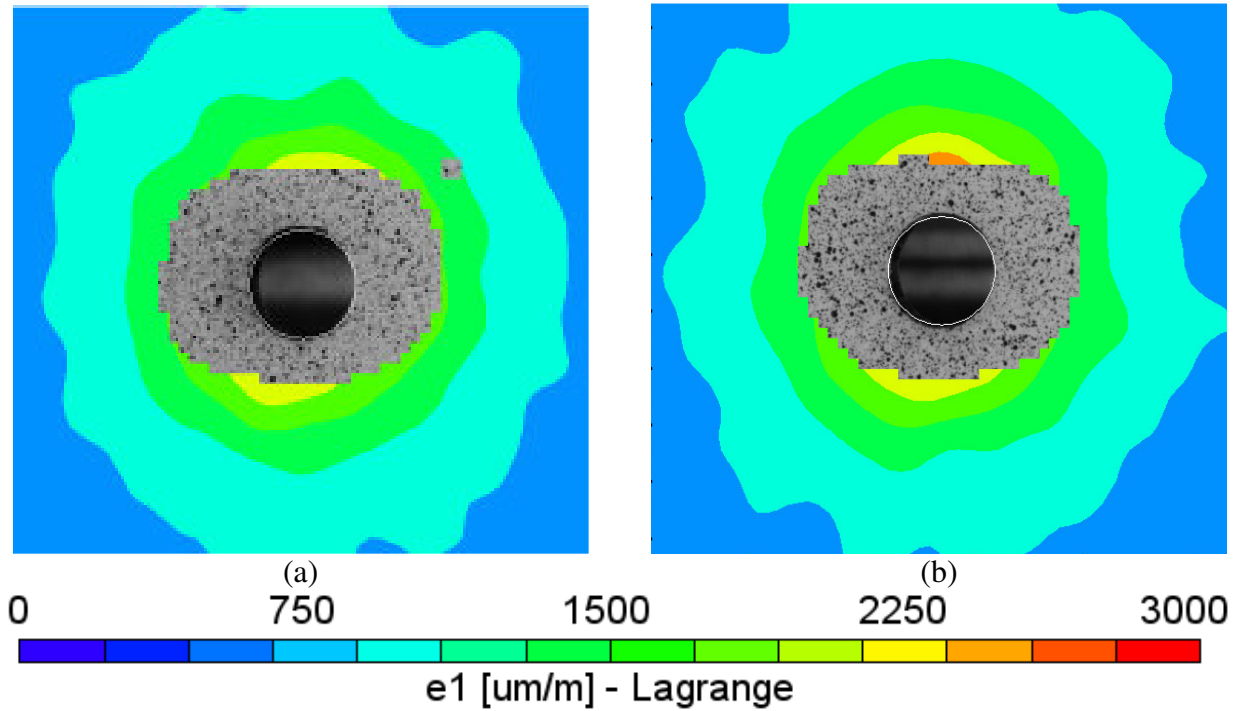
Figure 65: Maximum principal strains for 2024-T3 aluminum riveted coupons on driven head side for (a) specimen BL17 and (b) specimen BL19
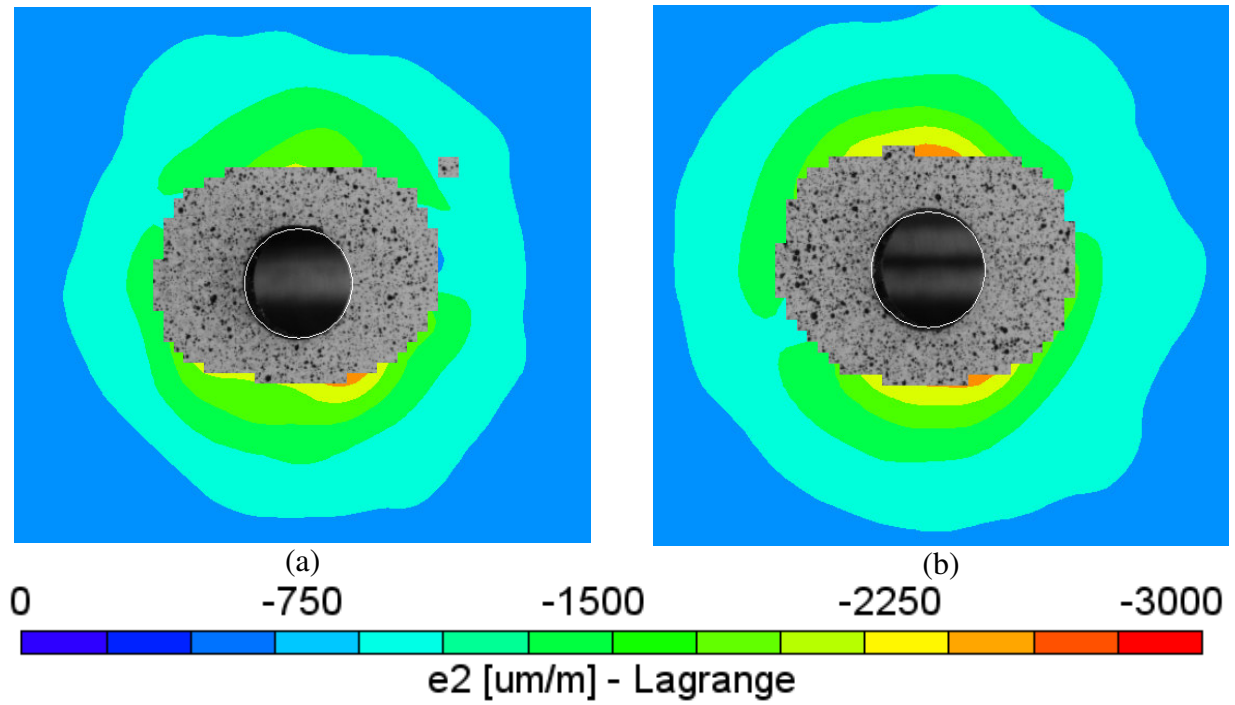
Figure 66: Minimum principal strains for 2024-T3 aluminum riveted coupon on driven head side for (a) specimen BL17 and (b) specimen BL19
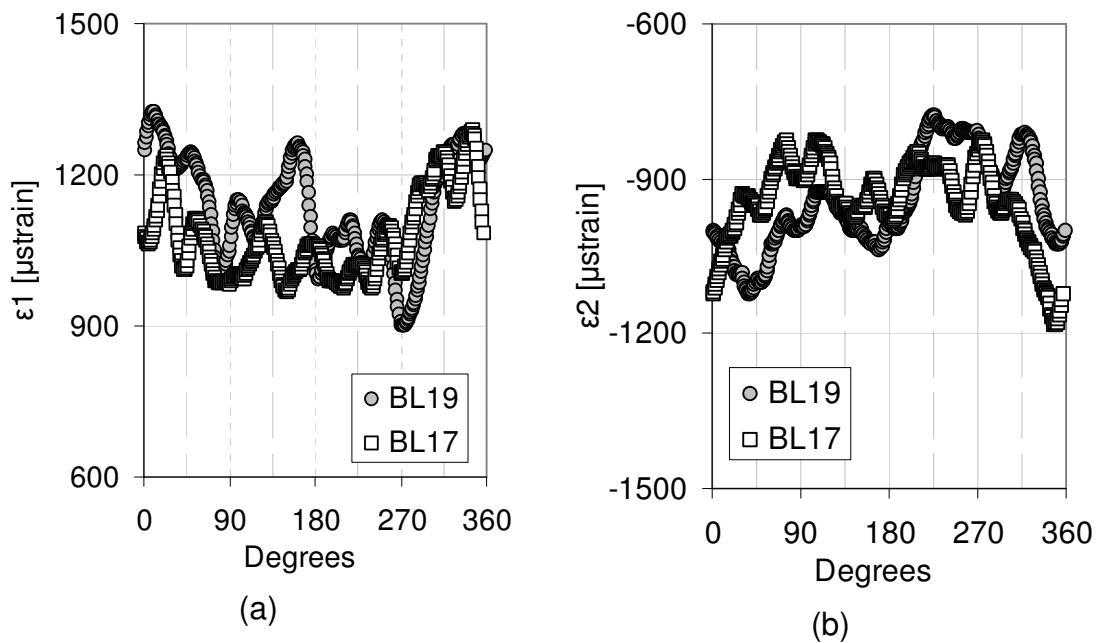
Figure 67: Plot of principal strains for riveted 2024-T3 coupon BL17 and BL19 (a) maximum principal strain and (b) minimum principal strain

6.6.2 Comparison Between FML 3 and FML 4 Rivet Results

Qualitative examination of the maximum principal strain (Figure 68) field shows that the strains surrounding the rivet in the aluminum are radially quite symmetric while those surrounding the rivet in FML show evidence of increased strain at 45° degree increments around the circumference of the rivet. The minimum principal strains surrounding the rivet in the FML coupon show slightly more bias, forming what could be described as a cross pattern around the rivet (Figure 69). Quantitative examination of the data from the radially extracted strains (Figure 70), shows an undulating strain field with reductions in minimum principal strain at 45° degree increments, corresponding with the direction of minimum modulus and minimum yield strength.
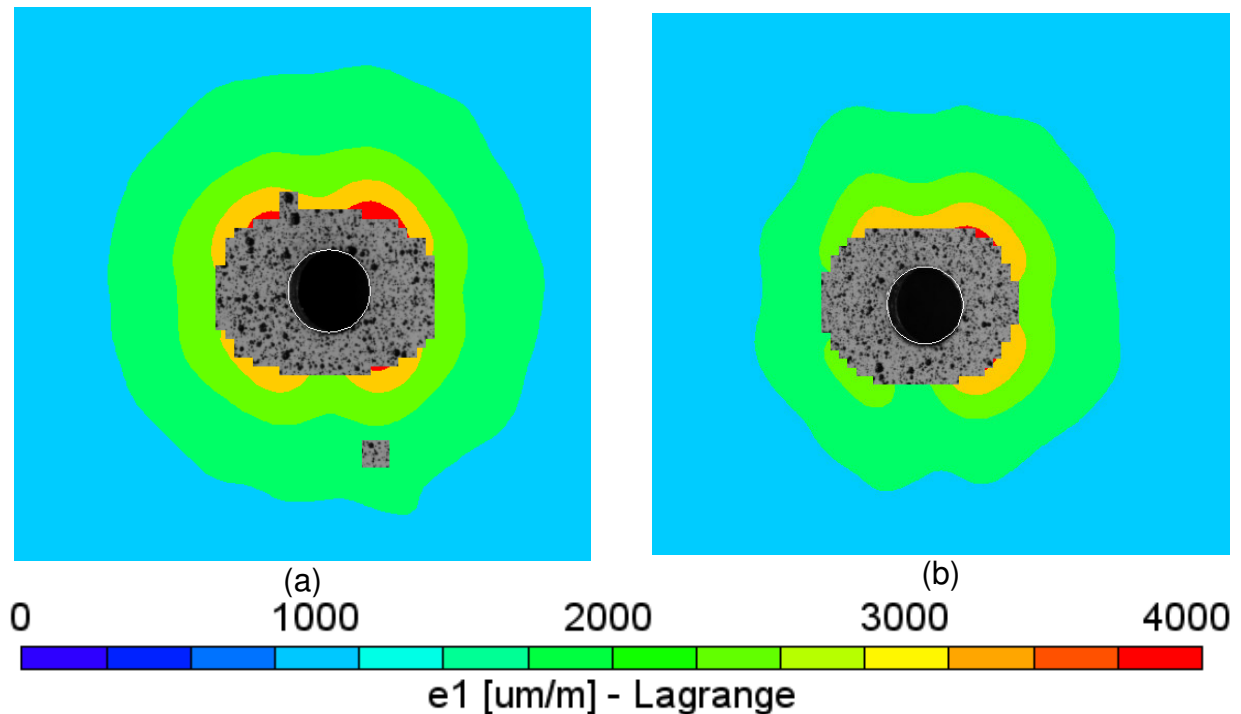
Figure 68: Maximum principal strains on the driven head side for (a) FML 3 (specimen GAL4) and (b) FML 4 (specimen GBL5)
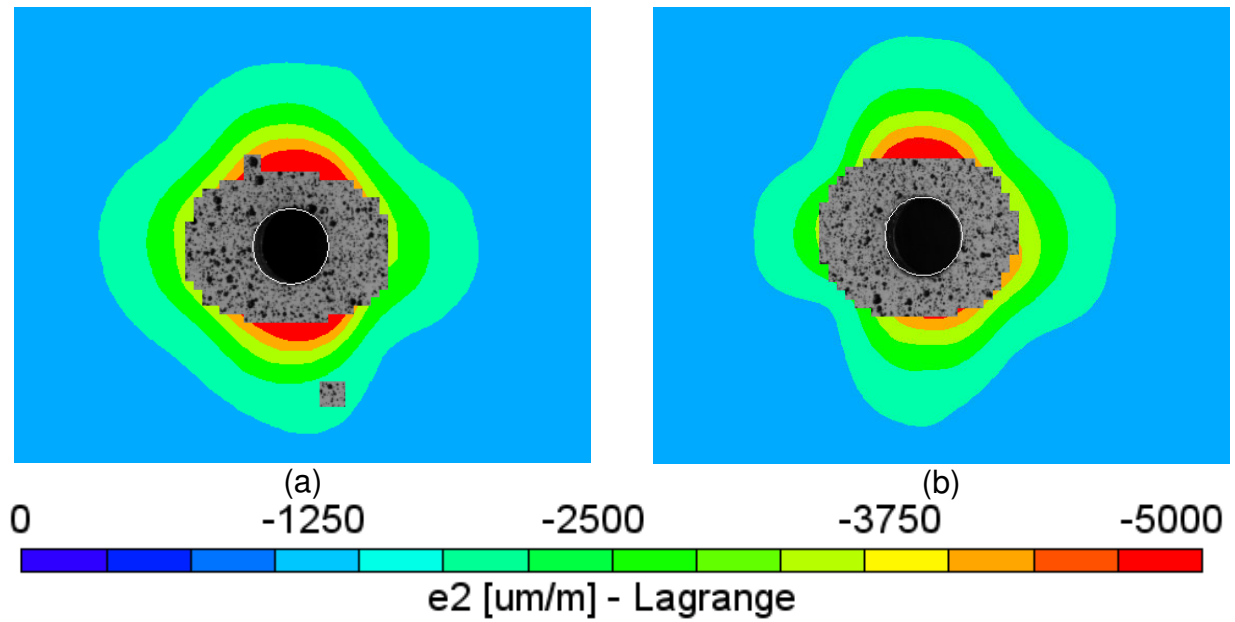
Figure 69: Minimum principal strains on the driven head side for (a) FML 3 (specimen GAL4) and (b) FML 4 (specimen GBL5)
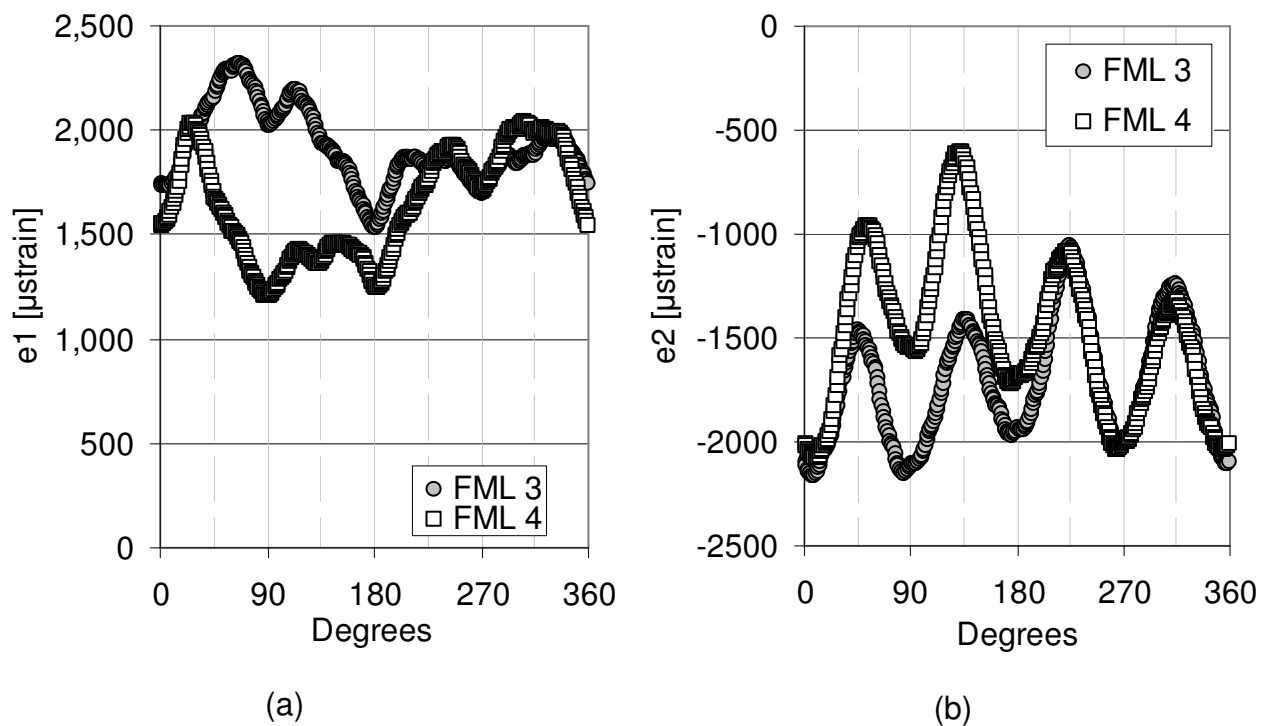
Figure 70: Plot of principal strains for riveted FML 3 (specimen GAL4) and FML 4 (specimen GBL5) for (a) maximum principal strain and (b) minimum principal strain

7.0 THEORETICAL ANALYSIS AND COMPARISON TO STATIC RESULTS

Any discussion regarding the theoretical basis behind hole cold expansion and riveting is best served by a brief foray into elasticity and plasticity theory as well as an examination of the yield criteria concept. A review of closed form solutions for the cold expansion process is provided, as well as a detailed overview of the approach used to model cold expansion and riveting in aluminum and FML materials as well as a comparison to the experimental results. The final section in the chapter provides an overview of classical laminate theory as it applies to FML and its application to the design and characterization of new FML 4 variants.

7.1 Discussion of Yield Criterion

One of the foundations behind elastic-plastic material models is the concept of a yield criterion that defines the combination of stresses that will cause a material to deform plastically. Mendelson[105] discusses some of the history behind the development of modern day yield criteria, which go back as far as Coulomb in 1773. The problem with many of these early yield criteria is that they were developed for brittle materials and then applied directly to ductile ones resulting in large errors between the theories and the experimental results. Coulomb's theory predicted failure of a specimen when the maximum shear stress reached the value of the maximum shear stress under uniaxial tensile loading. Although the maximum shear (Tresca) criterion has shown fair agreement with experimental results, its applicability is limited to ductile materials whose yield stress in tension and compression are equal (Figure 71). Another early yield criterion was the maximum strain energy theory which predicted failure when the strain energy per unit volume equalled the strain energy per unit volume as determined

by an axial tensile or compressive test of the same material. Since the maximum strain

energy theory has not been verified by experiment, it has been largely supplanted by

the maximum distortion energy theory[106].

7.1.1 Distortion Energy Yield Criteria

The majority of current elastic-plastic material models use a yield criterion generically

called the maximum distortion energy theory. This theory is also referred to as the

Huber-Hencky-Von Mises theory since it was first proposed by Huber in 1904 and also

independently by Von Mises of Germany in 1913[106]. The theory was further developed

by both Von Mises and Hencky in later years and is most commonly called the Von

Mises failure criteria in recognition of his contribution to the development of this theory.

What differentiates the maximum distortion energy theory from other failure theories is

the recognition that the portion of strain energy producing volume change does not

produce failure by yielding in isotropic materials.   This has been proven experimentally

in experiments by Bridgman[107,108] who showed that isotropic, homogenous materials

can withstand high hydrostatic pressures without yielding. This finding reinforced the

concept that yielding in a material results from the deviatoric portion of the total strain

energy applied to a material.

The maximum distortion energy theory can be derived by using strain energy concepts,

which provides background for a brief discussion of stress invariants and their

relationship to plasticity theory.

Using superposition, the standard stress tensor consisting of the three principal stresses σ_1, σ_2, σ_3 can be imagined to consist of two additive component tensors, one hydrostatic and one dilatational. The elements of the hydrostatic tensor are defined as the mean "hydrostatic" stress:

$$\bar{\sigma} = \frac{\sigma_1 + \sigma_2 + \sigma_3}{3} \qquad 7.1.1$$

The elements of the deviatoric or dilatational tensor are $(\sigma_1 - \bar{\sigma})$, $(\sigma_2 - \bar{\sigma})$ and $(\sigma_3 - \bar{\sigma})$ which are shown in matrix representation in Equation 7.1.2:

$$\begin{pmatrix} \sigma_1 & 0 & 0 \\ 0 & \sigma_2 & 0 \\ 0 & 0 & \sigma_3 \end{pmatrix} = \begin{pmatrix} \bar{\sigma} & 0 & 0 \\ 0 & \bar{\sigma} & 0 \\ 0 & 0 & \bar{\sigma} \end{pmatrix} + \begin{pmatrix} \sigma_1 - \bar{\sigma} & 0 & 0 \\ 0 & \sigma_2 - \bar{\sigma} & 0 \\ 0 & 0 & \sigma_3 - \bar{\sigma} \end{pmatrix} \qquad 7.1.2$$

With the principal stress state resolved into two components, it is now possible to calculate the strain energy due to the dilatational component of the stress tensor. First, the total strain energy must be derived, by integrating the area under the elastic portion of the stress-strain curve to get:

$$U_{total} = \frac{1}{2}\sigma_1\varepsilon_1 + \frac{1}{2}\sigma_2\varepsilon_2 + \frac{1}{2}\sigma_3\varepsilon_3 \qquad 7.1.3$$

Using the generalized Hooke's law for isotropic, linearly elastic materials, Equation 7.1.3 can be rewritten completely in terms of stress:

$$U_{total} = \frac{1}{2E}\left(\sigma_1^2 + \sigma_2^2 + \sigma_3^2\right) - \frac{v}{E}\left(\sigma_1\sigma_2 + \sigma_2\sigma_3 + \sigma_3\sigma_1\right) \qquad 7.1.4$$

Determining the strain energy of the dilatational component of the stress tensor can be approached by re-arranging the equation for the total internal energy to produce:

$$U_{distortional} = U_{total} - U_{hydrostatic}$$ 7.1.5

A state of stress will result in distortion only (no volume change) if the sum of the three normal stresses is zero. The total change in volume associated with these normal stresses is referred to as the volumetric strain (ε_v), and is simply the sum of the normal strains:

$$\varepsilon_v = \frac{dV}{V} = \varepsilon_x + \varepsilon_y + \varepsilon_z$$ 7.1.7

For an isotropic material the volumetric strain can be expressed in terms of stresses by using the generalized Hooke's law

$$\varepsilon_x = \frac{1}{E}\left[\sigma_x - v\left(\sigma_y + \sigma_z\right)\right]$$ 7.1.8a

$$\varepsilon_y = \frac{1}{E}\left[\sigma_y - v\left(\sigma_x + \sigma_z\right)\right]$$ 7.1.8b

$$\varepsilon_z = \frac{1}{E}\left[\sigma_z - v\left(\sigma_x + \sigma_y\right)\right]$$ 7.1.8c

and substituting Equation 7.1.7 into Equation 7.1.8 and collecting like terms to obtain Equation 7.1.9, which expresses the volumetric strain in terms of the hydrostatic stresses[106,109].

$$\varepsilon_v = \frac{1}{E}\left(1 - 2v\right)p$$ 7.1.9

113

The internal energy resulting from the hydrostatic stress (volume change) can be calculated from the expression for the total energy (Equation 7.1.4) by setting principal stresses $\sigma_1 = \sigma_2 = \sigma_3 = p$, and then replacing p by Equation 7.1.1, which gives the following expression for the internal energy due to hydrostatic stress[110]:

$$U_{hydrostatic} = \frac{3(1-2\nu)}{2E}p^2 = \frac{(1-2\nu)}{6E}(\sigma_1 + \sigma_2 + \sigma_3)^2 \qquad 7.1.10$$

By subtracting Equation 7.1.10 from Equation 7.1.4 and simplifying, an expression for the distortion energy can be obtained:

$$U_{distortional} = \frac{1+\nu}{6E}\left[(\sigma_1 - \sigma_2)^2 + (\sigma_2 - \sigma_3)^2 + (\sigma_3 - \sigma_1)^2\right] \qquad 7.1.11$$

The maximum distortion energy theory of failure states that plasticity will occur when the internal energy given by Equation 7.1.11 exceeds the limiting value from a uniaxial tensile test. In uniaxial tension, all but one of the principal stresses are zero. If we call this stress the yield stress (σ_{yp}) and set the other principal stresses to zero the internal energy of distortion is equal to:

$$U_{distortional} = \frac{1+\nu}{3E}\sigma_{yp}^2 \qquad 7.1.12$$

Substituting this value in Equation 7.1.11 and re-arranging, one obtains the more recognizable form of the maximum distortion energy yield criteria (7.1.13)

$$\sigma_{yp} = \frac{1}{\sqrt{2}}\sqrt{(\sigma_1 - \sigma_2)^2 + (\sigma_2 - \sigma_3)^2 + (\sigma_3 - \sigma_1)^2} \qquad 7.1.13$$

For plane stress, $\sigma_3 = 0$, and Equation 7.1.13 in dimensionless form becomes:

114

$$\left(\frac{\sigma_1}{\sigma_{yp}}\right)^2 - \left(\frac{\sigma_1}{\sigma_{yp}} \cdot \frac{\sigma_2}{\sigma_{yp}}\right) + \left(\frac{\sigma_2}{\sigma_{yp}}\right)^2 = 1 \qquad\qquad 7.1.14$$

Equation 7.1.14 is an equation of an ellipse as shown in Figure 71. Any stress falling within the ellipse indicates that the material behaves elastically and points on the ellipse boundary indicate that the material is yielding. As a result, the maximum distortion energy theory does not predict changes in material response when hydrostatic tensile or compressive stresses are added, since Equation 7.1.13 is based only on the differences in the stress state.
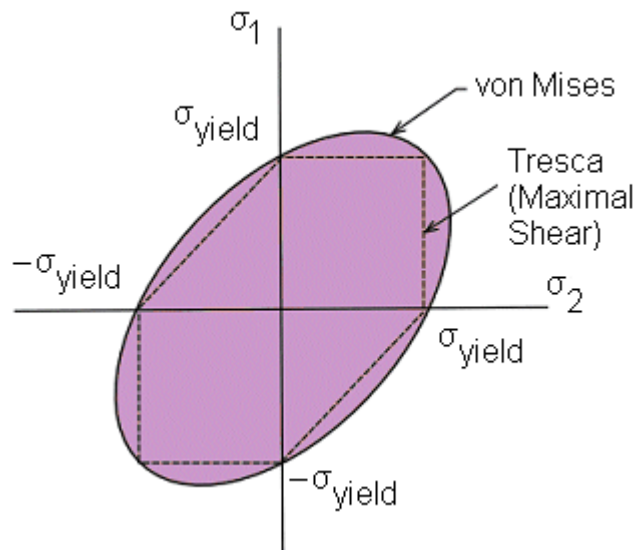
Figure 71: Comparison of Maximum Shear and Maximum Distortion Energy yield criteria

7.2   Failure Criteria for Fiber Metal Laminates

The Maximum Distortion Energy yield criterion has proven to be an effective tool in predicting failure for isotropic materials, as long as the yield stress is known and the given state of stress can be transformed into its principal directions. In the case of FML

115

or other composite materials the assumption of isotropy does not hold and a more generalized failure criterion is required.

As Tsai and Wu[111] pointed out, failure criteria in general do not address the microscopic failure modes of a material, they just provide a method for estimating load carrying capacity. The majority of reference handbooks on material strength agree with one another in terms of uniaxial and shear properties measured along a materials' axis of symmetry, however, these strength values are of little use when trying to determine failure for the combined stress state of a composite material.

Cortes and Cantwell[112] used three different yield criteria in an effort to predict failure in titanium based fiber metal laminate composites and showed that both the Tsai-Wu[113] and the Tsai-Hill[111] failure criteria offered improvements over the maximum stress failure model for these types of materials. Since these two failure criteria have shown good applicability for use with fiber metal laminate materials in these and other studies[112,114,115], the following sections provide some background information on their use.

7.2.1 Tsai-Hill Failure Criteria

Azzi and Tsai[113] put forward a generalized theory of anisotropic strength that used material properties derived from uniaxial tests to evaluate the strength of a composite

116

material. Building on the work of Hill[116], who postulated that the yield condition for anisotropic materials could be assumed to be a quadratic in the form of:

$$F(\sigma_2-\sigma_3)^2 + G(\sigma_3-\sigma_1)^2 + H(\sigma_1-\sigma_2)^2 + 2\left(L\cdot\tau_{23}^2 + M\cdot\tau_{13}^2 + N\cdot\tau_{12}^2\right)=1 \qquad 7.2.7$$

where F,G,H,L,M,N are material strength parameters, and $1,2,3$ are the principal axes of symmetry[117]. Expanding and collecting like terms from Equation 7.2.7 results in:

$$(G+H)\sigma_1^2 + (F+H)\sigma_2^2 + (F+G)\sigma_3^2 - 2\left[H\sigma_1\sigma_2 + F\sigma_2\sigma_3 + G\sigma_1\sigma_3\right]$$
$$+2\left[L\tau_{23}^2 + M\tau_{13}^2 + N\tau_{12}^2\right]=1 \qquad 7.2.8$$

If the failure strengths in the material axes are denoted by X,Y,Z, with shear failure denoted by S then Equation 7.2.8 can be solved experimentally by applying a uniaxial tensile stress in each of the three principal directions while keeping all other stresses zero. These conditions applied to Equation 7.2.8 yield the following three equations:

$$G+H = \frac{1}{X^2} \qquad\qquad 7.2.9a$$

$$H+F = \frac{1}{Y^2} \qquad\qquad 7.2.9b$$

$$F+G = \frac{1}{Z^2} \qquad\qquad 7.2.9c$$

Solving for the unknowns G,H and F yields the following three equations:

$$G = \frac{1}{2}\cdot\left[\frac{1}{Z^2} + \frac{1}{X^2} - \frac{1}{Y^2}\right]$$

$$H = \frac{1}{2}\cdot\left[\frac{1}{X^2} + \frac{1}{Y^2} - \frac{1}{Z^2}\right] \qquad 7.2.10$$

$$F = \frac{1}{2}\cdot\left[\frac{1}{Y^2} + \frac{1}{Z^2} - \frac{1}{X^2}\right]$$

Assuming a state of plane stress in the laminate ($\sigma_3 = \tau_{13} = \tau_{23} = 0$), then the plane stress

version of the failure criteria (Equation 7.2.8) can be written as:

$$G \cdot \sigma_1^2 + F \sigma_2^2 + H(\sigma_1 - \sigma_2)^2 + 2N\tau_{12}^2 = 1 \qquad \text{7.2.11}$$

Application of a pure shear stress τ_{12}, with $\sigma_1 = \sigma_2 = 0$ results in an expression for the

remaining parameter, N:

$$2N = \frac{1}{S^2} \qquad \text{7.2.12}$$

Substituting the failure parameters from Equation 7.2.10 and Equation 7.2.12 into the

plane stress failure criteria (Equation 7.2.11), results in a generalized form of the Tsai-

Hill failure criteria[117]:

$$\left(\frac{\sigma_1}{X}\right)^2 - \left(\frac{1}{X^2} + \frac{1}{Y^2} - \frac{1}{Z^2}\right)\sigma_1\sigma_2 + \left(\frac{\sigma_2}{Y}\right)^2 + \left(\frac{\tau_{12}}{S}\right)^2 = 1 \qquad \text{7.2.13}$$

For the case of an isotropic material, Equation 7.2.13 reduces to the standard Von

Mises yield equation[113]. If the assumption can be made that the material properties in

the through thickness (z direction) transverse to the fiber direction are equal, then the

material can be considered to be transversely isotropic. As a consequence the normal

strengths in the Y and Z direction would be considered equal, reducing Equation 7.2.13

to the more common form of the Tsai-Hill criteria for fiber metal laminate materials:

$$\frac{\sigma_x^2}{X^2} - \frac{\sigma_x\sigma_y}{X^2} + \frac{\sigma_y^2}{Y^2} + \frac{\tau_{xy}^2}{S^2} = 1 \qquad \text{7.2.14}$$

This Tsai-Hill failure criteria (Equation 7.2.14) was used successfully by Cortes and

Cantwell[112] in estimating the failure stress of titanium based fiber metal laminates.

Cortes and Cantwell[112] also showed that the Tsai-Wu failure criteria correlated well with experimental results.

7.2.2 Tsai-Wu Failure Criteria

The Tsai-Wu theory is based on a postulated failure envelope of the form:

$$F_i \sigma_i + F_{ij} \sigma_i \sigma_j = 1 \hspace{3cm} 7.2.15$$

where F_i and F_{ij} are strength tensors that are related to the material strengths in the principal lamina directions and must be determined experimentally. For an orthotropic lamina subjected to plane stress ($\sigma_3 = \tau_{13} = \tau_{23} = 0$) Equation 7.2.15 reduces to:

$$F_{11} \sigma_1^2 + 2F_{12} \sigma_1 \sigma_2 + F_{22} \sigma_2^2 + F_{66} \tau_{12}^2 + F_1 \sigma_1 + F_2 \sigma_2 = 1 \hspace{2cm} 7.2.16$$

Tsai and Wu[111] postulated that simple uniaxial strength experiments could be performed to determine the majority of the stress components. By measuring tensile failure in the principal material direction (*X*) and assuming all other stress components to be zero the failure criteria (Equation 7.2.16) reduces to :

$$F_{11} X^2 + F_1 X = 1 \hspace{1cm} \text{(for tension)} \hspace{2cm} 7.2.17a$$

$$F_{11} X'^2 - F_1 X' = 1 \hspace{1cm} \text{(for compression)} \hspace{2cm} 7.2.17b$$

These two equations can be solved simultaneously to give the following values for F_1 and F_{11} in terms of the ultimate strength in the *X* direction:

$$F_{11} = \frac{1}{XX'} \quad and \quad F_1 = \frac{1}{X} - \frac{1}{X'} \hspace{2cm} 7.2.18$$

A similar procedure can be performed to determine ultimate tensile strength in the orthogonal material principal direction (Y). Again assuming that all other stress components are zero, Equation 7.2.16 now becomes:

$$F_{22}Y^2 + F_2Y = 1 \qquad \text{(for tension)} \qquad 7.2.19a$$

$$F_{22}Y'^2 - F_2Y' = 1 \qquad \text{(for compression)} \qquad 7.2.19b$$

These two equations can again be solved to give the following values for F_2 and F_{22} in terms of the ultimate strength in the Y direction:

$$F_2 = \frac{1}{Y} - \frac{1}{Y'} \quad and \quad F_{22} = \frac{1}{YY'} \qquad 7.2.20$$

A similar procedure can be performed for an application of a pure shear stress (S), again assuming that all other stress components are zero, reducing Equation 7.2.16 to:

$$F_{66}S^2 + F_6S = 1 \qquad \text{(for } +\tau) \qquad 7.2.21a$$

$$F_{66}S'^2 - F_6S' = 1 \qquad \text{(for } -\tau) \qquad 7.2.22b$$

Solving Equations 7.2.21a and 7.2.21b simultaneously produces the following values for F_6 and F_{66}:

$$F_{66} = \frac{1}{S^2} \quad and \quad F_6 = 0 \qquad 7.2.22$$

The only remaining term is F_{12}, and in theory this could be determined by applying a biaxial stress state so that $\sigma_1 = \sigma_2 = 0$, however this poses practical difficulties and various values (Equations 7.2.23a-c) have been proposed for this term.

$$F_{12} = -\frac{1}{2X^2}$$

7.2.23a

$$F_{12} = -\frac{1}{2X \cdot X'}$$

7.2.23b

$$F_{12} = -\frac{1}{2} \cdot \sqrt{\frac{1}{(X \cdot X')(Y \cdot Y')}}$$

7.2.23c

The correct value is material dependent and requires experimental validation, with Cortes and Cantwell[112] applying the formulation in Equation 7.2.23c for use with titanium based fiber metal laminates.

7.3   Elastic-Plastic Material Models

The next step in building a closed form solution for the stresses and strains during cold expansion is to be able to mathematically describe material behaviour beyond the linear region. In 1943, Ramberg and Osgood[118] published a report detailing some simple formulas for describing the stress-strain (σ-ε) curve of a material in terms of Young's modulus (E) and two parameters (n and K – strain hardening coefficients) relating to the behaviour of the material during plastic deformation. The classic Ramberg-Osgood expression is shown in Equation 7.3.1

$$\varepsilon = \frac{\sigma}{E} + K\left(\frac{\sigma}{E}\right)^n$$

7.3.1

and has since been modified to take into account the yield stress (σ_y) of the material in question. This modified Ramberg-Osgood parameter was first proposed by Budiansky[119] in 1971 and it separates the material behaviour into linear and non-linear components:

121

$$\varepsilon = \frac{\sigma}{E} \quad \text{for } |\sigma| \leq \sigma_y \qquad\qquad 7.3.2$$

$$\varepsilon = \frac{\sigma}{E}\left(\frac{\sigma}{\sigma_y}\right)^{n-1} \quad \text{for } |\sigma| > \sigma_y \qquad\qquad 7.3.3$$

Analytical models trying to represent material behaviour after a reversal in the stress field or during cyclical plasticity need some way to account for the potential changes in material properties. If one performs a uniaxial tension or compression test and plots true stress versus true strain, it would be noted that for most materials the yield point in tension and compression are very similar. However, if one first deforms a material in uniform tension, unloads it and then deforms it in compression, the yield point in compression is typically reduced. This is referred to as the Bauschinger effect, and is most clearly illustrated in the case of a tensile specimen. Hill[120] suggested that this effect may be due to the distortion of the crystallographic planes into a preferred orientation, resulting in the material becoming increasingly anisotropic. Hill also hypothesized that this crystallographic distortion caused microscopic residual stresses to remain in the material, and, if the material was then loaded differently, for example in compression as opposed to tension, these residual stresses would significantly influence plastic yielding. There are two main models used to describe the Bauschinger effect; isotropic and kinematic hardening (Figure 72). In kinematic hardening it is assumed that the elastic unloading range will be double the initial yield stress. If the initial yield stress is σ_0, and the yield point during a subsequent loading cycles is σ_1 then the specimen will yield in compression according to the path ABCDE (Figure 72) after being stressed in tension. At the other end of the spectrum is the

theory of isotropic hardening that assumes that the mechanism that produces hardening

acts equally in tension and compression. As a result, if the tensile yield stress during a

load cycle is σ_1 then compressive yielding would occur at a stress of $-\sigma_1$ as shown by

the path ABCFG (Figure 72). Although this is the simplest theory to use and apply to

closed form solutions, test results show that the compressive yield stress lies between

points H and D in Figure 72[105]

Figure 72: Effect of isotropic versus kinematic hardening on the yielding of a material[105]

7.4   Review of Closed Form Solution for Cold Expansion

The basis for the current closed form solutions for cold expansion rests with Nadai[57] in

1943; whose interest in characterizing the joining of boiler tubes using radial expansion

led him to first explore much of the theoretical groundwork that is used today. Hsu and

Forman[71] improved upon Nadai's[57] work by using a modified Ramberg-Osgood

material model to better enable them to characterize material behaviour beyond yield.

Although the work by Hsu and Forman[71] modeled the unloading step, they assumed

that it was elastic and thus did not address reverse yielding or the development of a

reverse yield zone next to the hole. Budiansky[121] and Ball[122] put forward a closed

form solution that took into account elastic-plastic unloading and thus the creation of a

reverse yield zone, caused by the removal of the oversized mandrel from the expanded

hole. Ball's[122] derivation started by dividing up the cold expansion process into elastic

and plastic regions, with separate equations for each region. Guo[123] developed a very

complete solution that took into account finite boundary conditions, but did not

completely deal with mandrel unloading. Zhang et al's[124] paper explicitly built upon this

framework and attempted to complete Guo's[123] work by taking into account both the

insertion of the mandrel and the reverse unloading that takes place when the mandrel is

removed, as well as further subdividing the region around the hole into plastic, elastic-

plastic and elastic regions, thus providing a slightly more rigorous result than that

achieved by Ball[122] or Guo[123].

The basic assumptions remain the same as those initially presented by Hsu and

Forman[71], namely that the cold expansion process begins with a hole in a finite circular

plate with radius r, inner radius a, subjected to an internal pressure p that represents the

action of the oversized mandrel. Both Ball[122] and Hsu and Forman[71] represented the

plate as being infinite in radius while Zhang et al[124] explicitly defined an outer radius of

the plate (b).

An overview of the closed form solution begins with the definition of a polar co-ordinate

system as shown in Figure 73, with the initial boundary conditions as follow:

$$\sigma_r = 0 \text{ at } r = b \qquad\qquad 7.4.1$$

$$\sigma_r = -p \text{ at } r = 0 \qquad\qquad 7.4.2$$
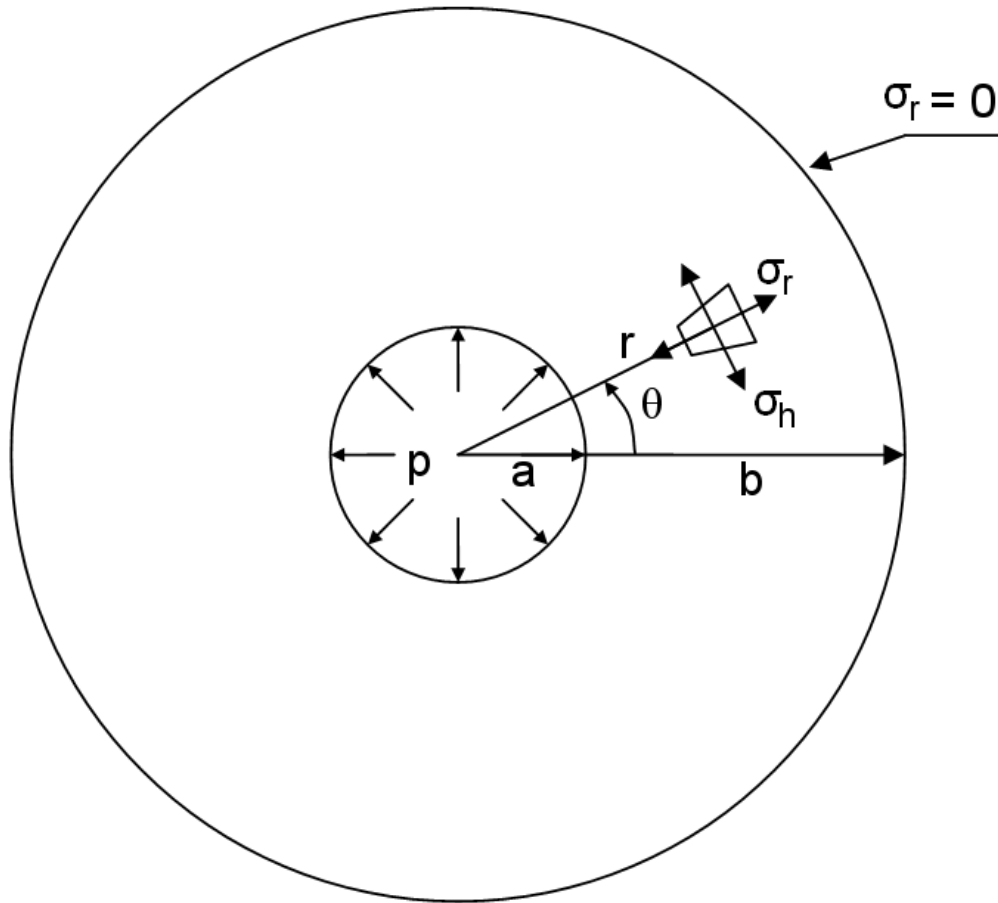
Figure 73: Free body diagram of a finite plate with circular hole[124]

In all cases, the material properties are modeled using the modified Ramberg-Osgood relationship:

$$\varepsilon = \frac{\sigma}{E} \text{ for } |\sigma| \leq \sigma_y \qquad\qquad 7.4.3$$

$$\varepsilon = \frac{\sigma}{E} \cdot \left| \frac{\sigma}{\sigma_y} \right|^{n-1} \text{ for } |\sigma| \geq \sigma_y \qquad\qquad 7.4.4$$

where ε is the true strain, σ is the true stress, E is the elastic modulus, σ_y is the initial yield stress and n is the strain hardening exponent. Both Ball[122] and Zhang et al[124] started the derivation of their respective closed form solutions by providing the fundamental relationships between strain and displacement in polar coordinates:

$$\varepsilon_r = \frac{du}{dr} \qquad\qquad 7.4.5a$$

$$\varepsilon_\theta = \frac{u}{r} \qquad\qquad 7.4.5b$$

where u is the displacement in the radial direction and r is the distance from the center of the hole. The total strains are then defined as the sum of both the elastic and plastic strains in both the radial and tangential directions:

$$\varepsilon_r = \varepsilon_r{}^{el} + \varepsilon_r{}^{pl} \qquad\qquad 7.4.6a$$

$$\varepsilon_\theta = \varepsilon_\theta{}^{el} + \varepsilon_\theta{}^{pl} \qquad\qquad 7.4.6b$$

In the elastic region, the relationship between stresses and strains can be defined using the generalized Hooke's law model:

$$\varepsilon_r{}^{el} = \frac{1}{E} \cdot \left(\sigma_r - v \cdot \sigma_\theta \right) \qquad\qquad 7.4.7a$$

$$\varepsilon_\theta{}^{el} = \frac{1}{E} \cdot \left(\sigma_\theta - v \cdot \sigma_r \right) \qquad\qquad 7.4.7b$$

where E is the Young's modulus of the material and v is the Poisson's ratio. The

relationship between stresses and strains in the plastic zone is more complex, for which

both Ball[122] and Zhang et al[124] rely on a model first put forward by Hsu[71]:

$$\varepsilon_r{}^{pl} = \left(\frac{1}{E_s} - \frac{1}{E} \right) \cdot \left(\sigma_r - \frac{R}{1+R} \cdot \sigma_\theta \right) \qquad\qquad 7.4.8a$$

$$\varepsilon_\theta{}^{pl} = \left(\frac{1}{E_s} - \frac{1}{E} \right) \cdot \left(\sigma_\theta - \frac{R}{1+R} \cdot \sigma_r \right) \qquad\qquad 7.4.8b$$

In Equations 7.4.8a and 7.4.8b, R is defined as the ratio of in-plane transverse plastic

strain to through thickness plastic strain in much the same way that the Poisson's ratio v

defines the ratio of lateral to transverse elastic strains. A value of $R=1$ would represent

a purely isotropic material and an $R=0$ would represent anisotropic plastic behaviour.

Testing a range of R values showed that $R=0.5$ provided the optimal match to the

experimental strain values for FML while $R=1$ was optimal for 2024-T3 aluminum. E_s is

the secant modulus at a point (σ,ε) on the stress strain curve and can also be obtained

from the modified Ramberg-Osgood model as:

$$\frac{1}{E_s} = \frac{\varepsilon}{\sigma} = \frac{1}{E} \cdot \left| \frac{\sigma}{\sigma_y} \right|^{n-1} \qquad\qquad 7.4.9$$

Since v has no effect on the stress solution $v=R/(1+R)$ can be used in conjunction with Equation 7.4.6, Equation 7.4.7 and Equation 7.4.8 to produce a relationship between the total strains and stresses[123] as shown:

$$\varepsilon_r = \frac{1}{E_s} \cdot \left(\sigma_r - \frac{R}{1+R} \cdot \sigma_\theta\right) \qquad \text{7.4.10a}$$

$$\varepsilon_\theta = \frac{1}{E_s} \cdot \left(\sigma_\theta - \frac{R}{1+R} \cdot \sigma_r\right) \qquad \text{7.4.10b}$$

Both Ball[122] and Zhang et al[124] divided the derivation of the residual stress field into two distinct parts – the first representing the insertion of the oversized mandrel and the second representing the reverse unloading in the material that occurs when the oversized mandrel is removed and the material exhibits some elastic spring back.

7.4.1 Stresses Due to Loading of Plate by Mandrel

The closed form solution for the stresses resulting from the oversized mandrel may also be suitable for describing the stresses induced through the riveting process or any other process where an oversized mandrel or fastener is inserted into a hole.

Although Ball[122], Guo[123] and Zhang et al[124] all started off with essentially the same derivation, Zhang et al[124] expanded the analysis to include plates of finite size b, instead of merely assuming an infinite plate. If a uniform pressure p applied at the hole boundary results in elastic deformation then the elastic solution for the radial and tangential stresses is[124,125]:

$$\sigma_r = -\frac{\left(b^2/r^2\right)-1}{\left(b^2/a^2\right)-1} \cdot p \qquad\qquad 7.4.11a$$

$$\sigma_\theta = -\frac{\left(b^2/r^2\right)+1}{\left(b^2/a^2\right)-1} \cdot p \qquad\qquad 7.4.11b$$

In the case where the plate undergoes elastic-plastic deformations, the stress solutions

in the elastic domain ($r_p \le r \le b$), with variables depicted graphically in Figure 74, are:

$$\sigma_r = -\frac{\left(b^2/r^2\right)-1}{\left(b^2/a^2\right)-1} \cdot p_p \qquad\qquad 7.4.12a$$

$$\sigma_\theta = -\frac{\left(b^2/r^2\right)+1}{\left(b^2/a^2\right)-1} \cdot p_p \qquad\qquad 7.4.12b$$

where p_p represents the pressure at the boundary between the elastic and plastic

domain at $r=r_p$. To determine p_p, the first step is to calculate the effective stress, which

in the plastic domain ($a \le r \le r_p$), is defined as:

$$\sigma = \left(\sigma_r^2 + \sigma_\theta^2 - \frac{2R}{1+R} \cdot \sigma_r \cdot \sigma_\theta \right)^{0.5} \qquad\qquad 7.4.13$$

The yield criterion for the effective stress is:

$$\sigma = \sigma_y \qquad\qquad 7.4.14$$

Since FML is a hybrid of aluminum and glass fibers and has a distinct yield point, this

formulation should be applicable for both aluminum and FML.
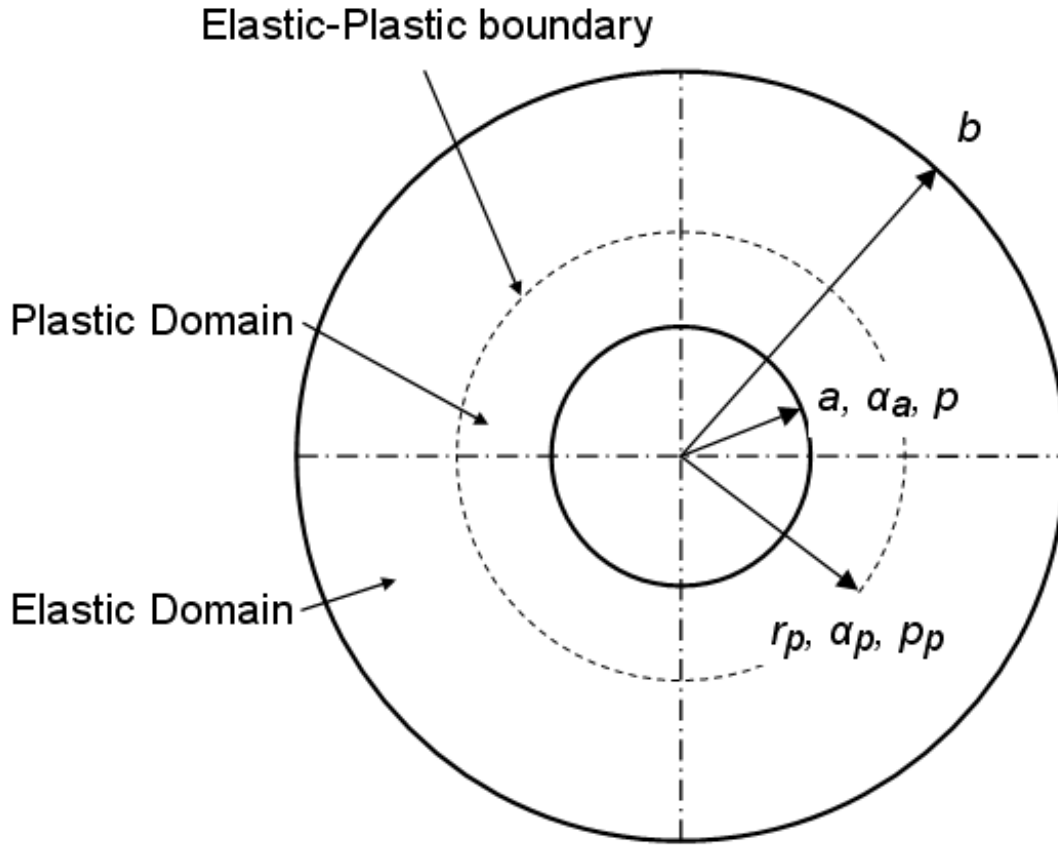
Figure 74: Diagram of the variables associated with elastic-plastic deformation[124]

The elastic solution for Equation 7.4.12 at $r=r_p$ should also satisfy Equation 7.4.13 and Equation 7.4.14 because of the continuity of the stress field at the elastic-plastic boundary[124]. By combining Equation 7.4.12, Equation 7.4.13 and Equation 7.4.14, it is possible to obtain the pressure at the elastic-plastic boundary (p_p) in terms of the yield stress:

$$p_p = \sigma_y \left(\frac{b^2}{a^2} - 1 \right) \cdot \left[2 \cdot \frac{b^4}{r_p^4} + 2 + \frac{2R}{1+R} \cdot \left(\frac{b^4}{r_p^4} - 1 \right) \right]^{-0.5} \qquad 7.4.15$$

By substituting Equation 7.4.15 into Equation 7.4.12a and Equation 7.4.12b it is possible to obtain an expression for the radial and tangential stresses in the elastic zone:

$$\sigma_r = -\sigma_y \cdot \left(\frac{b^2}{r^2} - 1\right) \cdot \left[2 \cdot \frac{b^4}{r_p^4} + 2 + \frac{2R}{1+R} \cdot \left(\frac{b^4}{r_p^4} - 1\right)\right]^{-0.5} \qquad \text{7.4.16a}$$

$$\sigma_\theta = \sigma_y \cdot \left(\frac{b^2}{r^2} + 1\right) \cdot \left[2 \cdot \frac{b^4}{r_p^4} + 2 + \frac{2R}{1+R} \cdot \left(\frac{b^4}{r_p^4} - 1\right)\right]^{-0.5} \qquad \text{7.4.16b}$$

In order to generate a solution for the stresses in the plastic zone, both Ball[122], Guo[123] and Zhang et al[124] used Budiansky's technique of writing the effective stress in terms of a parameter α, which varies monotonically from α_a at the edge of the hole to α_p at the edge of the plastic zone, to give the following two equations:

$$\sigma_r = \sigma \cdot \sqrt{\frac{1+R}{2}} \cdot \left[\cos(\alpha) - \frac{1}{\sqrt{1+2 \cdot R}} \cdot \sin(\alpha)\right] \qquad \text{7.4.17a}$$

$$\sigma_\theta = \sigma \cdot \sqrt{\frac{1+R}{2}} \cdot \left[\cos(\alpha) + \frac{1}{\sqrt{1+2 \cdot R}} \cdot \sin(\alpha)\right] \qquad \text{7.4.17b}$$

Zhang et al[124] combined Equation 7.4.16 and Equation 7.4.17 with $\alpha = \alpha_p$ and $r = r_p$ to produce two intermediate equations relating α_p and r_p:

$$\sin(\alpha_p) = \sqrt{1+2 \cdot R} \cdot \left(\frac{b}{r_p}\right)^2 \cdot \left[(1+2 \cdot R) \cdot \left(\frac{b}{r_p}\right)^4 + 1\right]^{-0.5} \qquad \text{7.4.18a}$$

131

$$\cos(\alpha_p) = \left[(1 + 2 \cdot R) \cdot \left(\frac{b}{r_p} \right)^4 + 1 \right]^{-0.5}$$

7.4.18b

$$\text{where, } 0 < \alpha_p \leq \pi/2$$

Both Ball[122] and Zhang et al[124] used Equation 7.4.9, Equation 7.4.10 and Equation

7.4.17 along with the stress equilibrium equation:

$$\frac{d\sigma}{dr} + \frac{\sigma_r - \sigma_\theta}{r} = 0$$

7.4.18c

and the compatibility equation:

$$\frac{d\varepsilon_\theta}{dr} + \frac{\varepsilon_\theta - \varepsilon_r}{r} = 0$$

7.4.19

To produce an expression that could be differentiated in terms of the effective stress (σ)

and the parameter α to give:

$$\frac{1}{\sigma} \cdot d\sigma = \frac{2 \cdot (1 + R) \cdot \sin(\alpha)}{(n + 1 + 2 \cdot R) \cdot \cos(\alpha) + (n - 1) \cdot \sqrt{1 + 2 \cdot R} \cdot \sin(a)} \cdot d\sigma$$

7.4.20

This can then be integrated to produce an expression relating the effective stress to the

yield stress:

$$\frac{\sigma}{\sigma_y} = \left(\frac{a_1 \cdot \sin(\alpha_p) + a_2 \cdot \cos(\alpha_p)}{a_1 \cdot \sin(\alpha_a) + a_2 \cdot \cos(\alpha_a)} \right)^\mu \exp\left(\frac{2a_1 \cdot (1 + R) \cdot (\alpha_a - \alpha_p)}{a_1^2 + a_2^2} \right)$$

7.4.21

$$\text{where}$$

$$a_1 = (n - 1)\sqrt{1 + 2R}$$

$$a_2 = n + 1 + 2R$$

$$\mu = \frac{2a_2 (1 + R)}{a_1^2 + a_2^2}$$

132

The relationship between the pressure p, and the parameter α_a and α_p can be derived using Equation 7.4.17a and Equation 7.4.21 along with the initial conditions provided by Equation 7.4.2 to give:

$$p = \sigma_y \sqrt{\frac{1+R}{2}} \cdot \left(\frac{\sin(\alpha_a)}{\sqrt{1+2R}} - \cos(\alpha_a) \right) \left(\frac{a_1 \cdot \sin(\alpha_p) + a_2 \cdot \cos(\alpha_p)}{a_1 \cdot \sin(\alpha_a) + a_2 \cdot \cos(\alpha_a)} \right)^{\mu}$$
$$\times \exp\left(\frac{2a_1 \cdot (1+R) \cdot (\alpha_a - \alpha_p)}{a_1^2 + a_2^2} \right)$$

7.4.22

The next step in the derivation is to produce an expression relating the edge ratio r/a to the parameter α. Combining Equation 7.4.18c and Equation 7.4.17 and integrating the resultant from $\alpha = \alpha_a$ at $r=a$ gives the following generalized equation:

$$\frac{r}{a} = \sqrt{\frac{\sin(\alpha_a)}{\sin(\alpha)}} \cdot \left(\frac{a_1 \cdot \sin(\alpha) + a_2 \cdot \cos(\alpha)}{a_1 \cdot \sin(\alpha_a) + a_2 \cdot \cos(\alpha_a)} \right)^{\gamma} \exp\left(\frac{\left(n^2 - 1\right) \cdot \sqrt{1+2R} \cdot (\alpha_a - \alpha)}{2 \cdot \left(n^2 + 1 + 2R\right)} \right)$$

where

$$\gamma = \frac{n \cdot (1+R)}{n^2 + 1 + 2R}$$

7.4.23

If r is set equal to r_p and α is set equal to α_a, then the relationship between r_p, α_a, and α_p can be defined as:

$$\frac{r_p}{a} = \sqrt{\frac{\sin(\alpha_a)}{\sin(\alpha_p)}} \cdot \left(\frac{a_1 \cdot \sin(\alpha_p) + a_2 \cdot \cos(\alpha_p)}{a_1 \cdot \sin(\alpha_a) + a_2 \cdot \cos(\alpha_a)} \right)^{\gamma} \exp\left(\frac{\left(n^2 - 1\right) \cdot \sqrt{1+2R} \cdot (\alpha_a - \alpha_p)}{2 \cdot \left(n^2 + 1 + 2R\right)} \right)$$

7.4.24

The maximum value of α, α_{max}, can be determined from Equation 7.4.24 by calculating the limit as $b \to \infty$, $p \to \infty$, and $r_p \to \infty$ resulting in the following equation:

$$\alpha_{\max} = \tan^{-1}\left[\frac{n+1+2R}{(1-n)\sqrt{1+2R}}\right]$$

7.4.25

Zhang et al[124] proposed a slightly different solution than Ball[122] who solved for r_p, α_a,

and α_p by using Equation 7.4.24, Equation 7.4.22 and Equation 7.4.18. In Zhang et

al's[22] solution, the trigonometric functions for α_p in Equation 7.4.18a and Equation

7.4.18b are substituted into Equation 7.4.21 and Equation 7.4.23 and then solved using

an iterative solver routine with $\alpha_p < \alpha_a < \alpha_{max}$. Since Ball's analysis[122] assumed b → ∞,

an iterative solution was possible by simply using Equation 7.4.22. With r_p, α_a, and α_p

determined, the radial and tangential stresses in the plastic zone can be calculated

using Equation 7.4.23, Equation 7.4.21 and Equation 7.4.17 with the elastic stresses

calculated using Equation 7.4.16.

The approach used by both Zhang et al[124] and Ball[122] up to this point, simulated the

stress resulting from the insertion of an oversized fastener or rivet into a hole. This

portion of the closed form solution may prove to be very useful in modeling the strain

response in FML since stress-strain solutions can be calculated in each of the principal

material directions by simply modifying the Ramberg-Osgood material model.

7.4.1.1 Calculation of the Interference Ratio

The next step in generating a closed form solution is to determine the interference ratio

resulting from the insertion of the oversized mandrel. Although both Ball[122] and Zhang

et al[124] solve the problem similarly, Zhang's work provides the more explicit

explanation. In both cases the main goal is to determine a relationship between the interference generated by the mandrel and the subsequent pressure applied at the edge of the hole.

The interference (I_a) should be equivalent to the difference between the radial displacement of the plate, $u_p(a)$, and the radial contraction of the mandrel, $u_m(a)$, at the edge of the hole (r=a). This relationship can be represented mathematically as:

$$I_a = a_m - a = u_p(a) - u_m(a)$$ 7.4.26

where a_m is the radius of the mandrel and a is the radius of the hole. Both Zhang et al[124] and Ball[122] made the assumption that the displacement of the mandrel was elastic and so u_m could be calculated using:

$$u_m(a) = -\frac{a_m \cdot p}{E_m} \cdot (1 - v_m)$$ 7.4.27

where E_m and v_m are the elastic modulus and Poisson's ratio of the mandrel respectively. The radial displacement of the plate can be calculated by rearranging and using Equation 7.4.5b at r=a:

$$u_p(a) = a \cdot \varepsilon_\theta(a)$$ 7.4.28

Zhang provides two analytical expressions for u_p, one assuming that the plate undergoes only an elastic deformation, and the other assuming that the plate undergoes a plastic deformation. The equation for u_p assuming plastic deformation takes into account the contribution due to both the elastic and plastic strains and is derived by

135

combining Equation 7.4.6b, Equation 7.4.7b and Equation 7.4.8b with Equation 7.4.17

and Equation 7.4.21 to give the following expression at $\alpha = \alpha_a$ and $r=a$:

$$u_p(a) = \frac{a \cdot \sigma_y}{E} \cdot \sqrt{\frac{1+R}{2}} \cdot \left[(1-\lambda) \cdot \cos(\alpha_a) + \frac{1+\lambda}{\sqrt{1+2R}} \cdot \sin(\alpha_a)\right] \cdot$$

$$\left[\left(\frac{a_1 \cdot \sin(\alpha_p) + a_2 \cdot \cos(\alpha_p)}{a_1 \cdot \sin(\alpha_a) + a_2 \cdot \cos(\alpha_a)}\right)^{\mu} \exp\left(\frac{2 \cdot a_1(1+R) \cdot \sqrt{1+2R} \cdot (\alpha_a - \alpha_p)}{a_1^2 + a_2^2}\right)\right]^n$$

7.4.28a

where

$$\lambda = \frac{R}{1+R} - \left(\frac{R}{1+R} - \nu\right) \cdot$$

$$\left[\left(\frac{a_1 \cdot \sin(\alpha_p) + a_2 \cdot \cos(\alpha_p)}{a_1 \cdot \sin(\alpha_a) + a_2 \cdot \cos(\alpha_a)}\right)^{\mu} \cdot \exp\left(\frac{2 \cdot a_1 \cdot (1+R) \cdot (\alpha_a - \alpha_p)}{a_1^2 + a_2^2}\right)\right]^{1-n}$$

Assuming only elastic deformation in the plate, it is possible to derive an equation for

the radial displacement of the plate at $r=a$ from Equation 7.4.7b and Equation 7.4.16:

$$u_p(a) = \frac{a \cdot \sigma_y}{E} \cdot \left[\frac{b^2}{a^2} + 1 + \nu \cdot \left(\frac{b^2}{a^2} - 1\right)\right] \cdot \left[2 \cdot \frac{b^4}{r_p^4} + 2 + \frac{2R}{1+R} \cdot \left(\frac{b^4}{r_p^4} - 1\right)\right]^{-0.5}$$

7.4.28b

The undeformed mandrel size, a_m can now be calculated using Equation 7.4.24 and

Equation 7.4.27 substituted into Equation 7.4.26 to produce the following expression[122]:

$$a_m = \frac{u_p(a) + a}{1 - \left[\frac{p}{E_m} \cdot (1 - \nu_m)\right]}$$

7.4.29a

The interference ratio, I_0, can now be easily calculated from:

$$I_0 = \frac{I_a}{a} = \frac{a_m - a}{a}$$

7.4.29b

In practice, the above equations are solved by deciding on a desired interference level (I_0) and iteratively varying the pressure (p) until the desired interference ratio is obtained.

7.4.2 Closed Form Solution for Elastic-Plastic Unloading

Both Zhang et al[124] and Ball[122] built upon the solution presented by Hsu and Forman[71] by explicitly dividing the cold expansion process into a loading regime (insertion of the mandrel) and an unloading regime (removal of the mandrel). Ball[122] divided his closed form solution into both a plastic and elastic regime while Zhang et al[124] went one step further and provided a closed form solution for an elastic-plastic transition regime. Due to the reverse yielding resulting from the withdrawal of the mandrel, the equation for the reverse yield stress (σ_y^*) depends on whether a point is in the elastic or plastic region. For points that were elastic during the loading process (i.e. insertion of the oversized mandrel) the equation for the reverse yield stress is:

$$\sigma_y^* = \sigma + \sigma_y \qquad\qquad 7.4.30$$

where σ is the effective stress as calculated from Equation 7.4.13. For points that underwent plastic deformation during the loading process, the equation for the reverse yield stress is:

$$\sigma_y^* = (1+\beta)\cdot\sigma_y + (1-\beta)\cdot\sigma \qquad\qquad 7.4.31$$

Equation 7.4.31 includes a β term that represents the Baushinger parameter. This parameter takes into account the strain hardening of the material due to plasticity. A

Baushinger parameter of $\beta=0$ implies isotropic hardening while a $\beta=1$ represents kinematic hardening.

The closed form solution for the unloading process is very similar to that followed for the loading process. All equations and variables used specifically for the unloading process are denoted with an "$*$". The relationship between the applied pressure, p, the parameter α_a^* at the hole edge (r=a), and the parameter α_p^* at the edge of the plastic zone (r=r_p^*) during the unloading process is defined as:

$$p = \sigma_y^* \sqrt{\frac{1+R}{2}} \cdot \left(\frac{\sin(\alpha_a^*)}{\sqrt{1+2R}} - \cos(\alpha_a^*) \right) \left(\frac{a_1 \cdot \sin(\alpha_p^*) + a_2 \cdot \cos(\alpha_p^*)}{a_1 \cdot \sin(\alpha_a^*) + a_2 \cdot \cos(\alpha_a^*)} \right)^{\mu}$$
$$\times \exp\left(\frac{2a_1 \cdot (1+R) \cdot \left(\alpha_a^* - \alpha_p^* \right)}{a_1^2 + a_2^2} \right)$$

7.4.32

The boundary of the reverse yield plastic zone, r_p^*, can be found using Equation 7.4.33 which is the same equation as Equation 7.4.24 except that all variables have a "$*$" denoting the unloading process:

$$\frac{r_p^*}{a} = \sqrt{\frac{\sin(\alpha_a^*)}{\sin(\alpha_p^*)}} \cdot \left(\frac{a_1 \cdot \sin(\alpha_p^*) + a_2 \cdot \cos(\alpha_p^*)}{a_1 \cdot \sin(\alpha_a^*) + a_2 \cdot \cos(\alpha_a^*)} \right)^{\gamma} \exp\left(\frac{\left(n^2 - 1 \right) \cdot \sqrt{1+2R} \cdot \left(\alpha_a^* - \alpha_p^* \right)}{2 \cdot \left(n^2 + 1 + 2R \right)} \right)$$

7.4.33

An iterative solver can now be used to solve for both r_p^* and α_a^*. The value of α_p^* can then be calculated using either Equation 7.4.18a or Equation 7.4.18b. For points at $a \leq r \leq r_p^*$, the unloading is plastic and the resulting radial and tangential stresses are given by:

$$\sigma_r^* = -\sigma^* \cdot \sqrt{\frac{1+R}{2}} \cdot \left[\cos(\alpha^*) - \frac{1}{\sqrt{1+2 \cdot R}} \cdot \sin(\alpha^*) \right]$$ 7.4.34a

$$\sigma_\theta^* = -\sigma^* \cdot \sqrt{\frac{1+R}{2}} \cdot \left[\cos(\alpha^*) + \frac{1}{\sqrt{1+2 \cdot R}} \cdot \sin(\alpha^*) \right]$$ 7.4.34b

Where the effective stress for the unloading step (σ^*) can be calculated using:

$$\frac{\sigma^*}{\sigma_y^*} = \left(\frac{a_1 \cdot \sin(\alpha_p^*) + a_2 \cdot \cos(\alpha_p^*)}{a_1 \cdot \sin(\alpha_a^*) + a_2 \cdot \cos(\alpha_a^*)} \right)^\mu \exp\left(\frac{2a_1 \cdot (1+R) \cdot \left(\alpha_a^* - \alpha_p^* \right)}{a_1^2 + a_2^2} \right)$$ 7.4.35

where the reverse yield stress (σ_y^*) is calculated using Equation 7.4.31. The

relationship between the radius r and the unloading Budiansky parameter α^* is defined

in a similar manner to Equation 7.4.33:

$$\frac{r}{a} = \sqrt{\frac{\sin(\alpha_a^*)}{\sin(\alpha^*)}} \cdot \left(\frac{a_1 \cdot \sin(\alpha^*) + a_2 \cdot \cos(\alpha^*)}{a_1 \cdot \sin(\alpha_a^*) + a_2 \cdot \cos(\alpha_a^*)} \right)^\gamma \exp\left(\frac{\left(n^2 - 1 \right) \cdot \sqrt{1+2R} \cdot \left(\alpha_a^* - \alpha^* \right)}{2 \cdot \left(n^2 + 1 + 2R \right)} \right)$$ 7.4.36

Ball[122] treated points between the reverse yielded zone and the plastic zone

($r_p^* \leq r \leq r_p$) as completely elastic whereas Zhang et al[124] treated this region as elastic

with a yield point based on the reverse yield criterion. The equations for the radial and

tangential stresses in the elastic-plastic region include the yield criterion from Equation

7.4.31 and are given by:

$$\sigma_r^* = \left[(1+\beta) \cdot \sigma_y + (1-\beta) \cdot \sigma \right] \cdot \left(\frac{b^2}{r^2} - 1 \right)$$

$$\times \left[2 \cdot \left(\frac{b^4}{r_p^*} \right)^4 + 2 + \frac{2R}{1+R} \cdot \left[\left(\frac{b^4}{r_p^*} \right)^4 - 1 \right] \right]^{-0.5}$$ 7.4.37a

139

$$\sigma_\theta^* = -\left[(1+\beta)\cdot\sigma_y+(1-\beta)\cdot\sigma\right]\cdot\left(\frac{b^2}{r^2}+1\right)$$

$$\times\left[2\cdot\left(\frac{b^4}{r_p^*}\right)^4+2+\frac{2R}{1+R}\cdot\left[\left(\frac{b^4}{r_p^*}\right)^4-1\right]\right]^{-0.5} \qquad 7.4.37b$$

For all points located outside the plastic zone ($r \geq r_p$), the unloading is purely elastic and the equations for the radial and tangential stresses include the reverse yield criterion from Equation 7.4.30 and are given by:

$$\sigma_r^* = (\sigma+\sigma_y)\cdot\left(\frac{b^2}{r^2}-1\right)\cdot\left[2\cdot\left(\frac{b^4}{r_p^*}\right)^4+2+\frac{2R}{1+R}\cdot\left[\left(\frac{b^4}{r_p^*}\right)^4-1\right]\right]^{-0.5} \qquad 7.4.38a$$

$$\sigma_\theta^* = -(\sigma+\sigma_y)\cdot\left(\frac{b^2}{r^2}+1\right)\cdot\left[2\cdot\left(\frac{b^4}{r_p^*}\right)^4+2+\frac{2R}{1+R}\cdot\left[\left(\frac{b^4}{r_p^*}\right)^4-1\right]\right]^{-0.5} \qquad 7.4.38b$$

The final radial and tangential residual stresses can now be calculated by simply summing up the stresses during both the loading and unloading portion of the cold expansion process:

$$\sigma_r^{res} = \sigma_r+\sigma_r^* \qquad 7.4.39a$$

$$\sigma_\theta^{res} = \sigma_\theta+\sigma_\theta^* \qquad 7.4.39b$$

7.4.3 Calculation of Radial and Tangential Strains

For the purposes of making a comparison between experimental and theoretical results, it was critical to have an explicit formulation for the strain values in both the elastic and plastic regimes. During the loading phase, the plastic strains can be calculated by using Equation 7.4.10 with the Ramberg-Osgood relationship for the secant modulus

(Equation 7.4.9), which results in the following explicit expression for the radial and tangential strains:

$$\varepsilon_r = \frac{1}{E} \cdot \left(\frac{\sigma}{\sigma_y} \right)^{n-1} \cdot \left[\sigma_r - \frac{R}{1+R} \cdot \sigma_\theta \right] \qquad \text{7.4.40a}$$

$$\varepsilon_\theta = \frac{1}{E} \cdot \left(\frac{\sigma}{\sigma_y} \right)^{n-1} \cdot \left[\sigma_\theta - \frac{R}{1+R} \cdot \sigma_r \right] \qquad \text{7.4.40b}$$

The elastic strains can then be calculated from the generalized Hooke's Law relationship given in Equation 7.4.7, except that the Poisson's ratio, v, is replaced by[71,123]:

$$v = \frac{R}{1+R} \qquad \text{7.4.41}$$

The calculation of the elastic and plastic strains for the unloaded case proceeds in a similar manner, with the inclusion of the corresponding stresses from unloading used in Equation 7.4.40 and Equation 7.4.42. The final residual strains are then simply the summation of the residual strains during loading and unloading, in a manner analogous to Equation 7.4.39.

$$\varepsilon_r = \frac{1}{E} \cdot \left[\sigma_r - \frac{R}{1+R} \cdot \sigma_\theta \right] \qquad \text{7.4.42a}$$

$$\varepsilon_\theta = \frac{1}{E} \cdot \left[\sigma_\theta - \frac{R}{1+R} \cdot \sigma_r \right] \qquad \text{7.4.42b}$$

7.5   Development of Closed Form Model for Riveting

Modifying the closed form solution used for the cold expansion process provided one possible method for developing an analytical solution for calculating the stresses and strains during the riveting process.

In the first stage of the closed form solution for cold expansion, an analytical solution was developed for calculating the stresses and strains during the insertion of an oversized mandrel into the fastener hole. In many ways this describes the riveting process, where an undersized rivet is placed into a hole, and compressed so that the rivet shank expands circumferentially. The key piece of information required is the final, expanded diameter of the rivet. This was measured by carefully polishing down the protruded head of the rivet until it was flush with the coupon. The coupon was then photographed using a stereomicroscope (Figure 75) with the lighting adjusted so that the expanded shank of the rivet was visible. A scale left in the field of view allowed for easy calibration between pixels and inches, and a macro written for ImageTool allowed the diameter to be calculated by selecting three opposing points on the circumference.
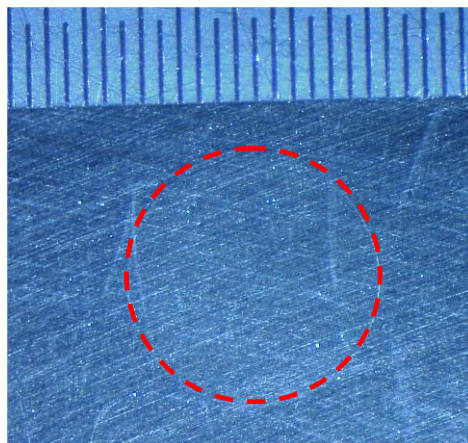
Figure 75: Polished surface used for rivet measurement with rivet diameter highlighted in red

Using the value of the expanded diameter of the rivet shank, the percent interference was calculated for the rivet in both the aluminum and the FML coupons. The average rivet diameter measured using this method was 4.191 mm in aluminum and 4.27 mm in FML 3, giving an average expansion of 3.0% and 4.5% respectively. The same closed

form solution used to calculate the strains during cold expansion was then used with only minor changes. In the case of riveting, there is no elastic-plastic spring back since the rivet remains in the coupon, so this portion of the closed form solution was removed. The material properties for the rivet were input in place of the mandrel properties and the starting diameter was set to be equivalent to the initial (oversized) hole size for the of rivet. The applied pressure was then varied iteratively until the calculated rivet radius (post expansion) matched the measured radius.

7.6 Closed Form Modelling of FML Properties

The properties of any fiber metal laminate material can be analytically predicted using an approach that combines micromechanic strength of materials methods along with classical laminated plate theory. The strength of materials approach is used to model the properties of the prepreg material (resin + glass fiber) while classical laminated plate (CLP) theory is used to determine the properties of the entire fiber metal laminate based on the number of plies and their orientation. As with any closed form approach, certain limitations exist: (1) the predicted FML properties are reliant on the accuracy of the fiber and matrix properties used (2) an assumption is made that the glass fibers behave isotropically and (3) the predicted properties and predicted strengths are upper bounds.

7.6.1 Micromechanics Approach to Modeling Prepreg Properties

Assuming that the elastic modulus of the glass fibers (E_f), the elastic modulus of the resin matrix (E_m), the volume fraction of glass fiber (V_f), the volume fraction of the resin matrix (V_m), the shear modulus of the glass fiber (G_f) and the shear modulus of the resin matrix (G_m) are known, then many of the prepreg properties, starting with the

143

modulus of the prepreg (E_1) in a direction parallel to the fibers can be calculated using a rule of mixtures approach. The derivation for the material properties of the prepreg is based on the representative volume element (RVE) approach that assumes the fibre, matrix and prepreg to be of the same height, but of different thicknesses (t_f, t_m and t_p) as shown in Figure 76.
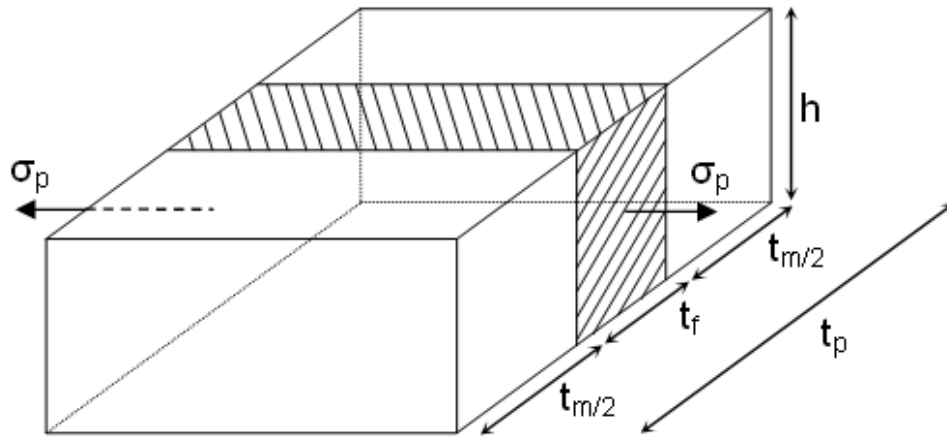
Figure 76: Representative volume element (RVE) showing applied stress in the direction of the fiber

If a unidirectional stress (σ_p) is applied to the RVE in the direction of the fiber, then it can be assumed that the corresponding force applied to the prepreg is equal to the sum of the force applied to the fiber and the force applied to the matrix. With the assumption of linear-elastic isotropic constituents, the force relationship can be re-written as:

$$E_1 \varepsilon_p A_c = E_f \varepsilon_f A_f + E_m \varepsilon_m A_m \qquad \qquad 7.6.1$$

where ε is the applied strain and A is the area of each component in the RVE. With the assumption that the displacements and thus the strains in each component of the RVE

144

are equal one can re-write Equation 7.6.1 in terms of the volume fraction (*V*) to produce

an expression for the elastic modulus in the fiber direction:

$$E_1 = V_f \cdot E_f + E_m \cdot (1 - V_f)$$ 7.6.2

For the elastic modulus transverse to the fiber direction, a force applied in this direction

will be distributed equally among all the components of the RVE (Figure 77) such that

the force in the prepreg equals the force in the matrix which equals the force in the

fibers.
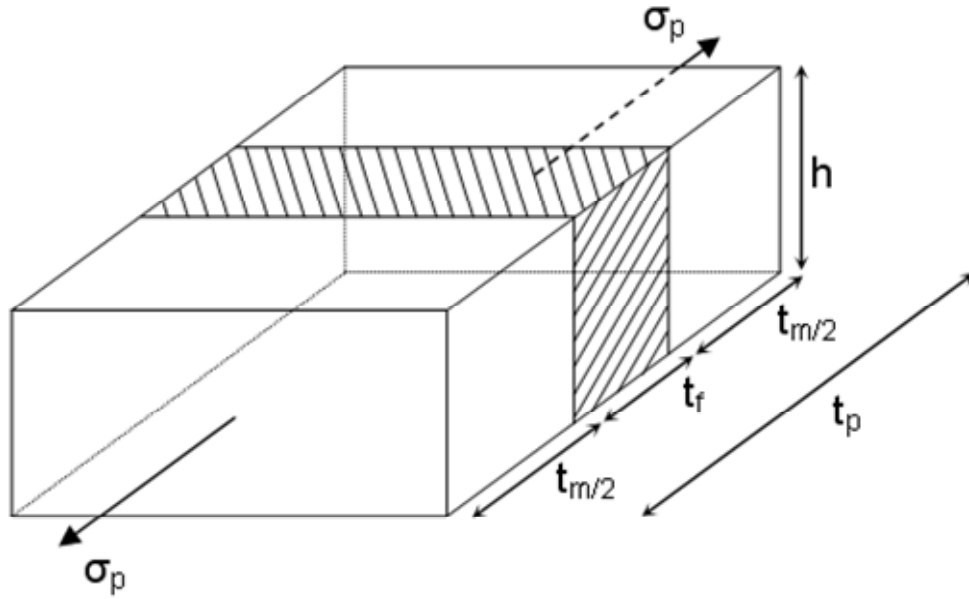
Figure 77: Representative volume element (RVE) showing applied stress transverse to the direction of the fiber

As a result the displacement of the prepreg in this direction is equal to the sum of the

displacements of the fiber and the matrix components. The individual components of

the displacement can be related to the strain in each component using:

$$\delta_p = t_p \cdot \varepsilon_p \qquad \delta_f = t_f \cdot \varepsilon_f \qquad \delta_m = t_m \cdot \varepsilon_m$$ 7.6.3

The strains can also be expressed using Hooke's law as:

$$\varepsilon_p = \frac{\sigma_c}{E_2} \qquad \varepsilon_f = \frac{\sigma_f}{E_f} \qquad \varepsilon_m = \frac{\sigma_m}{E_m} \qquad\qquad 7.6.4$$

The equation for the displacement of the RVE under a transverse load can then be re-written in terms of the stresses as follows:

$$\delta_p = \delta_f + \delta_m$$
$$t_p \frac{\sigma_c}{E_2} = t_f \frac{\sigma_f}{E_f} + t_m \frac{\sigma_m}{E_m} \qquad\qquad 7.6.5$$

Since the stresses are equivalent, they cancel out of Equation 7.6.5 and the ratio of the thicknesses can be equated to the volume fraction of the constituents, which after some rearranging, gives the modulus of the prepreg orthogonal (E_2) to the fiber:

$$E_2 = \frac{E_m \cdot E_f}{V_f \cdot E_m + (1 - V_f) \cdot E_f} \qquad\qquad 7.6.6$$

An analogous derivation can be used to determine the shear modulus of the prepreg (G_p):

$$G_p = \frac{G_m \cdot G_f}{V_f \cdot G_m + (1 - V_f) \cdot G_f} \qquad\qquad 7.6.7$$

A similar type of derivation can also be used to determine the Poisson's ratio for the prepreg (v_p) which is given by:

$$v_p = V_f \cdot v_f + (1 - V_f) \cdot v_m \qquad\qquad 7.6.8$$

If additional information is known regarding the coefficient of thermal expansion of both glass fiber (α_f) and the matrix (α_m) then the coefficient of thermal expansion of the

prepreg in the direction parallel to (α_1) and perpendicular to the orientation of the glass

fibers (α_2) can be determined using:

$$\alpha_1 = \frac{\alpha_f \cdot E_f \cdot V_f + \alpha_m \cdot E_m \cdot (1-V_f)}{E_1}$$ 7.6.9

$$\alpha_2 = (1+\nu_f) \cdot \alpha_f \cdot V_f + (1+\nu_m) \cdot \alpha_m \cdot (1-V_f) - \alpha_1 \cdot \nu_p$$ 7.6.10

With the four independent material constants (E_1, E_2, ν_p and G_p) of the prepreg

(unidirectional glass + resin matrix) determined, Hooke's law for orthotropic materials

can be used to determine both the compliance matrix [S] and the stiffness matrix [Q] of

the prepreg:

$$[S] = \begin{bmatrix} \dfrac{1}{E_1} & \dfrac{-\nu_p}{E_1} & 0 \\ \dfrac{-\nu_p}{E_1} & \dfrac{1}{E_2} & 0 \\ 0 & 0 & \dfrac{1}{G_p} \end{bmatrix}$$ 7.6.11

$$[Q] = \begin{bmatrix} \dfrac{E_1}{1-\nu_p^2} & \dfrac{\nu_p E_2}{1-\nu_p^2} & 0 \\ \dfrac{\nu_p E_2}{1-\nu_p^2} & \dfrac{E_2}{1-\nu_p^2} & 0 \\ 0 & 0 & G_p \end{bmatrix}$$ 7.6.12

In order to more generally relate [S] and [Q] to any orientation a transform matrix [T] is

required, where θ is the angle between the x-axis to the principal fiber axis. In general

for laminated plate analysis, the directions 1,2,3 refer to the principal fiber direction, the

147

in-plane perpendicular direction and the out-of-plane perpendicular direction

respectively. The loading direction for the entire laminate is designated using x,y,z.

$$[T] = \begin{bmatrix} \cos^2(\theta) & \sin^2(\theta) & 2 \cdot \cos(\theta) \cdot \sin(\theta) \\ \sin^2(\theta) & \cos^2(\theta) & -2 \cdot \cos(\theta) \cdot \sin(\theta) \\ -\cos(\theta) \cdot \sin(\theta) & \cos(\theta) \cdot \sin(\theta) & \cos^2(\theta) - \sin^2(\theta) \end{bmatrix} \qquad 7.6.13$$

The transform matrix [T] can be used to convert stress in the principal direction to that at

an arbitrary angle *θ* as shown:

$$\begin{Bmatrix} \sigma_1 \\ \sigma_2 \\ \tau_{12} \end{Bmatrix} = [T] \cdot \begin{Bmatrix} \sigma_x \\ \sigma_y \\ \tau_{xy} \end{Bmatrix} \qquad 7.6.14$$

The same transformation can also be used to convert strains in the principal direction to

strains at an arbitrary angle *θ* in a similar manner. The only change is the addition of

the Reuter's matrix [R] which allows one to transform the tensorial shear strain tensor

instead of the engineering shear strain tensor.

$$[R] = \begin{bmatrix} 1 & 0 & 0 \\ 0 & 1 & 0 \\ 0 & 0 & 2 \end{bmatrix} \qquad 7.6.15$$

With the addition of the Reuters matrix one can convert strain in the principal direction

to that in an arbitrary direction, in a manner similar to that done with the principal stress:

$$\begin{Bmatrix} \varepsilon_1 \\ \varepsilon_2 \\ \gamma_{12} \end{Bmatrix} = [R] \cdot [T] \cdot [R]^{-1} \begin{Bmatrix} \varepsilon_x \\ \varepsilon_y \\ \gamma_{xy} \end{Bmatrix} \qquad 7.6.16$$

Based on Hooke's law for angled lamina, one can relate the principal strains to the

principal stresses using the compliance matrix [S]:

$$\begin{Bmatrix} \varepsilon_1 \\ \varepsilon_2 \\ \eta_{12} \end{Bmatrix} = [S] \cdot \begin{Bmatrix} \sigma_1 \\ \sigma_2 \\ \tau_{12} \end{Bmatrix} \qquad \text{7.6.17}$$

Ideally one would like to determine the compliance matrix in the x-y-z system such that:

$$\begin{Bmatrix} \varepsilon_x \\ \varepsilon_y \\ \gamma_{xy} \end{Bmatrix} = \left[\overline{S} \right] \cdot \begin{Bmatrix} \sigma_x \\ \sigma_y \\ \tau_{xy} \end{Bmatrix} \qquad \text{7.6.18}$$

The value for $[\overline{S}]$ can be determined by replacing the stress and strain terms in

Equation 7.6.17 using Equation 7.6.14 and Equation 7.6.16 respectively and re-

arranging the equation to solve for strains in the x-y-z system as shown:

$$\begin{Bmatrix} \varepsilon_x \\ \varepsilon_y \\ \gamma_{xy} \end{Bmatrix} = [R] \cdot [T]^{-1} \cdot [R]^{-1} \cdot [S] \cdot [T] \begin{Bmatrix} \sigma_x \\ \sigma_y \\ \tau_{xy} \end{Bmatrix}$$

so,
$$\qquad \text{7.6.19}$$

$$\left[\overline{S} \right] = [R] \cdot [T]^{-1} \cdot [R]^{-1} \cdot [S] \cdot [T]$$

The same basic derivation can be performed for the stiffness matrix [Q], so that we can

determine the stiffness matrix in the x-y-z co-ordinate system.

$$\begin{Bmatrix} \sigma_1 \\ \sigma_2 \\ \tau_{12} \end{Bmatrix} = [Q] \begin{Bmatrix} \varepsilon_1 \\ \varepsilon_2 \\ \eta_{12} \end{Bmatrix}$$

so,

$$\begin{Bmatrix} \sigma_x \\ \sigma_y \\ \tau_{xy} \end{Bmatrix} = [T]^{-1} \cdot [Q] \cdot [R] \cdot [T] \cdot [R]^{-1} \begin{Bmatrix} \varepsilon_x \\ \varepsilon_y \\ \gamma_{xy} \end{Bmatrix} \qquad \text{7.6.20}$$

so,

$$\left[\overline{Q} \right] = [T]^{-1} \cdot [Q] \cdot [R] \cdot [T] \cdot [R]^{-1} = \left[\overline{S} \right]^{-1}$$

7.6.2 Classical Laminated Plate Approach to Laminate Properties

The approach so far has yielded the local and global stiffness [Q] and compliance [S]

matrices, allowing for a complete theoretical characterization of the stresses and strains

in an entire laminate or an individual ply. Next, a standard classical laminated plate

(CLP) approach will be used to determine the engineering constants of the lamina (E_x,

E_y, G_{xy}, v_{xy})[126-128]. The approach to determining the engineering constants of a

laminated composite material (like FML), can be best understood by examining the

stress – strain relations for an individual ply as shown:

$$\begin{Bmatrix} \varepsilon_x \\ \varepsilon_y \\ \Upsilon_{xy} \end{Bmatrix} = \begin{bmatrix} \dfrac{1}{E_x} & -\dfrac{v_{xy}}{E_x} & 0 \\ & \dfrac{1}{E_y} & 0 \\ Sym & & \dfrac{1}{G_{xy}} \end{bmatrix} \cdot \begin{Bmatrix} \sigma_x \\ \sigma_y \\ \tau_{xy} \end{Bmatrix} \qquad 7.6.21$$

To apply Equation 7.6.21 to a complete laminated composite material, one needs to

take into account that the stresses vary through the thickness, so one needs to define

the average stresses and relate them to strains. The average stresses ($\bar{\sigma}$) can be

approximated by integrating the stresses in the x,y,z direction over the thickness (t) of

the laminate, which by definition are related to N, the average force/unit width acting on

a specific face of the laminate:

$$\overline{\sigma}_x \equiv \frac{1}{t} \cdot \int_{-t/2}^{t/2} \sigma_x \cdot dz = \frac{N_x}{t}$$

$$\overline{\sigma}_y \equiv \frac{1}{t} \cdot \int_{-t/2}^{t/2} \sigma_x \cdot dz = \frac{N_y}{t} \qquad 7.6.22$$

$$\overline{\tau}_{xy} \equiv \frac{1}{t} \cdot \int_{-t/2}^{t/2} \sigma_x \cdot dz = \frac{N_{xy}}{t}$$

If we assume that the laminate is orthotropic and that the laminate layup is symmetric, it is possible to express the relationship between the laminate strains and the average stresses in a similar manner to that for an individual ply:

$$\begin{Bmatrix} \varepsilon_x \\ \varepsilon_y \\ \Upsilon_{xy} \end{Bmatrix} = \frac{1}{t} \cdot \begin{bmatrix} \dfrac{1}{E_x} & -\dfrac{v_{xy}}{E_x} & 0 \\ & \dfrac{1}{E_y} & 0 \\ Sym & & \dfrac{1}{G_{xy}} \end{bmatrix} \cdot \begin{Bmatrix} N_x \\ N_y \\ N_{xy} \end{Bmatrix} \qquad 7.6.23$$

The next step is to express Equation 7.6.23 in terms that can be solved explicitly, allowing one to determine the engineering constants by inspection. To do this it is instructive to examine the derivation used to determine stresses and strains in a laminated composite beam.

Classical beam theory is built on several fundamental assumptions including:

1. plane sections remain planar after deformation

2. plate thickness (t) remains constant

3. plate deformations are small enough that small angle assumptions are valid

151

In this case, for a uniform plate under a bending deformation, the strain at any point in the thickness (z) can be related to the mid-plane strains (ε^0) and the curvature (κ) as shown:

$$\begin{Bmatrix} \varepsilon_x \\ \varepsilon_y \\ \Upsilon_{xy} \end{Bmatrix} = \begin{Bmatrix} \varepsilon_x^0 \\ \varepsilon_y^0 \\ \Upsilon_{xy}^0 \end{Bmatrix} + z \begin{Bmatrix} \kappa_x \\ \kappa_y \\ \kappa_{xy} \end{Bmatrix} \qquad \text{7.6.24}$$

If one is dealing with a laminated plate, an assumption that there is perfect bonding between each of the laminate layers must be made. Stresses applied to a section of the beam will lead to an equivalent axial force (N) and a bending moment (M)

$$N = \int_{-t/2}^{t/2} \sigma_x \cdot dz = axial\ load\ /\ unit\ width$$

$$M = \int_{-t/2}^{t/2} \sigma_x \cdot z \cdot dz = moment\ /\ unit\ width \qquad \text{7.6.25}$$

One can use a Hookean definition for stress to substitute for σ_x in the equations for N and M and obtain the following relationships:

$$N = \int_{-t/2}^{t/2} \sigma_x dz = \int_{-t/2}^{t/2} E\varepsilon_x dz = \int_{-t/2}^{t/2} E\left(\varepsilon_x^\circ - z\kappa_x^\circ\right) dz \qquad \text{7.6.26}$$

which can then be re-arranged as:

$$N = \left(\int_{-t/2}^{t/2} E \cdot dz \right) \cdot \varepsilon_x^\circ + \left(\int_{-t/2}^{t/2} E \cdot z \cdot dz \right) \cdot \kappa_x^\circ$$

$$N = A \cdot \varepsilon_x^\circ + B \cdot \kappa_x^\circ \qquad \text{7.6.27}$$

the same can be done for M, which gives:

$$M = \int_{-t/2}^{t/2} E\left(\varepsilon_x^\circ + z \cdot \kappa_x^\circ\right) \cdot z \cdot dz$$

$$M = \left(\int_{-t/2}^{t/2} E \cdot z \cdot dz\right) \cdot \varepsilon_x^\circ + \left(\int_{-t/2}^{t/2} E \cdot z^2 \cdot dz\right) \cdot \kappa_x^\circ \qquad 7.6.28$$

$$M = B \cdot \varepsilon_x^\circ + D \cdot \kappa_x^\circ$$

In matrix form the above equations can be written as:

$$\left\{\begin{matrix} N \\ M \end{matrix}\right\} = \begin{bmatrix} A & B \\ B & D \end{bmatrix} \cdot \left\{\begin{matrix} \varepsilon_x^\circ \\ \kappa_x^\circ \end{matrix}\right\} \qquad 7.6.29$$

Where [A] is termed the extensional stiffness of the laminated plate, [B] is the coupling

stiffness of the laminated plate and [D] is the bending stiffness of the laminated plate.

Overall the stiffness expressions for [A], [B] and [D] can be generalized by replacing the

constant of integration as follows:

$$A = \int_{-t/2}^{t/2} E \cdot dz = \sum_{k=1}^{N} E_k \cdot \int_{Z_{k-1}}^{Z_k} dz = \sum_{k=1}^{N} E_k \cdot \left(z_k - z_{k-1}\right) \qquad 7.6.30$$

$$B = \int_{-t/2}^{t/2} E \cdot z \cdot dz = \sum_{k=1}^{N} E_k \cdot \int_{Z_{k-1}}^{Z_k} z \cdot dz = \frac{1}{2} \sum_{k=1}^{N} E_k \cdot \left(z_k^2 - z_{k-1}^2\right) \qquad 7.6.31$$

$$D = \int_{-t/2}^{t/2} E \cdot z^2 \cdot dz = \sum_{k=1}^{N} E_k \cdot \int_{Z_{k-1}}^{Z_k} z^2 \cdot dz = \frac{1}{3} \sum_{k=1}^{N} E_k \cdot \left(z_k^3 - z_{k-1}^3\right) \qquad 7.6.32$$

Where the thickness of the k_{th} layer is defined as $t_k = z_k - z_{k-1}$. Through the use of the [A],

[B], and [D] matrices we now have a way to use the engineering constants of the

individual plies to determine the overall engineering constants of the laminate. The

overall stiffness matrix of the laminated plate is given by Equation 7.6.29 and the

individual stiffness components can be written as:

$$[A] = \sum_{k=1}^{N} \left[\overline{Q} \right] \cdot (z_{k+1} - z_k)$$

7.6.33

$$[B] = \frac{1}{2} \sum_{k=1}^{N} \left[\overline{Q} \right] \cdot \left(z_{k+1}^2 - z_k^2 \right)$$

7.6.34

$$[D] = \frac{1}{3} \sum_{k=1}^{N} \left[\overline{Q} \right] \cdot \left(z_{k+1}^3 - z_k^3 \right)$$

7.6.35

where $[\overline{Q}]$ is given in Equation 7.6.20. If one inverts the stiffness formulation of the

laminate stress-strain relationship, one obtains the compliance formulation as shown:

$$\left\{ \begin{matrix} \{\varepsilon^0\} \\ \{k\} \end{matrix} \right\} = \begin{bmatrix} [A]_{3x3} & [B]_{3x3} \\ [B]_{3x3} & [D]_{3x3} \end{bmatrix}^{-1} \cdot \left\{ \begin{matrix} \{N\} \\ \{M\} \end{matrix} \right\} = \begin{bmatrix} \left[A^{'} \right]_{3x3} & \left[B^{'} \right]_{3x3} \\ \left[B^{'} \right]_{3x3} & \left[D^{'} \right]_{3x3} \end{bmatrix} \cdot \left\{ \begin{matrix} \{N\} \\ \{M\} \end{matrix} \right\}$$

7.6.36

Some additional matrix algebra is required to calculate the inverse of the [A], [B], and

[D] matrices and a summary of these operations is provided below:

$$\left[A^* \right]_{3x3} = [A]_{3x3}^{-1}$$
$$\left[B^* \right]_{3x3} = -\left[A^* \right]_{3x3} \cdot [B]_{3x3}$$
$$\left[C^* \right]_{3x3} = -\left[B^* \right]_{3x3}$$
$$\left[D^* \right]_{3x3} = [D]_{3x3} - [B]_{3x3} \cdot \left[A^* \right]_{3x3} \cdot [B]_{3x3}$$

7.6.37a

$$\left[D^{'}\right]_{3x3} = \left[D^{*}\right]_{3x3}^{-1}$$

$$\left[B^{'}\right]_{3x3} = \left[B^{*}\right]_{3x3} \cdot \left[D^{'}\right]_{3x3}$$

$$\left[C^{'}\right]_{3x3} = \left[B^{'}\right]_{3x3}^{T}$$

7.6.37b

$$\left[A^{'}\right]_{3x3} = \left[A^{*}\right]_{3x3} + \left[B^{'}\right]_{3x3} \cdot \left[B^{*}\right]_{3x3}^{T}$$

For symmetric laminates the coupling matrix $[B]=0$ and the compliance formulation of the stress strain relationship can be expressed as:

$$\begin{Bmatrix} \varepsilon_x^\circ \\ \varepsilon_y^\circ \\ \gamma_{xy}^\circ \end{Bmatrix} = \begin{bmatrix} A_{11}^{'} & A_{12}^{'} & A_{16}^{'} \\ & A_{22}^{'} & A_{26}^{'} \\ Sym & & A_{66}^{'} \end{bmatrix} \cdot \begin{Bmatrix} N_x \\ N_y \\ N_{xy} \end{Bmatrix} = \left[A^{1}\right] \cdot \begin{Bmatrix} N_x \\ N_y \\ N_{xy} \end{Bmatrix}$$

7.6.38

Equation 7.6.38 can now be written in a similar form to Equation 7.6.23 and by inspection, one can determine the following values for the in-plane engineering constants of the laminate:

$$E_x = \frac{1}{t \cdot A_{11}^{'}}$$

7.6.39a

$$E_y = \frac{1}{t \cdot A_{22}^{'}}$$

7.6.39b

$$v_{xy} = \frac{-A_{12}^{'}}{A_{11}^{'}}$$

7.6.39c

$$G_{xy} = \frac{1}{t \cdot A_{66}^{'}}$$

7.6.39d

The above equations and approach was used to estimate the material properties of FML with various layups, which will be further discussed in Chapter 9.0.

7.7 Comparison of Closed Form Results to Experimental Measurements

Based on the development of a closed form solution for cold expansion and riveting (Chapter 7.4), sample experimental strain data obtained from DIC measurements on the entry face (Chapter 6.0) of 2024-T3 aluminum and FML 3 coupons were compared to the closed form results. In addition to strain data, each comparison graph shows the location of the elastic-plastic boundary (r_p/a) as well as the reverse yielding elastic-plastic boundary (r^*_p/a) determined from the closed form solution (where r is the distance from the center of the open hole and a is the radius of the open hole).

In order to gain better fidelity in the comparison between the closed form solution and the experimental results, material property data for both the 2024-T3 aluminum[129] and FML coupons were taken in both the longitudinal and transverse direction. Modifications were then made to account for material property changes and edge distance changes in each direction.

7.7.1 Comparison to Cold Expansion Strains: 2024-T3 Coupons

The results for the 2024-T3 aluminum coupon (Figure 78 and Figure 79) shows the best corroboration in the elastic region, with some hint of divergence as the data gets closer to the plastic zone. The overall correlation between the two results is better for the maximum principal strains since the overall strain magnitude is lower. Greater divergence from the measured data is seen in the plot of minimum principal strain possibly due to the extremely high strain gradient near the edge of the hole and the limited strain resolution that was available at the magnification that was used. The average magnification was approximately 0.05 mm/pixel and the subset size measured

17 pixels x 17 pixels, meaning that each subset covered approximately 0.78 mm^2. The

closed form solution shows a predicted exponential increase in strain as one

approaches the edge of the hole (r/a=1). In the region of plastic strain between

approximately r/a=1 and r/a = 2.2 (linear distance of approximately 3.8 mm) only slightly

more than four full subsets cover this region. The magnification used for testing is

always a compromise between having a field of view large enough to view the full extent

of the cold expansion residual strains and having enough strain resolution to capture

some detail regarding what is happening at the edge of the cold expanded hole.
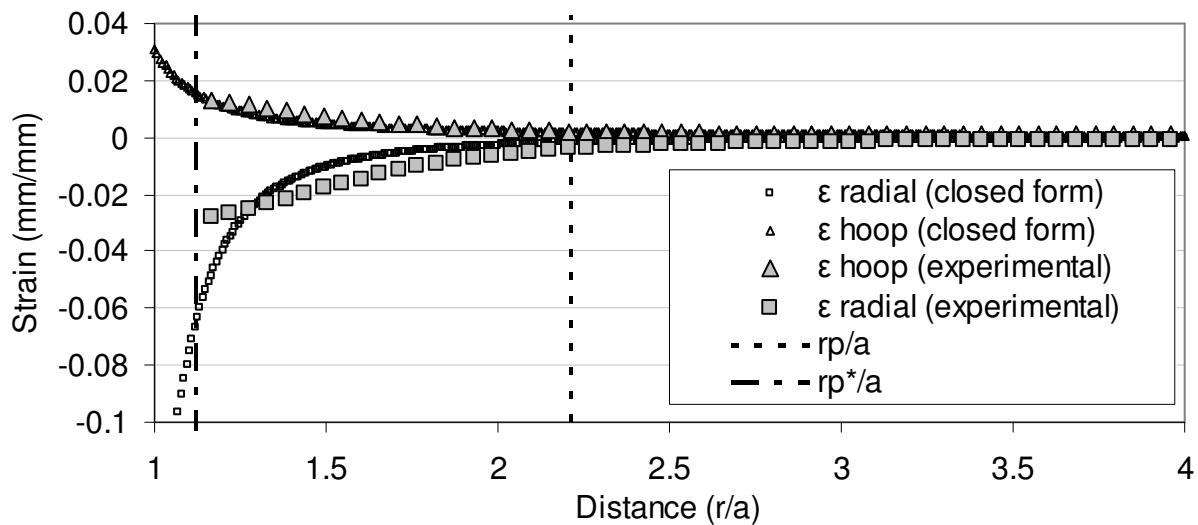
Figure 78: Comparison between closed form and experimental measurements for
aluminum coupon in transverse direction (specimen AL1)

The same effect is seen in the plot of the longitudinal strains (Figure 79) which shows

very similar results in both magnitude and form to those from the transverse direction.

This is to be expected since aluminum has similar properties between the longitudinal

and transverse directions.
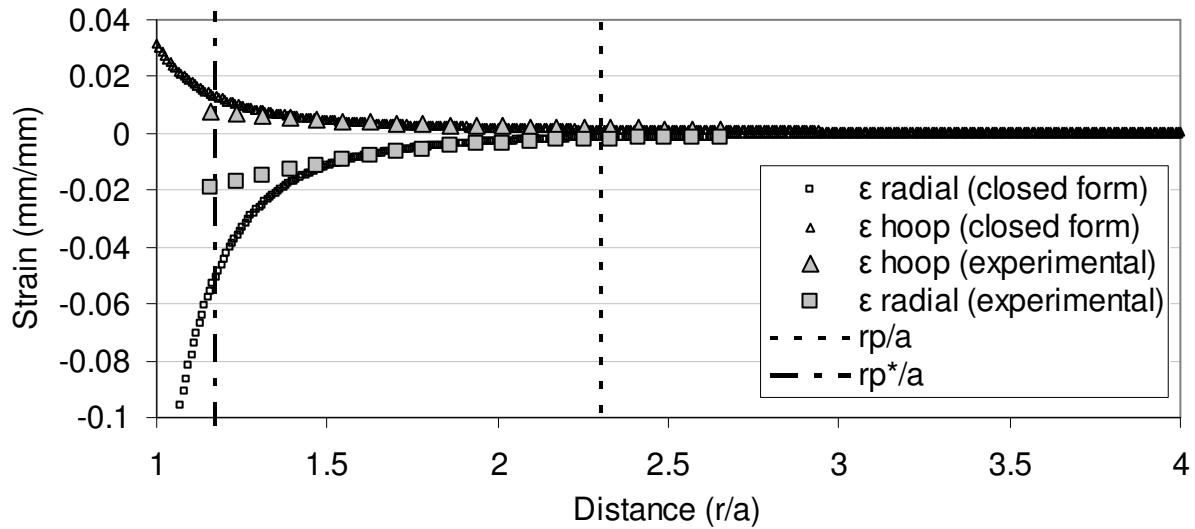
Figure 79: Comparison between closed form and experimental measurements for aluminum coupon in longitudinal direction (specimen AL1)

7.7.2 Comparison to Cold Expansion Strains: FML 3 Coupons

The same comparisons were made with an FML 3 coupon, and overall results showed much better corroboration than with the 2024-T3 aluminum coupons. As with the aluminum coupons, the experimental results for FML 3 (Figure 80 to Figure 82) show some divergence, especially as one approaches the plastic region. To make the comparisons more accurate, the experimental strain results were extracted in the longitudinal and transverse direction, as well as in the 45º degrees direction. This allowed for more accurate material properties to be used in the closed form solution. The results for the transverse direction (Figure 80) showed similar values to the closed form solution until near the reverse yield elastic-plastic boundary ($r_{p\_}/a$). At that point the experimental strain results started to diverge, with the maximum principal strains being overestimated by the closed form solution and the minimum principal strains being underestimated.
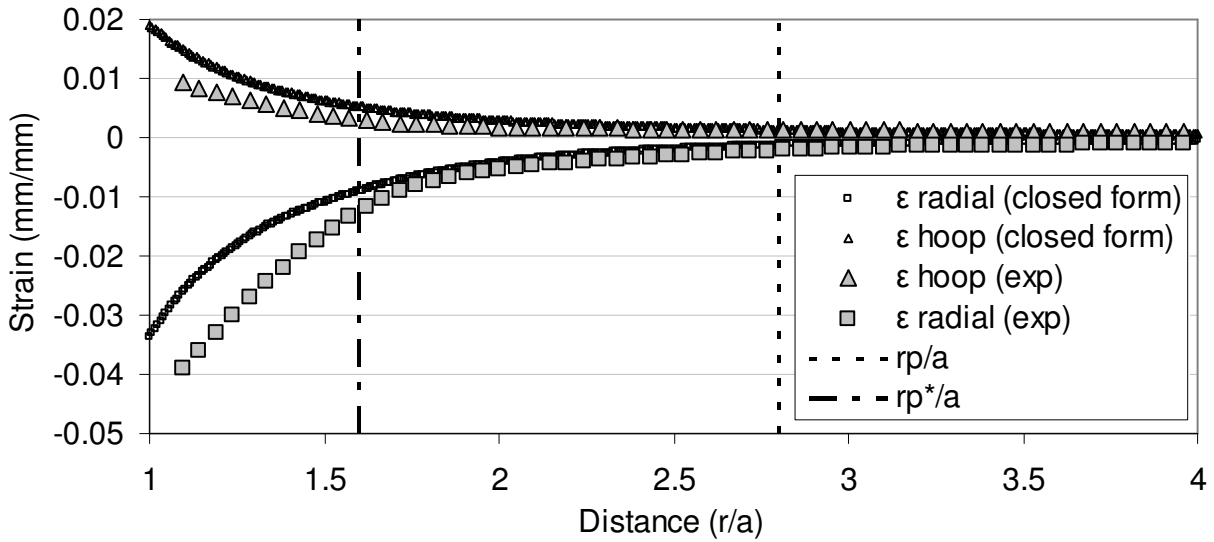
Figure 80: Comparison between closed form and experimental measurements for FML 3 coupon in transverse direction (specimen GAL1)

The results from the longitudinal direction (Figure 81) showed excellent corroboration with the closed form predictions, with only a slight deviation in the maximum principal strains just past the reverse yield elastic-plastic boundary.
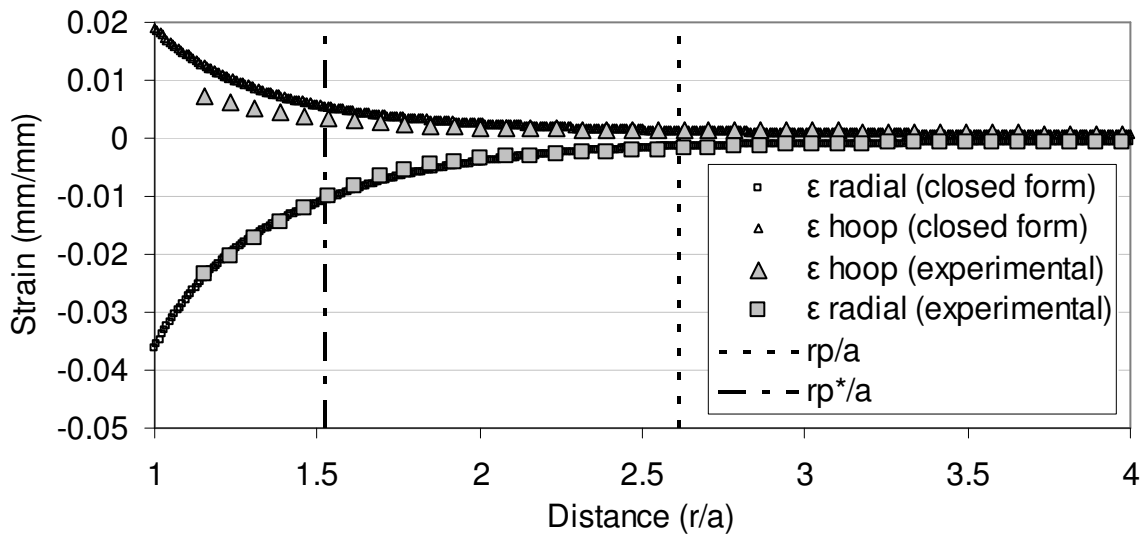
Figure 81: Comparison between closed form and experimental measurements for FML 3 coupon in longitudinal direction (specimen GAL1)

The results in the 45º degree direction (Figure 82) corroborated well with the closed form solution up to the elastic-plastic (r_p/a) boundary, at which point the closed form results appeared to underestimate both the maximum and minimum principal strains. Extracting data at exactly 45º degrees is difficult and certainly one likely source of error is the actual angle at which the data was extracted.

This approach to modeling the effect of cold expansion in FML appears reasonable and provided good corroboration of the experimental data. It should also be noted that the strains at 45º degrees were significantly higher than in either the longitudinal or transverse direction, meaning that this model was capturing the inherent orthotropy of the material to some extent.

Overall, the experimentally measured cold expansion strains in FML were lower than in the aluminum coupons. Since both the FML and the aluminum coupons were measured with the same experimental setup and had the same strain resolution, the lower strain gradient in FML may account for why better corroboration was seen with this material.
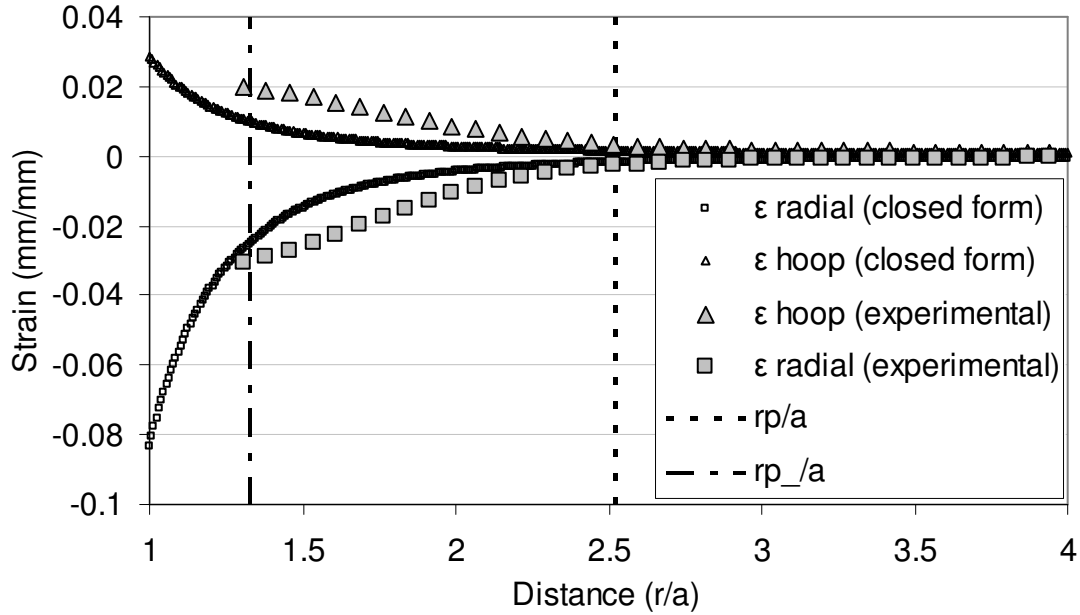
Figure 82: Comparison between closed form and experimental measurements for FML 3 coupon in 45 degree direction (specimen GAL1)

7.7.3 Comparison to Riveting Strains: 2024-T3 Coupons

One difficulty in validating a closed form model for riveting stemmed from the inability to measure strains under the driven or manufactured head. Compared to the cold expansion results, the experimental measurements for the riveted coupons tended to begin much farther away from the edge of the pilot hole, in the range of 1.75 < r/a < 2.75, which is well within the elastic range for both aluminum and FML.

The same approach was followed for the comparison to the riveting strains, where both longitudinal and transverse strain data were extracted so that the closed form model could be run with the appropriate material models. In the transverse direction (Figure 83) the experimental strain results appear to corroborate very well up to the elastic-plastic boundary (r/a=1.89).
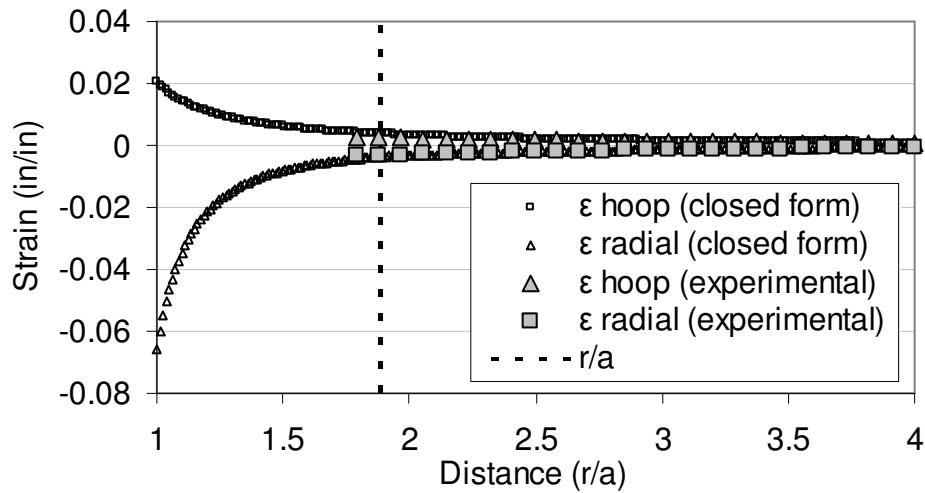
Figure 83: Comparison between closed form and experimental measurements for riveted aluminum 2024-T3 coupon in transverse direction (specimen AT8)

In the longitudinal direction (Figure 84) the experimental strain results also appear to corroborate very well up to the elastic-plastic boundary (r/a=1.97). The strain results from both directions appear to be quite similar overall, with only a small change in the location of the elastic-plastic boundary to suggest that different material properties were used for each direction.
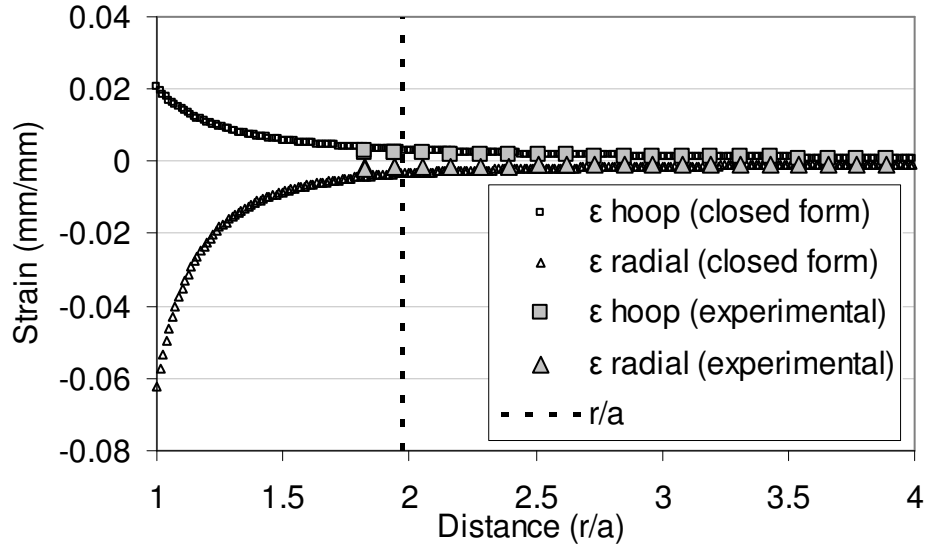
Figure 84: Comparison between closed form and experimental measurements for riveted aluminum 2024-T3 coupon in longitudinal direction (specimen AT8)

7.7.4 Comparison to Riveting Strains: FML 3 Coupon

The same procedure was used with the riveted FML coupons as with the cold expanded coupons, where material models in the transverse (Figure 85), longitudinal (Figure 86) and in the 45º degree direction (Figure 87) were input into the closed form solution. In the elastic range, the closed form solution seems to corroborate very well to the experimentally measured strains. The larger minimum principal strains predicted in the 45º direction are indicative that the approach used with the closed form model allows for better predictions with orthotropic materials such as FML.
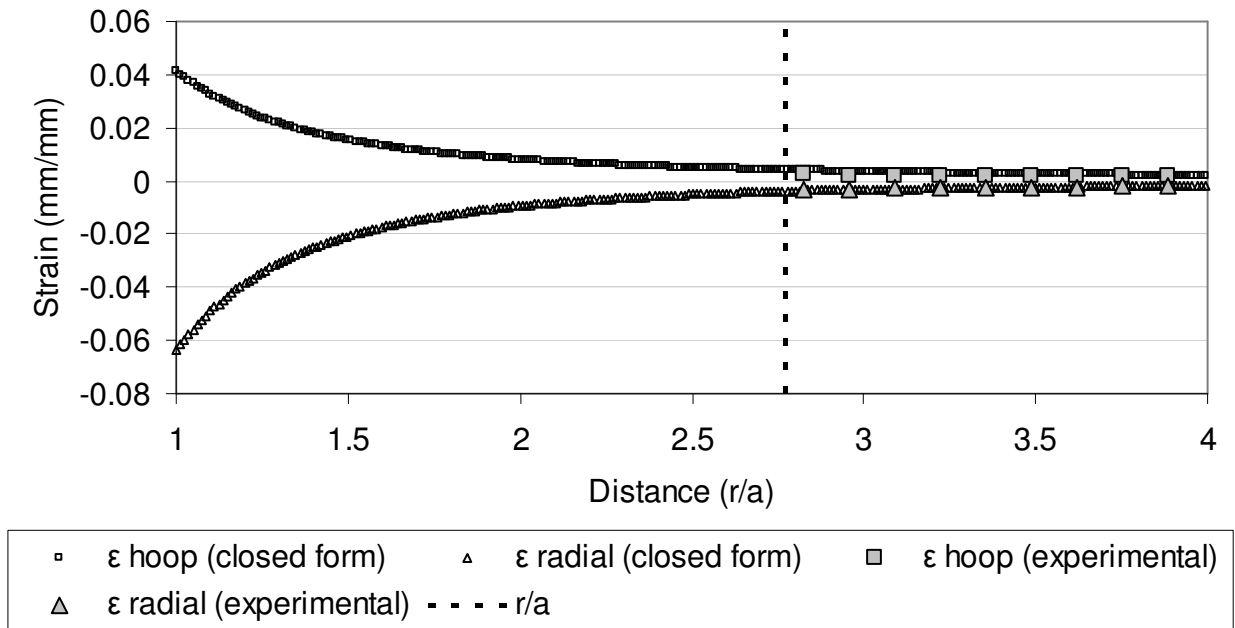
Figure 85: Comparison between closed form and experimental measurements for FML coupon in transverse direction (specimen GAL4)
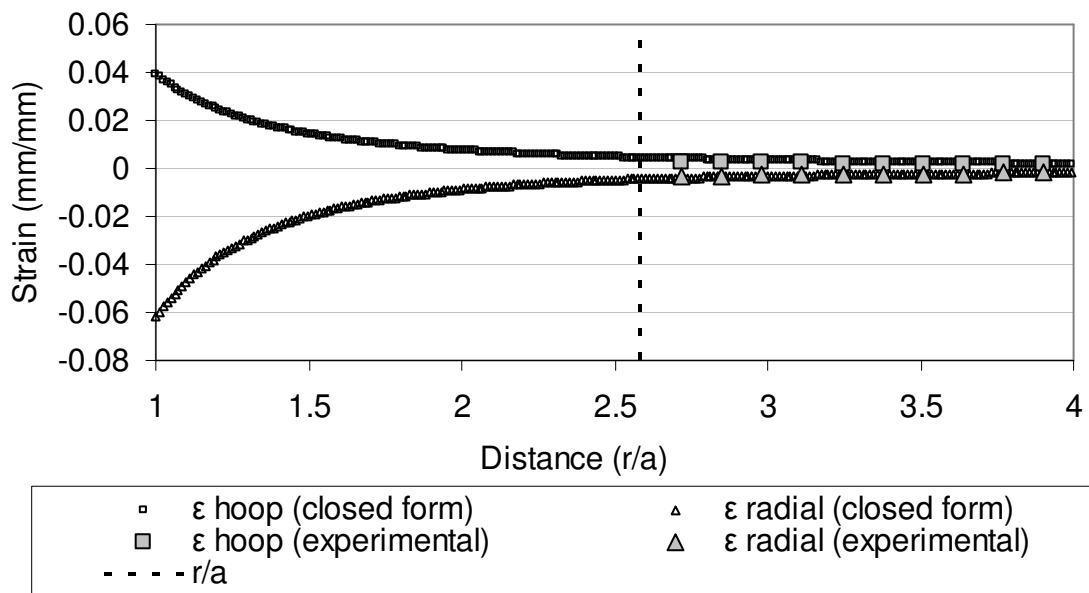
Figure 86: Comparison between closed form and experimental measurements for FML coupon in longitudinal direction (specimen GAL4)
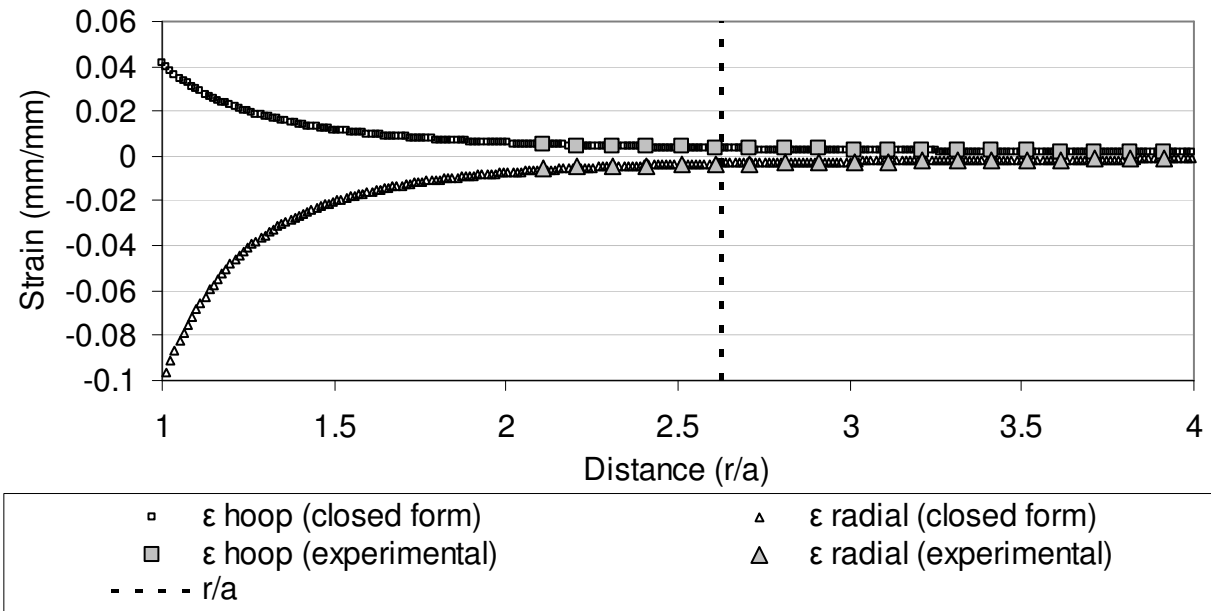
Figure 87: Comparison between closed form and experimental measurements for FML coupon in 45º degree direction (specimen GAL4)

8.0 BASELINE FATIGUE BEHAVIOUR

The baseline fatigue phase of this research program involved the fatigue testing of both aluminum and fiber metal laminate coupons at a net section stress ranging from 168-198 MPa, a loading frequency of 10 Hz and a load ratio of R=0.1 (see chapter 5.2 for additional details). The results from the aluminum coupons provided a baseline for comparing the fatigue life, the crack growth and the crack nucleation mechanisms of the FML coupons. The baseline fatigue testing involved screening 2024-T3 aluminum and FML coupons to determine their fatigue life after cold expansion and riveting. In addition, strain measurements made on either face of the coupons provided important information that was used to better understand the mechanism behind the fatigue life improvement seen from cold expansion and riveting

8.1 Fatigue Behaviour After Cold Expansion

Fatigue results are provided for both aluminum and FML, with detailed strain information provided for select coupons for the purpose of more in-depth discussion. As a concise way of presenting the large number of data sets, sample results from both the DIC and TSA systems are presented for both FML 3 and FML 4 at one stress level (198 MPa) and for one sample specimen.

For each specimen, results are presented pre-crack and at crack lengths of approximately 1, 2, and 3.7 mm. The final crack length of 3.7 mm was chosen as it represented the longest crack length that could be discerned in all coupons, given the field of view of the camera. In all cases, the data collected simultaneously from the TSA system was reflected about the loading (vertical) axis for ease of comparison to data from the DIC system on the opposite face. From an analysis perspective, the main

focus was on the maximum principal strains, since these are largely responsible for crack growth and provide the most information about what is occurring in the region close to the crack tip.

8.1.1 Aluminum: Cold Expansion Strain and Fatigue Results

8.1.1.1 Aluminum: Overall Fatigue Results

Overall fatigue results showing the number of cycles to failure against the net section stress are shown in Figure 88. Although the number of coupons tested at each stress level is relatively small (n=3 for the cold expanded coupons and n=2 for unexpanded coupons), the improvement in fatigue life as a result of cold-expansion, especially at lower stress levels, is still evident. These findings are supported by a number of researchers who have used residual stress measurements, using either the Sachs method[62,130] or x-ray diffraction[46,68,122], to show that the effectiveness of the cold expansion process is as a result of the compressive residual stresses created around the hole.
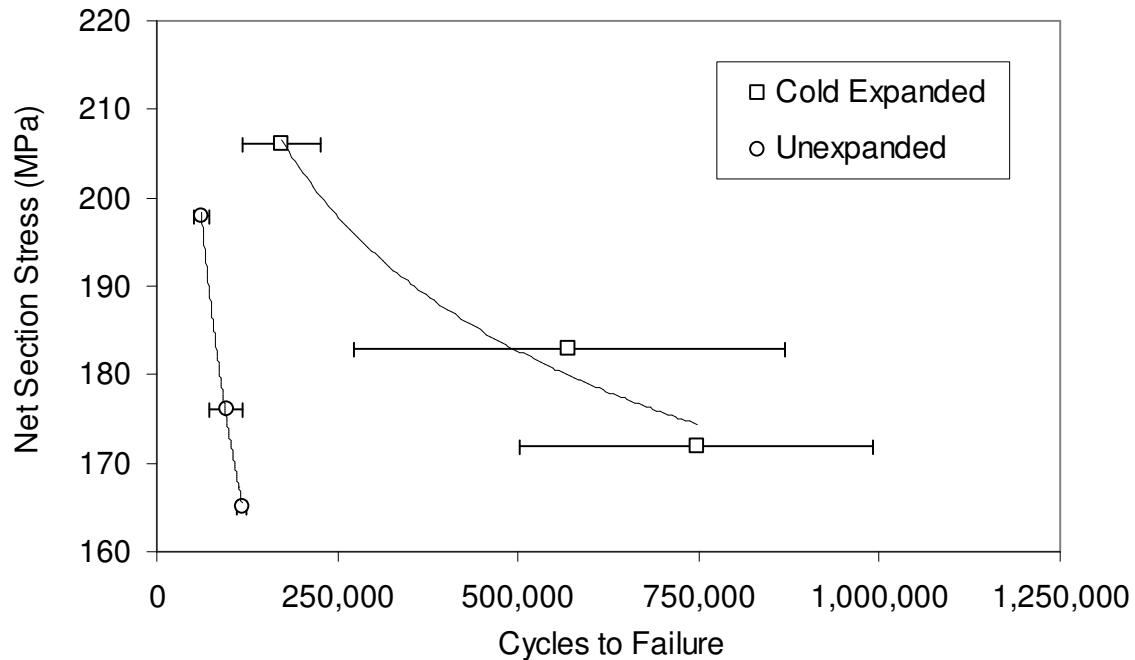
Figure 88: Mean fatigue results for aluminum coupons both with and without cold-expansion of the hole

8.1.1.2 Aluminum: Crack Growth Curves

Sample crack growth curves comparing the rate of crack growth for open hole and cold expanded coupons at each of the three net stress levels are given in Figure 89a,b and Figure 89c. The results support the overall fatigue results showing retardation in crack growth as a result of cold expansion. What is less clear is whether the cold expansion process is effective in extending life during the early stage of the fatigue process. The literature on this subject is also ambiguous, with researchers such as Chandawanich and Sharpe[20] showing that cold expansion has no effect on what they termed "fatigue crack initiation", while others such as Amrouche et al[131] suggesting that cold expansion does have an effect on "crack initiation". The optical measurements used for the current test program provided accurate results for cracks of 0.4 mm in length or greater, but

detecting the formation of cracks below that threshold was less consistent. The other important point is that all optical crack growth measurements were made on the entry face, and given that the exit face had higher residual strains, it seems likely that cold expansion would extend the early stage of the fatigue process on the exit face. Trying to verify this by simply examining the crack growth curves of Figure 89 can be misleading due to the difficulties in measuring very small initial crack sizes. However, if one arbitrarily uses 1 mm as the definition of a short crack, then it is possible to determine the number of cycles required to grow a crack of this size both before and after cold expansion. Figure 90 clearly shows that cold expansion increases the number of cycles required to grow a 1 mm crack, and that this increase appears to be related to the net section stress. Calculating the crack growth per number of cycles (da/dN) for all coupons also shows how cold expansion significantly reduces the overall rate of crack propagation in the aluminum coupons (Figure 90).
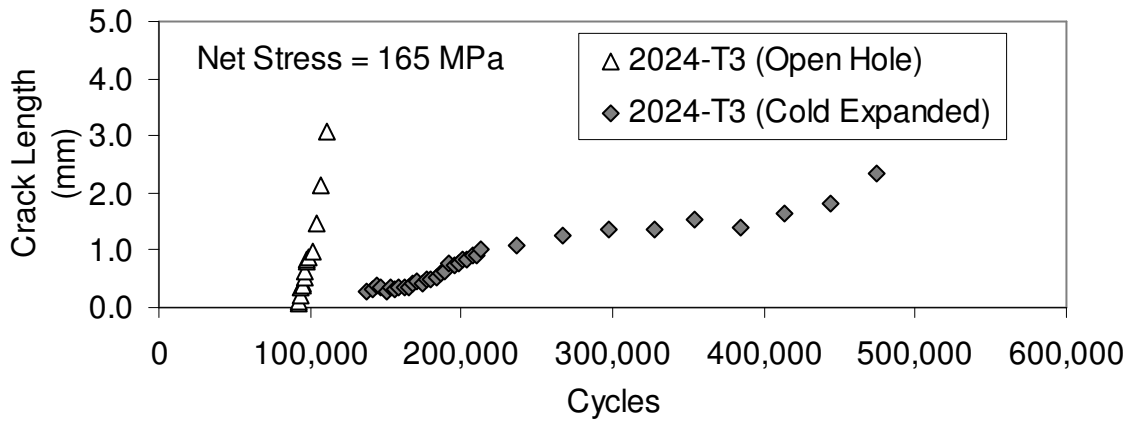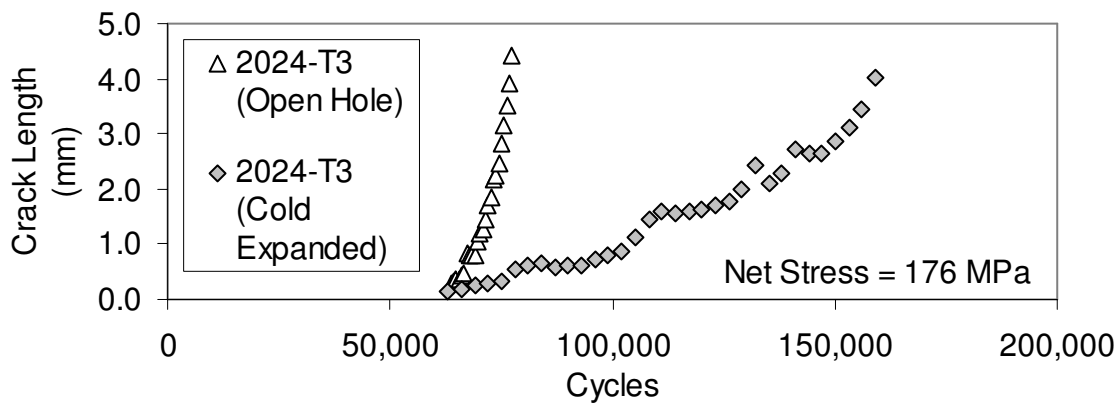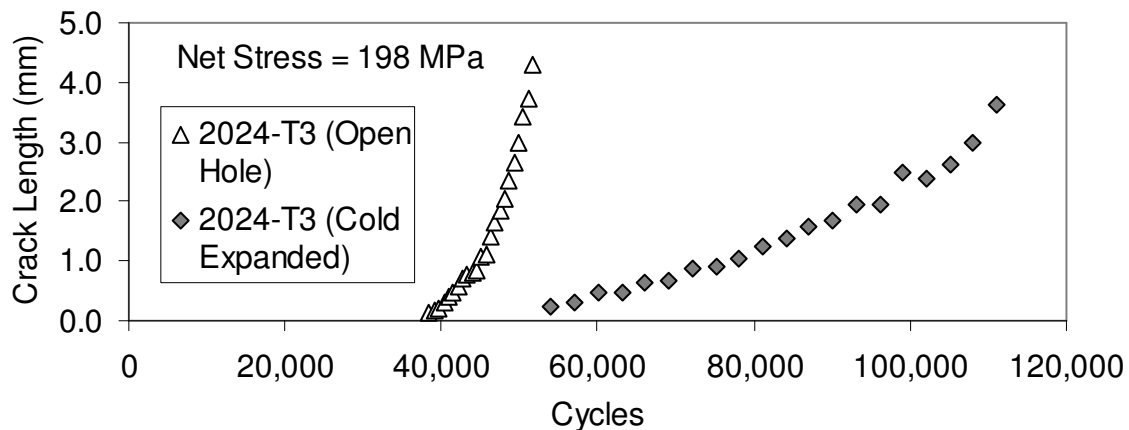
Figure 89: Crack growth curves for 2024-T3 aluminum coupons (a) Net Stress 165 MPa: Open Hole (specimen Al-L-20) and cold expanded (specimen Al-L-28) coupons (b) Net Stress 176 MPa: Open Hole (specimen AL-L-26) and cold expanded (specimen AL-L-29) coupons and (c) Net Stress 198 MPa: Open Hole (specimen AL-L-36) and cold expanded (specimen AL-L-35) coupons

Figure 90: Variation in number of cycles to 1 mm crack length (columns) versus da/dN (symbols) for 2024-T3 aluminum at various stress levels

8.1.1.3 Aluminum: DIC and TSA Measurements During Fatigue Loading

Although, it is possible to quantify the corresponding total residual strains using image correlation by selecting a reference state prior to cold expansion and collecting and processing multiple images during the cold expansion process[132], in this study, the reference state was chosen to be post cold expansion, so that data from image correlation would be analogous to that from thermoelastic stress analysis; i.e. the reference image was collected at the minimum (889 N), and the deformed image at the maximum (8896 N) load in the fatigue cycle. Thus the data from both digital image correlation and thermoelastic stress analysis represent the strain difference or the amplitude of strain during the cycle.

171

The maximum principal strains measured with DIC on the entry face of an aluminum coupon are shown in Figure 91 for unexpanded (UH) (*left column*) and cold-expanded (CX) (*right column*) holes precrack and for crack lengths of 1 mm, 2 mm and 3.7 mm. The crack lengths were obtained from the image of the coupon captured at maximum load and subsequently used for digital image correlation. As expected, based on the data shown in Figure 90, the number of cycles required to grow the fatigue crack with a cold-expanded hole is substantially greater than for an unexpanded hole; by a factor of two for a crack length of 1 mm rising to a factor of three for a crack length of 3.7 mm. Full-field maps of the thermoelastic stress analysis signal (in camera A/D units) captured during the same cycles are shown in Figure 92. These data maps are directly proportional to the amplitude of the temperature, *ΔT*, during the loading cycle, which in turn is proportional to the amplitude of the first stress invariant, $\Delta(\sigma_{11} + \sigma_{22})$.
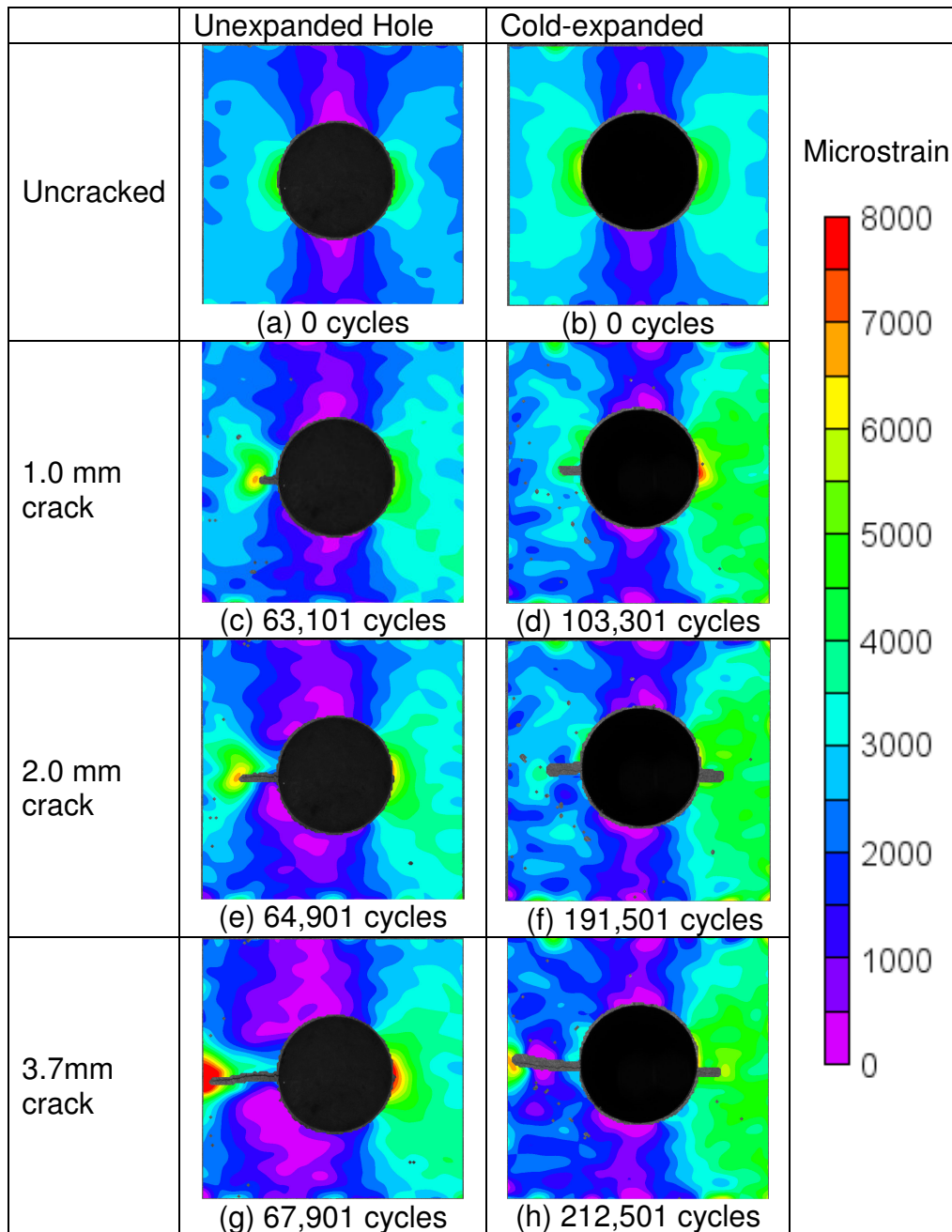
Figure 91: Maximum principal strains obtained from digital image correlation from aluminium coupons with both an unexpanded (*left, specimen AL-L-25*) and cold–expanded (*right, specimen AL-L-27*) hole pre-crack and with crack lengths of 1, 2 and 3.7 mm

Figure 92: Full-field maps of the thermoelastic signal (A/D units) from the exit face for unexpanded (*left*) and cold-expanded (*right*) holes. Date reflected about the loading axis for ease of comparison vertical) axis for ease of comparison

174

8.1.1.4 Discussion

There is little difference between the precrack coupons with the unexpanded (UH) and cold expanded (CX) holes (Figure 91), and the difference that does exist is likely due to the approximately 0.8% higher net section stress for the cold-expanded coupon. When the crack extends to 1 mm, a clear difference exists between the results for the UH (Figure 91c) and CX (Figure 91d) coupons. In the UH coupon a crack is clearly visible, with a circular contour of both maximum principal strain (Figure 91c) and TSA signal or first stress invariant (Figure 92c) at its tip. It is interesting to note that the strain amplitude deduced from TSA associated with the crack tip is lower than at the uncracked side of the hole. This effect is likely due to crack tip plasticity, which creates a small residual stress field ahead of the crack tip, so that when it is unloaded the plastic zone is compressed circumferentially and the surrounding elastic material experiences tension. The tension raises the minimum stress experienced during the cycle and thus lowers the stress amplitude. This behaviour has been observed previously[133] in TSA data in the vicinity of propagating cracks, however, the resolution of these images is too low for the plastic region to be visible. The data in Figure 92b and Figure 92d from the exit face of the cold-expanded hole exhibit no apparent difference between the uncracked case and when a 1 mm long crack was observed on the entry face. This implies that the crack did not extend to the exit face, and evidence for this is provided by the fracture surface for the coupon shown in Figure 93. The fracture surface was obtained after final failure of the coupon at which point the crack was considerably longer on the entry face than on the exit face with a maximum length in the mid-section. The crack front barely reached the exit face prior to final failure,

probably as a consequence of the substantially higher compressive residual stresses on the exit face. Thermoelastic stress analysis is not based on a purely surface phenomena but is sensitive to strain concentrations through the thickness, though this is dependent on loading frequency, as heat transfer needs to occur towards the surface in order for the through-thickness variation of strain and hence temperature to register. However, at the frequency employed in these tests (10Hz) it is inevitable that there would be a substantial three-dimensional non-adiabatic zone associated with the crack tip plasticity[133].

Additional fractographic analysis of an unexpanded coupon (Figure 94) shows a straight crack front perpendicular to the faces of the specimen; a fact supported by both the DIC and TSA results, which show approximately equal lengths of crack on each face at each increment of fatigue life shown in Figure 91 and Figure 92.

The extent of the plastic zone created during the cold expansion process was calculated from digital image correlation measurements made during the expansion process44. The strain tensors evaluated from the DIC data were converted to stress using the material properties of the 2024-T3 aluminum and then the von Mises yield criteria was used to determine where the onset of plasticity would occur. The plastic zone was found to extend about 2.5 mm from the hole edge so that for crack lengths of about 2 mm and less probably there is no distinct crack tip plastic zone and hence the classical crack tip stress/strain pattern is not seen until the crack grows out of this region. This is supported by the DIC data for the expanded hole in Figure 91 (right

column) which does not exhibit a crack tip strain distribution comparable to the unexpanded hole as in Figure 91 (left column) until the crack is of length 3.7 mm. There is some evidence in the TSA data (Figure 92h) that the crack tip plastic zone is beginning to emerge from this region at a crack length of 3.7 mm on the entry face.

When the crack extends in both the UH and CX coupons the load distribution becomes asymmetric as the cracked (left) ligament reduces in stiffness and more load is borne by the uncracked (right) ligament. This effect is magnified for the CX coupon because the extent of the uncracked and elastic ligament is also reduced by the plastic zone around the hole arising from the cold expansion. By the time the crack extends to 3.7 mm (Figure 91h), the stress in the previously uncracked ligament of the CX coupon has become so great that a small crack appears. This is not visible in the TSA data (Figure 92h) because the crack front is curved such that the crack has not reached the exit face as shown in Figure 93.

In the UH coupons, there is an increase in crack tip strain with increasing crack length as would be expected since the stress intensity factor is a function of crack length.
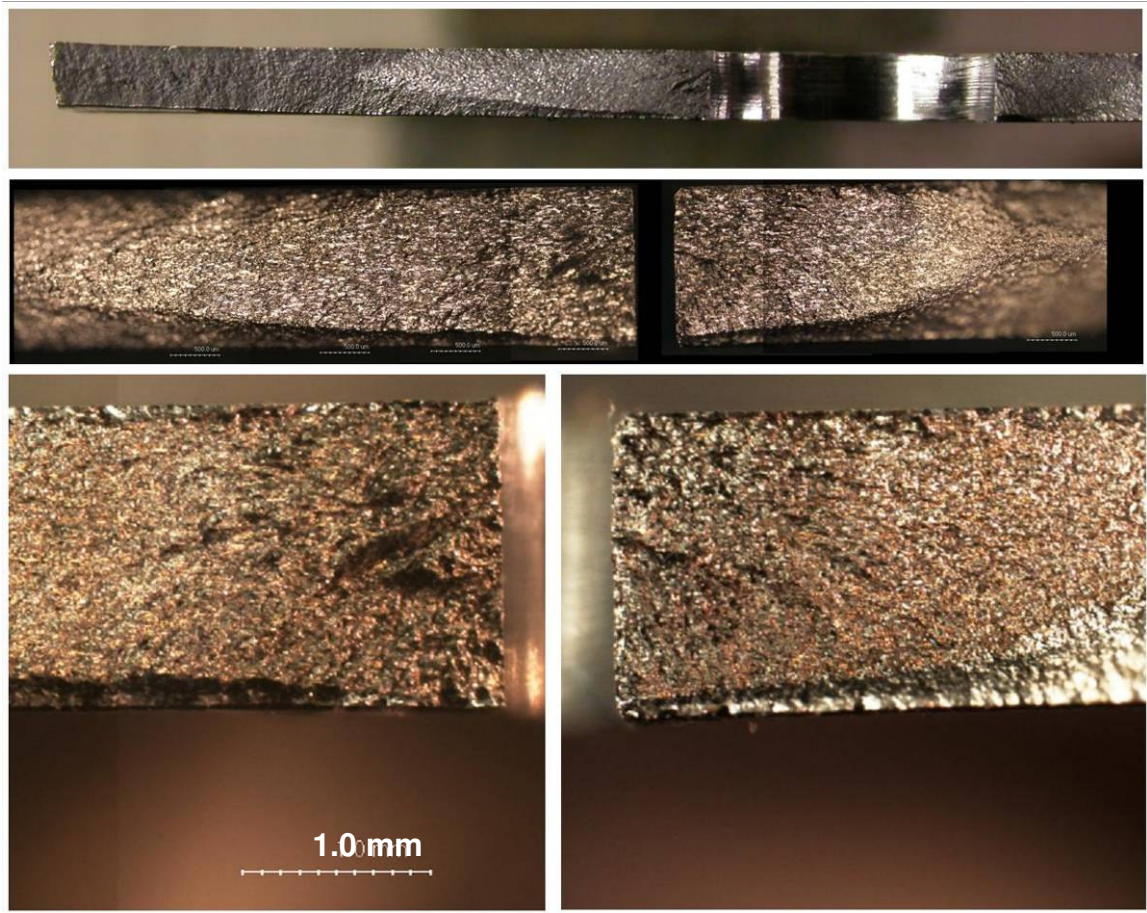
Figure 93: Fracture surface of the coupon with cold-expanded hole orientated as in Figure 92 with the exit face on the lower side and with increasing levels of magnification from top to bottom
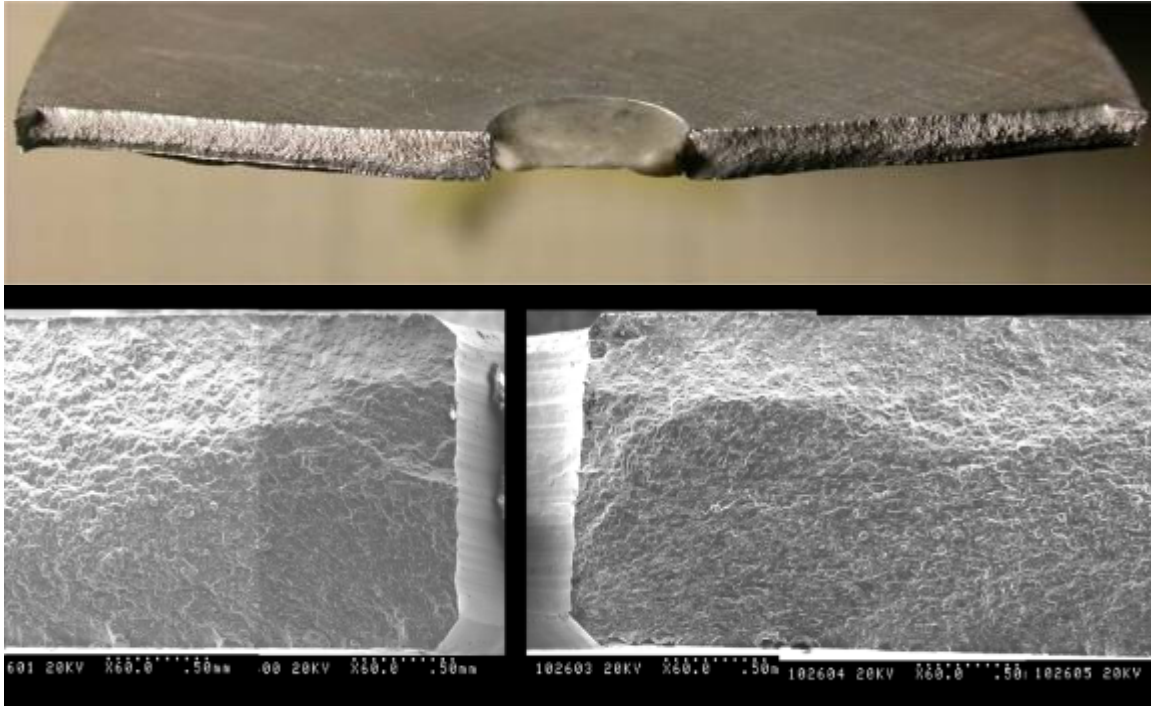
Figure 94: Optical (top) and SEM (bottom) images of the fracture surfaces for the coupon with the unexpanded hole at increasing levels of magnification from top to bottom and orientated with the exit face on the lower side

8.1.2 FML: Cold Expansion Strain and Fatigue Results

8.1.2.1 FML: Overall Fatigue Results

Overall fatigue results showing the number of cycles to failure against the net section stress are plotted for both FML 3 (Figure 95a) and FML 4 (Figure 95b). Although the number of coupons tested at each stress level is small, the improvement in fatigue life as a result of cold-expansion, especially at lower stress levels, is still evident. The overall results suggest that the cold expansion process is effective at increasing fatigue life for both grades of FML.
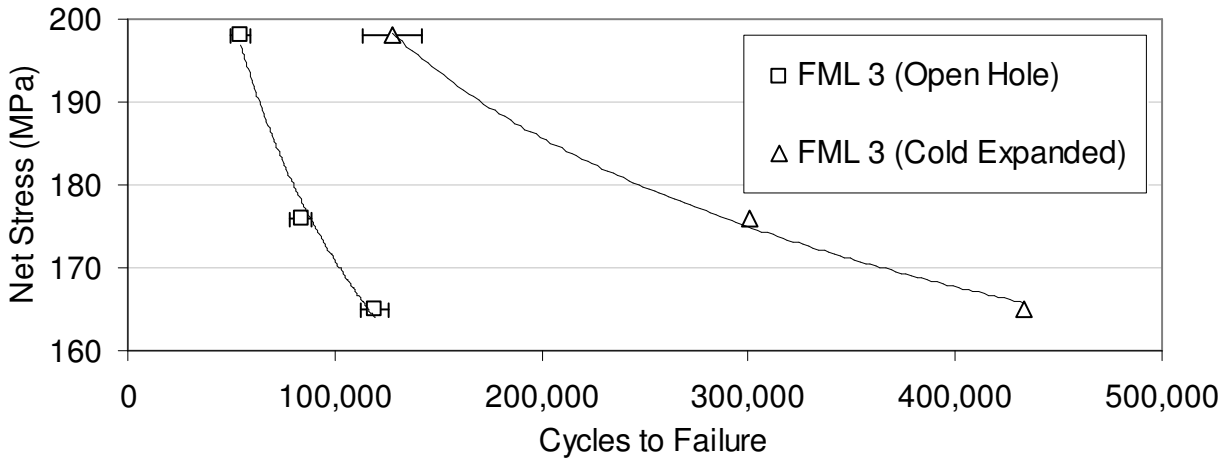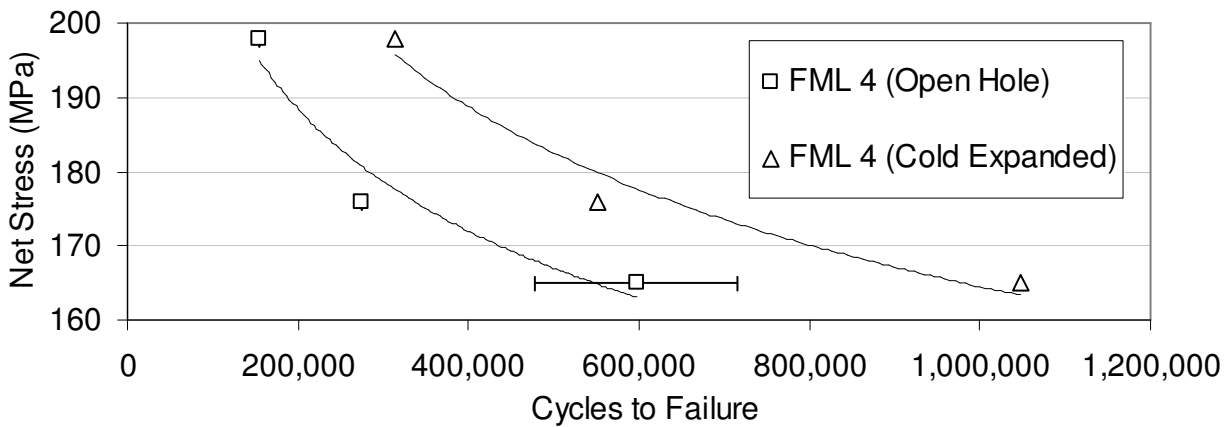
Figure 95: Mean fatigue results. (a) FML 3 [90/0] longitudinal coupons both with and without cold-expansion of the hole and (b) FML 4 [0/90/0] longitudinal coupons both with and without cold-expansion of the hole

8.1.2.2 FML: Crack Growth Curves

A closer examination of some typical crack growth curves, from open hole and cold

expanded coupons for both FML grades (Figure 96 and Figure 97) at the three net

stress levels, shows how difficult it can be to definitely comment on the effectiveness of

cold expansion at extending life on the entry face, in the early stage of the fatigue

process. However, in almost every case, short crack growth (defined as crack growth to

1 mm) appears to occur at the same cycle count in both the unexpanded and cold

expanded coupons. A better overview of the data is provided for FML 3 in Figure 98, which shows the overall number of cycles (taken from all FML 3 crack growth curves) required to grow a 1 mm crack as well as the crack growth rates, both before and after cold-expansion. From Figure 98 it appears that although cold expansion does have an effect at reducing short crack growth (on the entry face), for net stress levels less than 176 MPa, it is much less pronounced than in aluminum (Figure 90), where the reduction in short crack growth rates ranged from 50,000 to over 200,000 cycles, depending on the net stress level. However, from the crack growth curves in Figure 98, it appears that cold expansion is effective at reducing crack propagation rates for all net stress levels, with a slight increase in effectiveness at the highest net stress level (198 MPa). The same analysis performed for all the FML 4 crack growth curves (Figure 99) shows that cold-expansion has a relatively minimal effect on reducing short crack growth, with only small reductions of less than 10,000 cycles at all load levels. However, as with FML 3, cold-expansion is more effective at reducing crack propagation rates at all net stress levels, with a slight increase in effectiveness at the highest net stress (198 MPa). This suggests that the compressive residual stresses induced by cold expansion on the entry face are most effective when the crack has grown past 1 mm and crack bridging can become fully effective.
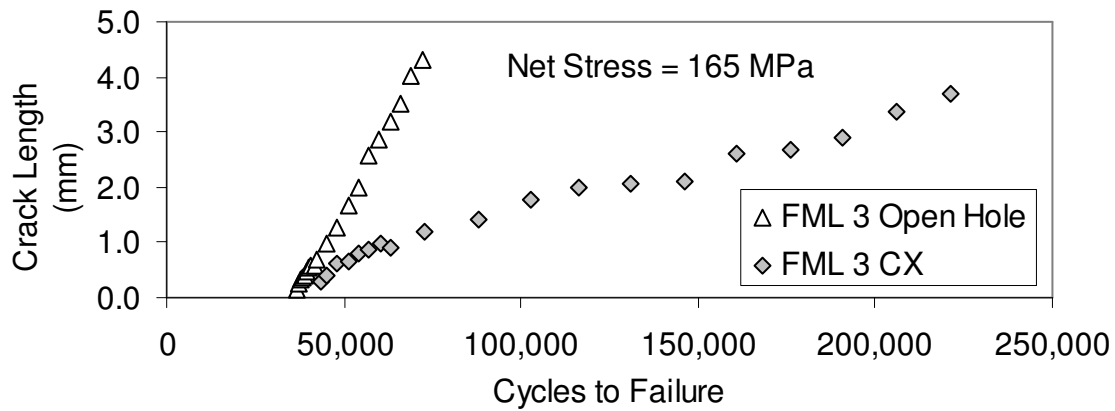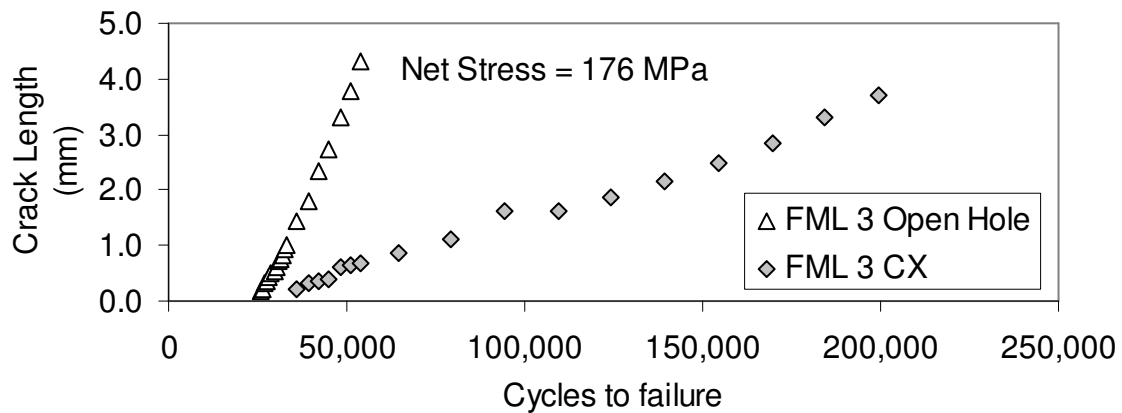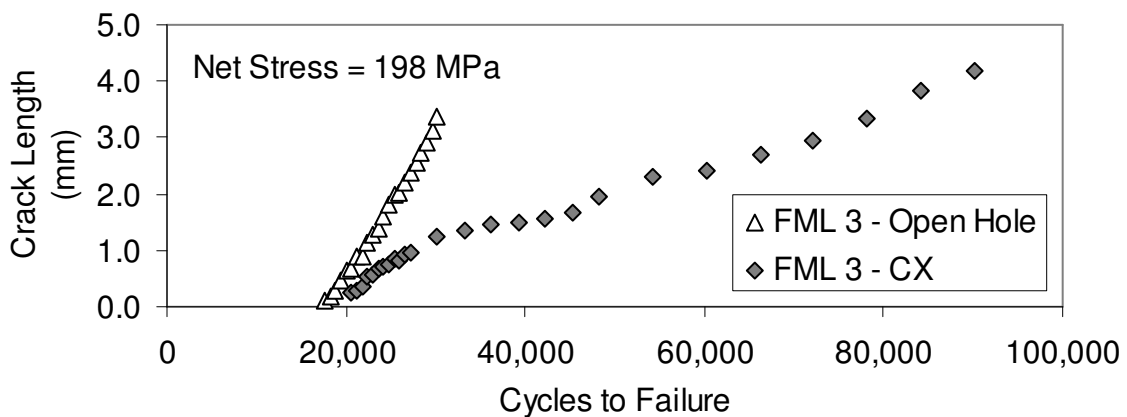
Figure 96: Crack growth curves for FML 3 coupons (a) Net Stress 165 MPa: Open Hole (specimen 15-A-3) and cold-expanded (specimen 15-A-6) coupons (b) Net Stress 176 MPa: Open Hole (specimen 15-A-2) and cold-expanded (specimen 15-A-5) coupons and (c) Net Stress 198 MPa: Open Hole (specimen 15-A-1) and cold-expanded (specimen 15-A-4) coupons
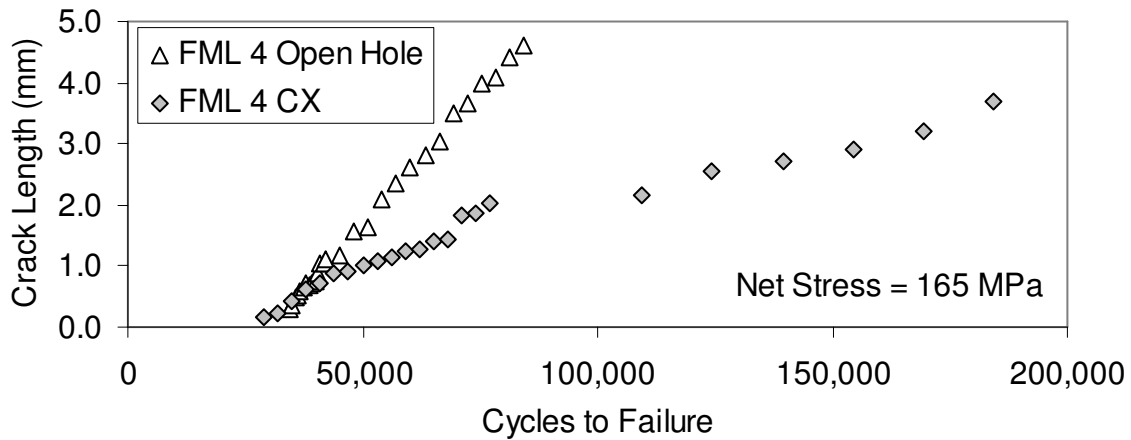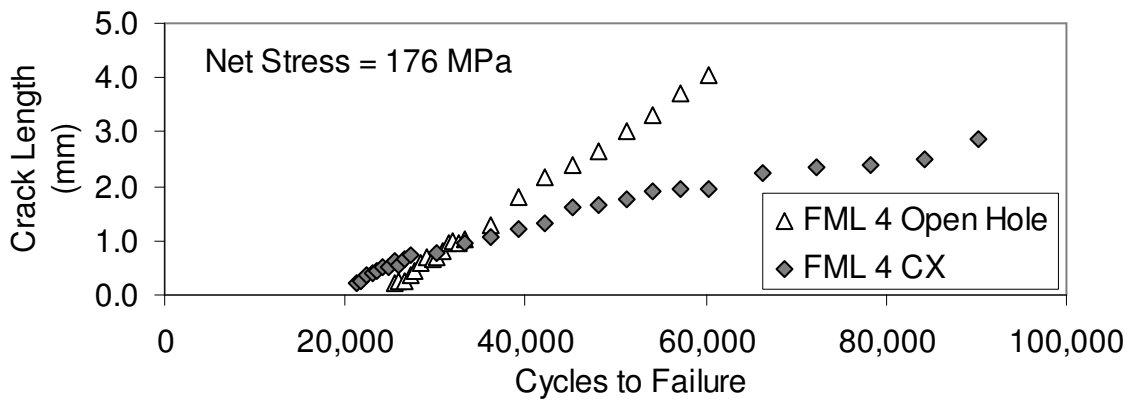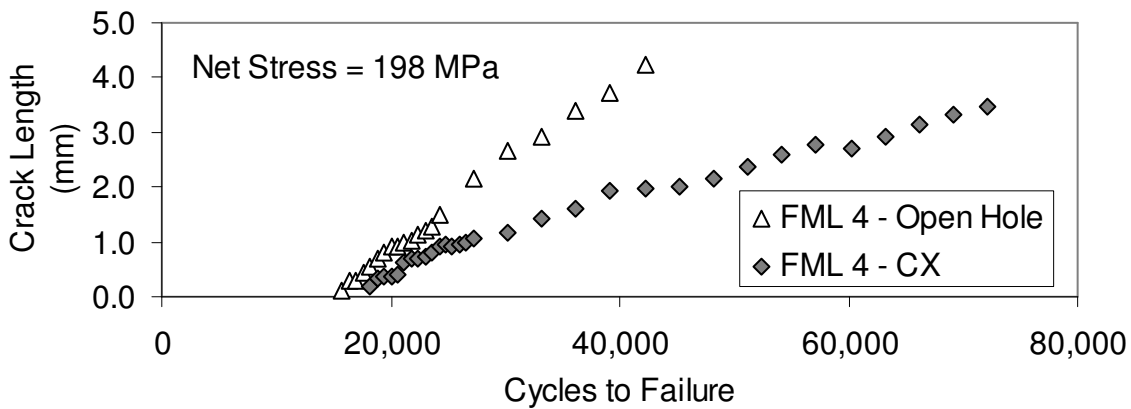
Figure 97: Crack growth curves for FML 4 [0/90/0] longitudinal coupons (a) Net Stress 165 MPa: Open Hole (specimen 16-B-4) and cold expanded (specimen 13-B-3) coupons (b) Net Stress 176 MPa: Open Hole (specimen 16-B-6) and cold expanded (specimen 13-B-2) coupons and (c) Net Stress 198 MPa: Open Hole (specimen 16-B-5) and cold expanded (specimen 13-B-1) coupons
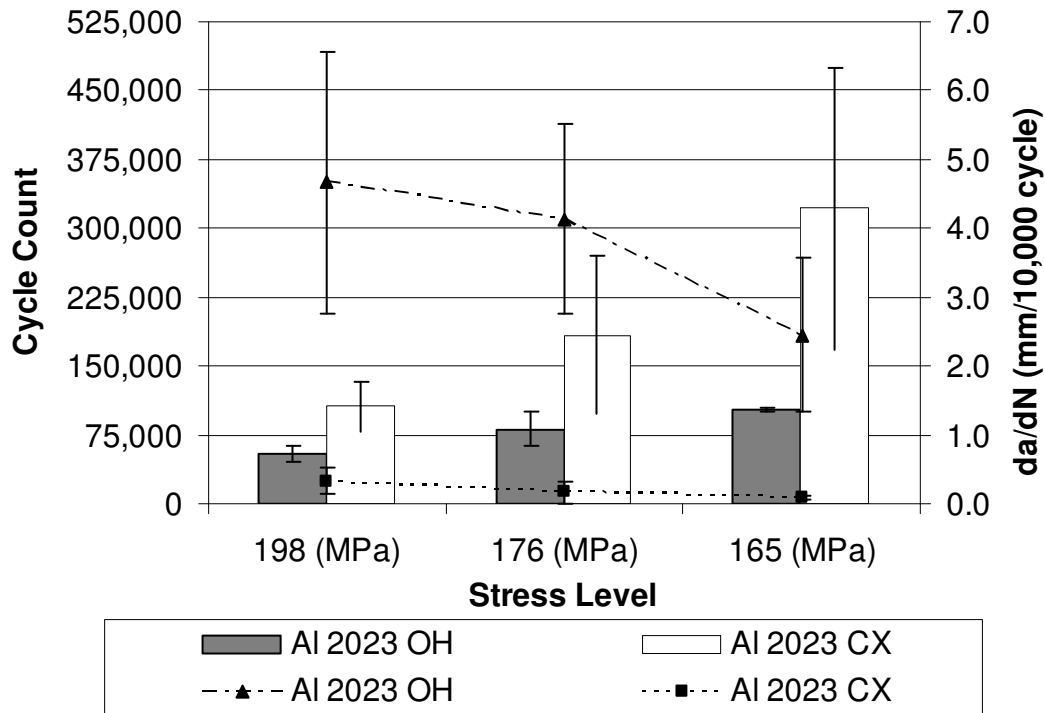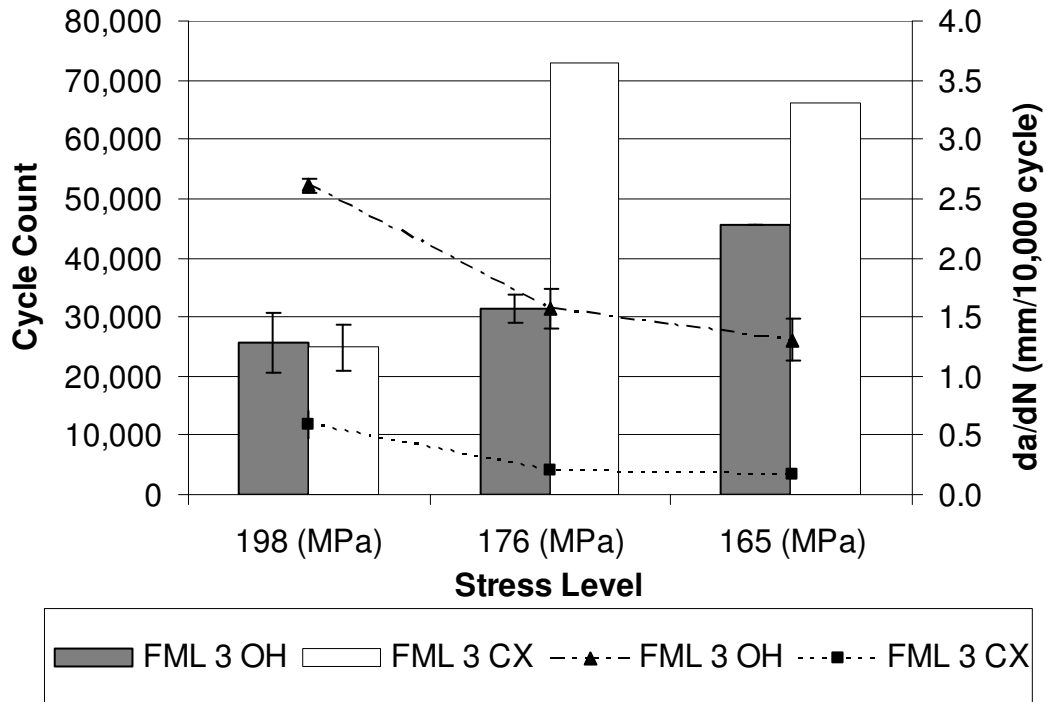
Figure 98: Variation in number of cycles to 1 mm crack length (columns) versus da/dN (symbols) for FML 3 at various stress levels
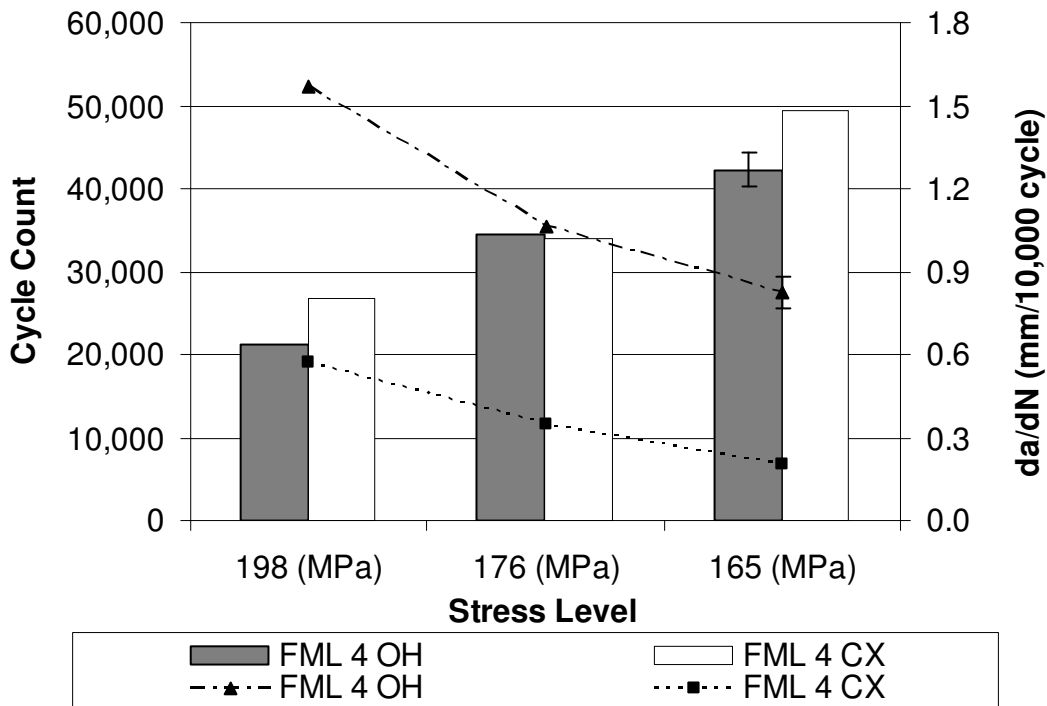
Figure 99: Variation in number of cycles to 1 mm crack length (columns) versus da/dN (symbols) for FML 4 [0/90/0], cut in the longitudinal direction, at various stress levels

184

8.1.2.3 FML: DIC and TSA Measurements During Fatigue Loading

As with the aluminum coupons, digital image correlation was used to capture strains on

the entry face of the FML coupons and thermoelastic stress analysis (TSA) was used to

capture strain information on the exit face during fatigue loading. One sample coupon

for each material was selected at the 198 MPa net stress level. On the entry face of the

sample FML coupon, the maximum principal strain measured using DIC is presented

pre-crack, and at 1 mm, 2 mm and 3.7 mm crack growth intervals. Information from the

TSA system is presented for the exit face at the same intervals. In all cases the

unexpanded coupon is shown in the left-column and the cold-expanded coupon is

shown in the right column. The crack lengths were obtained from images of the coupon

captured at maximum load and subsequently processed using digital image correlation.

8.1.2.3.1 FML 3 Results

In the pre-crack condition, a slightly larger difference in the strain field exists between

the unexpanded coupon (Figure 100a), and the cold expanded coupon (Figure 100b).

Part of this difference can be attributed to the slightly higher net stress in the cold

expanded coupon (~0.8 %) as a result of the slightly enlarged hole. Overall, the strains

at the crack tip on the entry face of the cold expanded coupon (Figure 100d,f,h) are

slightly lower than those of the unexpanded coupon (Figure 100c,e,g) likely as a result

of the compressive residual strains imparted during cold expansion. In addition, a

region of lower maximum principal strain on the unexpanded hole coupons, at the 0°

and 180° degree positions seems to grow in area along with the crack (Figure 100c,e,g).

This area of lower maximum principal strain may be indicative of through-crack growth,

which is an observation supported by the TSA data on the exit face (Figure 101c,e,g) as

the TSA signal shows a reduction in magnitude and movement of the peak TSA signal

away from the hole in the 90º and 270º degree direction, which is indicative of crack

growth.
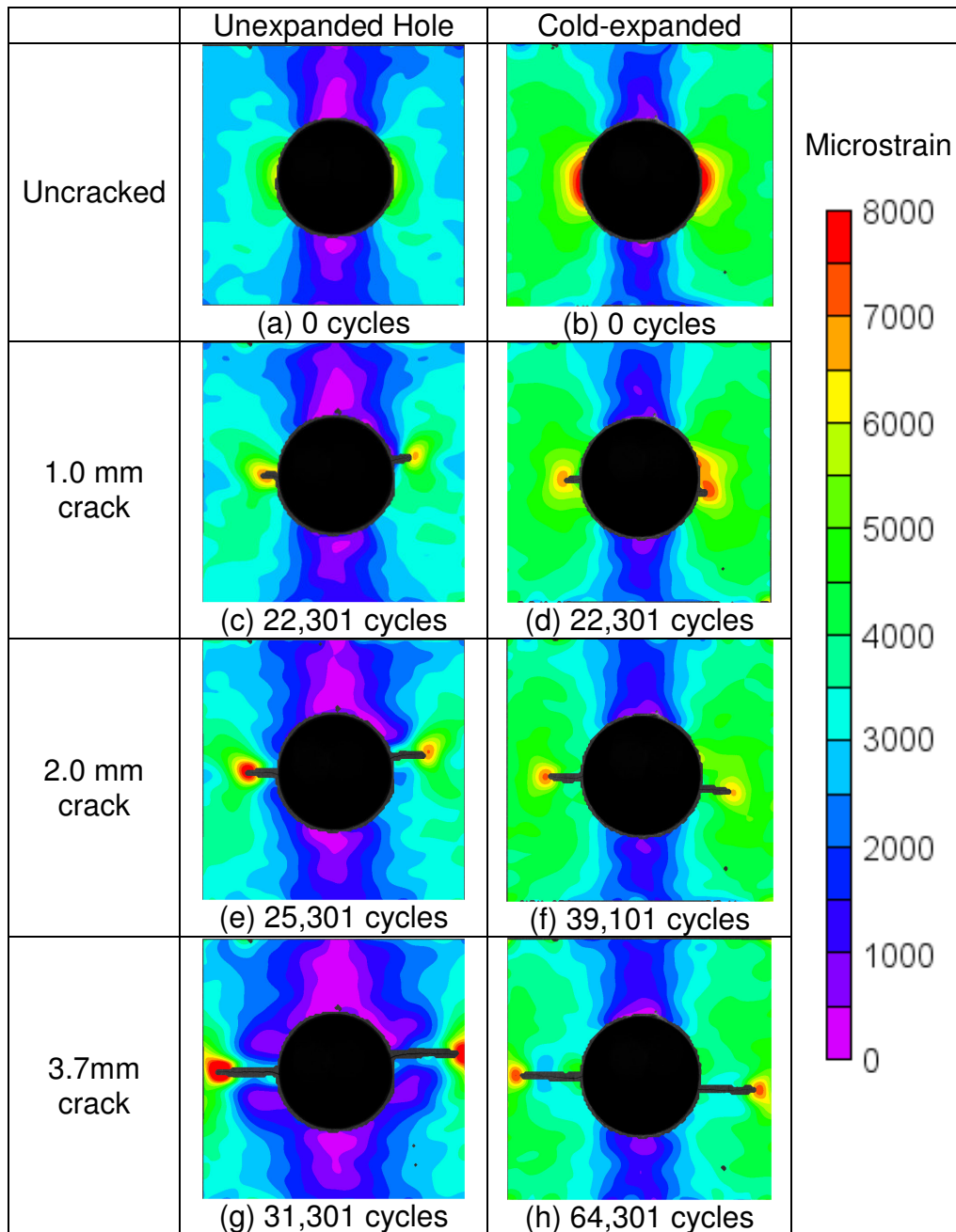
Figure 100: Maximum principal strains obtained from digital image correlation measurements on the entry face of FML 3 coupons with both an unexpanded (left, specimen 12-A-1) and cold–expanded (right, specimen 12-A-4) hole with crack lengths of 0, 1, 2 and 3.7mm
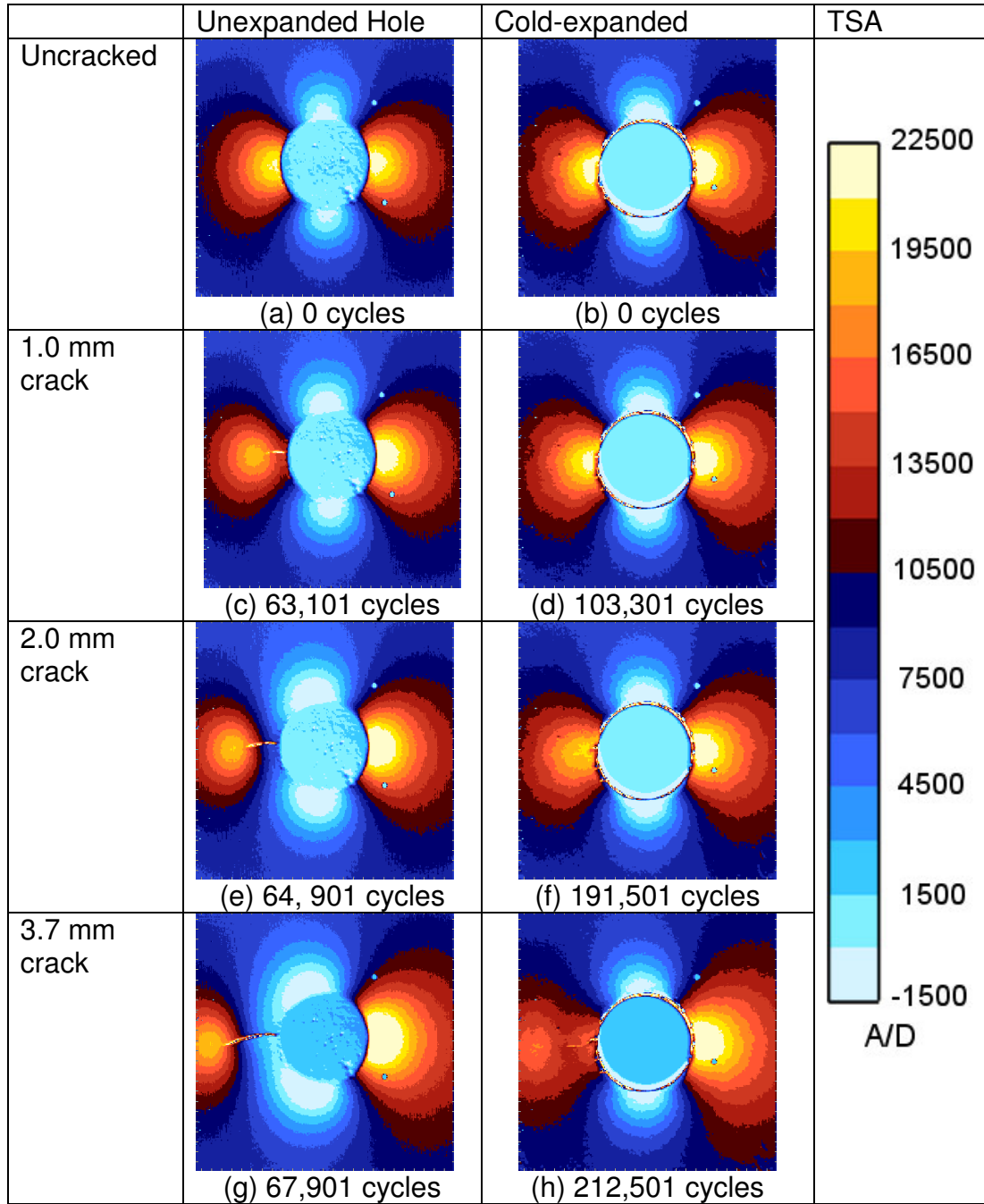
	Unexpanded Hole	Cold-expanded
Uncracked	(a) 0 cycles	(b) 0 cycles
1.0 mm crack	(c) 22,301 cycles	(d) 22,301 cycles
2.0 mm crack	(e) 25,301 cycles	(f) 39,101 cycles
3.7mm crack	(g) 31,301 cycles	(h) 64,301 cycles
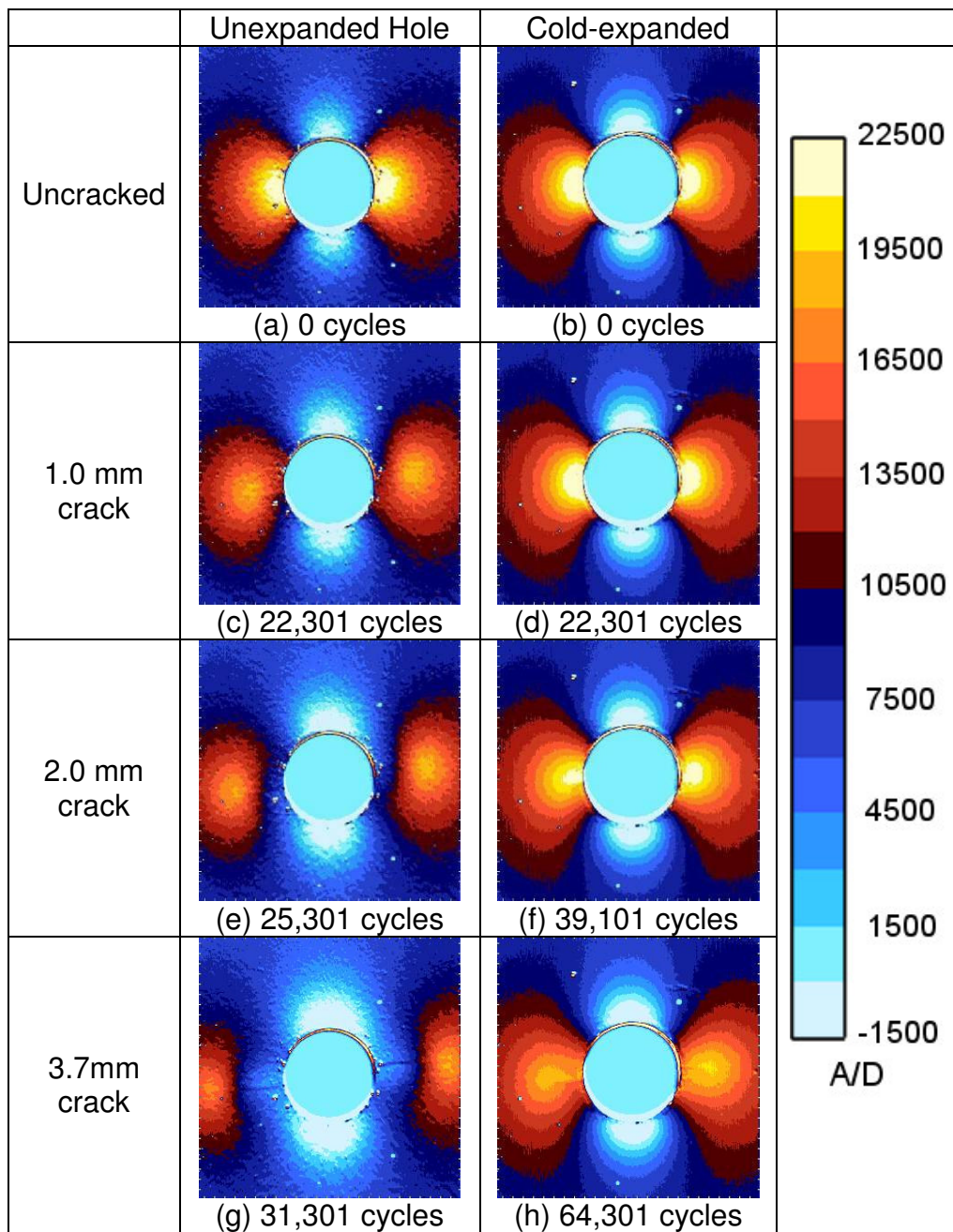
Figure 101: Full-field maps of the thermoelastic signal (A/D) units from the exit face for both unexpanded (left, specimen 12-A-1) and cold-expanded (right, specimen 12-A-4) FML 3 holes

8.1.2.3.2 FML 4 Results

In the pre-crack condition, only a very slight difference in the strain field exists between the unexpanded coupon (Figure 102a) and the cold expanded coupon (Figure 102b), which can be attributed to the slightly higher net stress in the cold expanded coupon (~0.8 %) as a result of the enlarged hole. As with the FML 3 coupons, overall, the strains at the crack tip on the entry face of the cold expanded coupon (Figure 102d,f,h) are overall slightly lower than those of the unexpanded coupon (Figure 102c,e,g), likely as a result of the compressive residual strains imparted during cold expansion. In the FML 4 unexpanded coupon (Figure 102c), a secondary crack appears to form beneath the main crack, but the propagation appears to arrest as soon as the crack length approaches 1 mm, likely as a result of crack bridging (Figure 102e and Figure 102f). The corresponding cold-expanded FML 4 coupon (Figure 102d and Figure 102f) only shows evidence of a primary crack forming and although there is a stress intensity at the crack tip in all cases, the stress intensity factor is lower than that of the unexpanded coupons.   In addition, as with FML 3, a region of lower maximum principal strain on the unexpanded hole at the 0° and 180° positions seems to grow in area along with the crack (Figure 102c,e,g). This area of lower maximum principal strain may be indicative of through crack growth, an observation supported by the TSA data on the exit face (Figure 103c,e,g) that shows a reduction in magnitude of the TSA signal and movement of the peak TSA signal away from the hole.
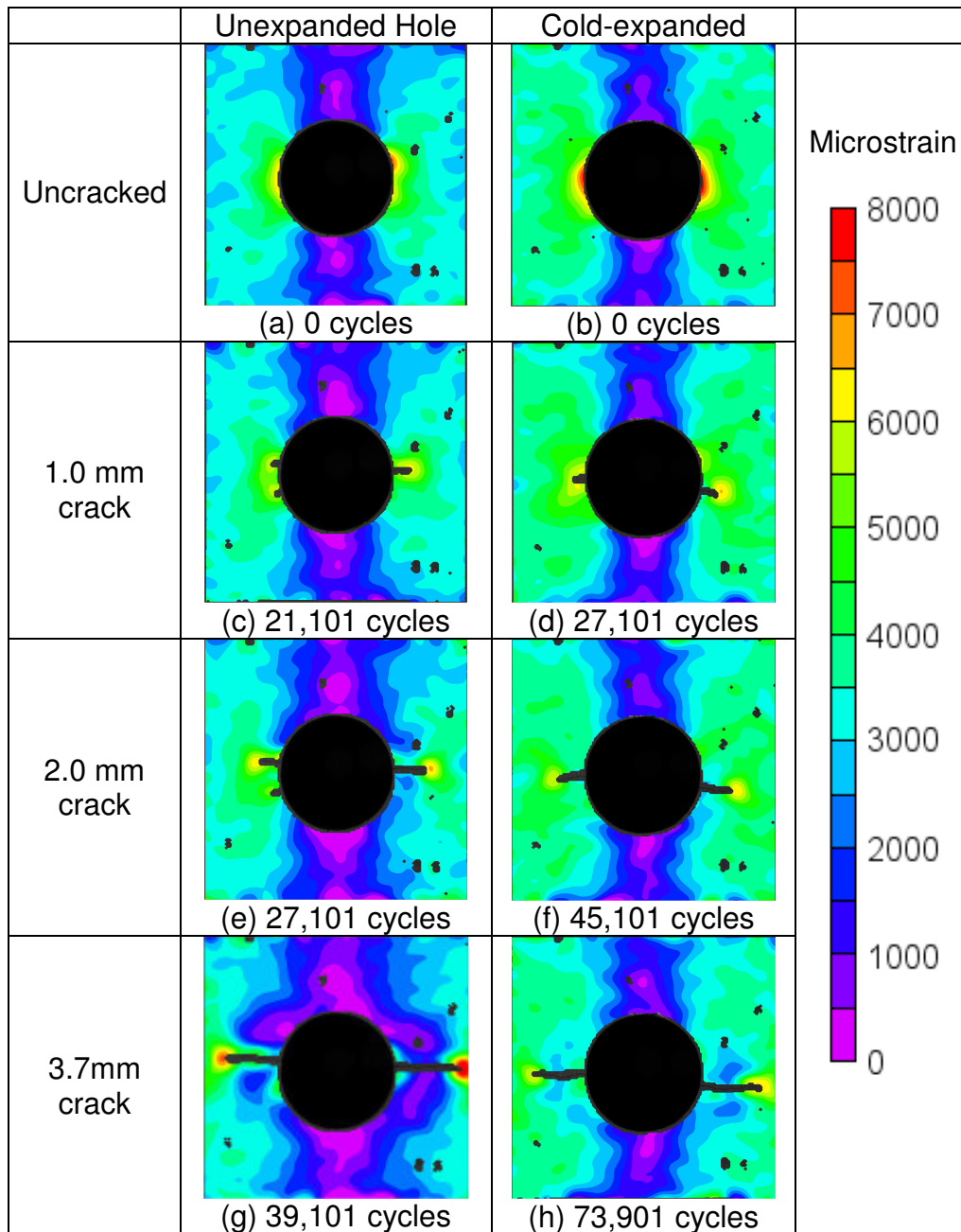
Figure 102: Maximum principal strains obtained from digital image correlation measurements on the entry face of FML 4 coupons with both an unexpanded (left, 16-B-5) and cold–expanded (right, specimen 13-B-1) hole with crack lengths of 0, 1, 2 and 3.7 mm

	Unexpanded Hole	Cold-expanded	TSA
Uncracked	(a) 0 cycles	(b) 0 cycles	
1.0 mm crack	(c) 21,101 cycles	(d) 27,101 cycles	
2.0 mm crack	(e) 27,101 cycles	(f) 45,101 cycles	
3.7 mm crack	(g) 39,101 cycles	(h) 73,901 cycles	
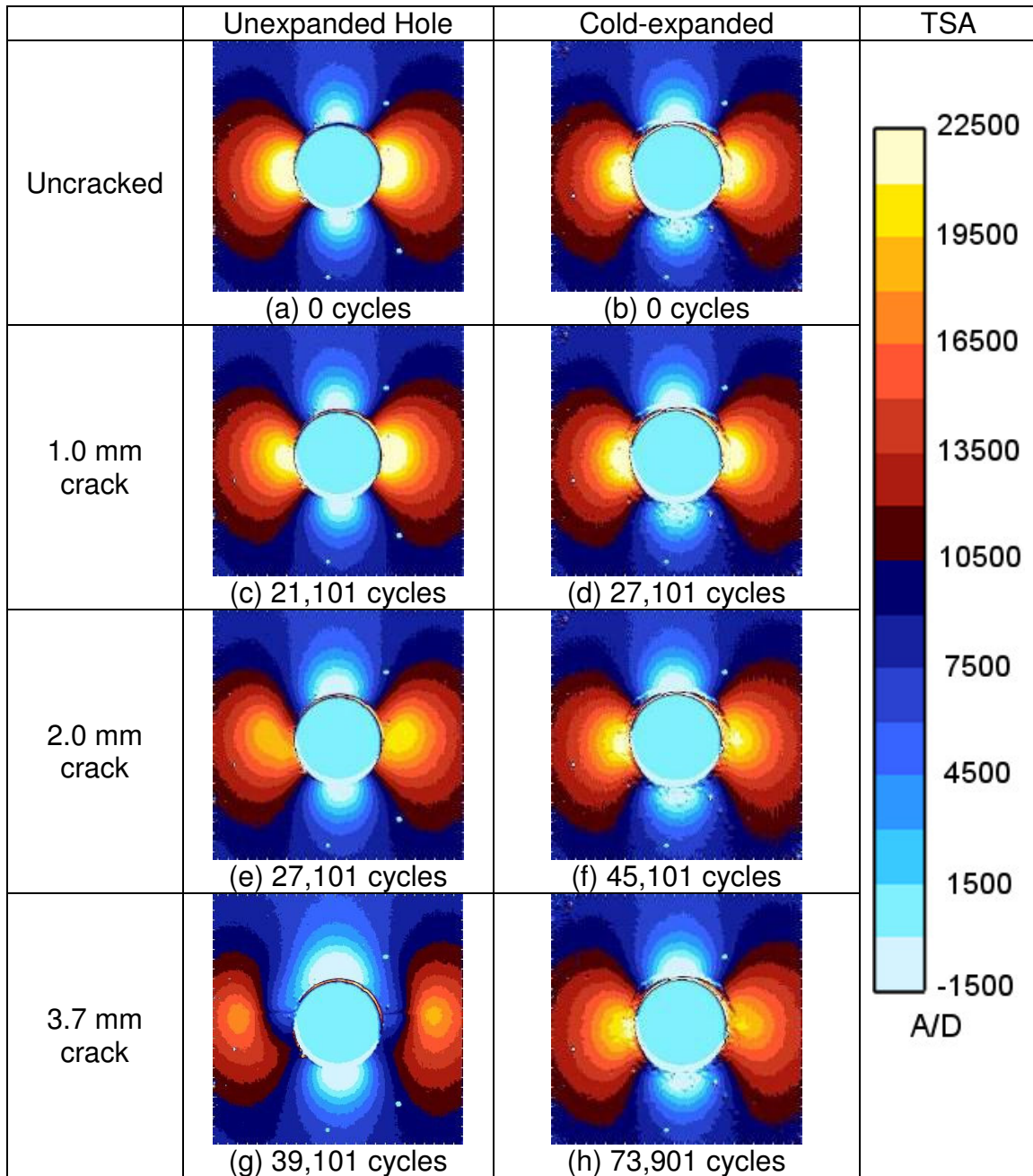
Figure 103: Full-field maps of the thermoelastic signal (A/D) units from the exit face for both unexpanded (left, 16-B-5) and cold-expanded (right, specimen 13-B-1) FML 4 holes

8.1.2.3.3 Ultrasonic Inspection of FML Coupons

Non-destructive evaluation performed post test, using pulse echo ultrasound (PE-UT), clearly highlighted the resulting area of delamination. Sample ultrasonic images for both unexpanded and cold expanded FML 3 (Figure 104) and FML 4 (Figure 105) specimens on both the entry and exit faces are provided. The color scale used for the pulse echo ultrasound (PE-UT) is qualitative, and visually denotes the differences in signal amplitude of the ultrasound wave. Although the disbond area appears greater than that measured by van der Kuip[89], this difference is likely due to the different failure criteria used for the coupon. Van der Kuip[89] used an automatic crack measurement system and was able to stop the fatigue cycles as soon as the crack reached the coupon edge, while for this test, a displacement limit of 0.89 mm (0.035 inches) was used to determine when fatigue cycling would stop. The extra fatigue cycles applied to these coupons likely allowed the disbond area to grow beyond that measured by van der Kuip[89]. Measurements of the disbond area were made by scaling the ultrasound images appropriately and using ImageTool (Department of Dental Diagnostic Science at The University of Texas Health Science Center, San Antonio, Texas) image analysis software to measure the area. The results are displayed in Table 10, and show no statistical difference in disbond area between the cold expanded and unexpanded coupons or between the entry and exit faces, although the disbond area and shape did differ between the two grades of FML.
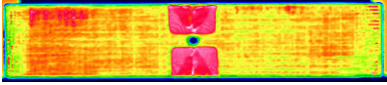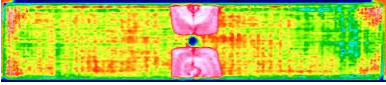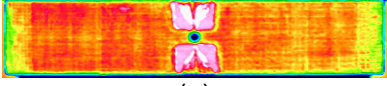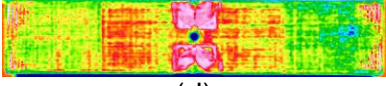
	Unexpanded Hole	Cold-expanded
Pulse Echo Entry Face	(a)	(b)
Pulse Echo Exit Face	(c)	(d)

Figure 104: Pulse echo ultrasonic scans of FML 3 specimen 12-A-1 (open hole) and specimen 12-A-4 (cold expanded). Image (a) unexpanded entry face (b) cold expanded entry face (c) unexpanded exit face and (d) cold expanded exit face
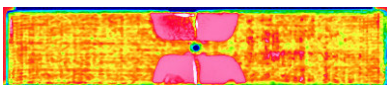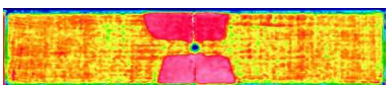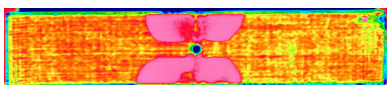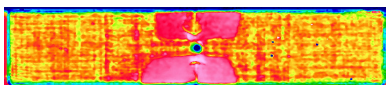
	Unexpanded Hole	Cold-expanded
Pulse Echo Entry Face	(a)	(b)
Pulse Echo Exit Face	(c)	(d)

Figure 105: Pulse echo ultrasonic scans of FML 4 specimen 16-B-5 (open hole) and specimen 13-B-1 (cold expanded). Image (a) unexpanded entry face (b) cold expanded entry face (c) unexpanded exit face and (d) cold expanded exit face

Table 10: Disbond area for cold expanded and unexpanded coupon

	Unexpanded Coupon: Disbond Area (cm^2)	
	Entry Face	Exit Face
Average	19.10	18.76
Std. Dev.	2.90	3.65

	Cold-Expanded Coupon: Disbond Area (cm^2)	
	Entry Face	Exit Face
Average	18.00	15.98
Std. Dev.	2.46	1.50

8.1.2.4 Discussion

For fiber metal laminates, the crack opening that occurs during the crack propagation

phase is due to shear deformation and delamination growth between the laminate

layers. Load transfer between the aluminum and the fiber prepreg induces cyclic shear stresses in the adhesive layer of the prepreg and results in a shear deformation[9]. This shear deformation serves to constrain the crack tip opening, but it is non-zero and thus there is a stress intensity at the crack tip in the aluminum layer that one can measure using image correlation.

The typical assumption for FML materials is that fatigue cracks propagate concurrently in the metal layers only, while the fiber layers remain intact to bridge the crack[9,134]. This assumption is supported by the results from the unexpanded FML coupons. Using the TSA images from the unexpanded FML 4 coupon as an example, at 1 mm of crack growth (Figure 103c) there is a small decrease in magnitude and a change in shape of the stress concentration on the left hand side of the hole. At 2 mm of crack growth (Figure 103e) there is an even greater decrease in magnitude and a slight elongation of the stress concentration, clearly suggesting the presence of a crack, perhaps with fiber bridging causing the elongation. At 3.7 mm of crack growth (Figure 103g) the crack has propagated far enough that the crack tip stress distribution is no longer adjacent to the central hole and a clear unloaded zone between the crack tip and the edge of the hole suggests that fiber bridging has become less effective as a result of a possible through-crack in the aluminum layers. Similar evidence is apparent in the maps of maximum principal strain obtained from DIC. By contrast, for the cold expanded coupon, at 1 mm of crack growth the TSA results (Figure 103d) are essentially identical to the precracked image (Figure 103b). At 2 mm (Figure 103f) and at 3.7 mm of crack

growth (Figure 103h), the magnitude of the stress concentration on either side of the cold expanded hole has decreased in magnitude slightly. This change is indicative of the existence of a small crack, probably with fiber bridging, but is definitely a smaller effect than seen on the entry side of the coupon. These observations are repeated with both grades of FML and suggest that cold expansion effectively changes the fatigue crack mechanism in FML from one where all the metal layers show similar fatigue crack growth[1,3,9], to one where only one surface, in this case the entry face, shows significant crack growth.

The work by van der Kuip[89] also showed that in the early stages of the fatigue process, a difference existed in the fatigue life between the exit and entry face of the cold expanded coupons. This phenomena has been well-documented in monolithic materials in terms of both the residual strain[41,42,44] and residual stress fields[46,62,68,122,130] and have shown that the cold expansion process leads to a triaxial stress/strain state even for relatively thin coupons[135]. The testing done by van der Kuip[89] showed that in most cases the area of delamination on the exit face of the cold expanded coupons was much less than on the entry face; however, what van der Kuip did not address was whether or not this difference was attributable to differences in the residual strain imparted by the cold expansion process.

Overall, the cold expansion of FML shares many similarities with cold expansion in monolithic aluminum materials. As with 2024-T3 aluminum, residual strains on the entry face are lower than those on the exit face and, as a result, crack propagation on the exit face is delayed with respect to the entry face. This is less of an issue with monolithic aluminum since the bulk of its fatigue life is in the crack nucleation phase, as opposed to the crack propagation phase, and the fact that the compressive residual stresses from cold expansion are able to retard crack propagation, makes it a desirable process from a manufacturing standpoint. The situation is reversed in FML where the bulk of its fatigue life is spent in the crack propagation phase; and, although cold expansion has a clear, beneficial effect on the overall fatigue life of FML, its effect on short crack growth on the entry face is not as straightforward. For FML 3 at stress levels of less than 176 MPa, cold expansion appears to delay the formation of short cracks (defined as cracks of 1 mm), while for FML 4, the effect of cold expansion on short crack growth is less pronounced, with a retardation in short crack growth of less than 10,000 cycles in all cases.

8.2   Fatigue Results After Riveting

Due to material supply constraints, the decision was made to test only a reduced set of coupons for the baseline riveting fatigue tests, so only 2024-T3 aluminum and FML 4 were tested for benchmark and comparison purposes.

The riveting and cold expansion processes share several similarities in terms of their effect on the underlying material. In both cases, the hole is expanded, but in the case of riveting, there is no re-collapse of the material surrounding the hole as the rivet shank remains in place, unlike with cold expansion. Another difference is the clamping force

generated around the hole as a result of the formation of the rivet driven head. In the case of a riveted joint, de Rijck et al[136] and Muller[23] have clearly outlined the positive role played by the rivet clamping force in reducing fretting fatigue. For the case of zero load transfer (ZLT) coupons with a rivet, the study by Petrak and Stewart[49] compared the fatigue life of ZLT coupons with Stress Wave rivets to those with cold expanded holes and showed that although the Stress Wave rivet improved fatigue life, it did not do so by as much as hole cold expansion. Little information was given regarding the Stress Wave rivet so it is difficult to determine how applicable these results would be to the current investigation.

Surprisingly, the initial fatigue testing of the riveted coupons at the same net stress levels used for the cold expanded coupons consistently resulted in run-out (defined as any coupon surviving 1,000,000 fatigue cycles with no failure). As part of this initial pilot study, additional fatigue testing at various stress levels was performed and the results showed (Figure 106) that to achieve fatigue life similar to that of cold expanded coupons, the net stress would need to be increased to approximately 263 MPa, almost 69 MPa higher than with the open hole coupons. Even at these higher stress levels, crack nucleation tended to occur away from the open hole, sometimes even starting at the edges of the coupon and gradually moving inward. Due to this variability in the crack nucleation location and due to the formation of multiple cracks, it was not possible to make crack growth measurements in a manner similar to the open hole coupons (where all cracks nucleated from the open hole). As a result, the riveted coupons were compared on the basis of percentage of life remaining. For the current results, 75% of

total life was used as the basis for comparing the aluminum and the FML coupons. This means that full-field strain images of the coupons were extracted and compared at a number of cycles equivalent to 75% of their total life as opposed to at set crack lengths.
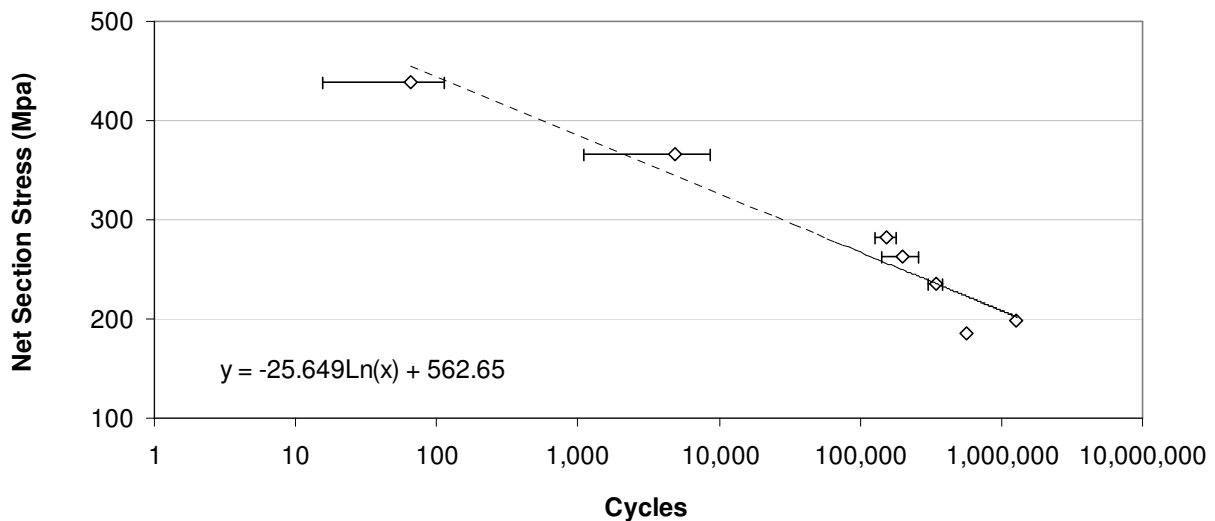
Figure 106: S-N curve for riveted aluminum 2024-T3 coupons at various stress levels

8.2.1 Aluminum: Rivet Fatigue Results

The average fatigue life of the (n=8) riveted 2024-T3 aluminum coupons tested at a net stress of 263 MPa was 199,763 ± 56,631 cycles. This value is overlaid on an S-N curve of the aluminum cold expansion fatigue results (Figure 107). This comparison between the riveted and cold expanded coupons serves to highlight the improvement in fatigue life achieved with riveting as opposed to cold expansion. As mentioned previously, another key difference between the riveted and cold expanded coupon was the location of the crack nucleation sites. With the cold expanded coupon, every coupon failed as a result of a crack nucleating from close to the diameter of the hole, and propagating in a direction perpendicular to the load application, until it reached the edge of the coupon. The aluminum coupons suffered from multi-site damage with some cracks initially

nucleating from the region of the rivet hole and others nucleating at random locations throughout the coupon and eventually linking up to cause coupon failure. The strain measurements from the driven and manufactured head face of the coupons (Figure 108) show how much more uniform the surface strains are, with a much more concentric strain concentration immediately around the hole.
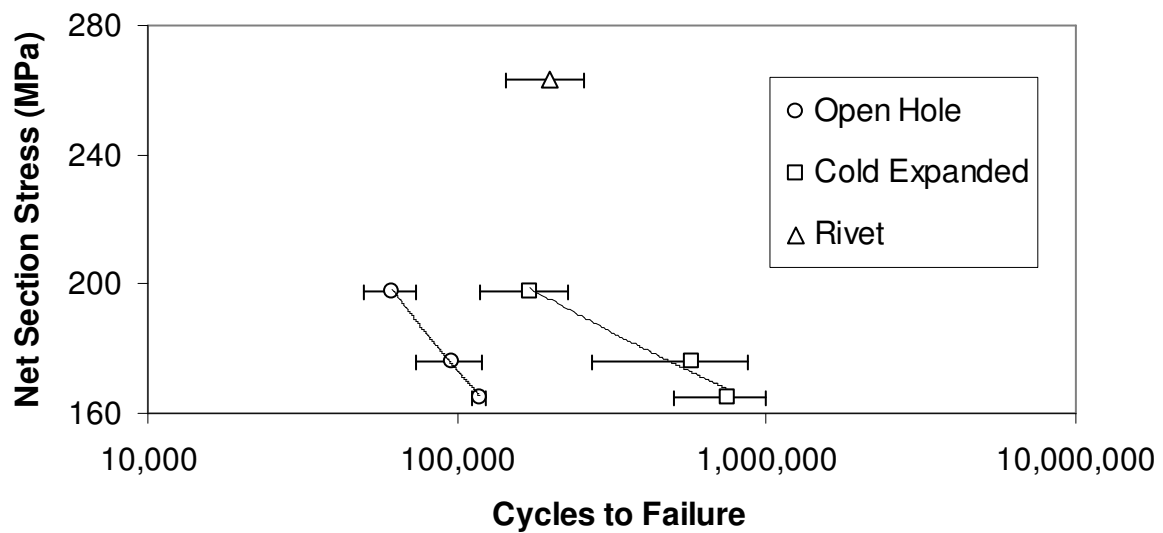
Figure 107: S-N curve for open hole, cold expanded and riveted 2024-T3 aluminum coupons
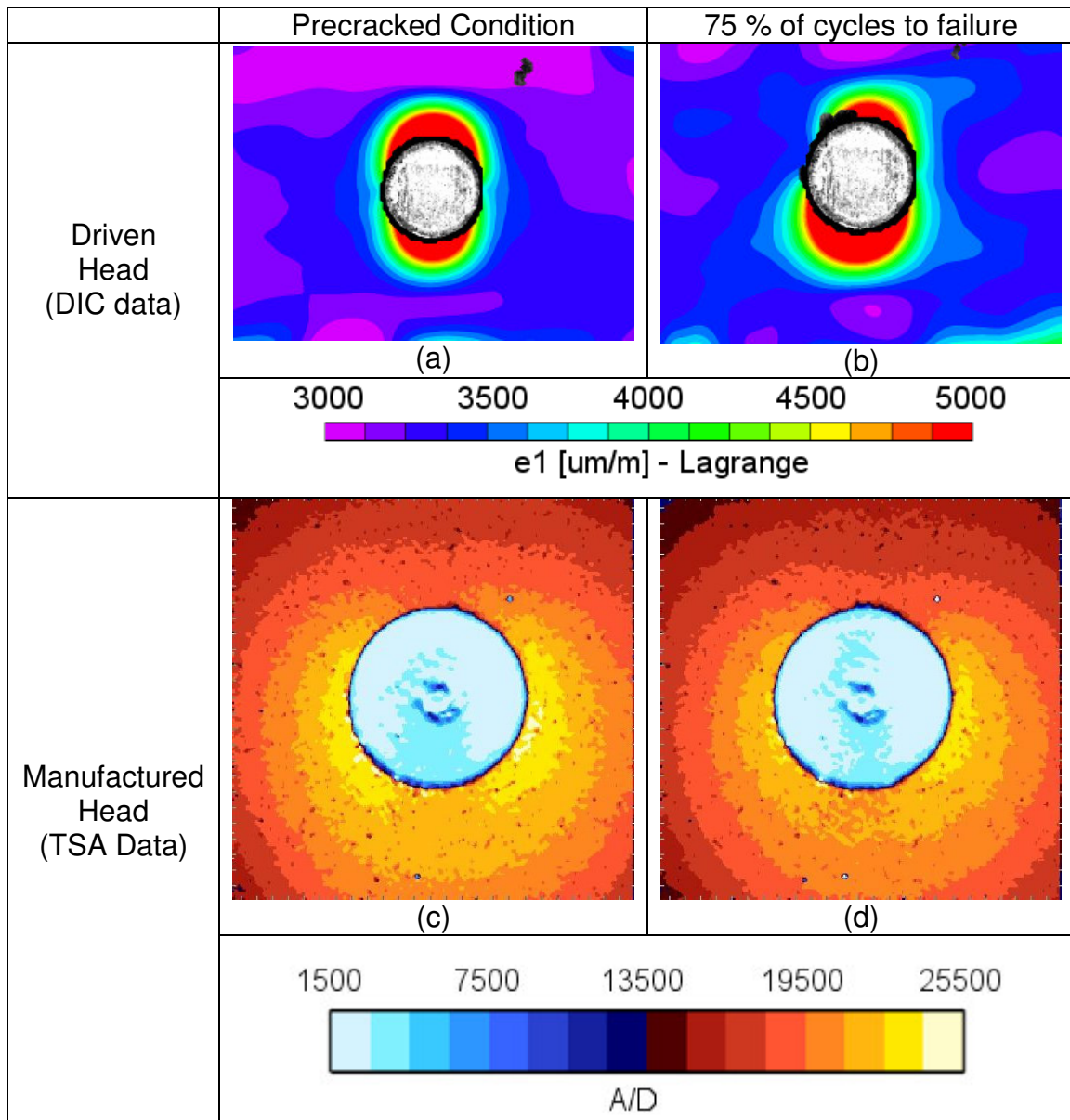
Figure 108: a-b) Maximum principal strain from rivet driven face and c-d) TSA strain information from rivet manufactured head face for the aluminum 2024-T3 coupon, at pre-crack formation and at 75% of the number of cycles to failure (specimen Al-L-15). Note: Net stress of 263 MPa

Several of the failed coupons were examined with both an optical and scanning electron microscope (SEM) to better determine the origin of the crack. A sample image of one specimen is shown in Figure 109.
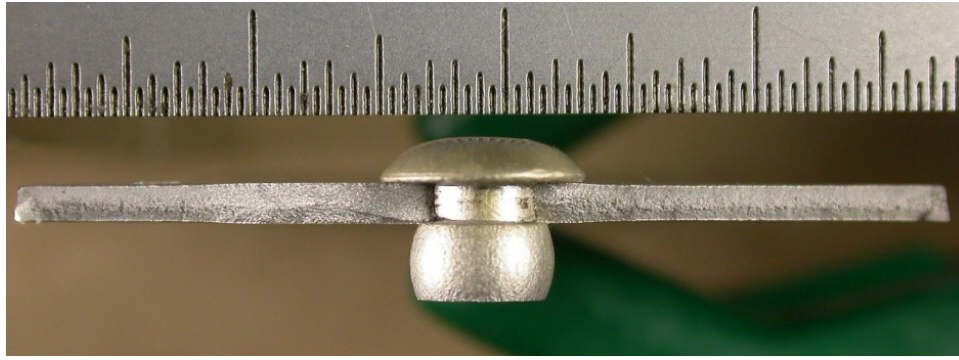
(a)
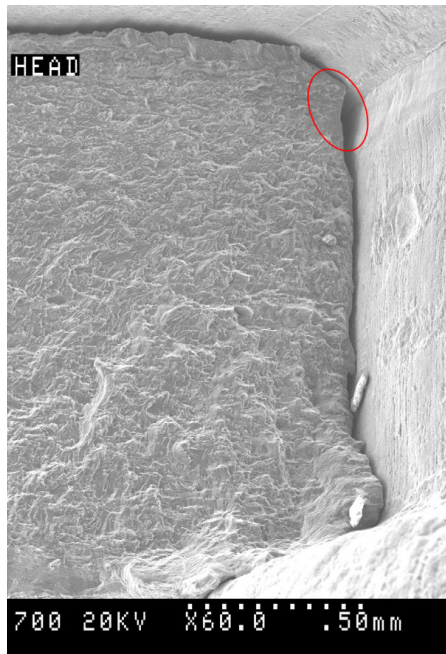
(b)
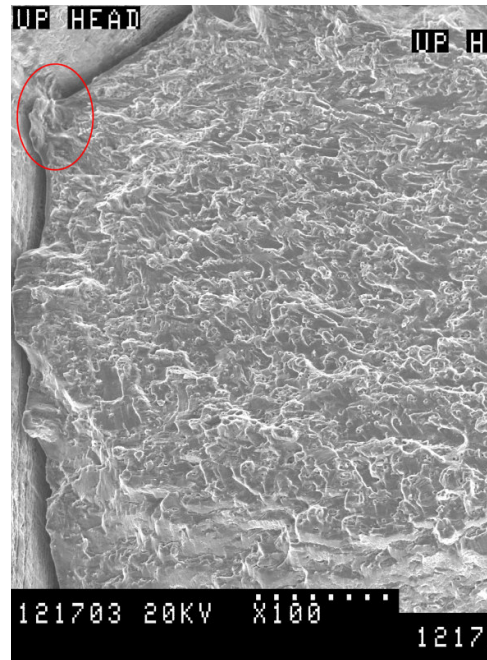
(c)

Figure 109: (a) Optical micrograph of failure surface of AL-L-14 (b) Scanning electron micrographs of left hand specimen surface below manufactured head. (c) Right hand side of specimen. Note: Crack nucleation origin highlighted in red

Four coupons underwent fractographic analysis and the results of these tests are summarized in Table 11. Overall, the initial cracks nucleated from somewhere in the vicinity of the rivet hole, with no one location being dominant. The multi-site nature of the failure made it impossible to measure crack growth, since often a secondary crack growing from the edge or middle of the coupon would propagate inwards towards the

rivet, linking up with cracks growing from the rivet hole and causing coupon failure. One important point to note is the effectiveness of the rivet at protecting the hole from fatigue damage as highlighted by the variability in the crack nucleation locations.

Table 11: Summary failure locations from fractography of aluminum coupons

Specimen Identifier	Failure location(s)
AL-L-14	Below manufactured head
AL-L-15	Below manufactured head and internal
Al-L-16	Multi site: Below driven and manufactured head and internal
AL-L-17	Below manufactured head and internal

8.2.2 FML: Rivet Fatigue Results

The average fatigue life of the (n=5) riveted longitudinal FML 4 [0/90/0] coupons was 161,325 ± 21,080 cycles and this datum was overlaid on an S-N curve for the cold expanded FML coupons (Figure 110) to demonstrate how effective the riveting process was for this material. The crack nucleation location was just as varied as with the aluminum coupons, so comparisons were performed in the same way, taking data from images corresponding to 75% of the cycles to failure. Figure 111 shows the maximum principal strain field pre-crack growth (Figure 111a) and at 75% cycles to failure (Figure 111b). Even with the apparent strain concentration centered on the rivet, no clear fatigue cracks have formed in this area. The TSA images obtained from the manufactured head face show even less change between the pre-crack condition (Figure 111c) and the coupon at 75% of its cycles to failure (Figure 111d). One possible hypothesis is that the compression afforded by the rivet head could be the main driver in changing the nucleation region from under the rivet head to the edge of

the coupon. This effect is interesting in light of the consistent failure mode for the cold

expanded coupons, where crack nucleation consistently occurred at the outer diameter

of the cold expanded hole and may suggest a mechanism for future improvements in

fastener technology.
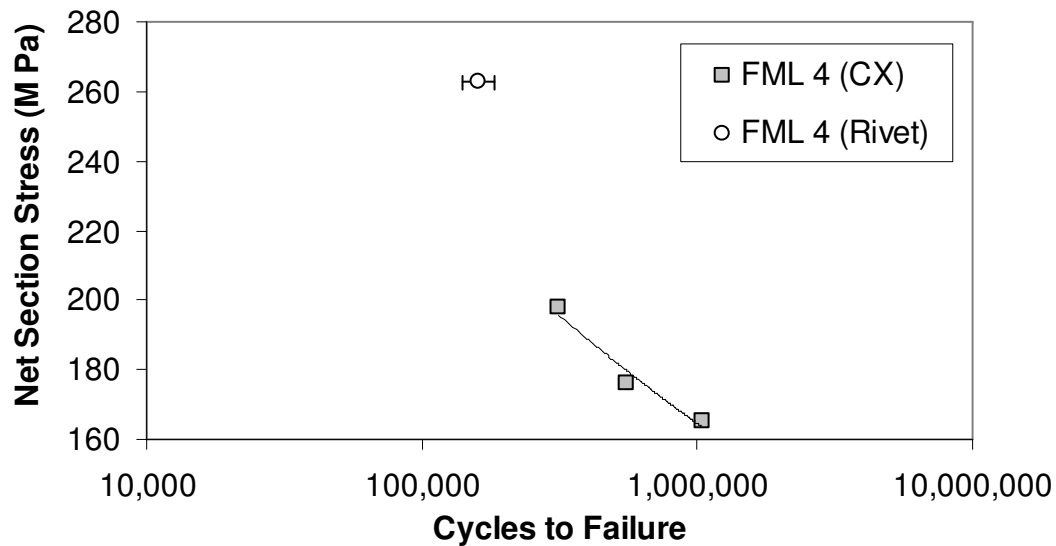
Figure 110: Fatigue results for FML 4 [0/90/0] riveted coupon, overlaid on S-N curve
data for FML 4 cold expanded coupon fatigue data

	Precracked Condition	75 % of cycles to failure
Driven Head (DIC data)	(a)	(b)

3000   3500   4000   4500   5000

e1 [um/m] - Lagrange

| Manufactured Head (TSA Data) | (c) | (d) |

1500   7500   13500   19500   25500

A/D
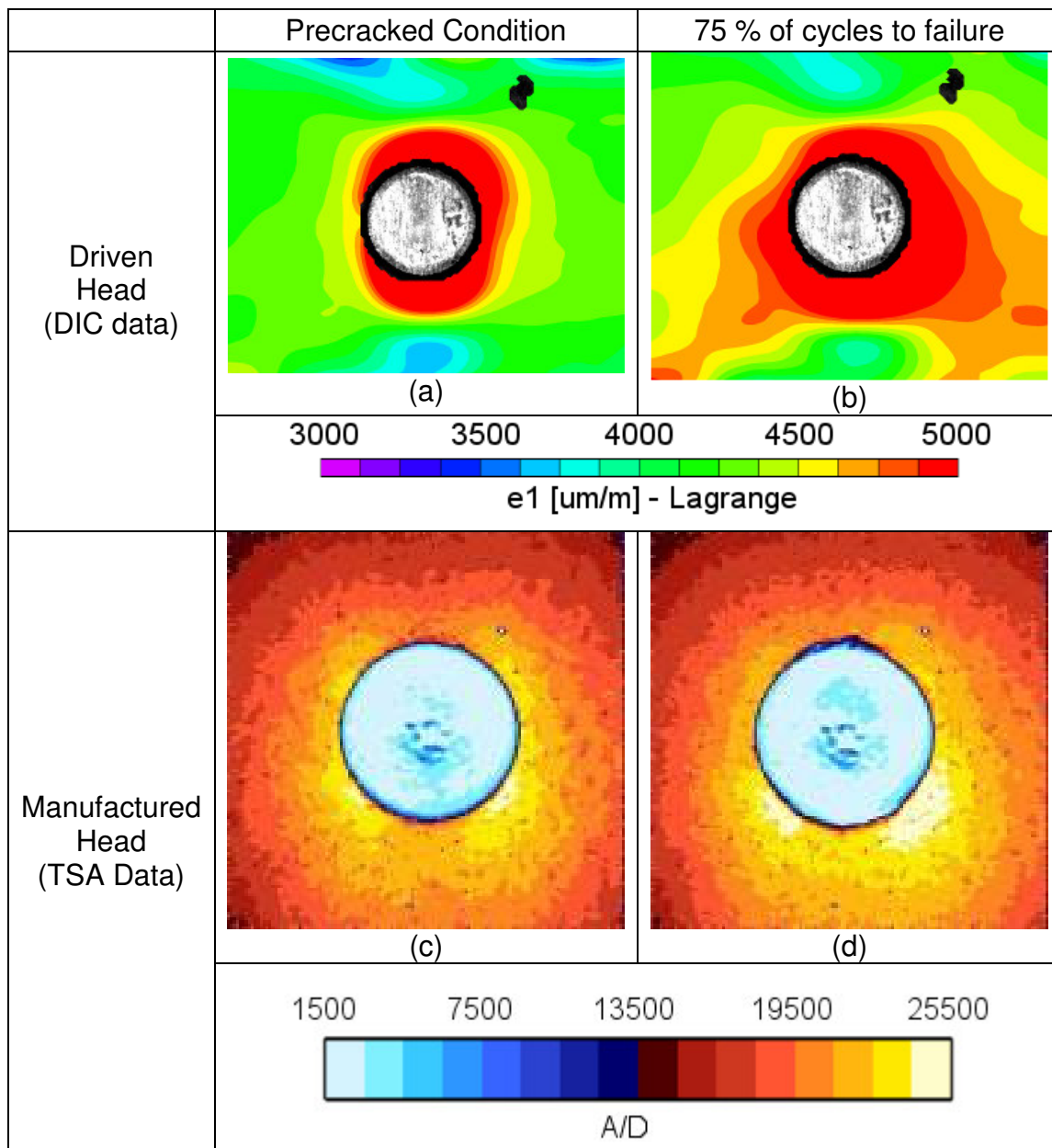
Figure 111: a-b) Maximum principal strain information from rivet driven face and c-d) TSA strain information from rivet manufactured head face for the FML 4 [0/90/0] coupon, at pre-crack formation and at 75% of the number of cycles to failure (specimen 13-B-5). Note: Net stress of 263 MPa

Table 12 summarizes the crack nucleation location in both the aluminum and FML

coupons and shows that the rivet is effective at retarding crack formation, shifting the

crack nucleation location away from central rivet hole in many instances. Post-test

ultrasonic inspection was used to further support this observation by determining the

areas of disbond in the coupon on both the driven and manufactured faces, which are associated with crack formation. A sample image was provided for an FML 4 coupon in Figure 112. For the ultrasonic results, sharp colour changes delineate the area of disbond and by this measure show the dispersed nature of the disbond around the rivet. Examining the ultrasound images in general, it is evident that the disbonded regions are spread out more randomly in the central section of the coupon which is in contrast to the constrained disbond pattern seen with the cold expanded coupons (Figure 104 and Figure 105).

Table 12: Summary of crack nucleation locations for aluminum and FML riveted coupons

	Rivet	Edge	Multi Site
FML 4	3	2	
2024-T3 AL	8	1	1
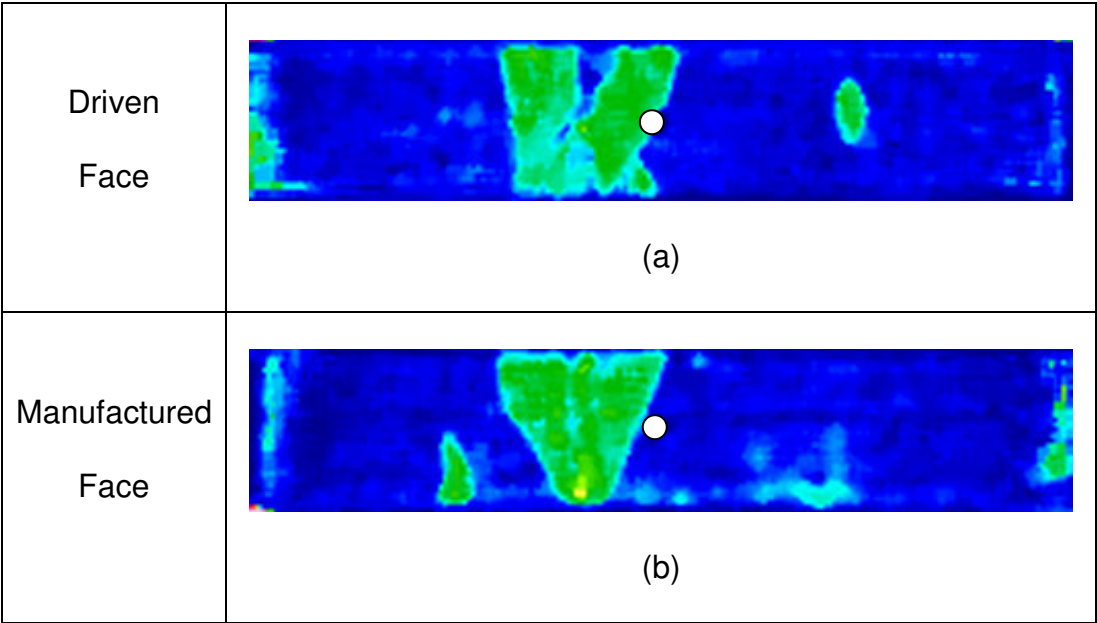
Figure 112: Pulse-echo ultrasonic images post test for: (a) FML 4 coupon (Specimen 13-B-5 driven face and (b) FML 4 manufactured face

9.0   DESIGN AND TESTING OF A NEW FML VARIANT

The observation that drove the design of a new FML variant was the effect that cold expansion had on the FML coupons in the 45º degree orientation (Figure 48 and Figure 49). In this orientation the split sleeve was aligned with the direction of lowest elastic modulus and lowest yield strength and the characteristic butterfly shape of the strain field was replaced with a lower and more uniform maximum and minimum principal strain field. These observations reinforced the idea that the orthotropic nature of FML made it difficult to predict the results of cold expansion without having full knowledge of the orientation and properties of the FML grade being used. These observations also presented an opportunity for mitigating the situation, if it was possible to reduce the orthotropy of the material and design a more isotropic layup.

9.1   Theoretical Design of New FML 4 Variants

One of the first steps in the design process for a new FML variant was to determine a method of estimating FML material properties analytically. Kawai et al[114] had success using a classical laminated plate approach to model FML properties, and this approach was adopted in this work to estimate the elastic modulus, shear modulus and Poisson's ratio of any new FML material (Chapter 7.6.2). As part of the brainstorming process, the first FML variant was designed to reinforce the ±45º degree direction with a proposed layup sequence of [+45/90/-45]. The second variant was an accidental discovery and was produced as a result of the inadvertent misorientation of two of the prepreg layers in an early attempt at producing a quasi-isotropic material. Measurements of the ply angles after ultrasonic inspection showed that a layup sequence of [+30/0/-30] had been made instead of the desired prepreg layup. Since

two panels had been produced, the decision was made to include this material as part of the investigation.

The final proposed FML variant stemmed from a review of classical laminated plate theory, specifically the concept of a quasi-isotropic composite[126-128]. It has been shown in classical laminated plate theory that if three or more identical plies are stacked at equal angles (i.e the angle separating each of the n plies is π/n radians) then the in-plane properties of the laminate are isotropic. For an FML 4 variant with n=3 plies, this would mean an angle of 60º between plies. From a theoretical perspective, a [+60/0/-60] layup would ensure that the in-plane stiffness coefficients were constant (i.e [A_{ij}]=constant), however, this new material would only be considered to be quasi-isotropic since the bending stiffness coefficients [D_{ij}] would not be constant.

Looking at tables of standard FML layup orientations it was evident that no FML variants used non-orthogonal plies except for FML 6 which uses a [-45/45] ply orientation and that the idea of a quasi-isotropic FML did not appear in the open literature. Classical laminate plate (CLP) theory was then used to generate a theoretical modulus distribution for the three new FML variants for comparison to standard FML 4 (Figure 113).

From a theoretical perspective the initial concept of adding more glass fibers along the ±45º degree direction did appear to reduce the degree of orthotropy, between the

material orientations of highest and lowest modulus. Compared to FML 4 which has a difference of approximately 13 GPa between orthogonal material directions, FML 4 [-45/90/+45] only had a difference of approximately 7 GPA. Unfortunately, this new FML 4 is strongest along the 60º degree direction, which makes it difficult to use in a practical setting. The FML 4 [+30/0/-30] that was produced accidentally, showed a fairly monotonic decrease in elastic modulus with a difference of approximately 14 GPa between the 0º degree (most stiff) and 90º degree (least stiff) directions. The results from the CLP analysis of the quasi-isotropic FML 4 [+60/0/-60] showed a constant elastic modulus of approximately 50 GPa, slightly lower than that of FML 4 [0/90/0] in the 0º degree orientation (58 GPa) but with the advantage of having a uniform elastic modulus regardless of material orientation. Classical laminate plate theory also predicted that this material would have a shear modulus of 19 GPa and a Poisson's ratio of 0.33, both values theoretically constant regardless of material direction.
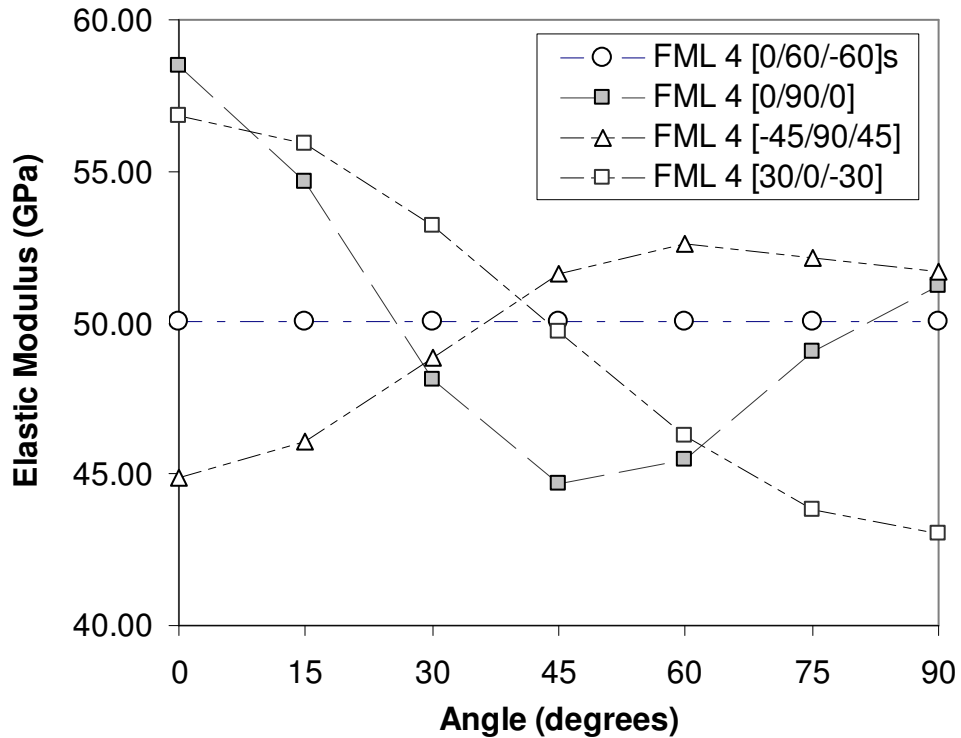
Figure 113: Theoretical modulus as a function of orientation for FML 4 [0/60/-60],
FML 4 [-45/90/45], FML 4 [30/0/-30], and standard FML 4-3/2 [0/90/0]

9.1.1 Baseline Mechanical Testing of New FML 4 Variants

From the analytical work done on all three FML 4 layups, it was clear that the quasi-
isotropic FML 4 had material properties that would likely best address our needs with
regards to cold expansion and riveting. However, as part of this investigation, two
panels of FML 4 [45/90/-45] and FML 4 [-30/0/+30] were produced in addition to the
quasi-isotropic FML 4 [-60/0+60] . Fatigue coupons in the 0º degree orientation
(longitudinal direction) were cut from each panel so that a basic S-N curve comparing
unexpanded and cold expanded fatigue life could be determined. The strains after hole
cold expansion were also measured using digital image correlation.

9.1.1.1 Static and Fatigue Behaviour of FML 4 [-45/90/+45]

Figure 114 shows the maximum principal strains on the entry and exit face of the FML 4 [-45/90/+45] after cold expansion. Although the strain field no longer displays the classic butterfly shape evident with FML 4 [0/90/0], a small degree of asymmetry is evident in the strain field at 135º from the split sleeve (white arrow in Figure 114). The minimum principal strains (Figure 115) appear much more radially symmetric and except for the relatively poor fatigue performance (Figure 116) and the difficulty caused by the orientation of the peak modulus at 60º degrees, this FML 4 layup would appear promising.
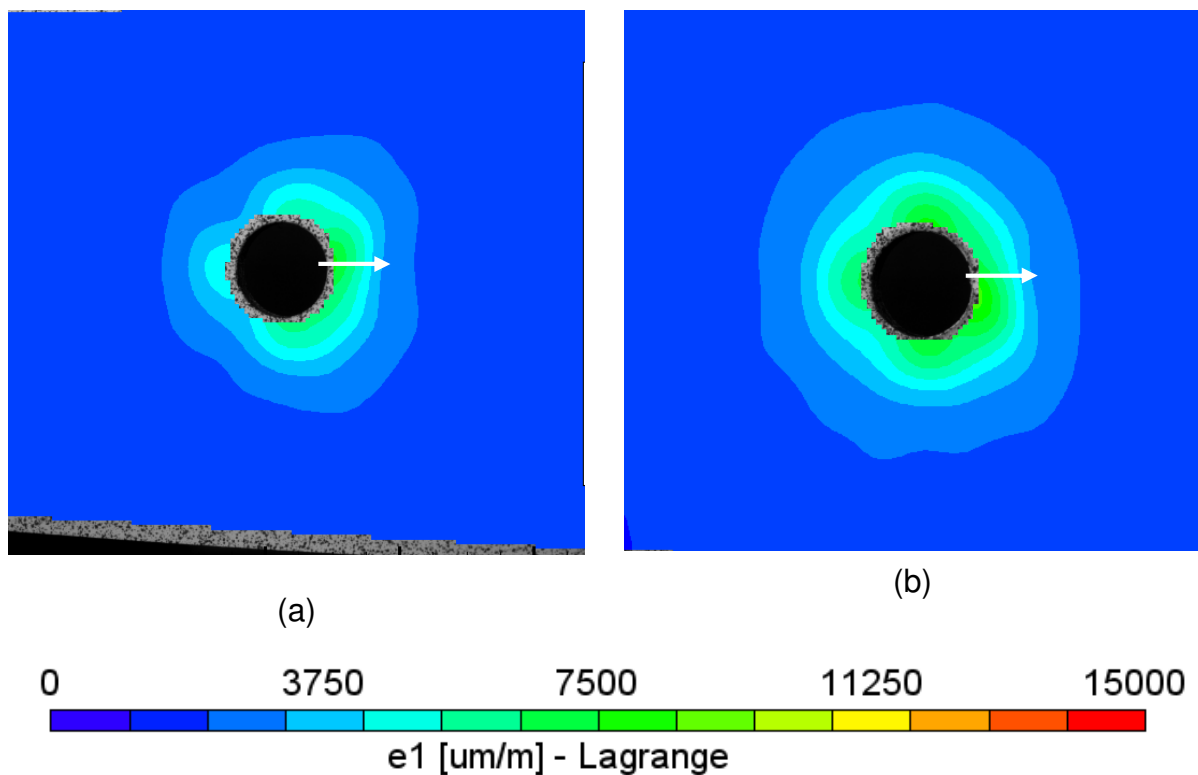
Figure 114: Maximum principal strains for cold expanded FML 4 [-45/90/+45] (specimen 17-C-7) on the (a) entry face and (b) exit face

(a)   (b)

0   -10000   -20000   -30000   -40000

e2 [um/m] - Lagrange
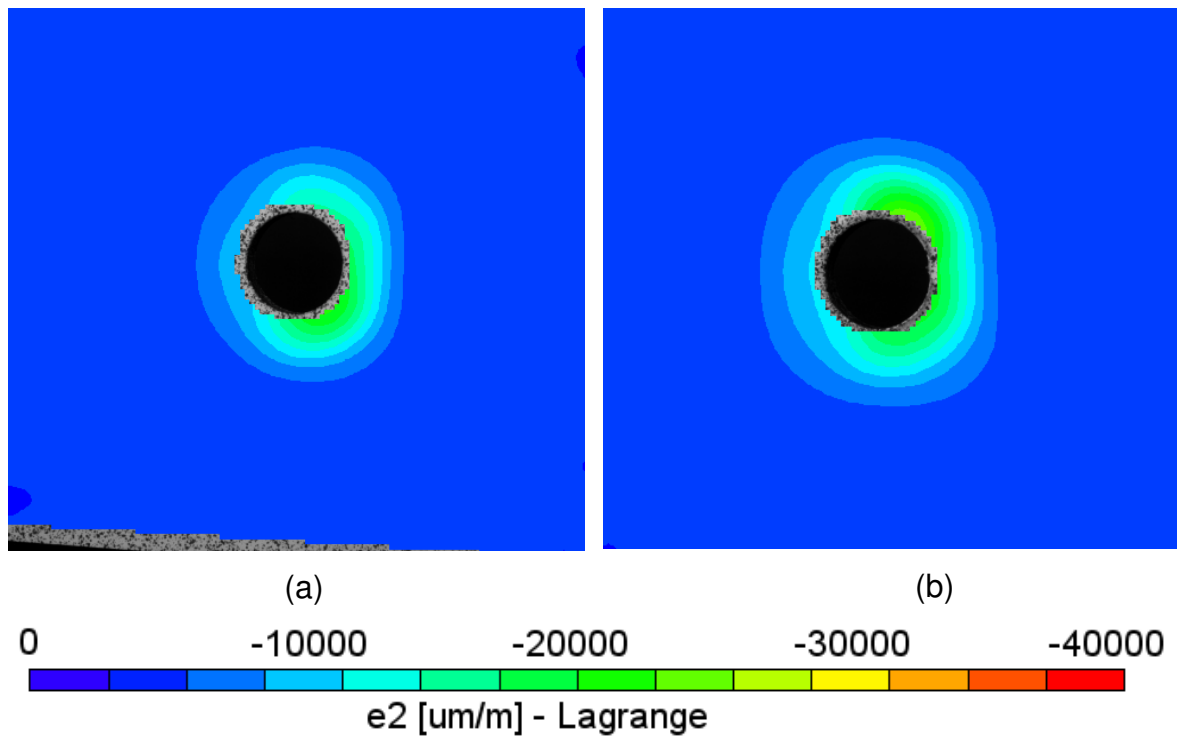
Figure 115: Minimum principal strains for cold expanded FML 4 [-45/90/+45] (specimen 17-C-7) on the (a) entry face and (b) exit face
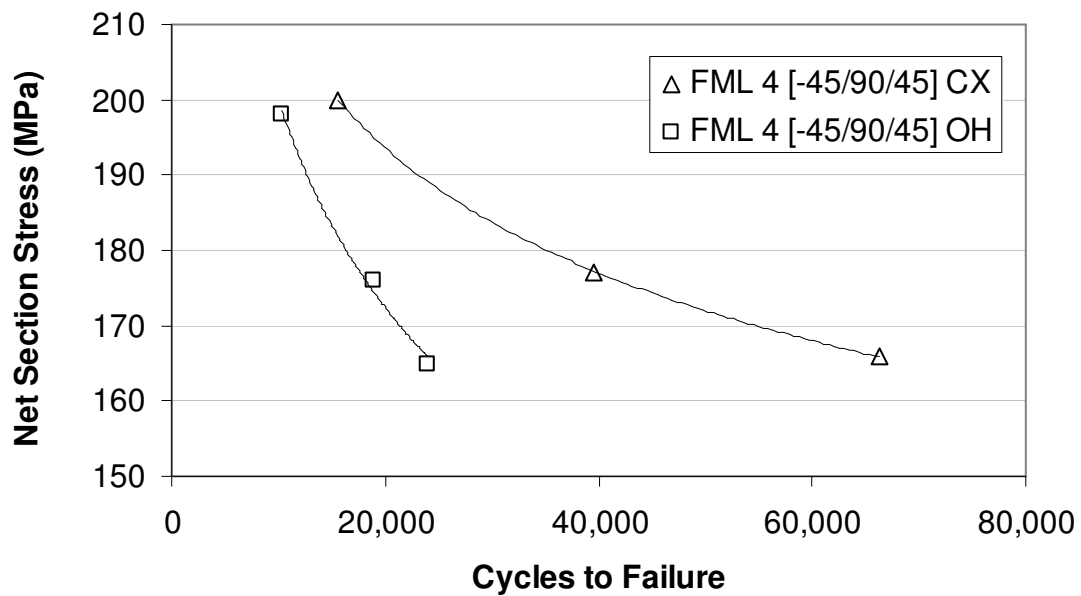
Figure 116: Mean fatigue results for FML 4 [-45/90/45] coupons both with and without cold-expansion of the hole

9.1.1.2 Static and Fatigue Behaviour of FML 4 [-30/0/+30]

The maximum principal strain results for FML 4 [-30/0/+30] after cold expansion are shown in Figure 117 and also show a more concentric strain field than FML 4 [0/90/0], with only a small amount of asymmetry. The minimum principal strain results (Figure 118) are even more concentric and even the fatigue results in Figure 119 show reasonable fatigue performance for coupons cut in the longitudinal (0º degree) material orientation. However, the closed form solution shows that the elastic modulus drops monotonically between the 0º degree and 90º degree direction and in the 90º degree direction is even lower than in FML 4 [-45/90/45], suggesting that the corresponding fatigue life would be lower as well.

(a)   (b)
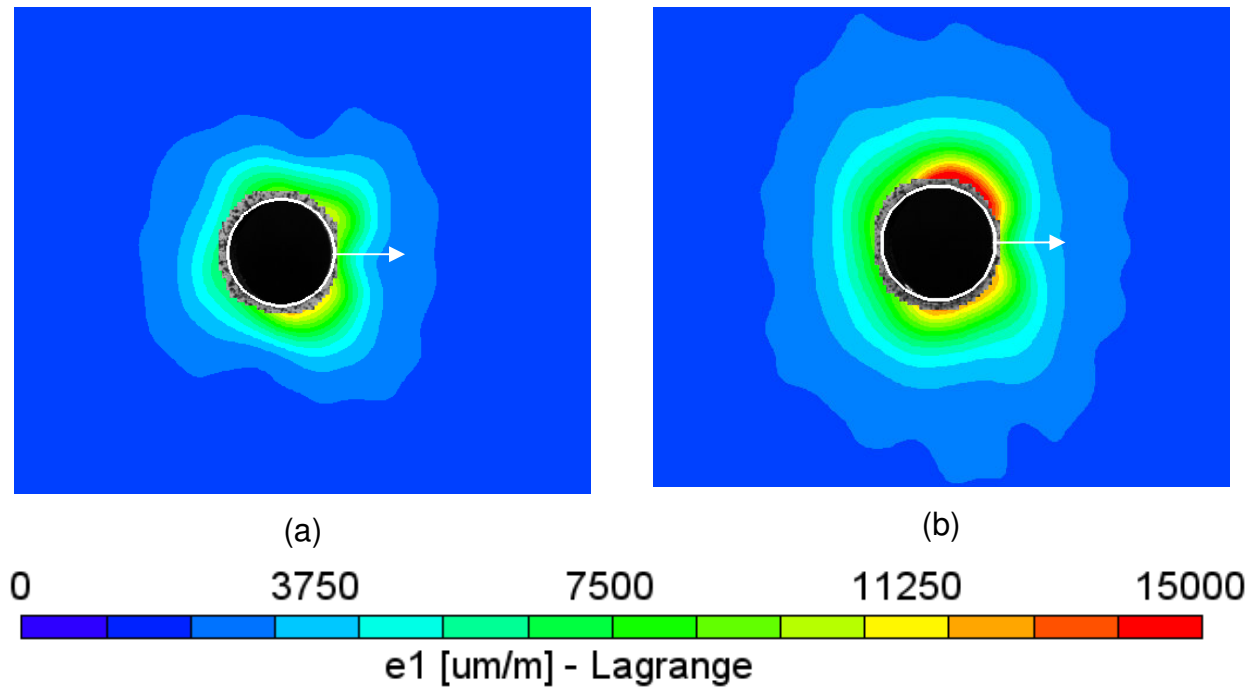
Figure 117: Maximum principal strains for cold expanded FML 4 [-30/0/+30] (specimen 18-D-7) on the (a) entry face and (b) exit face
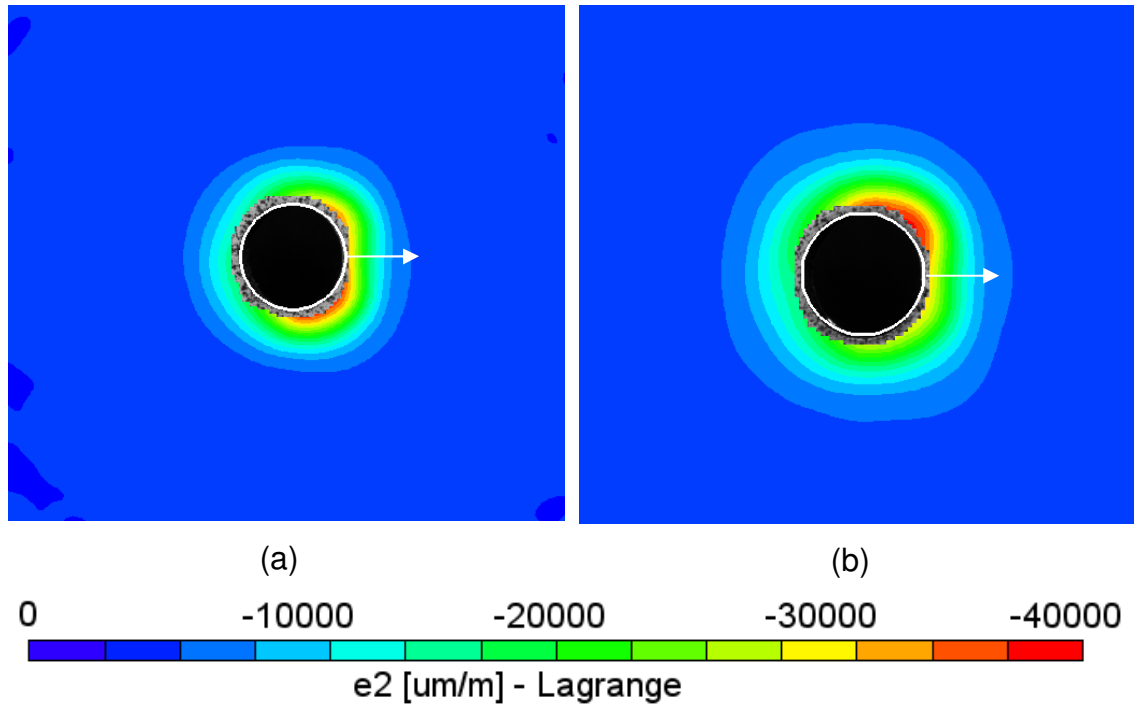
Figure 118: Minimum principal strains for cold expanded FML 4 [-30/0/+30] (specimen 18-D-7) on the (a) entry face and (b) exit face
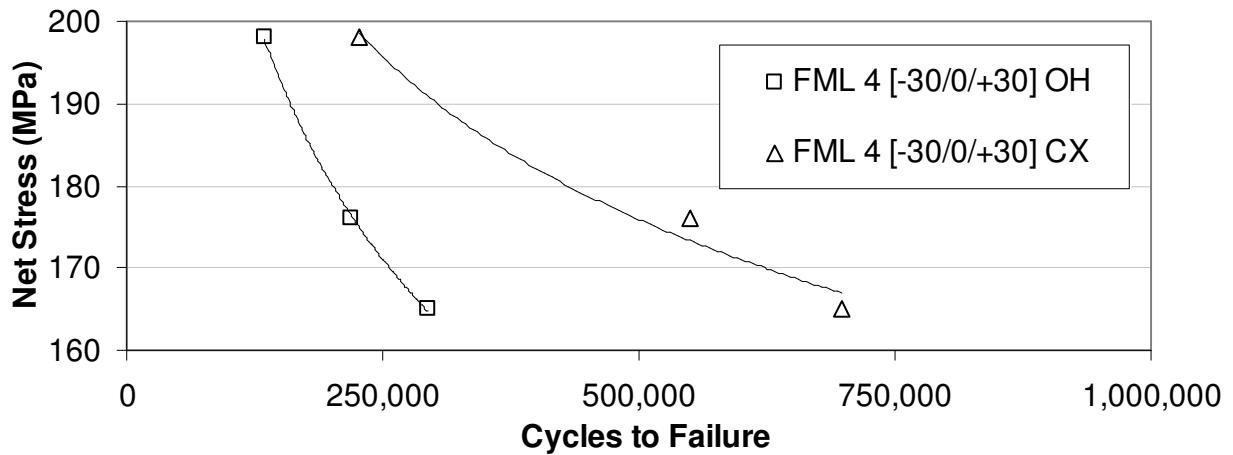
Figure 119: Mean fatigue results for FML 4 [-30/0/+30] coupons both with and without cold-expansion of the hole

9.1.1.3 Static and Fatigue Behaviour of FML 4 [-60/0/+60]

The maximum principal strain results after hole cold expansion for the quasi-isotropic

FML 4 [-60/0/+60] are given in Figure 120 and show a much more uniformly concentric

strain field than FML 4 [0/90/0] . The same is true for the plot of full-field minimum

principal strains (Figure 121), where only a small strain concentration is seen to the right

of both images near the location of the split in the split sleeve. An examination of the

radial strain extraction (Figure 122) shows the typical drop in strain at 270º degrees,

coincident with the location of the split in the split sleeve. Otherwise, there is little

indication of the repeating strain concentrations at 45º degree increments as was seen

with FML 4 [0/90/0] (Figure 47).
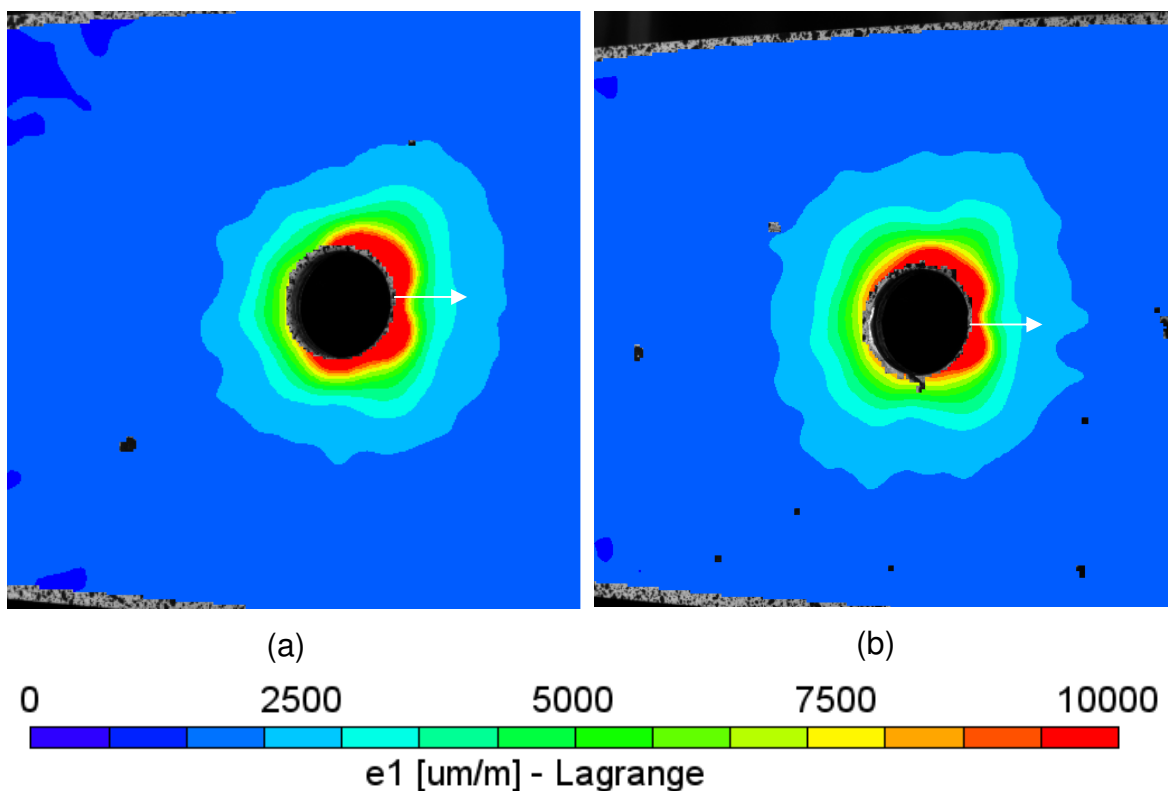
Figure 120: Maximum principal strains for cold expanded FML 4 [-60/0/+60] (specimen 26-D-1-T) on the (a) entry face and (b) exit face
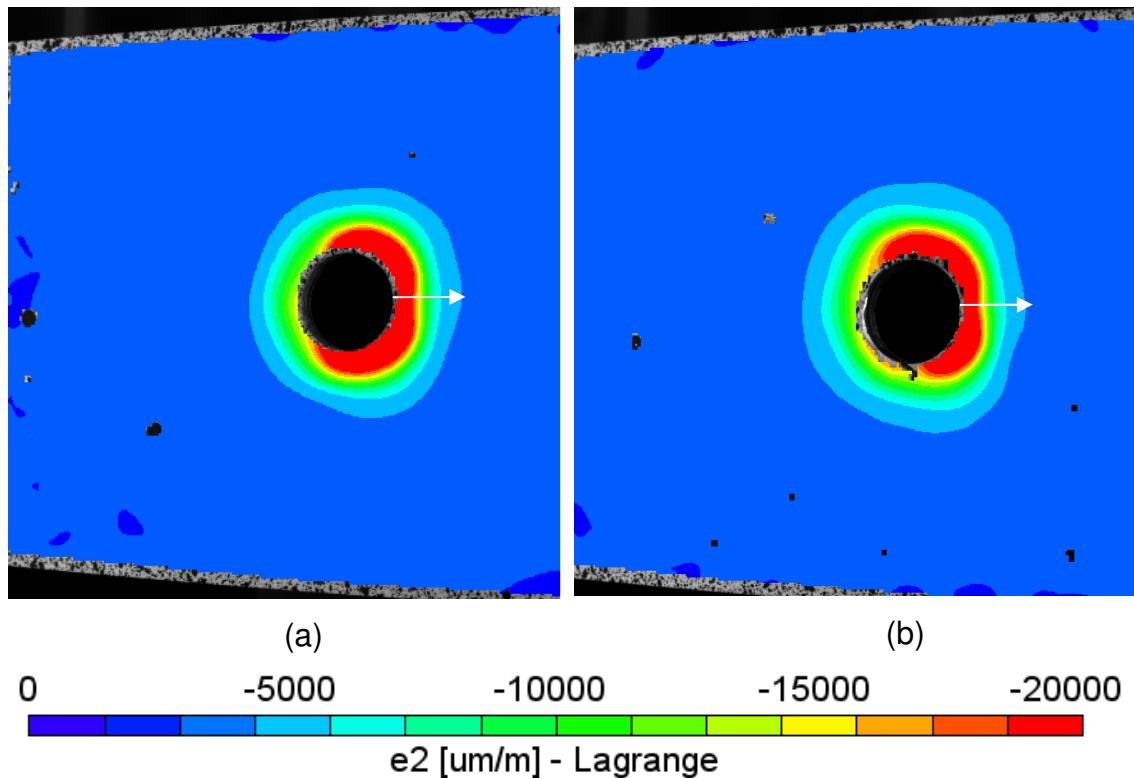
Figure 121: Minimum principal strains for cold expanded FML 4 [-60/0/+60] (specimen 26-D-1-T) on the (a) entry face and (b) exit face

One panel of FML 4 [-60/0/+60] was used to determine the baseline fatigue performance of unexpanded and cold expanded coupons at three net stress levels ranging from 165 MPa to 198 MPa (Figure 123). Overall, fatigue life in the longitudinal direction, for this material was better than for FML 4 [-45/90/45] but not as good as for either FML 4 [0/90/0] or FML 4 [-30/0/+30]. To more fully evaluate the fatigue life of this quasi-isotropic FML 4 [-60/0/+60], it needs to be compared to a baseline grade of FML, such as FML 4 [0/90/0], in all three primary material orientations (longitudinal, 45º degree and transverse). This is because, given the static properties of FML 4 [-60/0/+60], it is expected that the fatigue life should be fairly constant, irrespective of material orientation.
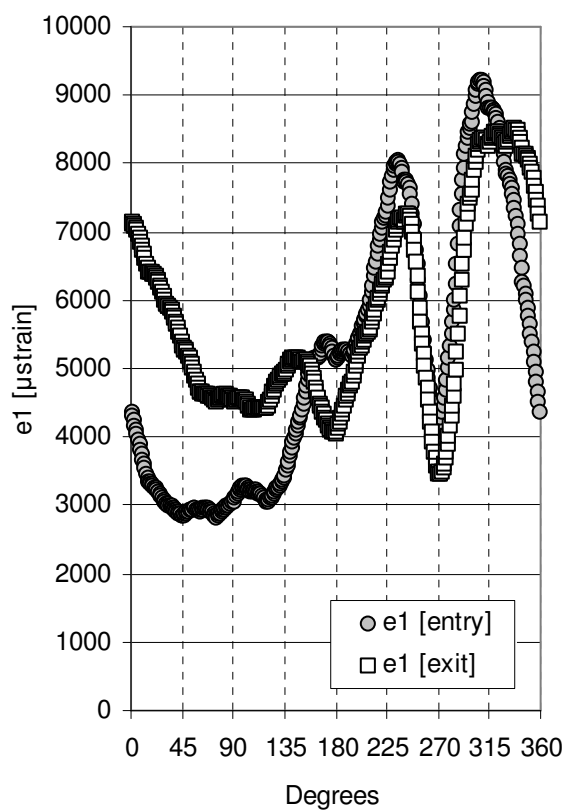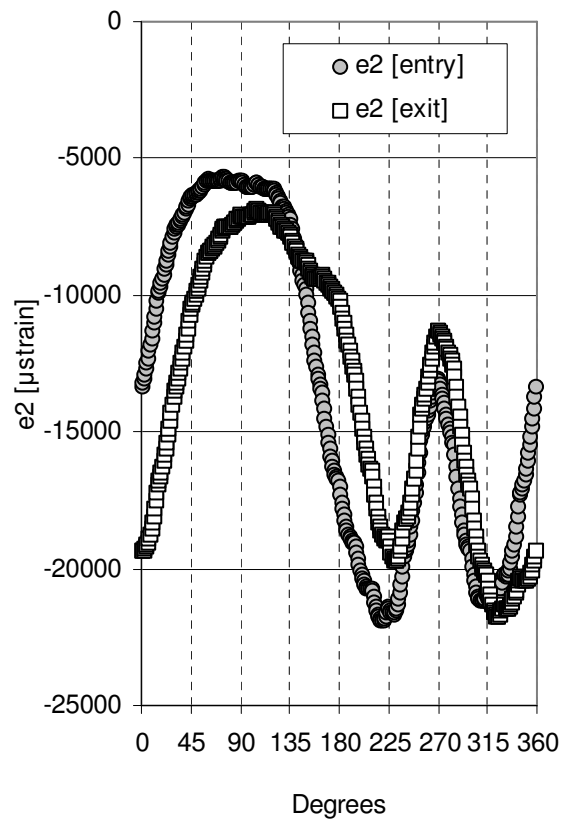
Figure 122: Plot of entry and exit face principal strains for (specimen 26-D-1-T) FML 4 [-60/0/+60] (a) maximum principal strains and (b) minimum principal strains
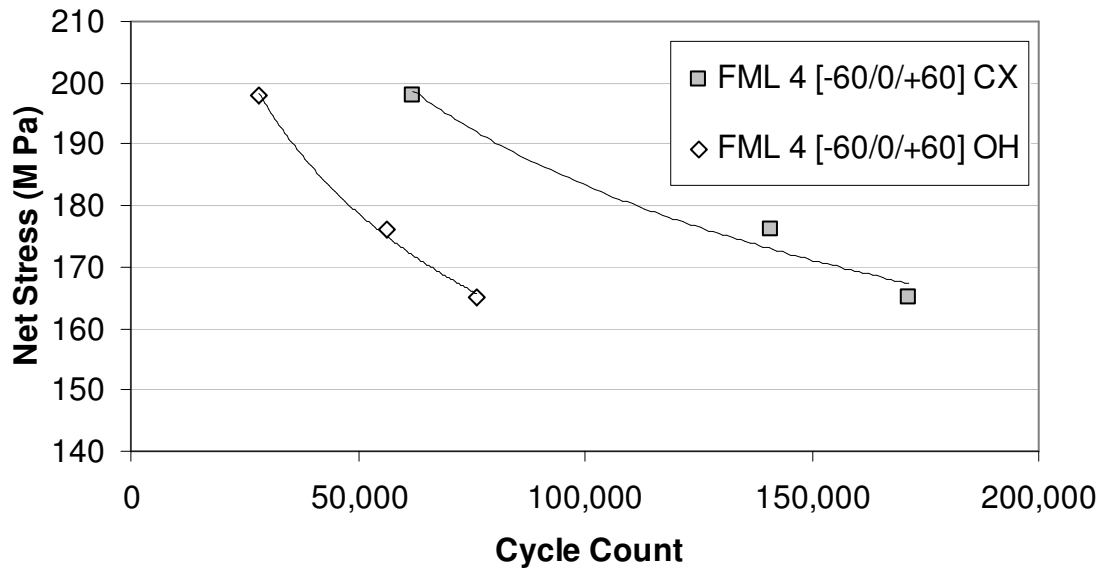
Figure 123: Baseline fatigue data for FML 4 [-60/0/+60]. Comparison between unexpanded and cold expanded coupons

The encouraging initial results with FML 4 [-60/0/+60] led to an additional test to determine the strain field after riveting. The maximum principal strain result from the riveted FML 4 [-60/0/+60] is shown in Figure 124 and qualitatively, appear more uniformly concentric than the strain results from standard grade FML 4 (Figure 69) without the slight undulations in strain at every 45º degree increment as seen with FML 3 and FML 4.
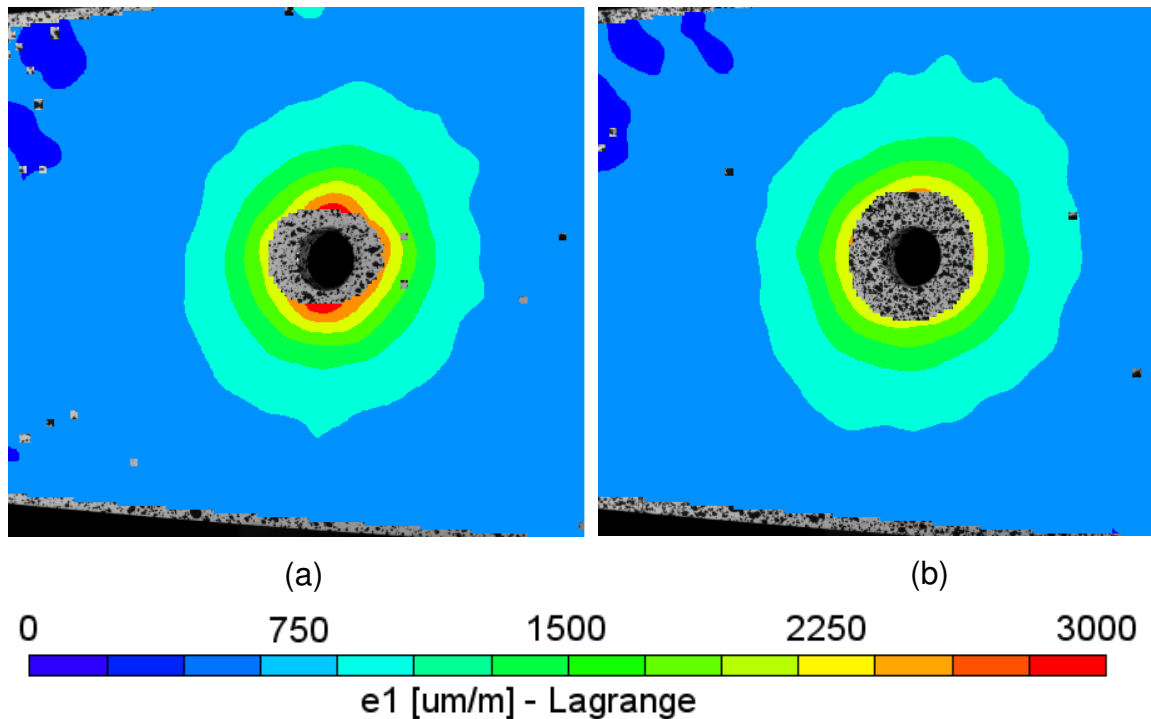
Figure 124: Maximum principal strains due to riveting for FML 4 [-60/0/+60] (specimen 26-D-7-L) coupons (a) driven and (b) manufactured head face

A summary of the fatigue data from all the various FML variants (including FML 4 and FML 3) is provided in Figure 125. This data provides insight into the fatigue performance of the FML coupons in only one orientation, and it is important to consider that fatigue performance in other orientations could be adversely affected by a drop in the elastic modulus. Considering the analytical and experimental results for FML 4 [-45/90/45] and FML 4 [-30/0/30], it was clear that neither of these FML 4 variants completely met our design intent and that the quasi-isotropic FML 4 [-60/0/60] was the best option for additional testing and analysis. Note: from this point on the term FML 4 variant will be used to refer to an FML 4 with a [-60/0/+60] layup unless otherwise specified.
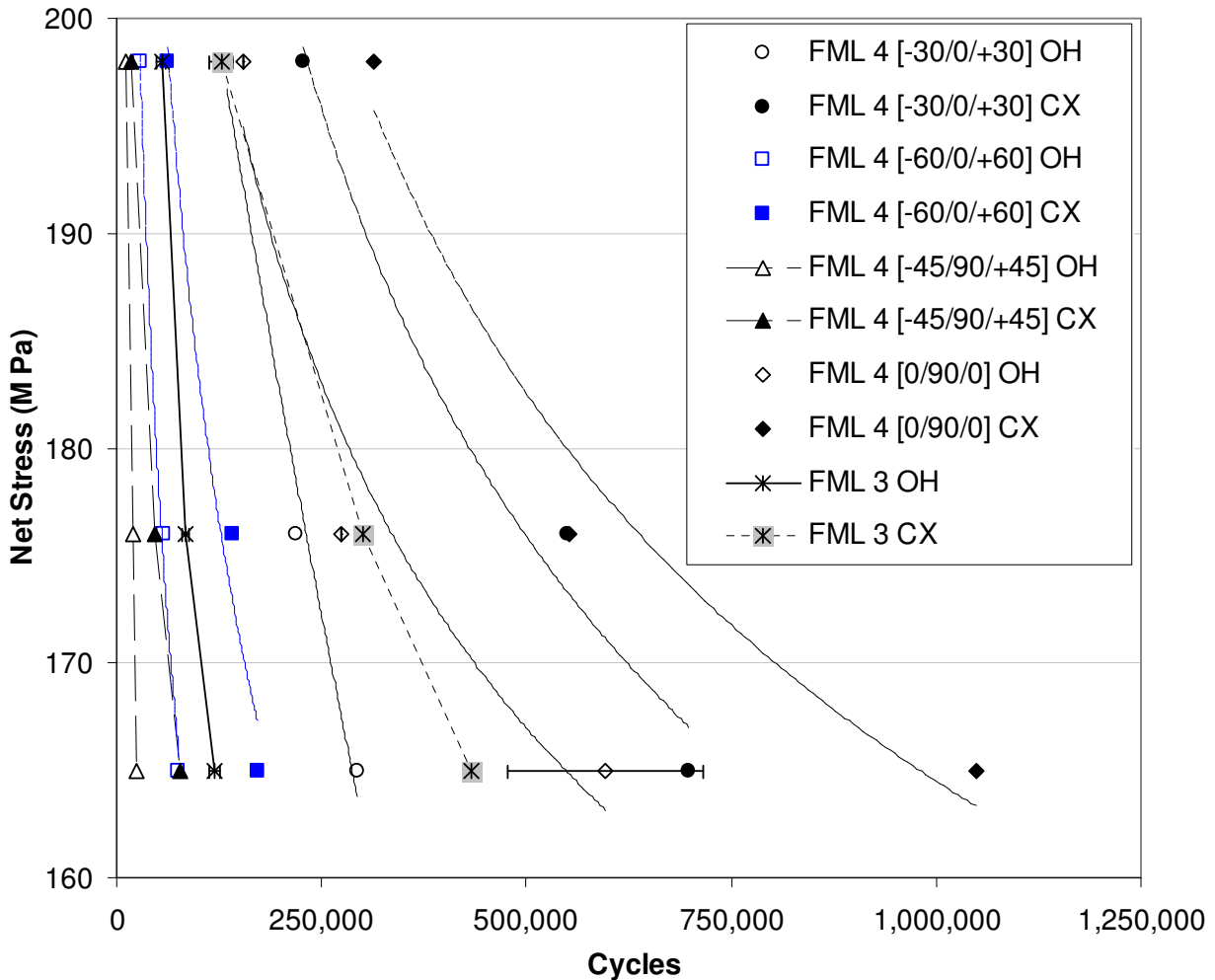
Figure 125: Summary fatigue graph highlighting fatigue performance of all grades of FML tested, both in the open hole and cold expanded configuration. Note: Dotted lines are for visualization purposes only and FML 4 [-60/0/60] is highlighted with blue symbols

9.2   Validation of New Prepreg Batch

For the fatigue testing of the new FML 4 variant, additional FML panels were required

and thus additional FM-94 prepreg had to be procured from the manufacturer. A

rigorous validation procedure was used to ensure that the new prepreg material would

allow for the production of FML panels with similar static and fatigue properties to those

produced previously.

For this portion of the research program several additional FML 4 [90/0/90] panels were produced. Soon after it was discovered that a manufacturing error had occurred early on and that the original FML 4 panels were produced with a [0/90/0] orientation instead of a [90/0/90]. The material properties of these two grades of FML 4 are identical but oriented at 90º degrees to one another. As a result, in addition to verifying the performance of the prepreg, these results also serve to confirm that FML 4 [0/90/0] in the 0º degree orientation (longitudinal) is identical to FML 4 [90/0/90] in the 90º degree (transverse).

A review of the manufacturer's quality certificate from both batches of prepreg showed similar constituent proportions of both matrix and fiber as detailed in Table 13.

Table 13: Summary material information regarding Cytec FM-94

	FM-94 (Old)	FM-94 (new)	% Diff.
Matrix Wt (avg)	255.7 g/m^2	258.9 g/m^2	1.2%
Fiber Wt (avg)	186.2 g/m^2	188.9 g/m^2	1.4%

Although no static strength data existed for the initial FML 4 [0/90/0] panels, test data from a previous experimental program[11] was obtained which provided comprehensive elastic modulus and yield strength data for FML 4 in orientations ranging from 0º degrees to 90º in 15º increments. Separate plots were prepared for the elastic modulus measurements (Figure 126), combining data from the previous FML 4 coupons (old prepreg) with data from the new FML 4 (new prepreg) and in the case of the elastic

modulus, overlaid with predictions from classical laminated plate theory. Comparison

between FML 4 [90/0/90] made with the new batch of FM-94 prepreg and the previous

batch of FM-94 showed little difference in the elastic modulus results, with a maximum

difference of less than 5% for FML 4 in the 90º orientation.
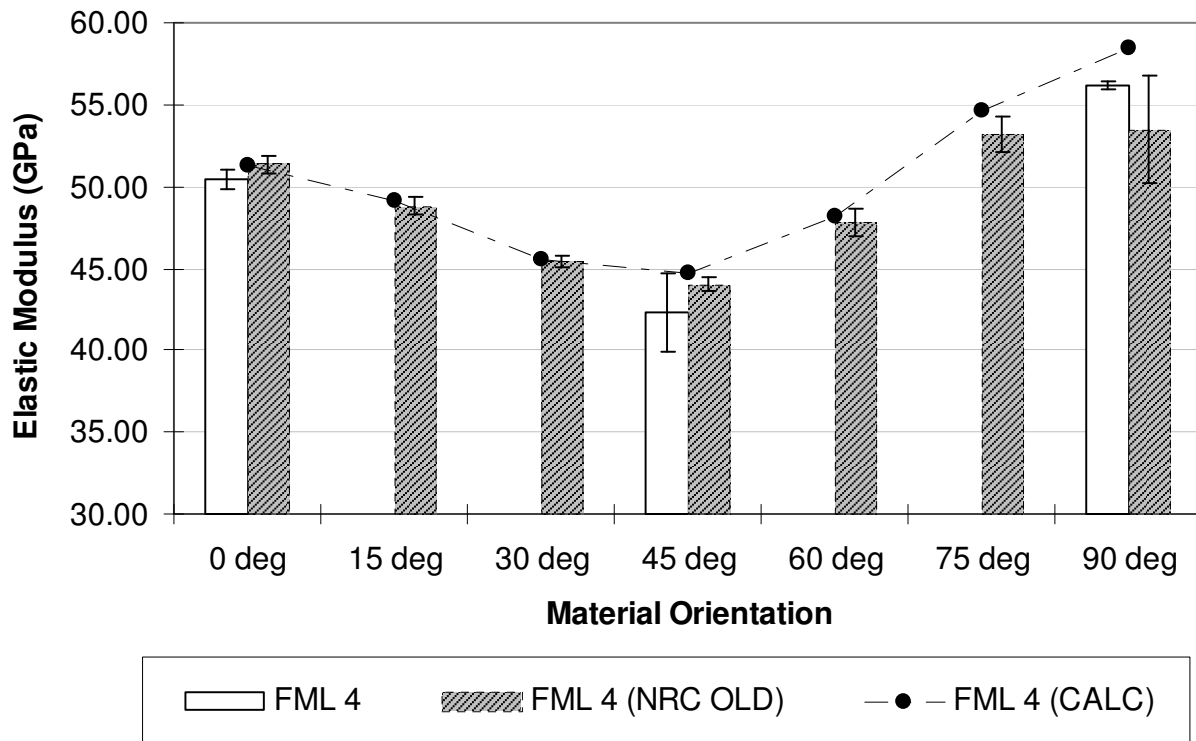
Figure 126: Experimentally determined elastic modulus for current FML 4 [90/0/90] with new prepreg and FML 4 [90/0/90] made from old prepreg[11] with analytical results. Note: Dotted line for visualization purposes only

Several baseline fatigue tests were carried out at a net section stress of 198 MPa on

FML 4 [90/0/90] coupons made with the new prepreg material. A small sample size

(n=2) of coupons were tested with both unexpanded and cold expanded holes and the

information from the test was compared to the FML 4 (old prepreg) results from

Chapter 8.0. Ultrasonic inspection of both sets of coupons allowed the total disbond

area to be measured (Figure 127) and showed no significant difference between FML 4 (new prepreg) and FML 4 (old prepreg) coupons on the basis of the disbond measurements.
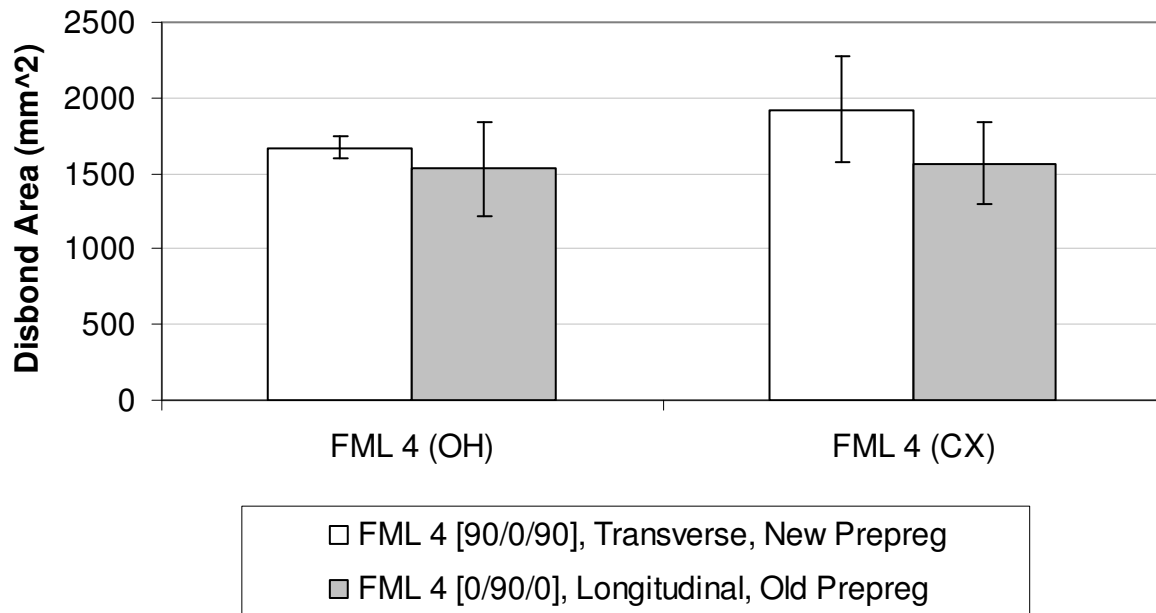
Figure 127: Disbond measurements for FML 4 made with old and new prepreg

Crack growth rates were also compared between the coupons made with the two batches of prepreg, and crack growth curves for the unexpanded (Figure 128a) and cold expanded (Figure 128b) coupons showed very similar trends.
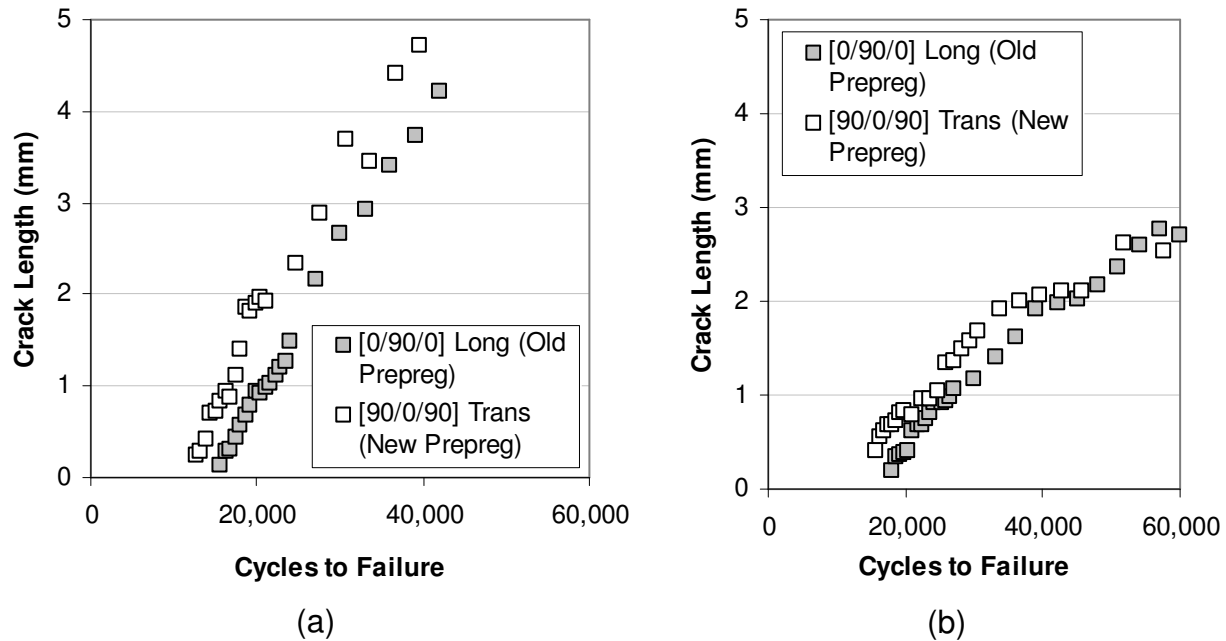
Figure 128: Comparison between old and new batches of prepreg (a) in FML 4 unexpanded coupons and (b) in FML 4 cold expanded coupons

The elastic modulus estimated from classical laminated plate theory also appeared to be a reasonable match for the experimental data thus suggesting that variables such as volume fraction of glass fiber and glass fiber mechanical properties have remained constant between prepreg batches. With the fatigue results showing that both prepreg batches produced FML coupons with similar fatigue lives, two overall conclusions were reached: first, the two batches of prepreg were identical and produced FML 4 with similar properties and second, FML 4 [0/90/0] and FML 4 [90/0/90] have identical mechanical properties at 90º degrees to one another.

9.2.1 Manufacture of a New FML 4 Variant

Building the new quasi-isotropic FML 4 [-60/0/+60] variant encompassed the same basic steps as building standard FML 3 and FML 4. The phosphoric anodized aluminum sheets were sheared to 305 mm x 305 mm (12 inches x 12 inches) and set aside. A special template was designed and built to allow for easy and accurate cutting

223

of the 60º degree prepreg plies (Figure 129). The combined [-60/0/+60] plies were

debulked separately and then layered between the aluminum sheets before being

debulked again. The final FML panels were then vacuum bagged and readied for the

autoclave. After this, all panels were inspected ultrasonically before being sent for

waterjet cutting and then finally milled to their final size.
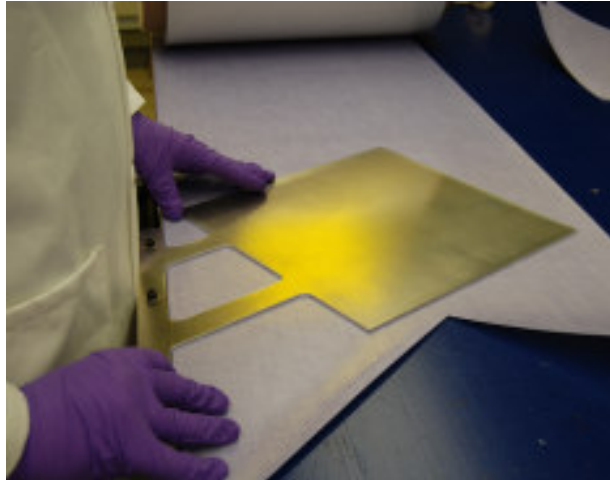
Figure 129: Template tool for cutting precise 60º plies

9.3   Static Strength of FML 4 Variant

Static strength tests were performed on n=2 FML 4 [90/0/90] and n=2 FML 4 variant

[-60/0/60] coupons in the longitudinal, transverse and 45º direction to determine the

actual variation in elastic modulus with coupon orientation. The analytical results

corroborated well with the experimental findings (Figure 130), with less than 1.5% error

for the FML 4 variant results and less than 3% error for the FML 4 results.
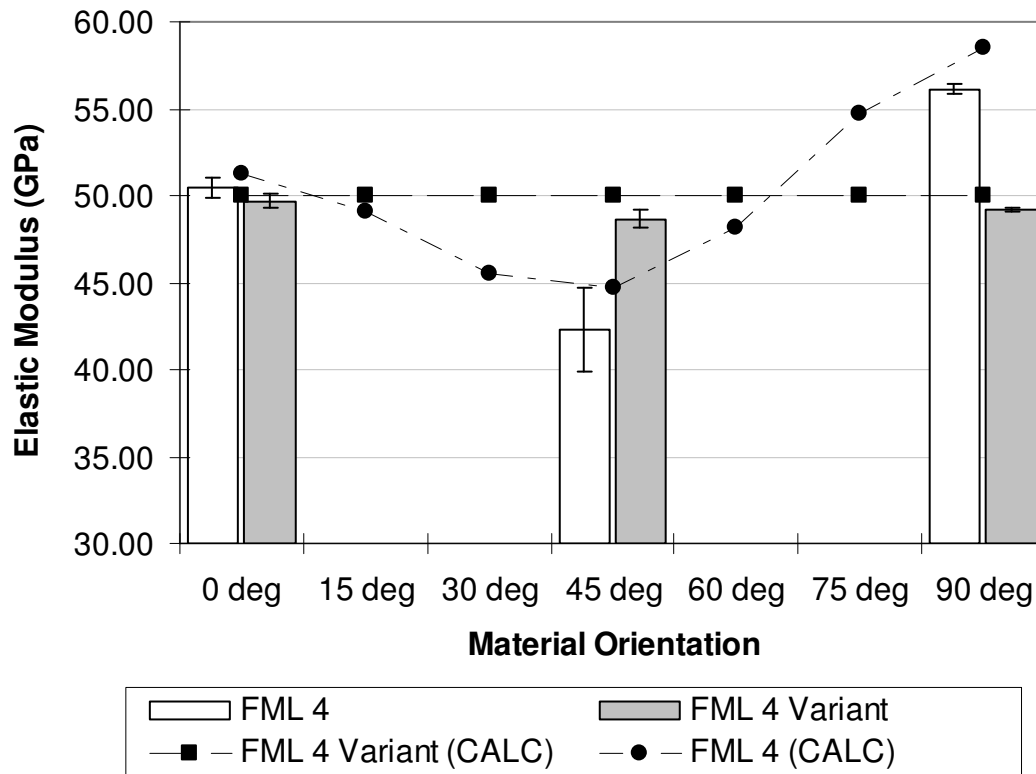
Figure 130: Elastic modulus for FML 4 [90/0/90] and FML 4 [-60/0/60] measured from static failure tests (columns) combined with results from elastic modulus calculated using classical laminated plate theory (symbols). Note: Dotted line for visualization purposes only

Yield stress for the material was calculated from the stress-strain curves using the 0.2%

offset methodology and the results for FML 4 [90/0/90] and the new FML 4 variant are

shown in Figure 131.
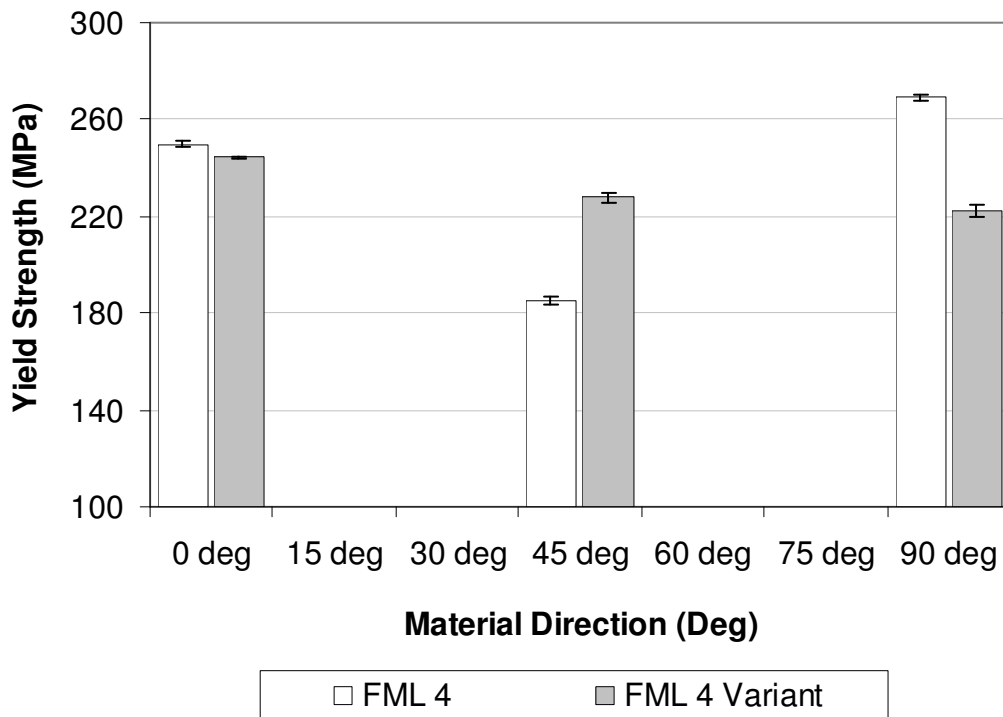
Figure 131: Yield strength plotted against laminate direction for FML 4 [90/0/90] and FML 4 variant [-60/0/60]

10.0   FATIGUE TESTING AND RESIDUAL STRENGTH OF FML 4 [-60/0/60]

The static strength tests (Figure 130) showed that the in-plane elastic modulus of the new FML 4 variant was independent of material orientation. The resultant strain field after cold expansion and riveting was more uniform than with other grades of FML, and appeared to more closely resemble that of monolithic aluminum. Based on these results it was expected that the new FML 4 variant would have a fairly constant fatigue life irrespective of material orientation, both in the unexpanded and cold expanded configuration.

For this phase of fatigue testing, additional panels of FML 4 [90/0/90] and FML 4 variant [-60/0/60] were produced.   The cut plan for the coupons was modified (Figure 29) to allow n=2 coupons to be produced in the longitudinal, transverse and 45º degree directions respectively. With the reduced number of coupons per panel, fatigue testing of the new FML 4 variant was focused on only one stress level (198 MPa) and two conditions: unexpanded and cold-expanded open hole. The hole diameter after cold expansion and reaming was measured using a ball gauge and the applied load was reduced in order to ensure that both the unexpanded and cold expanded coupons had a net stress of 198 MPa.

Although all the FML coupons in this phase of testing were fatigued until a displacement limit of 0.89 mm, fatigue life comparisons for the unexpanded and cold-expanded FML 4 [90/0/90] and the FML 4 variant, were based on the number of cycles to a crack size of 3.7mm as this provided a basis of comparison that was less affected by changes

in modulus. The riveted coupons, due to their distributed crack growth, used a displacement limit of 0.89 mm as the basis for determining their fatigue life. Residual strength testing was then performed on several coupons after the completion of the fatigue testing.

10.1 FML 4 and FML 4 Variant Overall Fatigue Results

The fatigue testing was designed to determine the off-axis fatigue performance of both FML 4 [90/0/90] and the new FML 4 variant. Although transversely oriented FML 4 [90/0/90] coupons had over twice the life of transversely oriented FML 4 variant coupons (Figure 132), the FML 4 variant coupons tested in the longitudinal and 45° degree orientation showed an improvement in fatigue life over FML 4 [90/0/90] and both grades of FML 4 showed an improvement in fatigue life as a result of cold expansion.
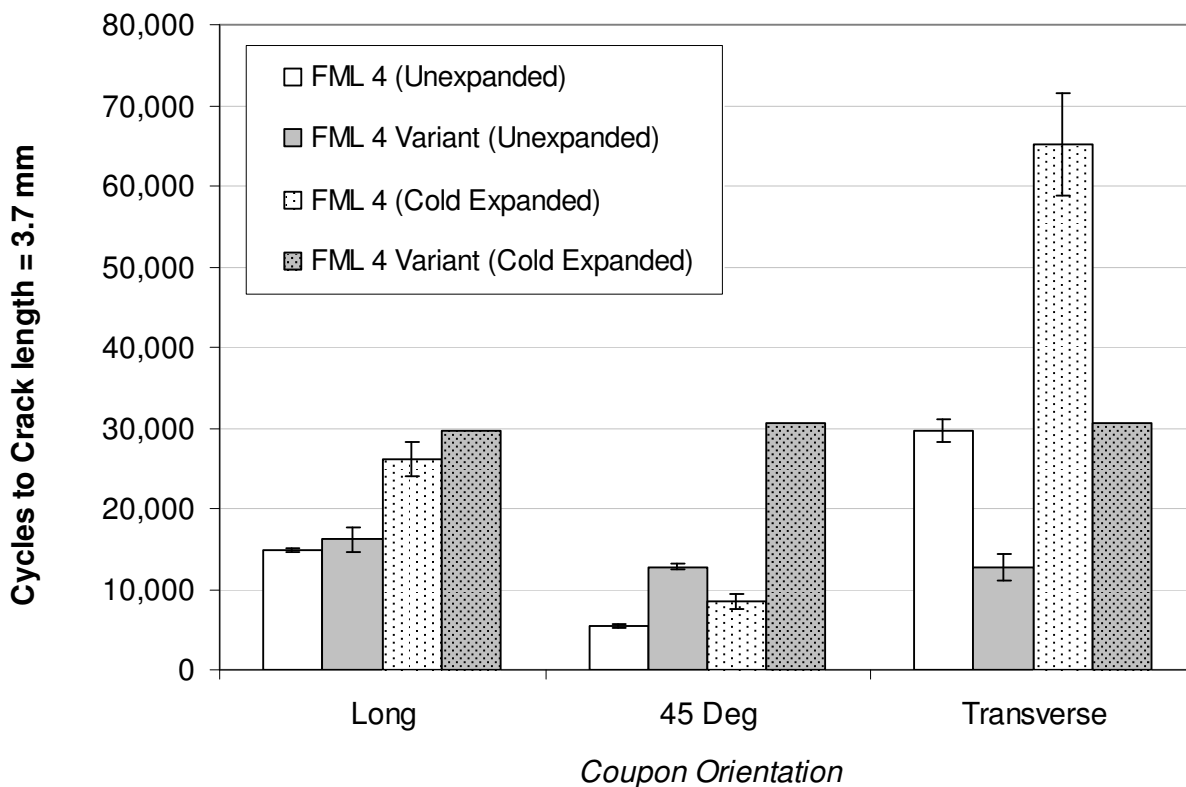
Figure 132: Fatigue results for unexpanded and cold expanded FML 4 and FML 4 variant tested at a net stress of 198 MPa

For the riveted FML 4 variant coupons, a significant increase in fatigue life was seen when compared to that of an unexpanded or cold expanded coupon (Figure 133).
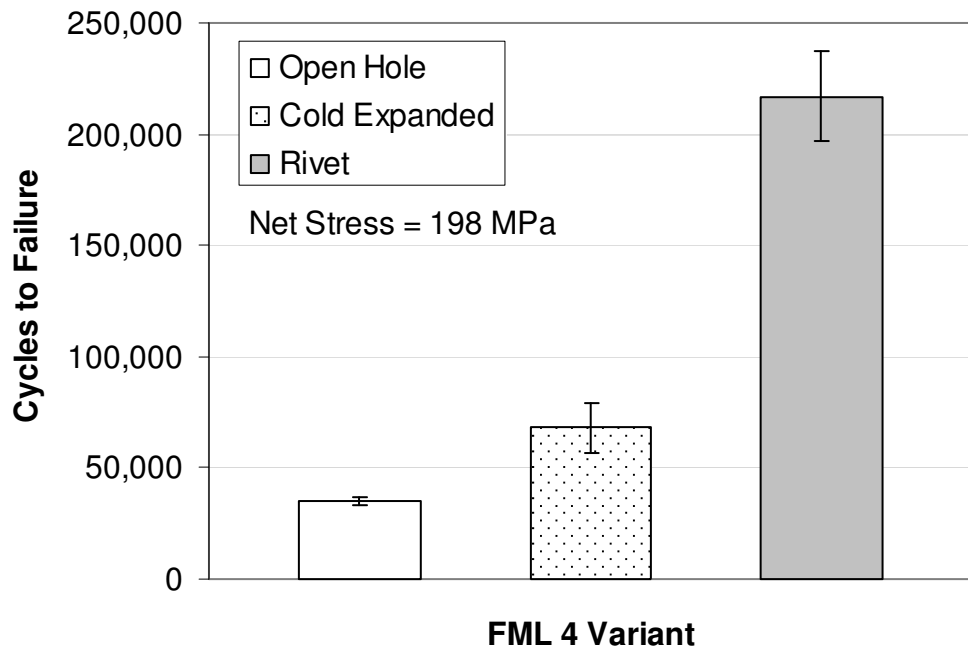
Figure 133: Comparison of fatigue results for FML 4 variant (longitudinal) showing cycles to failure of open hole, cold expanded and riveted coupons tested at a net stress of 198 MPa

Individual crack growth curves from both grades of FML were analyzed with and without cold expansion to determine the number of cycles required to grow a 1 mm crack, as well as the crack propagation rate (da/dN). The results for standard FML 4 [90/0/90] are provided in Figure 134 and the results for the new FML 4 variant are provided in Figure 135. The results for FML 4 [90/0/90] in the transverse orientation are, as expected, similar to those of FML 4 [0/90/0] in the longitudinal direction, as seen in the first round of fatigue testing (Figure 99). Since FML 4 [90/0/90] has a lower modulus in the longitudinal and 45º degree orientations, crack growth rates are significantly higher when compared to found in the transverse direction; however, cold expansion is still effective at reducing crack growth rates. Cold expansion appears minimally effective at

retarding short crack growth (crack growth to 1 mm), with retardation of no greater than 5,000 cycles on average. The same analysis performed for all the FML 4 variant coupons showed more constant crack propagation rates (da/dN) in all material orientations, and a fairly uniform decrease in crack propagation rates (da/dN) after cold expansion. As with the FML 4 [90/0/90] coupons, the effect of cold expansion on short crack growth was fairly minimal with crack growth being retarded by no more than 6,500 cycles on average.

The overall conclusions from this more comprehensive data set are similar to what was concluded earlier; cold expansion is effective at reducing crack propagation rates in FML, in all material orientations, but is only minimally effective at retarding short crack growth on the entry face.
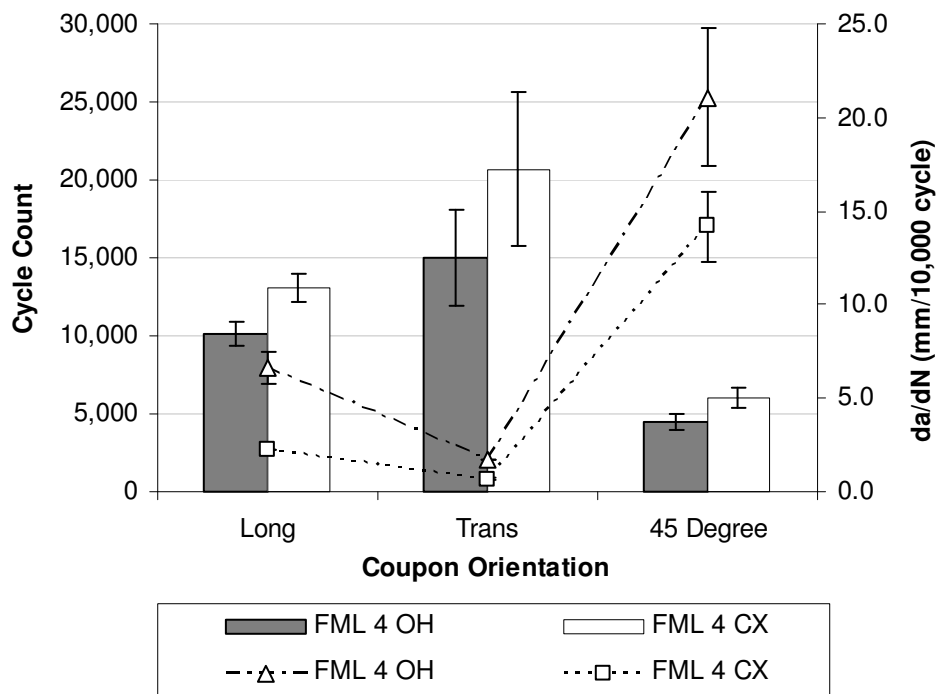
Figure 134: Variation in number of cycles to 1 mm crack length (columns) versus da/dN (symbols) for FML 4 in various material orientations
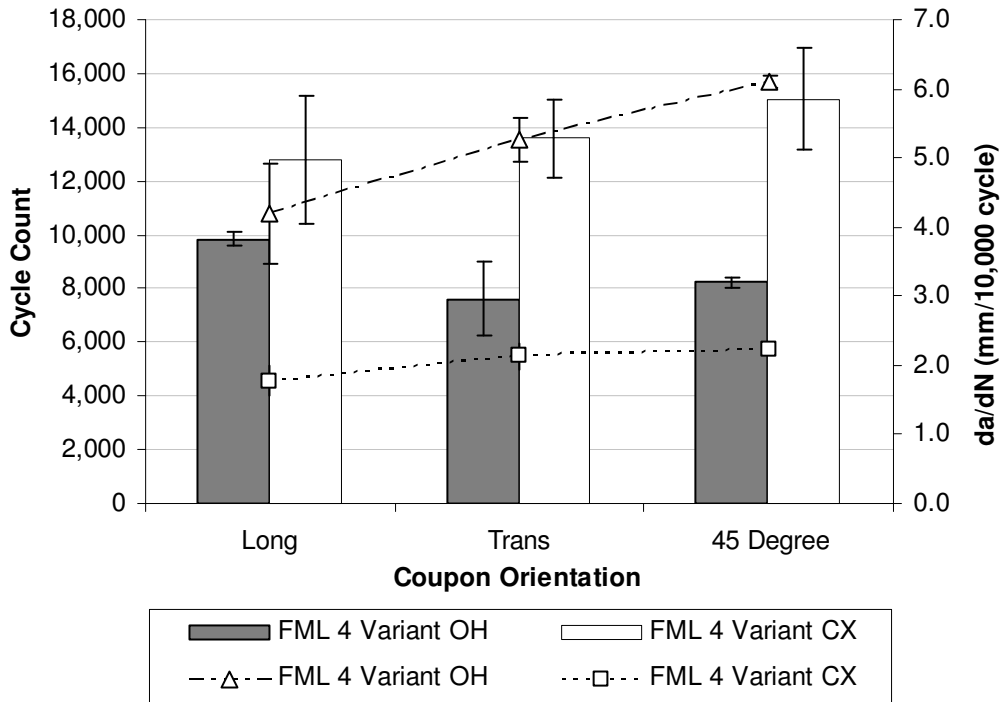
Figure 135: Variation in number of cycles to 1 mm crack length (columns) versus da/dN (symbols) for the FML 4 variant in various material orientations

10.2 Residual Strength Results

Since the end of fatigue cycling for all FML coupons was defined on a compliance basis, meaning that fatigue cycling was stopped when coupon displacement reached 0.89 mm (0.035 in), all FML coupons were left with a certain degree of residual strength. In order to quantify the degree of residual strength each "failed" FML coupon was submitted to a uniaxial tensile test to failure, at a pseudo-static loading rate of 0.025 mm/sec (0.001 in/sec). The data for FML 3 only includes data in the longitudinal direction, while the data for FML 4 [90/0/90] and the new FML 4 variant includes data for all three material orientations. An initial review of the results, segregated according to net stress as well as condition (i.e unexpanded or cold-expanded), did not show a noticeable effect from either factor, but the sample size was too small to draw a definitive conclusion. Since elastic modulus was a function of material orientation, the decision

was made to separate the coupons on the basis of material orientation but aggregate them across net stress and condition thus allowing for a minimum of n=5 specimens in each group. By measuring the initial gauge length of the coupon and calculating the cross-sectional area through the central hole, the force and displacement data from the servohydraulic testing machine could be converted into stress and strain. This conversion allowed for the residual elastic modulus (Figure 136) as well as the peak load at failure (Figure 137) to be estimated.

The classical laminated plate (CLP) solution for the elastic modulus was modified in an attempt to predict the residual elastic modulus of the fatigued coupons. By reducing the modulus of the aluminum sheets, it was possible to determine the effective modulus with varying contributions from the aluminum layer. Two scenarios were attempted, in the first, all aluminum layers had their elastic modulus reduced to near zero. In the second, only the outermost aluminum layers had their elastic modulus reduced. This second scenario provided results that best fit the experimental findings and suggested that in the majority of cases, the edge to edge cracking seen on the entry and exit face was not present on the inner aluminum layer. Since the closed form solution does not take into account fiber damage or breakage, it was assumed that the modulus derived from the CLP solution would form an upper bound on the experimental values. It was interesting to note that for this was essentially true for coupons in the longitudinal and transverse direction, but not for coupons in the 45º degree direction. One possible explanation is that although a complete surface crack was evident in the 45º degree coupons, nearest to the hole, the outermost aluminum layers nearest to the outer edges

may not have cracked completely through and may have actually retained some residual strength. The closed form model showed that if the entry/exit aluminum layers retained even 40% of their elastic modulus it would explain these results for the 45º degree coupons. This phenomenon may have been biased to the 45º degree coupons since FML 4 has the lowest modulus in this orientation and would be more likely to displace enough to meet the 0.89 mm displacement limit as the surface cracks in the outermost aluminum layers propagated towards the edge of the coupon.
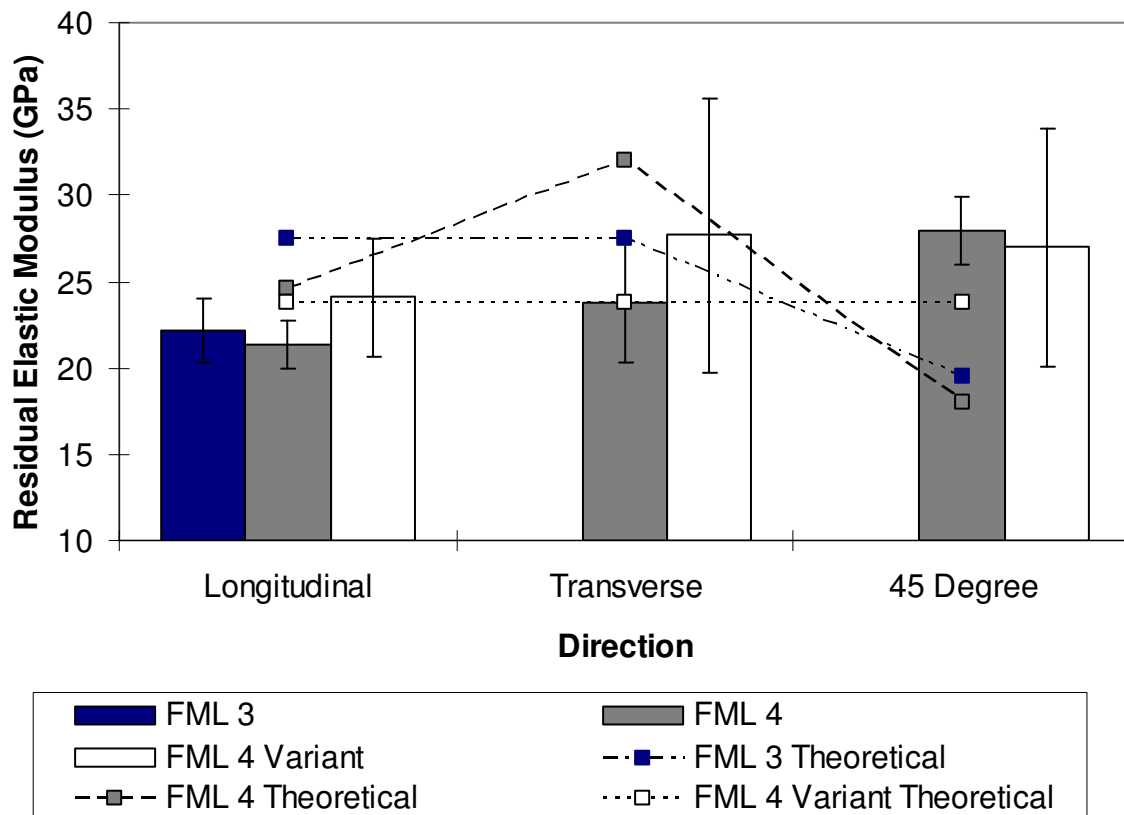
Figure 136: Residual elastic modulus for FML 3, FML 4 [90/0/90] and FML 4 variant coupons after fatigue failure. Note: Analytical results overlaid with dotted lines for visualization purposes only
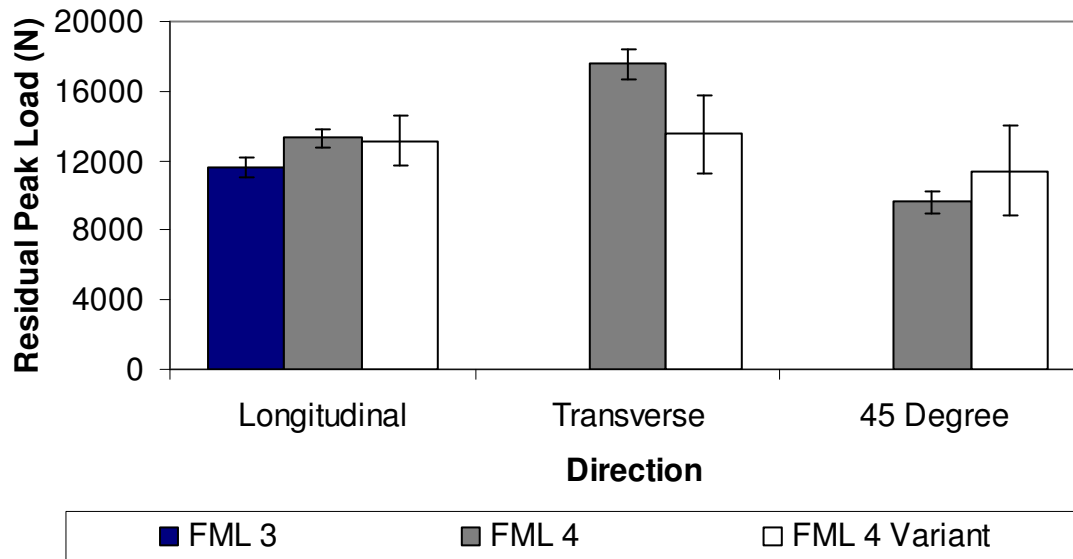
Figure 137: Residual peak load for FML 3, FML 4 [90/0/90] and FML 4 variant coupons after fatigue failure

10.3 FML 4: DIC and TSA Measurements

10.3.1 FML 4: Unexpanded Coupons

Maximum principal strain measurements from DIC are provided for the entry face of the FML 4 unexpanded coupons in Figure 138. Strain measurements are provided for coupons in all three material orientations (longitudinal, transverse and 45° degree) in both pre-crack and cracked conditions. A small variation is seen among the pre-cracked FML 4 coupons (Figure 138a,e,i), but this is to be expected given the difference in elastic modulus between the three material directions. This difference becomes more noticeable as the crack length increases, with the difference being the most striking for a crack length of 3.7 mm (Figure 138d,h,l). At this crack length the coupon in the transverse direction (which has the highest modulus) shows the lowest crack tip strains, while the longitudinal coupon has slightly higher crack tip strains, and the 45° degree coupon has the highest crack tip strains, with the strain field extending out at angles of

45º degrees from the horizontal crack tip, in line with the longitudinal and transverse orientations of the material.

The TSA images provide a corresponding view of the strain field on the exit surface of the coupon. Comparing the precrack images from coupons in all three material orientations (Figure 139a,e,i) to those at 1 mm of crack growth on the entry face (Figure 139b,f,j), little evidence of crack growth is seen. At 2 mm of crack growth on the entry face, both the longitudinal and the 45º degree coupon show movement of the TSA signal at the crack tip, away from the left side of the hole, clearly indicative of crack growth (Figure 139c,k). The transverse coupon shows a change in magnitude and shape of the TSA signal, which is indicative of a smaller crack forming in the same location. At 3.7 mm of crack growth on the entry surface, TSA images from the longitudinal and 45º degree coupon both show signs of bilateral crack growth (Figure 139d,l). The transversely oriented coupon shows clear signs of crack growth on the left hand side of the hole, and a change in magnitude and shape of the TSA signal on the right hand side, indicative of the formation of a smaller crack in this area (Figure 139h).

Overall the results for the unexpanded hole show that crack growth on the exit face lags only slightly behind that seen on the entry face of the coupon, behaviour that corresponds to that seen with the previous batch of fatigue coupons.

	Longitudinal	Transverse	45º Degree
Pre-Crack	(a) 0 cycles	(e) 0 cycles	(i) 0 cycles
1.0 mm crack	(b) 10,300 cycles	(f) 16,900 cycle	(j) 4,300 cycles
2.0 mm crack	(c) 12,100 cycles	(g) 21,100 cycles	(k) 4,900 cycles
3.7 mm crack	(d) 14,500 cycles	(h) 30,700 cycles	(l) 5,500 cycles

e1 [um/m] - Lagrange
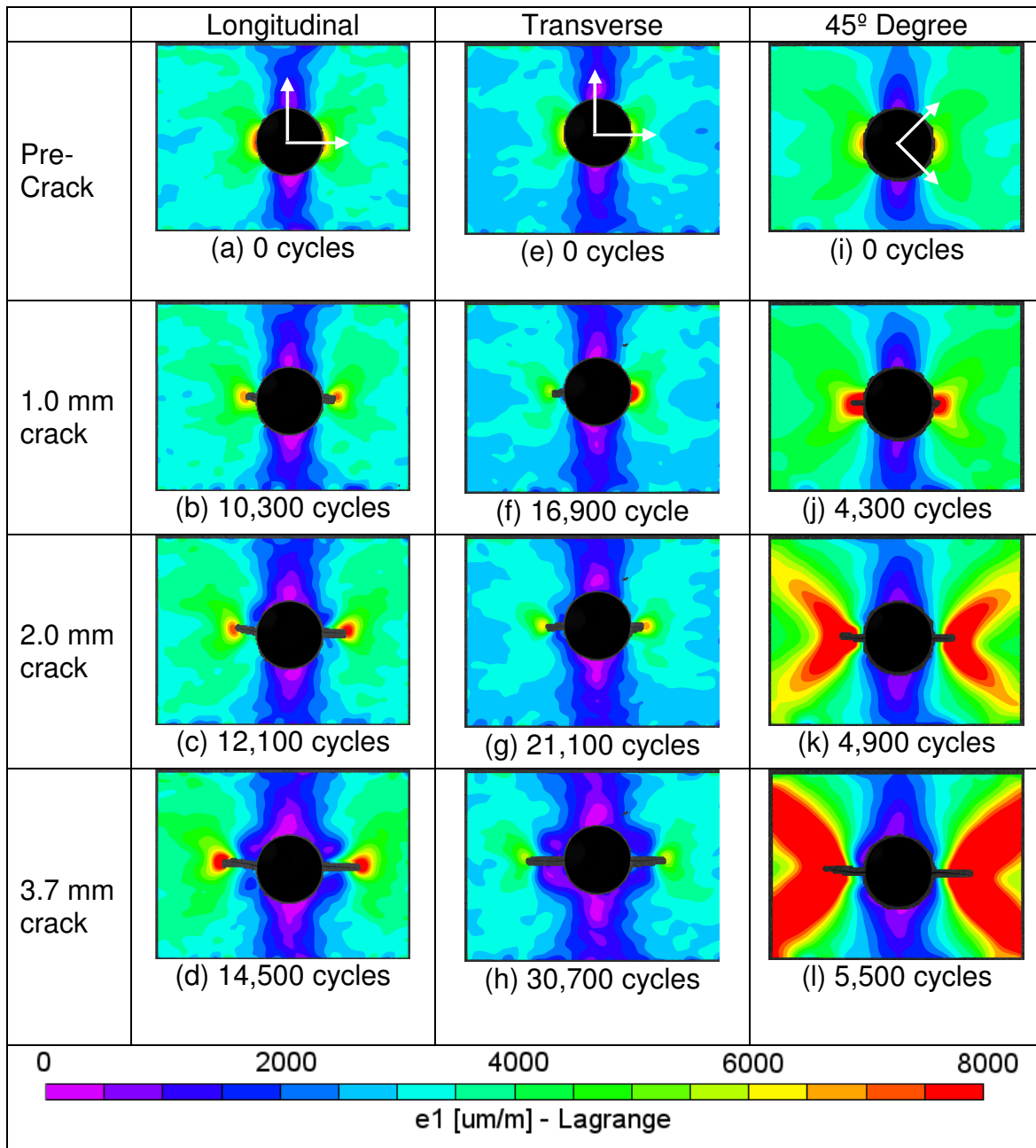
Figure 138: FML 4 [90/0/90] maximum principal strains from the entry face (a-d) unexpanded longitudinal coupon (Specimen 30-B-3-L), (e-h) unexpanded transverse coupon (Specimen 30-B-1-T) and (i-l) unexpanded 45º degree coupon (Specimen 27-B-4-F)
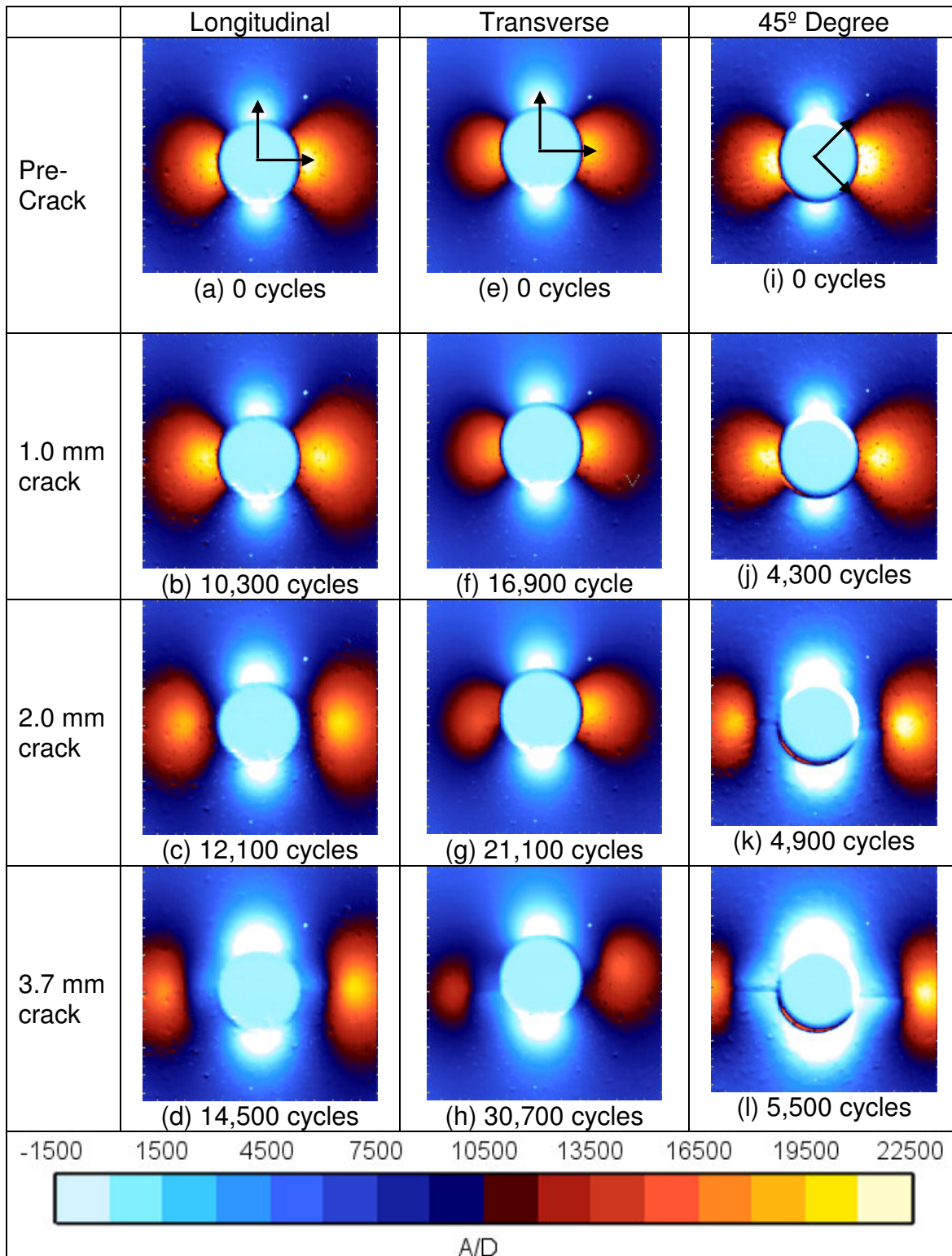
Figure 139: FML 4 [90/0/90] TSA images from the exit face (a-d) unexpanded Longitudinal coupon (Specimen 30-B-3-L), (e-h) unexpanded transverse coupon (Specimen 30-B-1-T) and (i-l) unexpanded 45º degree coupon (Specimen 27-B-4-F)

10.3.2 FML 4: Cold Expanded Coupons

Examining a similar series of images after cold expansion, one can clearly see the effect that the cold expansion process has on the crack tip strains. Compared to the results of Figure 138, the strain field at the crack tip after cold expansion shows a significant reduction in size and magnitude in all cases. Even for the cracks at 3.7 mm (Figure 140d,h,l), the crack tip strains show a slight reduction in magnitude in all material orientations compared to the unexpanded coupons (Figure 138d,h,l). As with the unexpanded coupons, the differences in strain at the crack tip appear to follow the same trend as the elastic modulus, with the transverse direction (highest modulus) showing the lowest crack tip strain, and the coupons cut in the 45º degree orientation showing the highest crack tip strain.

The TSA images taken on the exit side of the cold expanded hole, show a slight delay in crack formation on this face. As with the unexpanded hole, no clear indication of crack formation exists when a 1 mm crack is present on the entry face, except on the longitudinal coupon (Figure 141b) where a reduction of the strain field on the left hand side may indicate the presence of a small crack. At 2 mm of crack growth, the longitudinal and transverse coupons show additional signs of crack growth (Figure 141c,g). At 3.7 mm of crack growth, bilateral cracks are visible with the longitudinal and 45º degree coupons (Figure 141d,l), however, the transverse coupon (Figure 141h) only shows clear signs of crack growth on the left hand side of the hole. Overall, the results after cold expansion show a retardation in crack propagation as well a slight extension of the fatigue life in the early stage of the fatigue process.
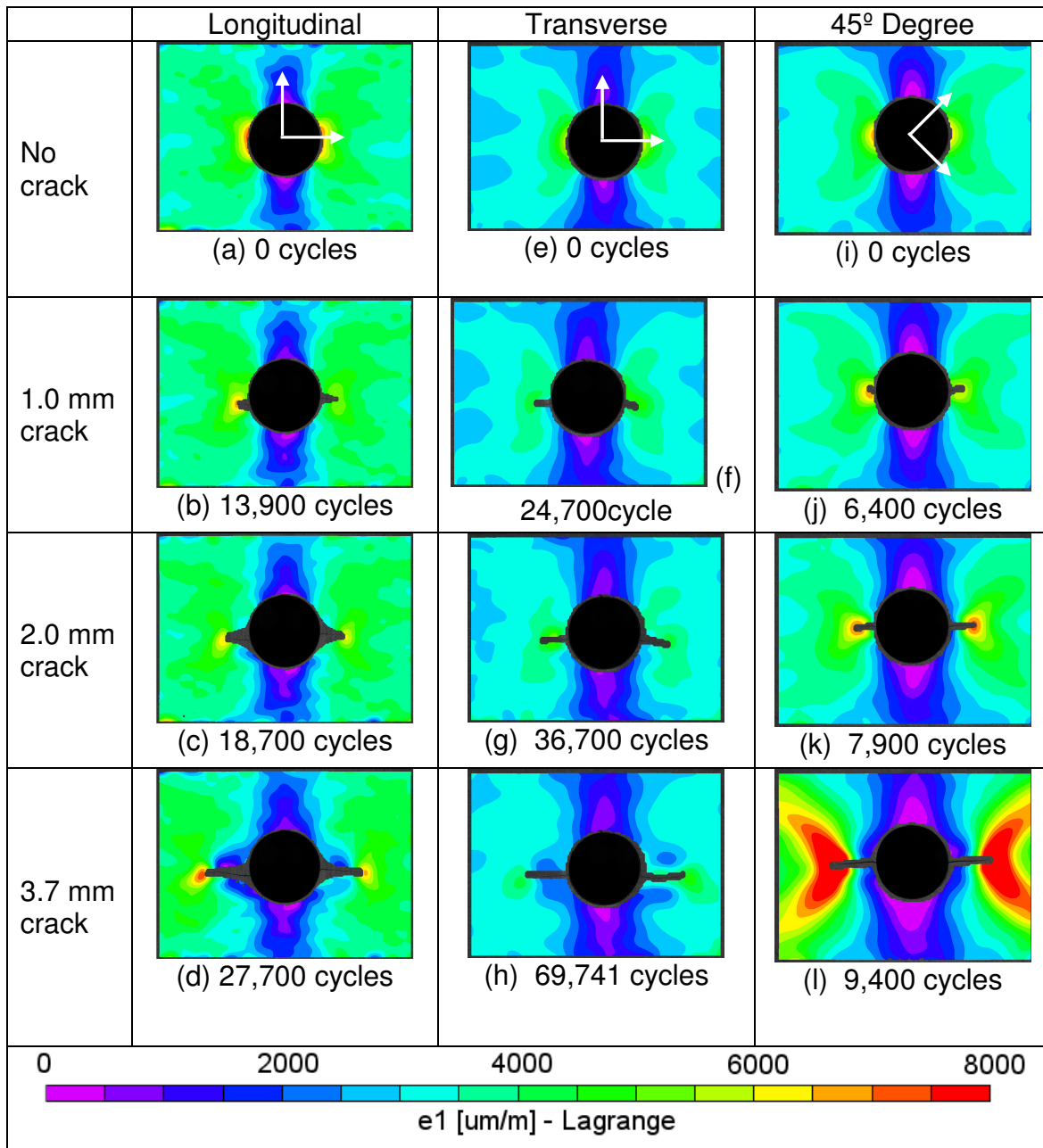
Figure 140: FML 4 [90/0/90] maximum principal strains from the entry face (a-d) cold expanded longitudinal coupon (Specimen 33-B-3-L), (e-h) cold expanded transverse coupon (Specimen 30-B-2-T) and (i-l) cold expanded 45º degree coupon (Specimen 33-B-6-F)
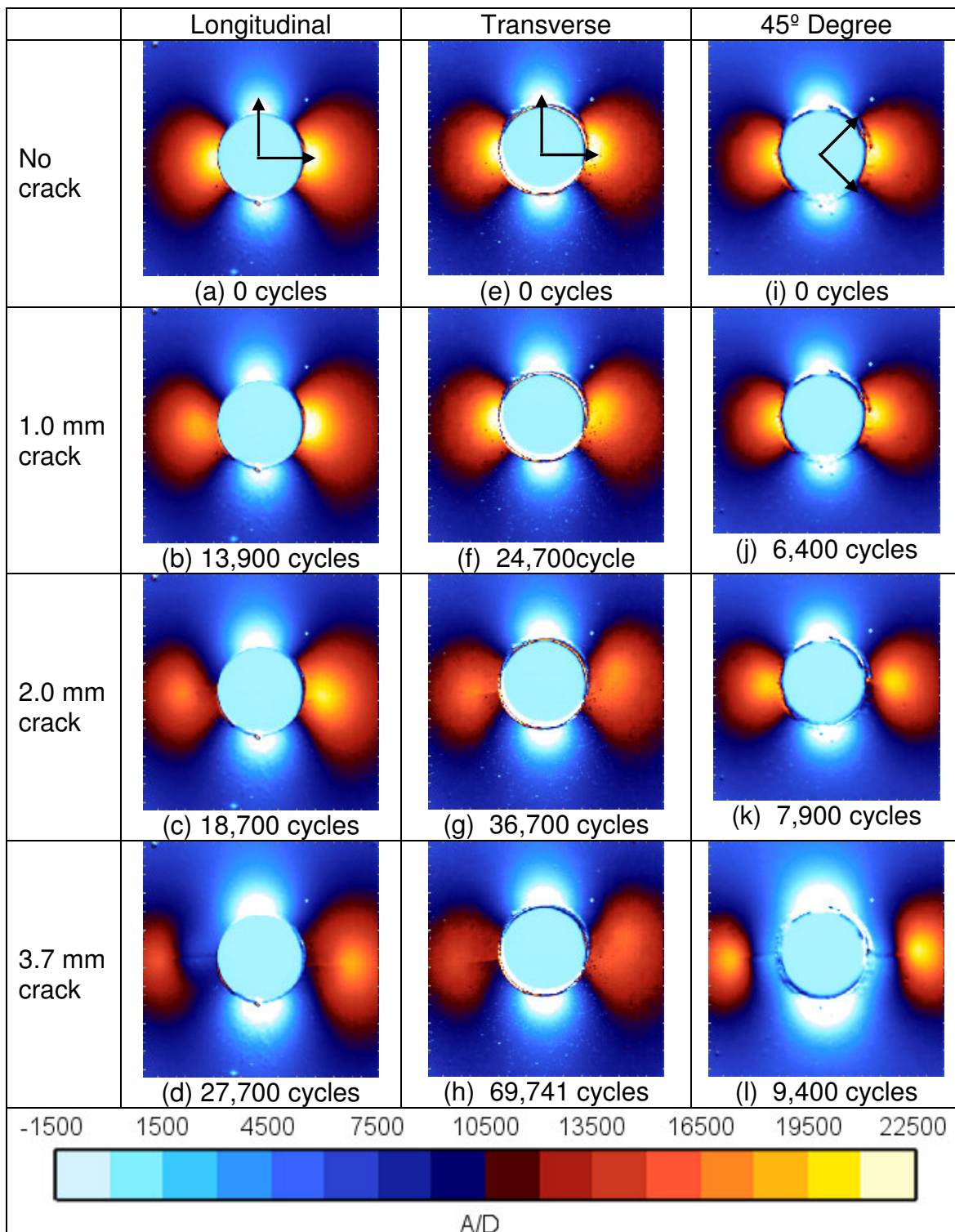
Figure 141: FML 4 [90/0/90] TSA images from the exit face (a-d) cold expanded longitudinal coupon (Specimen 33-B-3-L), (e-h) cold expanded transverse coupon (Specimen 30-B-2-T) and (i-l) cold expanded 45º degree coupon (Specimen 33-B-6-F)

10.4 FML 4 Variant: DIC and TSA Measurements

10.4.1 FML 4 Variant: Unexpanded Coupons

Maximum principal strain measurements from DIC are provided for the entry face of the

FML 4 variant unexpanded coupons in Figure 142. Strain measurements are provided

for coupons in all three material orientations (longitudinal, transverse and 45º degree) in

both pre-crack and cracked conditions. A small variation in strain is also seen among

the pre-cracked FML 4 variant coupons (Figure 142a,e,i), which is somewhat surprising,

given that static testing showed the difference in elastic modulus between the various

directions to be within 1 GPa. However, the differences may be reflective of this small

difference since the longitudinal direction had the (nominally) highest modulus, followed

by the transverse coupon, and the 45º degree coupon, which had the lowest modulus

(and the correspondingly highest strains).

The region of relatively low maximum principal strain at 0º and 180º degrees tends to

grow with increasing crack growth. This is often indicative of through crack growth in

the coupon, as the applied load is now being more fully transferred to the crack tip and

away from the top (0º degree) and bottom (180º degree) of the hole. The TSA images

(Figure 143) that provide a corresponding view of the exit surface seem to support this

hypothesis.

Equipment failure from the TSA camera meant that no information is available for the

45º degree precrack condition (Figure 143i). However, comparing the precrack images

from coupons in the other two material orientations (Figure 143a,e) to those at 1 mm of

crack growth on the entry face (Figure 143b,f,j) show little evidence of crack growth on

the exit face. At 2 mm of crack growth on the entry face, both the longitudinal and the 45º degree coupon (Figure 143c,k) show movement of the TSA signal at the crack tip, away from the left side of the hole, clearly indicative of crack growth. The transverse coupon (Figure 143g), shows a change in magnitude and shape of the TSA signal, indicative of a small crack forming in that location. At 3.7 mm of crack growth on the entry surface, TSA images from the longitudinal and 45º degree coupon (Figure 143d,l) both show signs of bilateral crack growth.   The transverse coupon (Figure 143h) shows clear signs of crack growth on the left hand side of the hole, and a change in magnitude and shape of the TSA signal on the right hand side of the hole are indicative of the formation of a small crack in this region.

Overall the results for the unexpanded hole show that crack growth on the exit face lags slightly behind that seen on the entry face of the coupon, behaviour that corresponds to that seen with the previous batch of fatigue coupons.
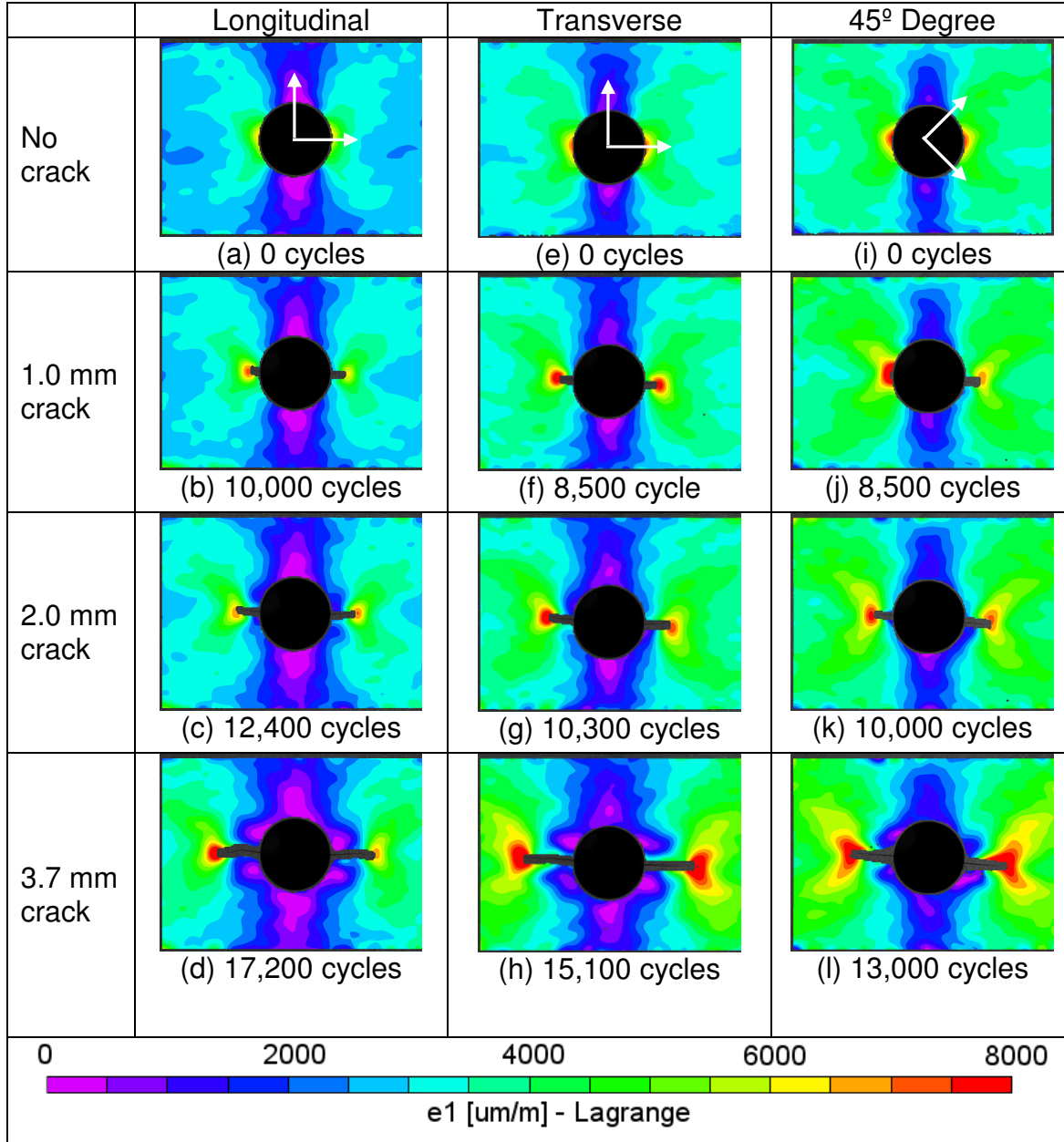
Figure 142: FML 4 variant maximum principal strains on entry face for (a-d) unexpanded longitudinal coupon (Specimen 32-D-2-L), (e-h) unexpanded transverse coupon (Specimen 32-D-4-T) and (i-l) unexpanded 45º degree coupon (Specimen 32-D-6-F)

	Longitudinal	Transverse	45º Degree
No crack	 (a) 0 cycles	 (e) 0 cycles	Image Not Available (i) 0 cycles
1.0 mm crack	 (b) 10,000 cycles	 (f) 8,500 cycle	 (j) 8,500 cycles
2.0 mm crack	 (c) 12,400 cycles	 (g) 10,300 cycles	 (k) 10,000 cycles
3.7 mm crack	 (d) 17,200 cycles	 (h) 15,100 cycles	 (l) 13,000 cycles

-1500   1500   4500   7500   10500   13500   16500   19500   22500

A/D
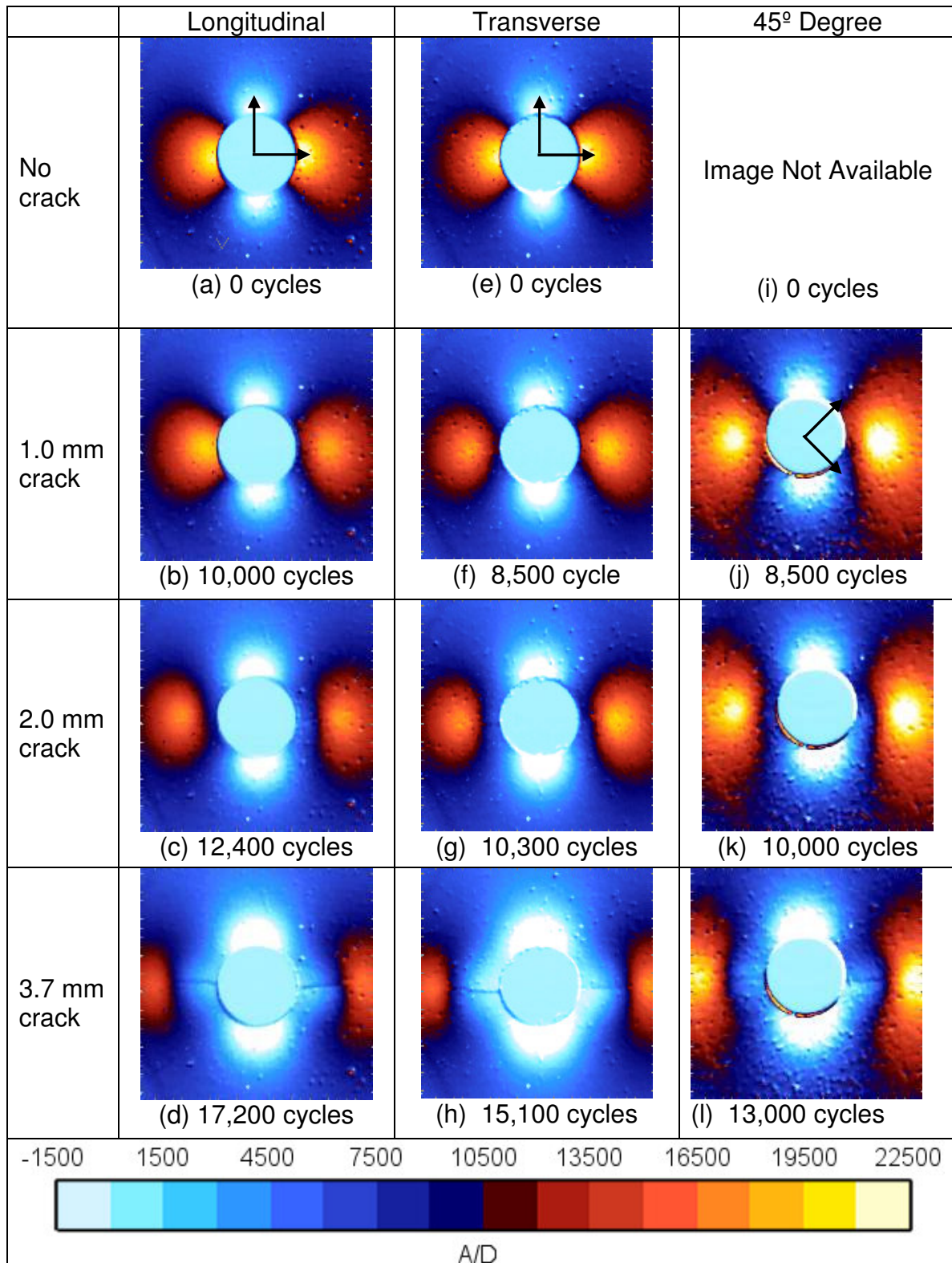
Figure 143: FML 4 variant TSA images on exit face for unexpanded (a-d) longitudinal coupon (Specimen 32-D-2-L), (e-h) transverse coupon (Specimen 32-D-4-T) and (i-l) 45º degree coupon (Specimen 32-D-6-F)

10.4.2 FML 4 Variant: Cold Expanded Coupons

After cold expansion, the maximum principal strains for the pre-crack FML 4 variant coupons (Figure 144a,e,i) appeared fairly similar among all three material orientations, with only the transverse orientation showing slightly lower strains. Overall, cold expansion appears to have significantly reduced crack tip strains up to 3.7 mm, at which point crack tip strains started to increase, possibly as a result of the crack growing past the elastic-plastic boundary (approximately 3.3 mm from hole edge) created by the cold expansion process. Examination of the TSA images (Figure 145) for supporting evidence of this found that after 2 mm of crack growth on the entry face (Figure 145g), coupons from all three material orientations start to show subtle indications of crack growth, consisting of a reduction in magnitude and a slight change in shape of the TSA signal on the exit surface. When the crack had grown to 3.7 mm on the entry face, the transverse coupon (Figure 145h) showed the clearest indication of crack growth, with a bilateral separation of the TSA signal away from the edge of the hole. The longitudinal and 45º degree coupon (Figure 145d,l), showed a change in shape as well as a reduction in the magnitude of the TSA signal, clearly indicative of early crack formation on this face
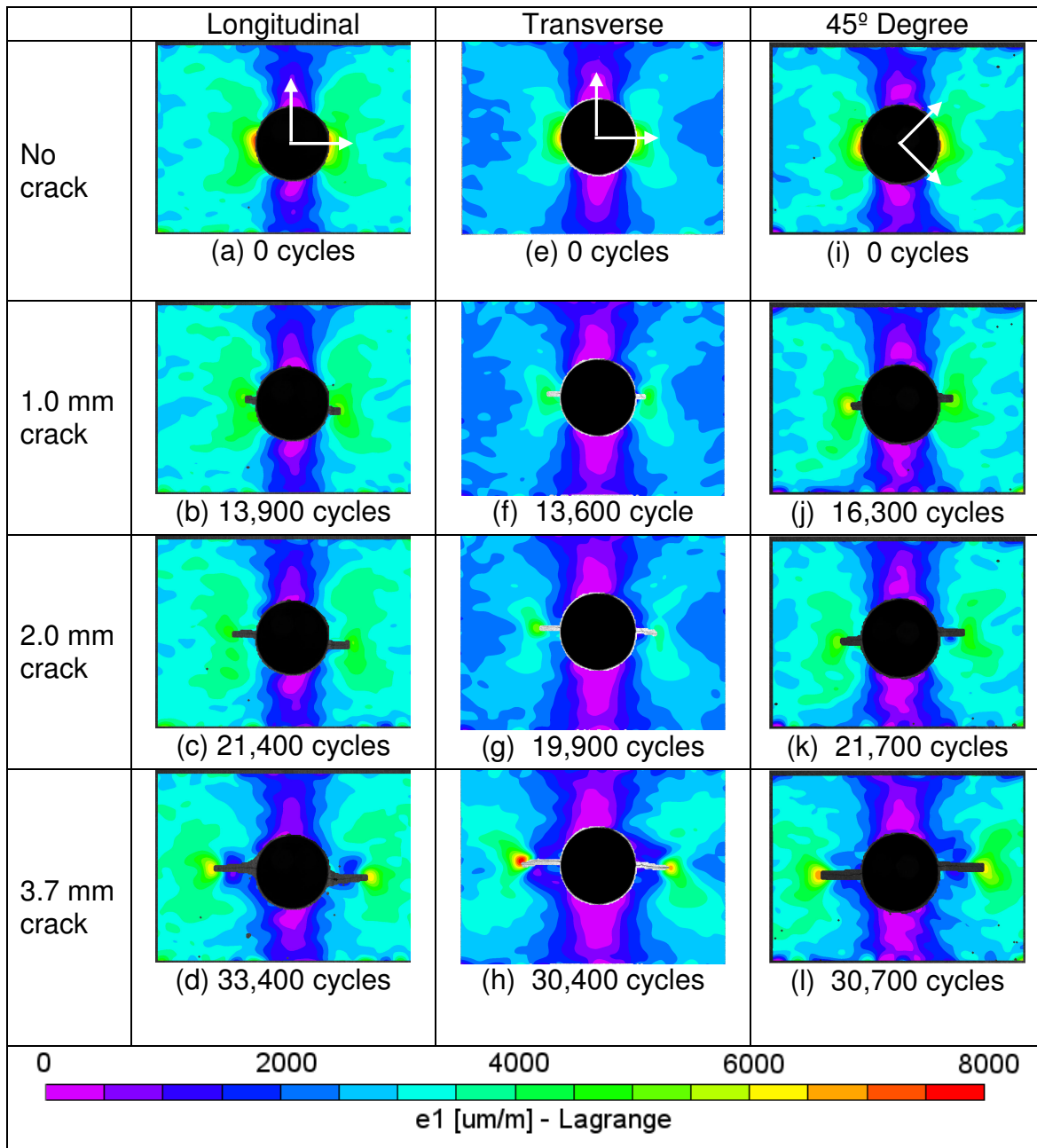
Figure 144: FML 4 variant maximum principal strains for (a-d) cold expanded
longitudinal coupon (Specimen 29-D-2-L), (e-h) cold expanded transverse coupon
(Specimen 29-D-3-T) and (i-l) cold expanded 45º degree coupon (Specimen 35-D-3-F)
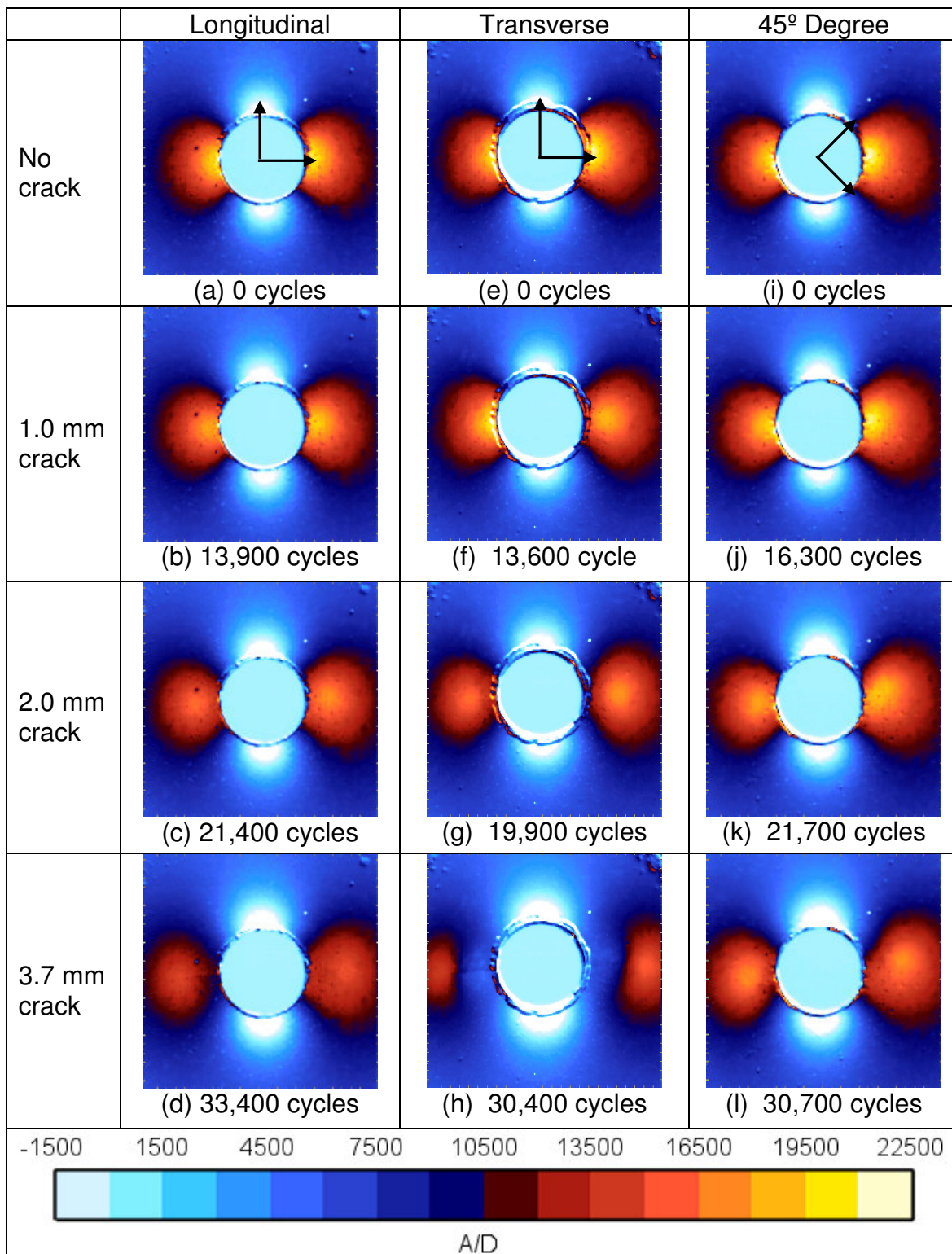
Figure 145: FML 4 variant TSA images for (a-d) cold expanded longitudinal coupon (Specimen 29-D-2-L), (e-h) cold expanded transverse coupon (Specimen 29-D-3-T) and (i-l) cold expanded 45º degree coupon (Specimen 35-D-3-F)

10.4.3 FML 4 Variant: Riveted Coupons

A sample size of n=3 FML 4 variant coupons were riveted and then fatigue tested at a net stress of 198 MPa and of the three coupons tested, two failed in the grip region. Figure 146 shows the strain results from DIC and TSA on both the manufactured and driven face of the coupon that failed in the gauge area. At 75% cycles to failure, crack nucleation has occurred near the outer edge of the coupon and the crack has begun propagating towards the rivet hole, demonstrating how effective the rivet is in increasing fatigue life.
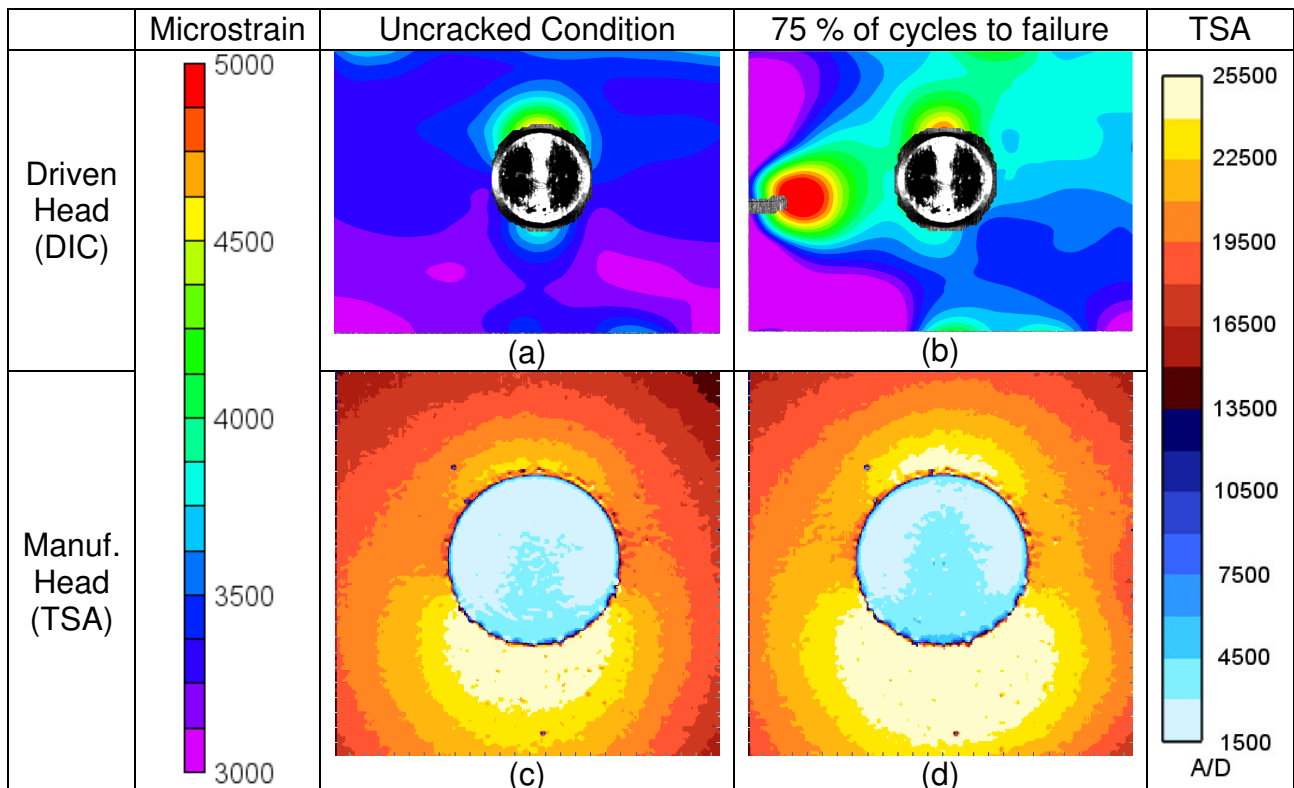
Figure 146: a-b) Maximum principal strain information from rivet driven face and c-d) TSA strain information from rivet manufactured head face for the FML 4 variant coupon, at pre-crack formation and at 75% of the number of cycles to failure (specimen 35-D-2-L). Note: Net stress of 198 MPa

An earlier comparison between the fatigue lives of FML 4 variant coupons in the unexpanded, cold-expanded, and riveted configuration (Figure 133) clearly showed almost a 350% increase in fatigue life for the riveted coupons versus unexpanded coupons. These results demonstrate that the mechanism behind the fatigue life increase in cold expansion and riveting is also effective with the new FML 4 variant coupons.

10.5 Ultrasonic Inspection of FML 4 and FML 4 Variant Coupons

Non-destructive evaluation was again performed post test, using pulse echo ultrasound to highlight the area of delamination. Sample ultrasonic images are provided for the entry and exit faces of unexpanded FML 4 (Figure 147) and cold expanded FML 4 (Figure 148) as well as unexpanded FML 4 variant (Figure 149) and cold expanded FML 4 variant (Figure 150) coupons in all three material orientations. The color scale used for the pulse echo ultrasonic is qualitative only and visually denotes differences in signal amplitude of the ultrasound wave.

From a qualitative perspective, little difference appears to exist between the shape and area of disbond for the open hole or cold expanded FML 4 coupons. As well, the ultrasound signal appears to be slightly less pronounced on the exit side of the coupon compared to the entry side. The transverse coupon shows the largest area of disbond in both the unexpanded (Figure 147c,d) and cold expanded coupons (Figure 148c,d). The longitudinal coupon shows the second largest area of disbond in both unexpanded (Figure 147a,b) and cold expanded (Figure 148a,b) coupon while the 45º degree coupons shows the smallest area of disbond in both unexpanded (Figure 147e,f) and cold expanded (Figure 148e,f) coupons.

	Pulse Echo UT Entry Face	Pulse Echo UT Exit Face
Long.	(a) N_f=23,770	(b)
Trans.	(c) N_f=194,448	(d)
45º	(e) N_f=7,891	(f)
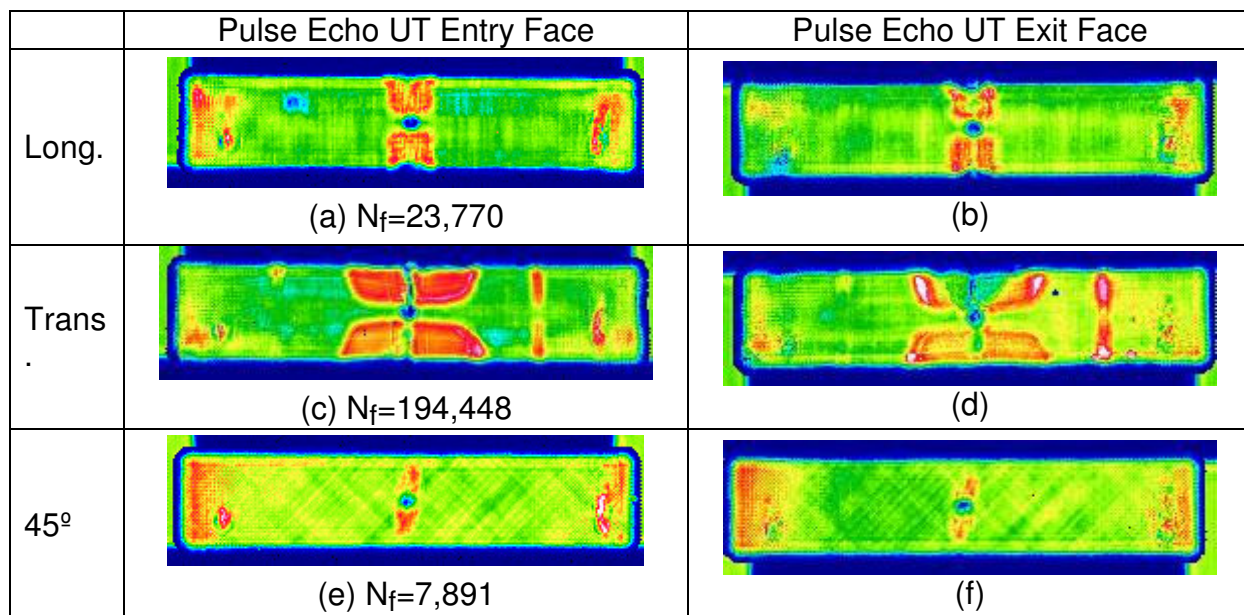
Figure 147: FML 4 open hole tested at a net stress of 198 MPa with cycles to failure (N_f) provided. Longitudinal (specimen 30-B-3-L), transverse (specimen 30-B-1-T) and 45º degree (specimen 27-B-4-F)

	Pulse Echo UT Entry Face	Pulse Echo UT Exit Face
Long.	(a) N_f=43,187	(b)
Trans.	(c) N_f=613,298	(d)
45º	(e) N_f=12,611	(f)
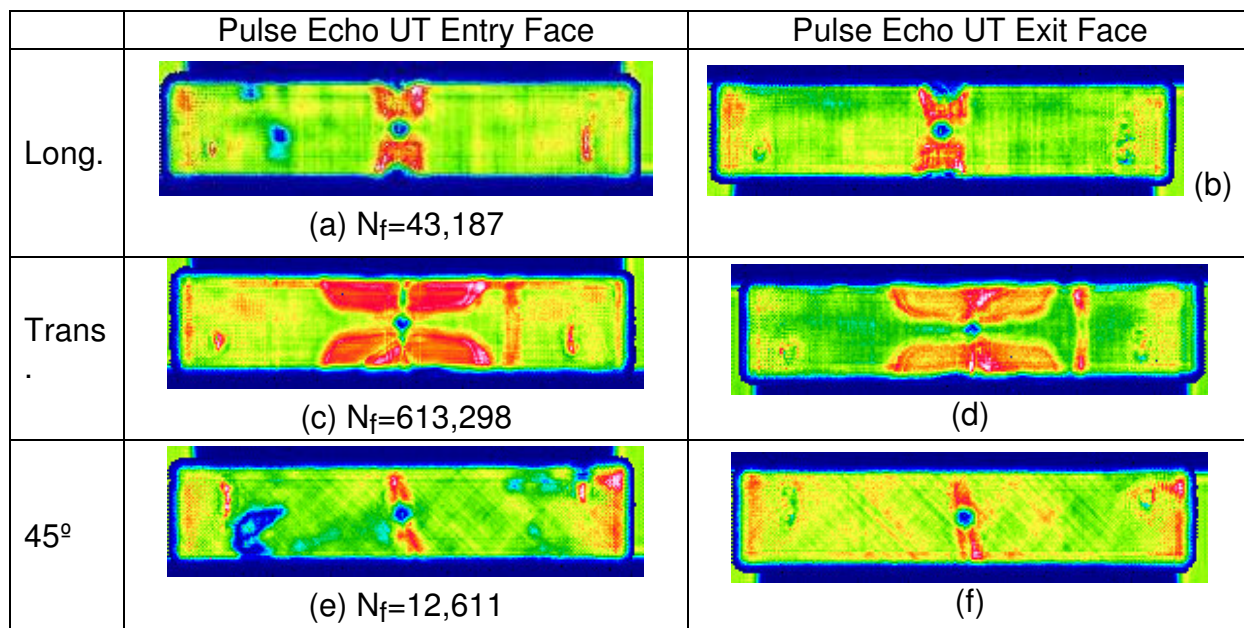
Figure 148: FML 4 cold expanded hole tested at a net stress of 198 MPa with cycles to failure (N_f) provided. Longitudinal (specimen 33-B-3-L), transverse (specimen 30-B-2-T) and 45º degree coupon (specimen 33-B-6-F)

From a qualitative perspective, the area of disbond around the unexpanded open hole in the FML 4 variant are more similar in size and shape to that of the FML 4 coupons oriented at 45º degrees. As with the FML 4 coupons, the ultrasound signal on the exit face appears to be slightly less pronounced than on the entry face. The FML 4 variant cold expanded coupons all have self-similar disbond areas and shapes, but these appear to be slightly larger than those from the FML 4 variant unexpanded coupons.

The ultrasound results for the riveted FML 4 variant coupons are shown in Figure 151 for all three coupons. Of these three coupons, two failed in the grip region (Figure 151a,b and Figure 151e,f) with the red disbond region clearly visible in these images. A closer visual examination of the failure region showed what appeared to be fretting by-products in the grip area, suggesting that perhaps micro-slip in this region may have precipitated failure. Even the one coupon that appeared to fail in the gauge area (Figure 151c,d) showed some signs of disbonding in the grip region, along with an indication of disbonding (due to crack growth) at the edge of the coupon. If grip failures could be eliminated from future tests, there is a possibility that the actual fatigue life might even be higher than what was reported here.

	Pulse Echo UT Entry Face	Pulse Echo UT Exit Face
Long.	(a) N_f=36,432	(b)
Trans.	(c) N_f=27,582	(d)
45º	(e) N_f=24,724	(f)
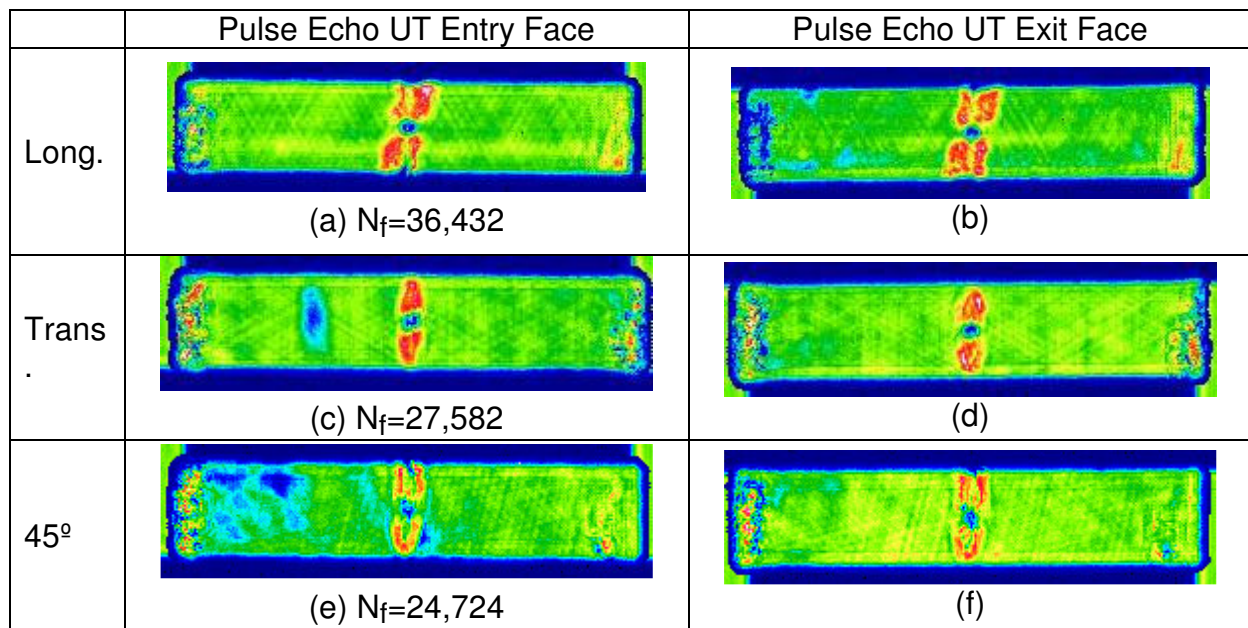
Figure 149: FML 4 variant open hole tested at a net stress of 198 MPa with cycles to failure (N_f) provided. Longitudinal (specimen 32-D-2-L), transverse (specimen 32-D-4-T) and 45º degree coupon (specimen (32-D-6-F)

	Pulse Echo UT Entry Face	Pulse Echo UT Exit Face
Long.	(a) N_f=60,367	(b)
Trans.	(c) N_f=56,802	(d)
45º	(e) N_f=60,716	(f)
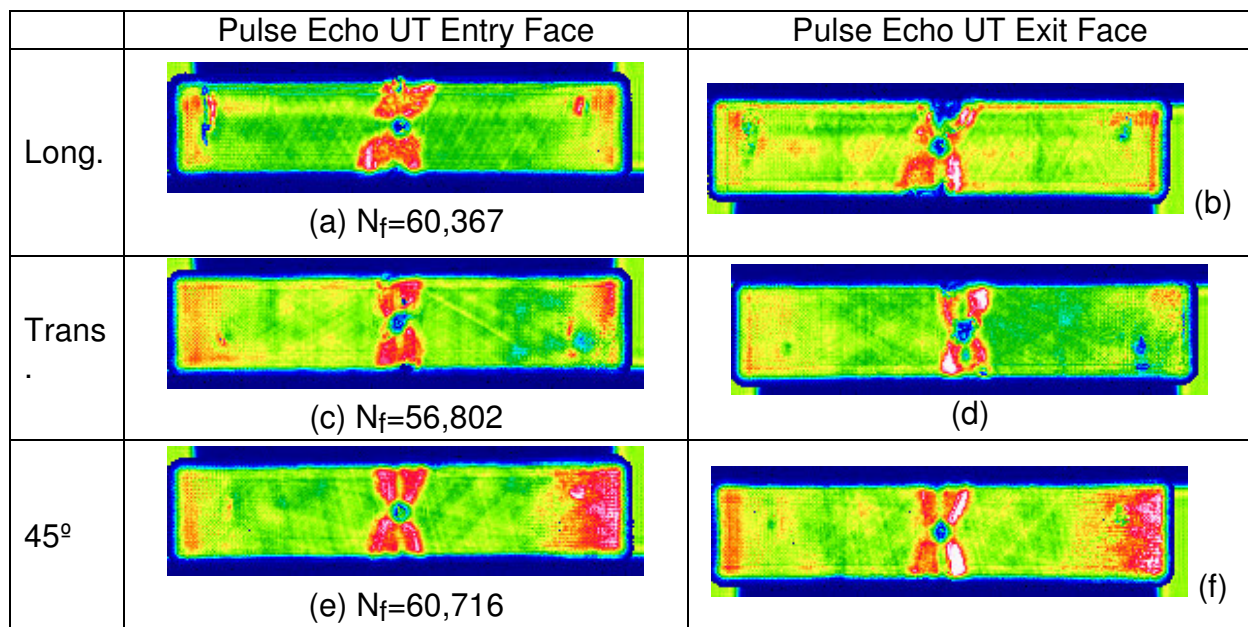
Figure 150: FML 4 variant cold expanded hole tested at a net stress of 198 MPa with cycles to failure (N_f) provided. Longitudinal (specimen 29-D-1-L), transverse (specimen 35-D-1-T) and 45º degree coupon (35-D-4-F)
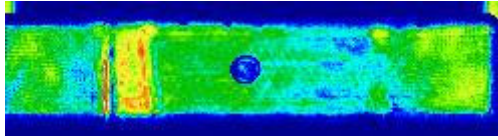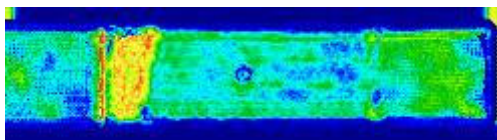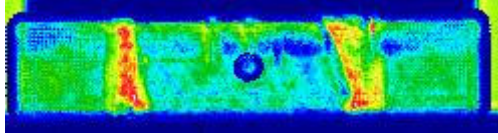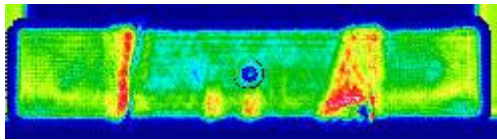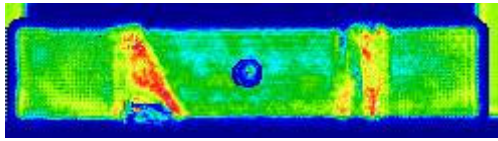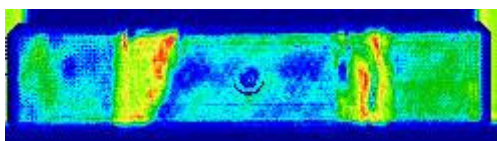
Spc #	Pulse Echo UT Manuf. Head Face	Pulse Echo UT Driven Head Face
26-D-7-L.	(a) N_f=196,189	(b)
35-D-2-L.	(c) N_f=236,750	(d)
35-D-5-L	(e) N_f=217,704	(f)

Figure 151: Ultrasonic inspection of FML 4 Variant coupons post riveting tested at a net stress of 198 MPa with cycles to failure (N_f) provided. Note: Only coupon 35-D-2-L failed in grip

10.6 Discussion

One interesting aspect, revealed by the multiple phases of fatigue testing, is the occasional difference in strain between the unexpanded and cold expanded coupons under the initial static load. In theory, there should be no detectable difference under static loading after cold expansion, since the compressive residual strains do not change the material properties in a way that would be measurable under a simple static load. A review of the initial aluminum and FML coupons showed that the small difference detected was likely due to the increase in hole size due to cold expansion, which resulted in a 0.8% increase in the net section stress and a corresponding increase in strain. For this most recent phase of the fatigue testing the loads were adjusted to compensate for the slightly larger hole in the cold expanded coupons and the net section stresses were equivalent between the open hole and cold expanded coupon. While many FML coupons now showed essentially equivalent strains between

253

the unexpanded and cold expanded coupons during static loading, in some cases there still appeared to be some small differences in strain during static loading, with the cold expanded coupons typically showing slightly higher strains. One hypothesis that seems plausible is that cold expansion increases the amount of disbonding that occurs around the hole and effectively "enlarges" the hole by reducing the structural integrity around its circumference, thereby reducing the net section area through the hole, raising the net section stress and consequently the net section strain. The research by van der Kuip[89] used chemical etching and mechanical milling to remove the aluminum layers and visualize the disbonding around the hole. Van der Kuip[89] observed that even drilling the initial open hole caused an annular region of disbonding around the hole (no measurement provided), with cold expansion increasing the disbond to 0.3 mm from the hole edge.

The first approach to verifying this aspect of the drilling/cold expansion process involved cross-sectioning several FML coupons, and performing a microscopic examination of the area around the hole at various magnifications. Figure 152 shows an unexpanded FML 3 coupon at x10 and x20 magnification. The two plies in this FML 3 coupon are easily differentiated as in one ply the fibers are oriented normal to the plane of the cross-section, and appear as small pin heads, and in the other ply the fibers run in the plane of the cross-section, and appear as long strands. A small area of disbond is assumed to exist in the top ply, as a result of the disruption in the orientation of the fibers adjacent to the hole (see highlighted region in Figure 152b). Measurement of the

disbond length was done using ImageTool image analysis software and that the disbond measured approximately 0.06 mm in length.

(a)   (b)
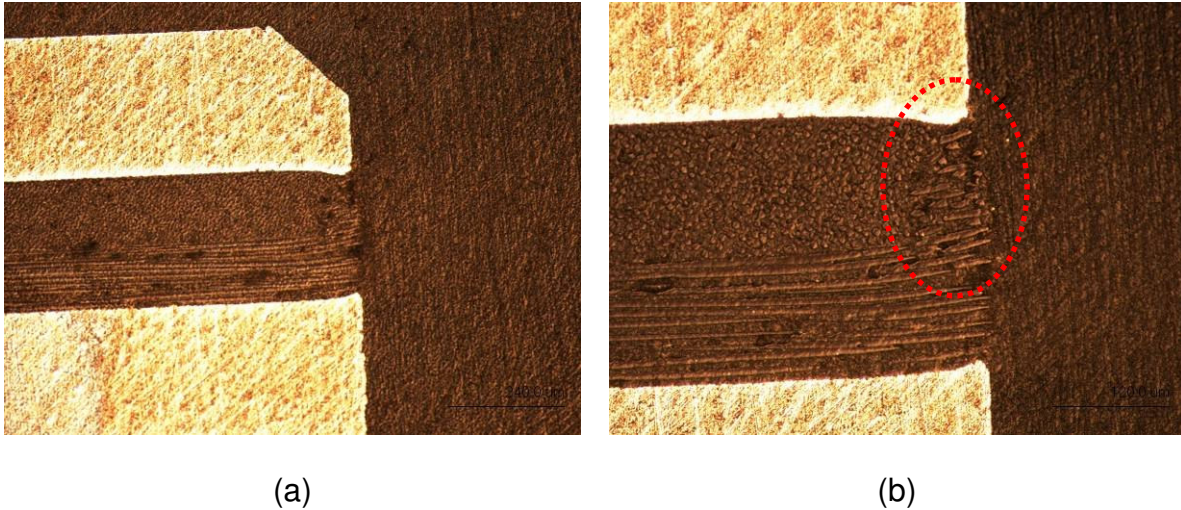
Figure 152: Cross-section of an unexpanded hole in FML 3 (a) x10 magnification and (b) x20 magnification with area of possible disbond highlighted in red

Next, an FML 3 coupon that had been cold expanded but not reamed was cross-sectioned and viewed microscopically at the same magnifications (Figure 153).   In this case, the fiber plies now appeared to extend out from the edge of the hole on the exit side. Given the mismatch in elastic modulus between the 2024-T3 aluminum (72 GPa) and the FM-94[90] prepreg (51 GPa), it would appear that the compressive residual strains induced by the oversized mandrel had elastically compressed the prepreg layer, while at the same time plastically deforming the aluminum layer. With the removal of the oversized mandrel, the prepreg attempted to spring back, with the spring back force exceeding the shear strength of the aluminum-prepreg interface (approximately 45 MPa), resulting in a small amount of prepreg extending past the aluminum at the outer edge of the hole. Analysis of the image showed that the length of fiber extending

into the hole measured approximately 0.06 mm, which suggests that this is the same

region of fiber that disbonded during the initial open hole drilling process.
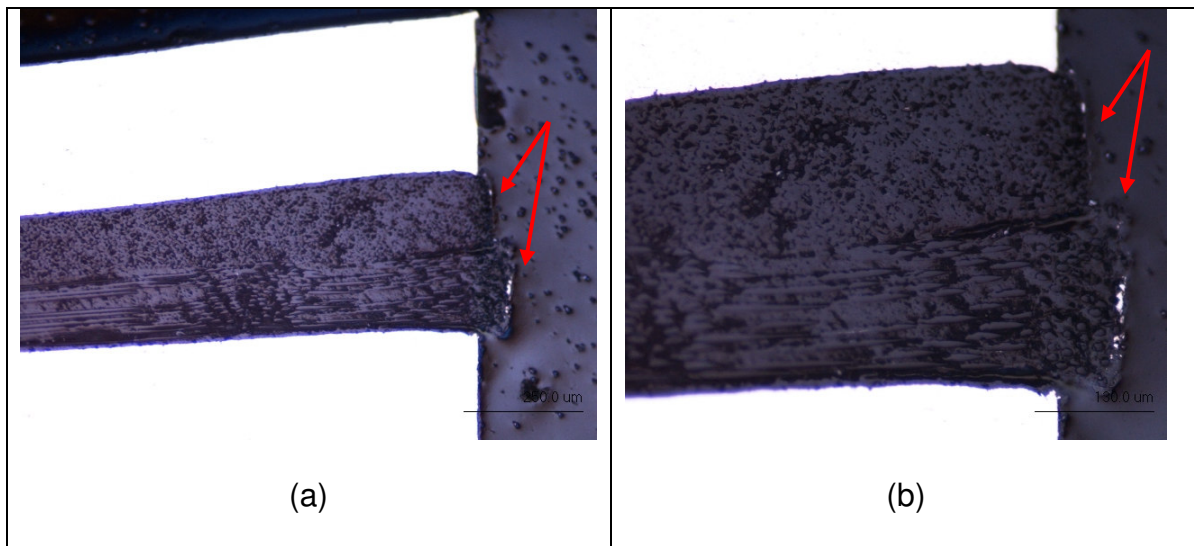
Figure 153: Cross-section of FML 3 coupon (exit side) after cold expansion but before reaming at (a) x10 magnification and (b) x20 magnification with area of disbond highlighted with arrows

Finally, two additional FML 3 coupons were cold expanded, reamed and

cross-sectioned for microscopic examination (Figure 154). It is apparent that the

reaming process removed any fibers in the hole, along with remnants of the "pip"

created by the split in the split sleeve. The area of disbond appears to be less

consistent, with approximately 0.09 mm of fibers disrupted in Figure 154a, and a smaller

length (approximately 0.05 mm) of disrupted fiber in Figure 154b. What is difficult to

ascertain is whether the fibers to the left of the disbond region are actually bonded to

the aluminum or whether the adhesive bond has been disrupted resulting in a situation

often referred to as a "kissing bond".
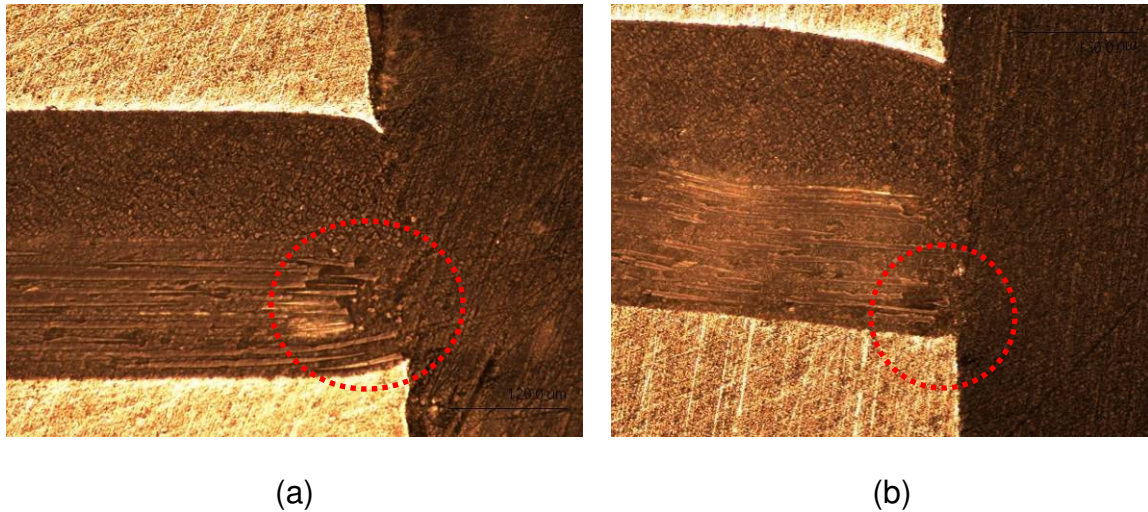
Figure 154: Cross-section of two FML 3 coupons (exit face) at x20 magnification (a) specimen with 0.09 mm disbond length and (b) specimen with 0.05 mm disbond length

Another approach to quantify this disbond area and to verify van der Kuip's[89] results was attempted using two non destructive inspection (NDI) methods. Both high resolution ultrasonics and pulsed thermography methods were used, but neither could conclusively detect the area of disbond. The difficulty detecting the area of disbond likely stems from the small size of the disbond, an assumption based on both the current microscopic examination (0.06 mm) as well as from van der Kuip's[89] results (0.30 mm). Although there is a large difference between the current disbond estimate and that of van der Kuip's[89], his etching/milling method is better suited to reveal "kissing bonds" and it is not inconceivable that cold expansion results in an 0.30 mm radius of disbond surrounding a cold expanded hole. What van der Kuip[89] did not address was the variability in this measurement, and the current results seem to suggest that there may be a degree of variability associated with the area of disbond.

Reviewing the cases where the static strains appeared to be different before and after cold expansion, one interesting observation was made. It was noted that as part of the experimental procedure, immediately after cold expansion, static loads identical to those placed during the fatigue cycle were applied. The strain field at this point, often appeared to be more similar to the unexpanded strains. Also, the pre-crack images were taken after at least 100 fatigue cycles had been applied to help seat the coupon in the hydraulic grips, and it is possible that in some cases these fatigue cycles caused the disbond to grow slightly and lowered the observed strains. Although this phenomena is of interest, it did not adversely affect the fatigue life of the cold expanded specimens, as in all cases the specimens with cold expanded holes outlasted those with unexpanded holes.

A final approach used to investigate the potential disbond around the hole after cold expansion involved subjecting both open hole and cold expanded coupons to static loads until failure, and measuring the resultant elastic modulus. For this experiment two groups of three (n=3) longitudinal FML 4 [90/0/90] coupons were produced. The unexpanded coupons were reamed such that their central hole was of the same diameter (6.63 mm) as the hole produced after cold expansion. The engineering stress-strain curve that would be used to determine the elastic modulus was based on the net section stress through the central hole in the coupons, and the strain was based on the global elongation of the coupons measured by crosshead displacement. It was recognized early on that to successfully prove the hypothesis that the disbond resulting

from cold expansion could affect the mechanical properties of a notched coupon, the modulus results would have to have little scatter and the difference between unexpanded and cold expanded coupons would have to be quite large. The results showed very similar material properties between the two coupons, with the unexpanded coupons having an average elastic modulus of 50.04 ±0.46 GPa and an average max load of 31.27 ± 0.41 kN, while the cold expanded coupons had an average elastic modulus of 50.43 ± 1.5 GPa and an average max load of 31.27 ± 0.24 kN. Although the results of this experiment did not conclusively prove or disprove the existence of a disbond around cold expanded holes in FML, at a minimum, it showed that the static strength of FML is not significantly affected by the cold expansion process.

The pulse echo ultrasonic inspection used to inspect all coupons after fatigue failure was very useful at highlighting the differences in the disbond area for coupons with different material orientations and different FML grades. What is known about fatigue failure in FML is that the cyclic shear stresses in the adhesive layer are related to the fiber bridging stresses. It is these cyclic shear stresses that are responsible for the growing delamination between the aluminum and fiber layers. As this delamination area grows, the length over which the fibers are elongated increases, lowering the fiber strains. In essence, there is a balance between delamination growth in the prepreg and the bridging strains[9]. For the FML 4 [90/0/90] in the transverse direction, the area of delamination is greatest (Figure 147d,c) and correspondingly so is the fatigue life. As the transverse coupon is being fatigued, two of the three fiber plies are aligned parallel to the loading direction and the prepreg has the highest elastic modulus. When loaded

in tension, tensile stress in the aluminum layer is transferred to the fiber prepreg layer through shear, causing elongation of the fibers. In the transverse direction, the fibers are aligned to best resist the load and to most effectively bridge any cracks that form in the aluminum. Conversely, in the 45º degree direction (Figure 147e,f), the same mechanisms are in place to transfer load, except in this orientation the fiber prepreg has a lower elastic modulus and does not transfer the load as effectively. The effectiveness of the fiber bridging in the aluminum layer is thus reduced, and crack propagation occurs more quickly. This reduction in fiber bridging effectiveness also means that the delamination area is reduced, since, except for the local region near the propagating crack, the fiber prepreg layer is more elastic and less likely to cause adhesive shear failure.

For the FML 4 variant coupons, all fiber orientations (Figure 148) have essentially the same elastic modulus and thus provide an equivalent degree of fiber bridging in all material orientations. Consequently the delamination area is also fairly consistent as all material orientations result in approximately the same degree of shear strain at the aluminum/prepreg interface. The slight difference that appears between the unexpanded and cold expanded coupons is likely a result of the longer fatigue life in the cold-expanded coupons. An increased number of fatigue cycles results in more cyclic adhesive stresses, and thus an increased disbond area. Measurement of the disbond area for both the FML 4 [90/0/90] (Figure 155) and the FML 4 variant (Figure 156) coupons confirms that overall, cold expanded coupons do show a slight increase in disbond area over that of the unexpanded coupons.

One possible approach to increasing the fatigue life would be to use a higher stiffness reinforcement material in the prepreg. This would both increase the modulus of the prepreg and improve fiber bridging and effectively lower the stress in the aluminum layer under the applied load. While this approach may have theoretical merit, the greatest drawback is that both steps would require changing the constituent components of FML. Over the long term this approach may result in a fundamental improvement to the FML being used today, it would also require recertification of this new material, where perhaps a more pragmatic approach would be to examine and modify the current process parameters to improve overall material performance.

Overall, a comparison between the unexpanded and cold expanded coupons from each FML grade showed qualitatively similar disbond patterns with only small increases in disbond area after cold-expansion. This supports the idea that the effectiveness of cold- expansion in FML is related to its effect on the monolithic aluminum layers and does not affect crack bridging or overall disbond of the fiber layers.
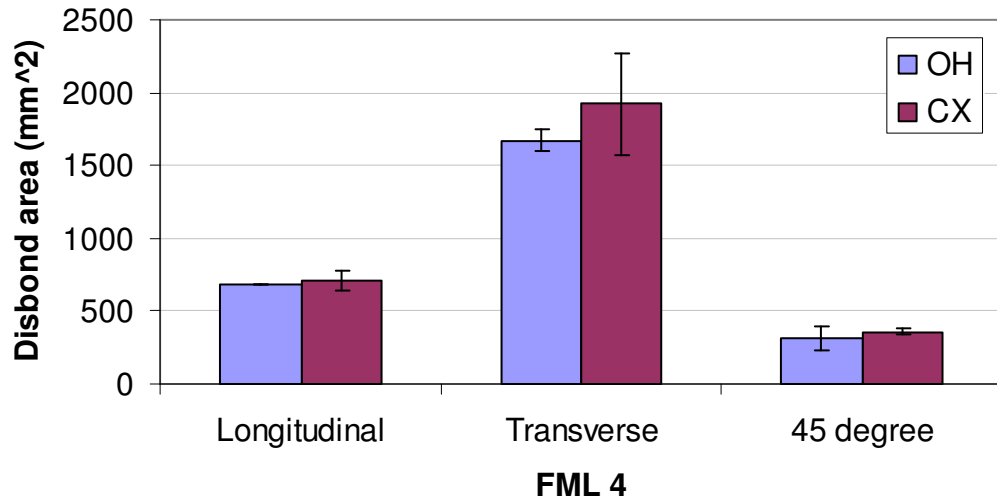
Figure 155: Measured area of disbond from pulse echo ultrasound for FML 4 [90/0/90] in both unexpanded and cold expanded conditions [combined entry and exit face average of n=2 coupons]
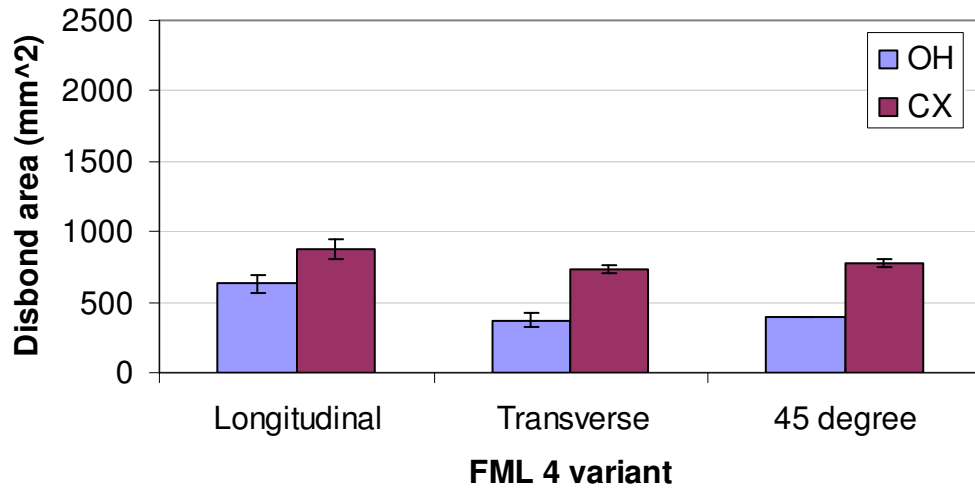
Figure 156: Measured area of disbond from pulse echo ultrasound for FML 4 variant in both open hole and cold expanded conditions [combined entry and exit face average of n=2 coupons]

11.0 DISCUSSION

The motivation for this research was the increasing use of fiber metal laminates in aircraft structures, with the corresponding suggestion that fiber metal laminate materials could be used as direct replacements for aluminum; suitable for riveting or cold expansion as the need arose. A review of the literature surrounding riveting and cold expansion showed that although these processes were well understood for monolithic materials, little research had been performed to ascertain the effect of riveting on fiber metal laminates and even less research had been performed to determine the effect of cold expansion.

These gaps in the current body of knowledge led to this research program, which was aimed at understanding the effects of cold expansion and riveting on FML, using both experimental and analytical methods, to see if the information gained could be used to design an FML variant optimized for use with cold expansion and riveting.

The results obtained met all the objectives of this research program and extended the body of scientific knowledge in this area. Although the research was constrained to the stated objectives and did not directly set out to examine the underlying mechanism behind cold expansion in FML, several observations made during the course of this investigation addressed this issue and are discussed further. An overall discussion of the results is provided which centers on the primary research objectives and discusses what has been achieved in each area as well as how this information was related to the ultimate goal of producing an optimized FML variant.

11.1 Cold Expansion of FML

The results from the static tests provided a unique opportunity to measure full-field strains in real time during the cold expansion process. Although measuring full-field strains in aluminum coupons during cold expansion and riveting was not new, using the image correlation technique to gather this information provided a unique insight into both processes. For the FML coupons, only two researchers had explored the cold expansion process in FML[89,90] and neither had made experimental measurements of the strains resulting from this process. Although manual cold expansion equipment had previously been used by Beaver et al[43], it had never been used in the current manner, where individual strain measurements were taken at specific increments of mandrel displacement through the coupon. This allowed the low speed (5 frames per second) video cameras, used for image correlation, to effectively "slow down" the cold expansion process and provide a more complete visualization of the change in residual strains during this process.

The pseudo-static measurement of the surface strains during cold expansion showed several similarities between the aluminum and FML coupons. In the case of the aluminum coupon, insertion of the mandrel (Figure 157a) resulted in an expansion of the elastic-plastic boundary as predicted by the analytical solution. Withdrawal of the mandrel (Figure 157b) resulted in recollapse of the material surrounding the hole, and reverse yielding, with a new elastic-plastic boundary being created close to the hole.
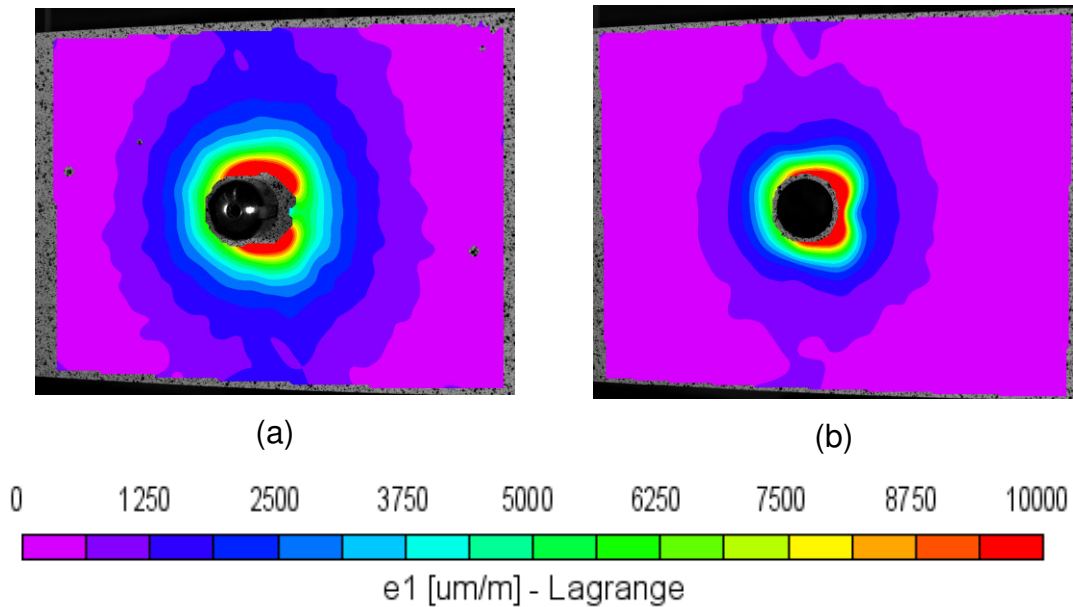
Figure 157: Maximum principal strains in aluminum coupon (specimen AL1): (a) mandrel fully inserted and (b) mandrel removed

Interestingly, the same mechanism appears to be at work in the FML coupon. Complete mandrel insertion (Figure 158a) results in a larger elastic-plastic boundary, and withdrawal of the mandrel (Figure 158b) results in recollapse of the material surrounding the hole, causing reverse yielding in the aluminum layer and formation of a new elastic-plastic boundary closer to the hole. Although the processes have similarities, the change in strain field symmetry is a clear indication that the material properties of this FML 3 coupon are much more orthotropic than aluminum. Another difference between FML and aluminum after cold-expansion, is the delamination that occurs at the aluminum/prepreg interface due to the cold-expansion process (Chapter 10.6).
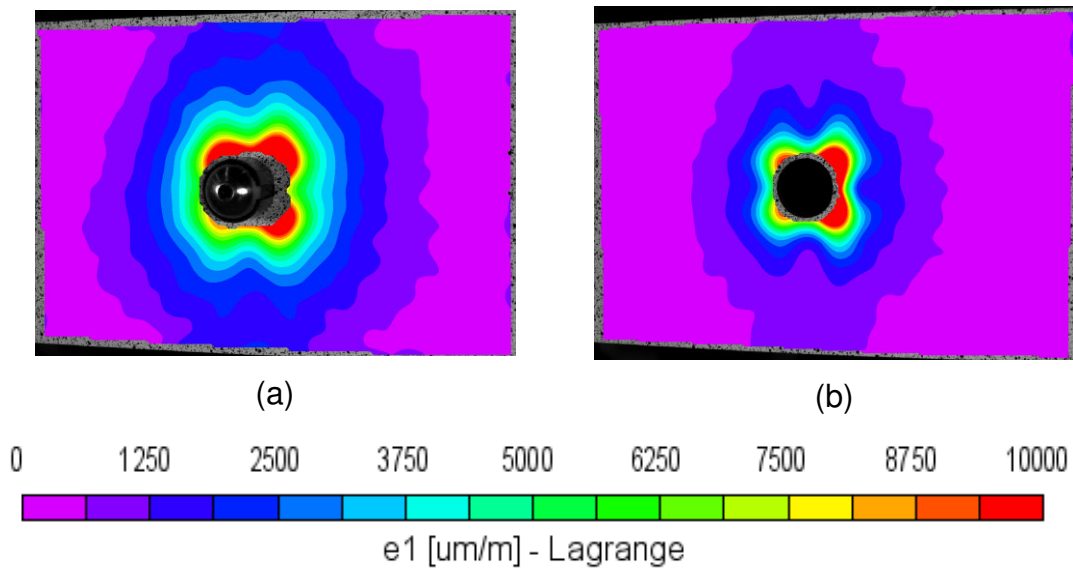
Figure 158: Maximum principal strains in FML 3 coupon (specimen GAL1): (a) mandrel fully inserted and (b) mandrel removed

The observations and measurements made seem to support the hypothesis that the improvement in fatigue life for FML is because of the compressive residual stresses imparted by the oversized mandrel into the aluminum layer. Cold-expansion appears to play a fairly minimal role in extending life in the early stage of fatigue process on the entry face, possibly as a result of the delamination at the aluminum/prepreg interface adjacent to the hole. The reason this does not have a detrimental affect on fatigue life is that crack bridging in FML is not fully effective until a crack has reached a radial length of approximately 1.0 mm, which is significantly longer than the radial length of the disbond area. The TSA results from the exit face of the coupon suggest that cold expansion may better extend life in the early stage of the fatigue process, an observation that has been confirmed by van der Kuip[89] during his fatigue testing of cold-expanded FML. This difference may be due to the higher residual strains on the exit face, a phenomena well documented in aluminum coupons[41,43,44,47,52,60-63].

266

Although it has been shown in this research that cold expansion does result in higher residual strains on the exit face, it seems likely that the higher residual strains would need to act in tandem with a reduction in the level of disbond on this face. Conclusively proving this would likely need to be done using chemical etching to remove the aluminum layers after cold-expansion to determine the exact area of disbond on both faces.

The static testing provided a means of measuring the surface residual strains resulting from cold-expansion and allowed for a comparison to be made between the aluminum and FML. These results graphically demonstrated the effect of material orthotropy on the residual strains. Material data sheets about the standard FML grades often provide only material properties in the two principal directions, and the cold expansion results were a graphic reminder that, as a laminated composite, the in-plane material response can be anisotropic with both elastic modulus and yield strength being a function of the material orientation.

Static testing clarified that although FML 3 and FML 4 are often referred to as quasi-isotropic[137,138], due to their similar material properties in the longitudinal and transverse direction, they are not quasi-isotropic in the classical laminate sense. By definition, a quasi-isotropic laminate is one with three or more identical plies at equal angles (i.e the angle separating each of the n plies is π/n) with the resulting in-plane properties being isotropic. Changing material orientations made it clear that the high strains at the split in the split sleeve were reduced if it was aligned with the 45º direction,

coincident with the material orientation with the lowest elastic modulus. This key

observation, that the residual strain field due to cold expansion was much more uniform

with coupons cut in the 45º degree material orientation, eventually led to the design of a

true, quasi-isotropic FML 4 [-60/0/60] variant.

11.1.1 Influence of Mandrel Geometry

The use of a manual cold expansion tool, combined with strain measurements

performed at regular increments of mandrel insertion, made it possible to observe a

relationship between the size and shape of the strain field and the position of the

mandrel. By attempting to understand the effect mandrel geometry may play in the cold

expansion process one gains a more complete understanding of this dynamic process,

including a possible explanation for the difference in strain field between the entry and

exit face. Relatively little attention has been paid to mandrel geometry in the open

literature, although O'Brien[44] published the basic dimensions of the mandrel he used for

cold-expanding thick section aluminum coupons (Figure 159a). Manufacturer data

regarding the actual dimensions of each mandrel are not given, likely due to the

proprietary nature of the information. For this research program, a laser measuring

system (LT-9030M, Keyence Inc, Osaka Japan) was used to determine the profile of the

mandrel (Figure 159b and Figure 159c) to see if the dimensions of the mandrel could

help explain some features of the cold expansion process. The design of this mandrel,

designated as type 8-1-N (FTI Inc, Seattle WA) is similar in function to the one used by

O'Brien[44], but with very different overall dimensions. The same gradually increasing

taper region exists (designated as region A and B in Figure 159c) but the flat region,

which produces the maximum interference (Region C in Figure 159c) is significantly

longer than on the mandrel used by O'Brien[44]. In this case, the flat region is long

enough (4.8 mm) to ensure that the full thickness of the coupon (t=1.64 mm) is

expanded at the same time. Another interesting difference is at the tail end of the

mandrel (region D in Figure 159c), which is much shorter and more blunt than the

mandrel used by O'Brien[44] (Figure 159a), which had a much more gradual taper.

During the cold expansion process, the gradual slope of the mandrel (region A in Figure

159c) ensures that both the entry and exit faces are gradually expanded up to the

maximum expansion. As soon as the mandrel is displaced past the flat landing

(region C Figure 159c) the blunt nose of the mandrel, results in the rapid recollapse of

the material. By the time the mandrel is poised to leave the exit face of the coupon, the

majority of the material radially constraining the hole has been expanded and plastically

deformed by the mandrel and has subsequently recollapsed as a result of its removal.

In contrast, the mandrel used in O'Brien's study[44] had a gradual taper on either side of

the flat landing, that allowed the material to gradually recollapse during mandrel removal

process. Further investigation may be warranted to determine if the addition of a

gradual taper to the cold expansion mandrel has an effect on delamination in fiber metal

laminate materials.

The manner in which the geometry of the mandrel interacts with the material

surrounding the open hole may influence the resultant residual strains and explain why

there is a difference between the entry and exit face. An examination of the situation

immediately before the mandrel leaves the entry face (Figure 160a) shows how the rigid

steel mandrel in conjunction with the tool housing provides constraint in the axial

direction (through shear) during the reverse yielding of the material at the entry surface.

This more uniform three-dimensional constraint may lead to a greater hydrostatic

component of strain, and hence less yielding, resulting in lower and less extensive

residual stresses at the entry surface. The situation is reversed at the exit surface

(Figure 160b) where reverse yielding of the exit face material occurs at the instant that

the mandrel leaves the coupon. With the rigid steel mandrel no longer providing

constraint in the axial direction, increased shear deformation and thus increased

yielding can occur, resulting in higher and more extensive residual strains on the exit
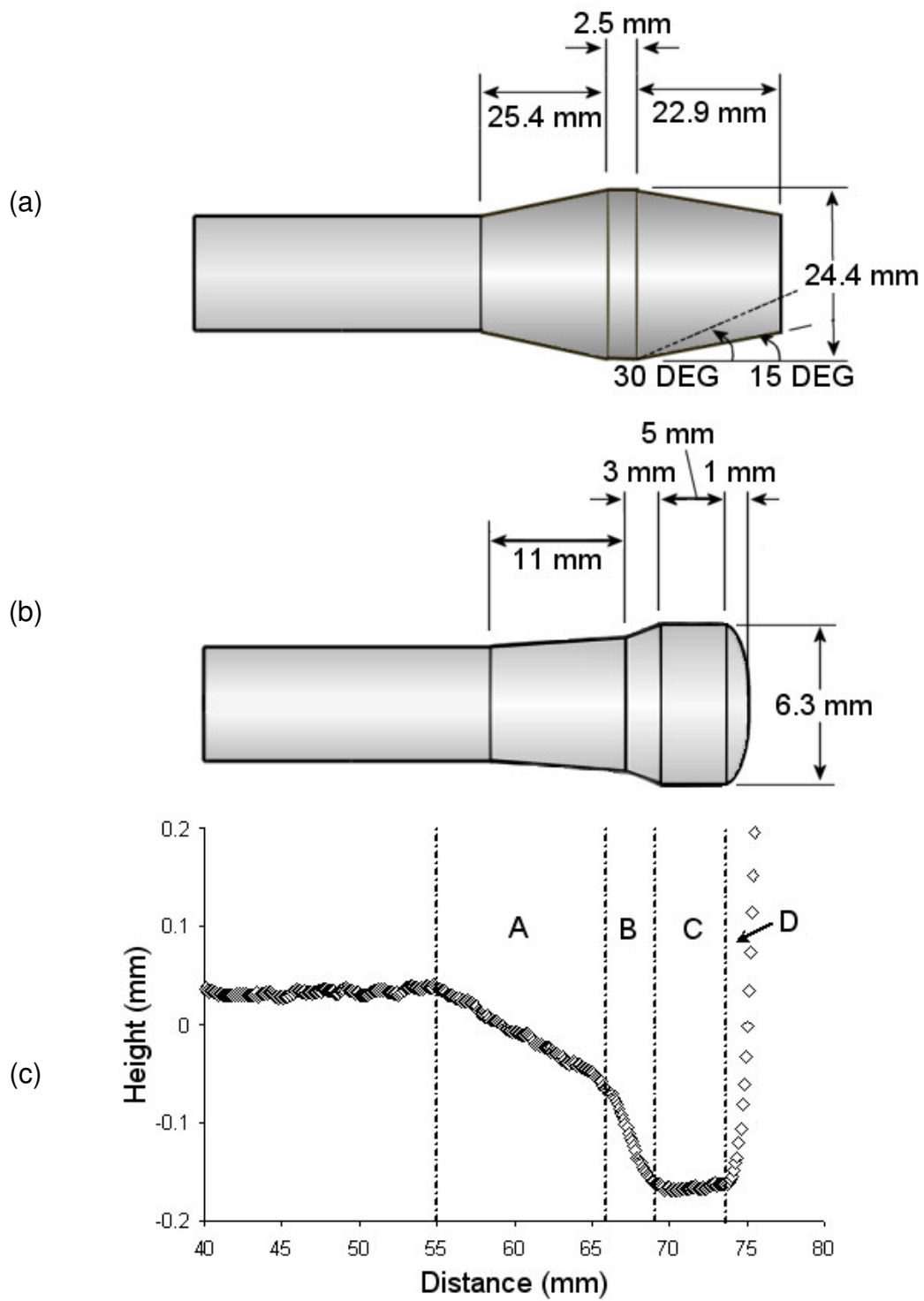
face.

Figure 159: Mandrel profile used for cold expansion process with schematic of the full mandrel overlaid

(a)   (b)
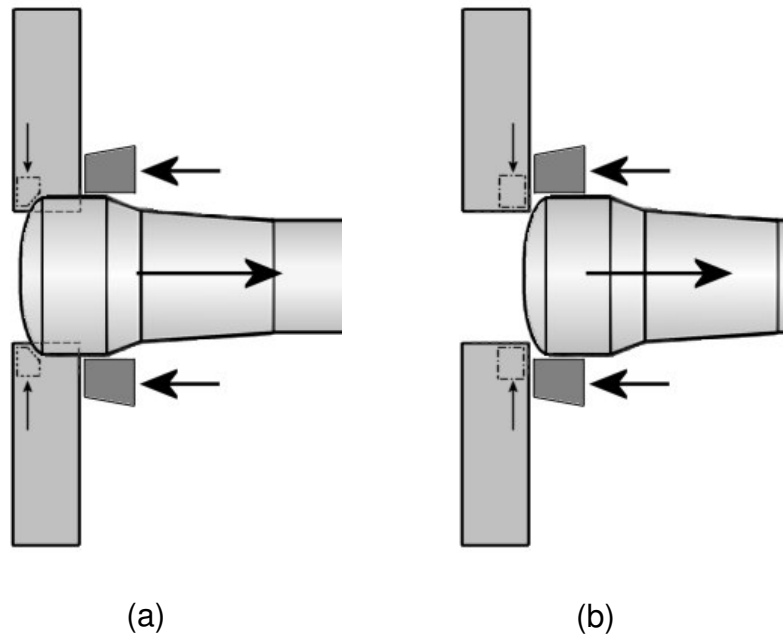
Figure 160: Geometric constraint conditions for a nominal material element (a) at the entrance face and (b) at the exit face

11.2 Fatigue Testing of Cold Expanded Coupons

The fatigue test was the final phase in the research program and was broken down into two stages. The first stage was the baseline fatigue stage, designed to generate baseline fatigue information for unidirectional coupons of 2024-T3 aluminum, FML 3 and FML 4 in the open hole configuration (unexpanded and cold expanded) and determine baseline fatigue life for three different net stresses (S-N curves). Fatigue information was also gathered for riveted coupons made from the same materials, but tested at only one net stress level (263 MPa) due to the significantly improved fatigue life after riveting. One constraint on the design of these experiments was the limited amount of raw materials for making FML as well as limited fatigue test frame availability.

To make efficient use of the available load frame access, FML coupons were fatigued until a crack had extended across the full width of the specimen. During initial pilot

testing, a peak displacement of 0.89 mm (0.035 inches) was associated with bilateral

crack propagation to the outer edge of the coupon for all specimens and thus this

displacement was used as the failure criteria. In effect, failure for FML coupons, was

defined as a change in coupon compliance, while for the aluminum coupons, failure was

defined as crack propagation across the full width and complete physical separation of

the specimen. Thus the number of cycles to failure for aluminum and FML are not

directly comparable, with the FML coupons still retaining substantial residual strength

after "fatigue failure", with residual failure loads ranging from 11.6 kN for FML 3, to

9.6 kN (minimum) for FML 4 [90/0/90] to 11.4 kN (minimum) for the FML 4 variant. The

residual elastic moduli ranged from 22.2 GPa for FML 3, to 21.4 GPa (minimum) for

FML 4 [90/0/90] and 24.12 GPa (minimum) for the FML 4 variant (Chapter 10.2).

11.3 Fatigue Testing of Riveted Coupons

The initial static measurements of the strains during riveting highlighted that riveting is a

manufacturing operation that is very sensitive to the initial placement of the rivet and to

the riveting force. The static riveting results showed more concentric strains around the

rivet hole and stood in contrast to the strain distribution from cold expansion, which

showed a large strain gradient at the location of the split in the sleeve. Unfortunately,

the true magnitude of the strains adjacent to the rivet hole are difficult to measure since

this region is obscured by the driven head on one face and the manufactured head on

the other.

The inclusion of riveting in this research program was deemed important as it is still one

of the dominant fastening methods in the aerospace industry, and one of the benefits of

FML is that it can be riveted in much the same way as monolithic aluminum. From an

experimental mechanics perspective, riveting combines aspects of hole cold expansion from the expanded rivet shank with through-thickness compression from the driven and manufactured heads. The study of riveted joints is a well-established field and although few researchers have published work looking at the effect of riveting with FML, researchers such as Lanciotti and Lazzeri[139] and Lazzeri[88] have clearly shown that this is a viable process and provides a life improvement compared to riveted 2024-T3 aluminum joints.

Although the literature on riveting and the effects of fatigue on riveted joints is relatively extensive for aluminum alloys, often this work has focused on the performance of the joint itself as opposed to the riveting process. However, researchers such as Muller[23] have focused on the applied compression as a variable in the fatigue life of a riveted joint. For a joint, rivet compression can influence the degree of fretting that occurs as well as the degree of expansion of the rivet shank. Schijve[16] in his book on the fatigue of structures discusses how the location of initial crack nucleation can be influenced by rivet compression, with higher degrees of compression moving the crack nucleation location away from the rivet hole. In the idealized case of a zero load transfer joint, compression is still an important variable in fatigue life. Consistent rivet compression ensures that the expansion and degree of interference of the rivet shank is consistent, ensuring proper hole filling. For a zero load transfer rivet, the compression of the rivet and formation of a driven head likely serves to generate a triaxial strain field around the initial pilot hole. The expansion of the rivet shank provides in-plane compression around the pilot hole and the compression provided by the driven head adds a through

thickness strain component. Given the hydrostatic nature of these triaxial strains, it seems likely that less yielding would occur in the material surrounding the rivet hole compared to the cold expansion process.

Proving or disproving the above hypothesis is difficult since in the region of highest strain, near the rivet hole, the area is obscured on one face by the driven head and on the other face by the manufacture head. In an attempt to verify this hypothesis regarding the nature of the strain field close to the hole, an innovative approach using a 2024-T3 aluminum coupon was attempted to measure strains in this region. Using the same static test fixture described in Chapter 5.2.1, a higher resolution camera (PCI Imaging, Sensicam QE, 1280x1024 resolution) along with high magnification optics were used to take a reference image of an aluminum coupon at a magnification of 0.0094 mm/pixel. After the reference image was taken the coupon was coated with high strength tape to protect the surface and then riveted. After riveting the coupon was placed on a mill and both the rivet driven and manufactured heads were carefully milled away, leaving just a small section of the rivet shank in the hole. The coupon was then mounted back in the static test fixture and a "deformed" image was taken and processed using the Vic-2D correlation software (Correlated Solutions Inc). At this magnification, surface disparities on the coupon itself were adequate to perform image correlation and the resultant maximum and minimum strain fields are shown in Figure 161. The images were scaled similarly to the cold expanded coupon results to highlight how much lower the strain values were close to the hole. Of course, these strain values

cannot take into account the compression provided by the rivet head and so a separate approach was used to measure its contribution.

Given the uniformly high rivet squeeze force of approximately 13.3 kN it is reasonable to assume that the manufactured head of the rivet, which is in direct contact with the coupon body, not only compresses the material under the manufactured head but also provides resistance to the extensional load being applied to the coupon during fatigue. To get an approximate sense of the magnitude of this load, pressure sensitive film was placed on both sides of the aluminum coupon to measure the resultant normal pressure after riveting.
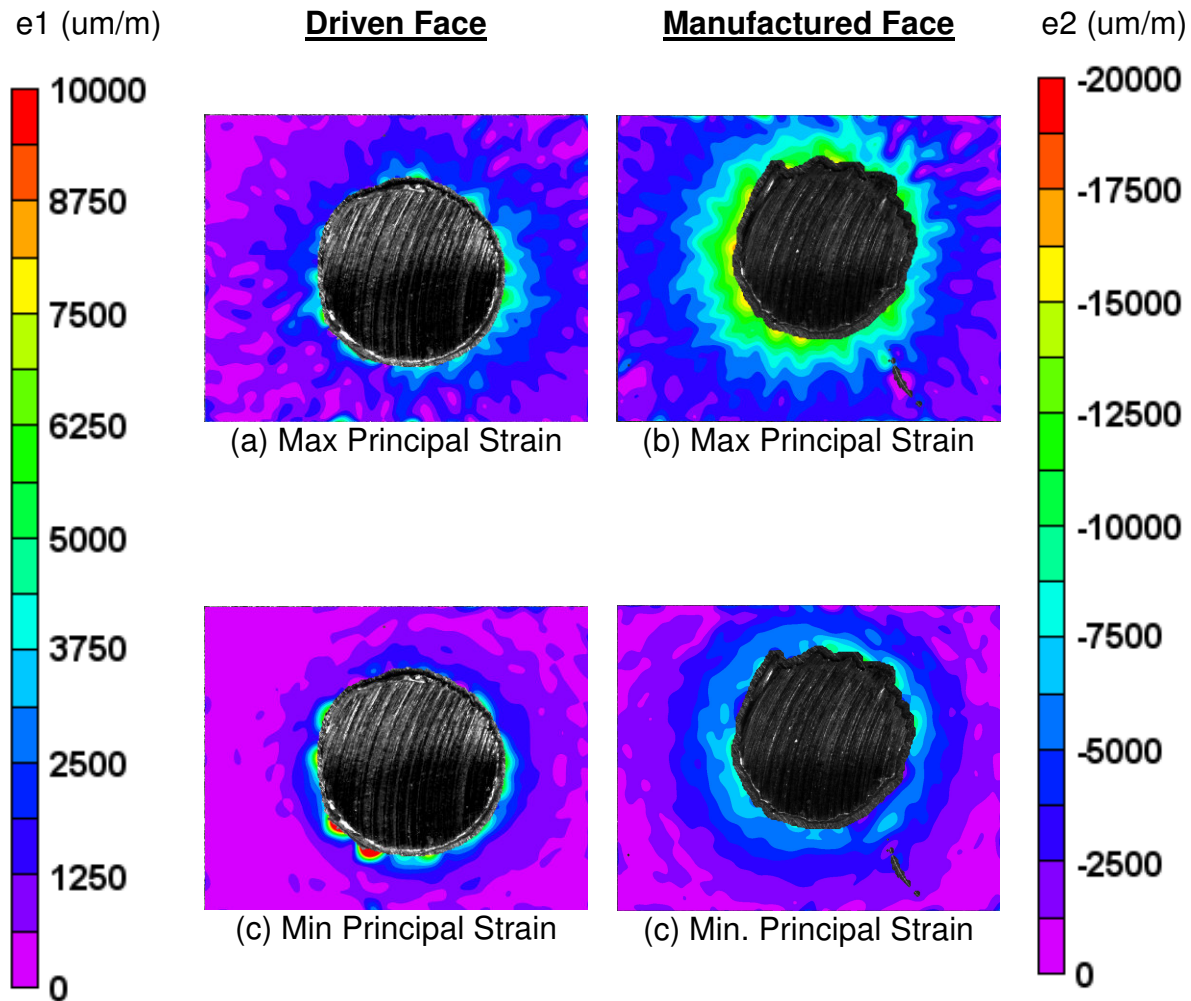
Figure 161: Minimum principal strains for an aluminum coupon (specimen AL-L-64) on both the driven and manufactured faces with shank

Pressure sensitive film comes in various grades, rated according to the pressure it is sensitive to. When a normal force is applied to the film, ink capsules within the film rupture and cause the film to turn a reddish-pink color. The intensity of the film stain can be measured using a scanner, which can digitize the film, allowing the stain to be converted to pressure using a previously determined calibration curve. As part of a previous research program[140] a calibration equation (Equation 11.3.1) and

corresponding coefficients (Table 14) were determined for use in calibrating low, medium and high pressure film.

$$P = a + b \cdot y + cy^2 + d \cdot y^3 + ex + fxy + gxy^2 + hxy^3$$ 11.3.1

where P is the pressure in MPa, x is the humidity at the time the stain was taken, y is the grayscale pixel intensity value from the pressure film stain and a,b,c,d,e,f,g,h are the coefficients from Table 14.

Table 14: Coefficients for determining pressure from pixel intensity values

Coefficient	Low	Medium	High
a	1.189E+02	1.379E+02	-3.357E+02
b	-1.555E+00	-1.384E+00	7.378E+00
c	7.538E-03	6.862E-03	-3.595E-02
d	-1.263E-05	-1.325E-05	5.033E-05
e	-1.082E+00	2.074E-01	2.310E+01
f	1.469E-02	-5.519E-03	-3.260E-01
g	-7.255E-05	3.126E-05	1.524E-03
h	1.225E-07	-5.442E-08	-2.350E-06

Figure 162 shows a greyscale representation of the various grades of pressure film placed under the manufactured head, while Figure 163 shows the corresponding pressure distribution from these images. Pressure film was also placed under the driven head of the rivet, but the pressure distribution was so localized around the rivet hole that a discernable pressure stain could not be measured.
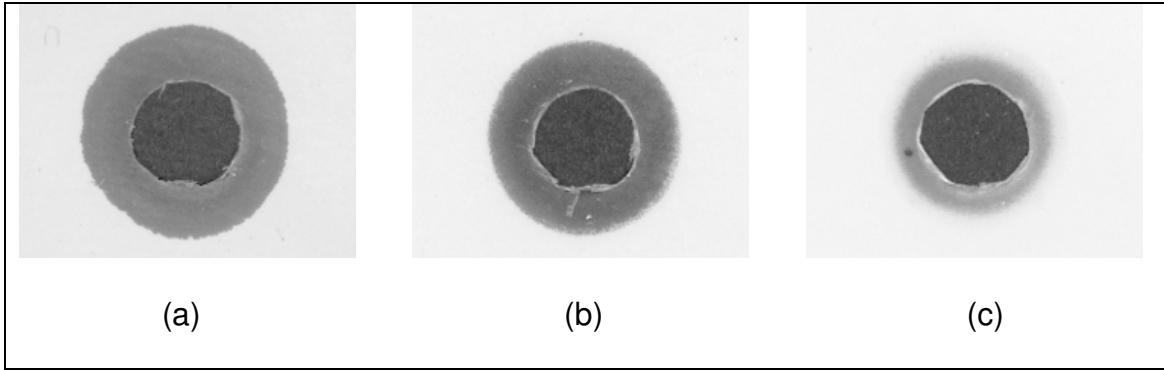
Figure 162: Pressure film stains from (a) low (b) medium and (c) high grade films taken from the manufactured head of a rivet
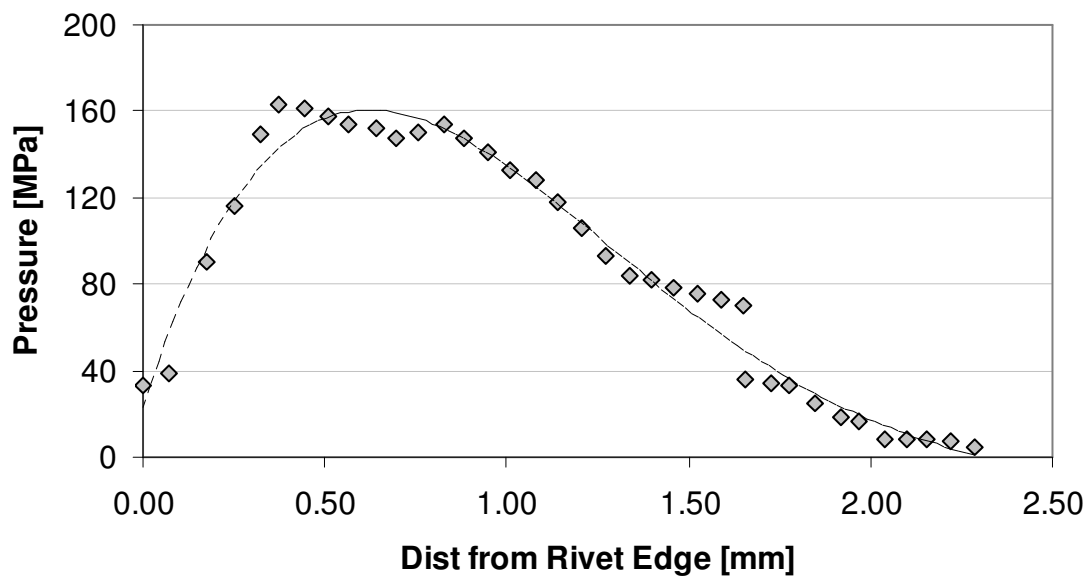
Figure 163: Pressure distribution for consolidated pressure film stains on manufactured head of a riveted coupon. Regression line for visualization purposes only

At this point, two separate measurements are now available. The first is the in-plane residual strain field surrounding the rivet (after the manufactured and driven heads have been removed) and the second is the normal pressure distribution measured under the manufactured head of the rivet.

For the case of the rivet, a linear-elastic superposition approach was used to estimate the total strain field under the rivet head. The total strain field was assumed to be comprised of radial (ε_r), hoop (ε_h) and through thickness strains (ε_z). For the in-plane measurements, the radial and hoop strains were measured using image correlation. Assuming from the magnitude of these strains that some plastic deformation was occurring close to the hole, the triaxial strains (ε_z) in the through-thickness direction were estimated by assuming volume constancy[34,109]:

$$0 = \varepsilon_z + \varepsilon_r + \varepsilon_h \qquad\qquad 11.3.2$$

It is interesting to note that this approach suggests that the through-thickness strains closest to the hole are actually tensile in nature due to the large radial and hoop strains being applied. This finding seems to support the work done by Poolsuk and Sharpe[34] who used a linear variable displacement transducer (LVDT) to measure the change in thickness near cold expanded holes.

The compression applied by the manufactured head of the rivet was assumed to result in radial and hoop strains as well as strains in the through thickness direction. Since the normal stresses measured with pressure film were well in the elastic range for aluminum, a very simple linear elastic approach was used to calculate the applied strains using the equations below:

$$\varepsilon_z = \frac{\sigma_N}{E} \qquad\qquad 11.3.3a$$

$$\varepsilon_r = -v\frac{\sigma_N}{E} \qquad\qquad 11.3.3b$$

$$\varepsilon_h = -v\frac{\sigma_N}{E} \qquad\qquad 11.3.3c$$

where σ_N is the normal stress measured using pressure sensitive film, v is the Poisson's ratio of the aluminum and E is the elastic modulus.

The linear superposition of the strains due to the compression of the rivet and the strains due to the expansion of the rivet shank provided an estimate of the total strain field underneath the rivet head. Radial and hoop strains from a cold expanded coupon with a similar interference ratio (rivet – 3.0%, cold expansion – 4.0%) were measured previously using image correlation techniques. The same approach was used to estimate the through thickness strains and a comparison of rivet and cold expansion strains is shown in Figure 164. An analysis of the Von Mises stresses shows that the elastic-plastic boundary is located at approximately 0.4 mm from the hole edge for the riveted coupons, but that for cold expansion, the strains in the entire region shown in Figure 164 are beyond yield.
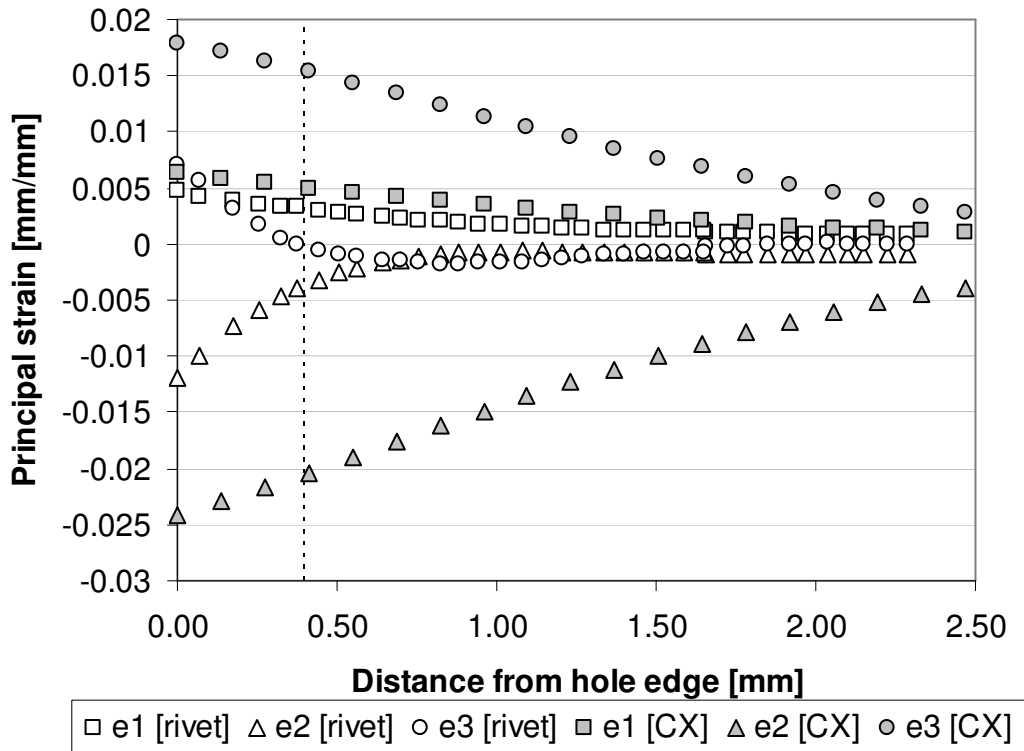
Figure 164: Hoop (e1), radial (e2) and through thickness strains (e3) for both a riveted and cold expanded (cx) coupon. Note: dotted line denotes the elastic-plastic boundary for the riveted coupon only

From a fatigue perspective, the cold expansion process appears to be more successful in plastically deforming the material around the hole and creating a large region of compressive residual stress. However, under fatigue loading, the strain field around the rivet also shows some significant differences from that after cold expansion. After cold expansion, and before the formation of a crack, the strain field due to the applied load (excluding residual stresses) is essentially identical to that of an open hole, which is not the case after riveting as shown in Figure 165. Research by Lanciotti and Polese[91] provides an interesting perspective on these results, as Lanciotti and Polese[91] performed a series of tests using interference fit steel pins to provide varying degrees of

interference ranging from 0.5-2.5%, in zero load transfer aluminum coupons. Their

research showed that hole cold expansion (performed with a similar level of

interference) was more effective in increasing fatigue life[91], but since the results from

this research program show the opposite effect, it seems likely that it is not just the

radial expansion of the shank, but also the compression afforded by the rivet head that

plays a role in improving fatigue life. A recent paper by Keshavanarayna et al[92], looking

at fatigue-based severity factors for different types of joints, also noted the effectiveness

of riveted zero load transfer coupons. Keshavanarayna et al[92] explained the improved

fatigue performance on the reduction in the stress amplitude and the increase in mean

stress level that occurs locally due to hole filling by the expanded rivet shank.

Aluminum Cold Expanded	Aluminum Rivet
(Net Section Stress = 198 MPa)	(Net Section Stress = 263 MPa)
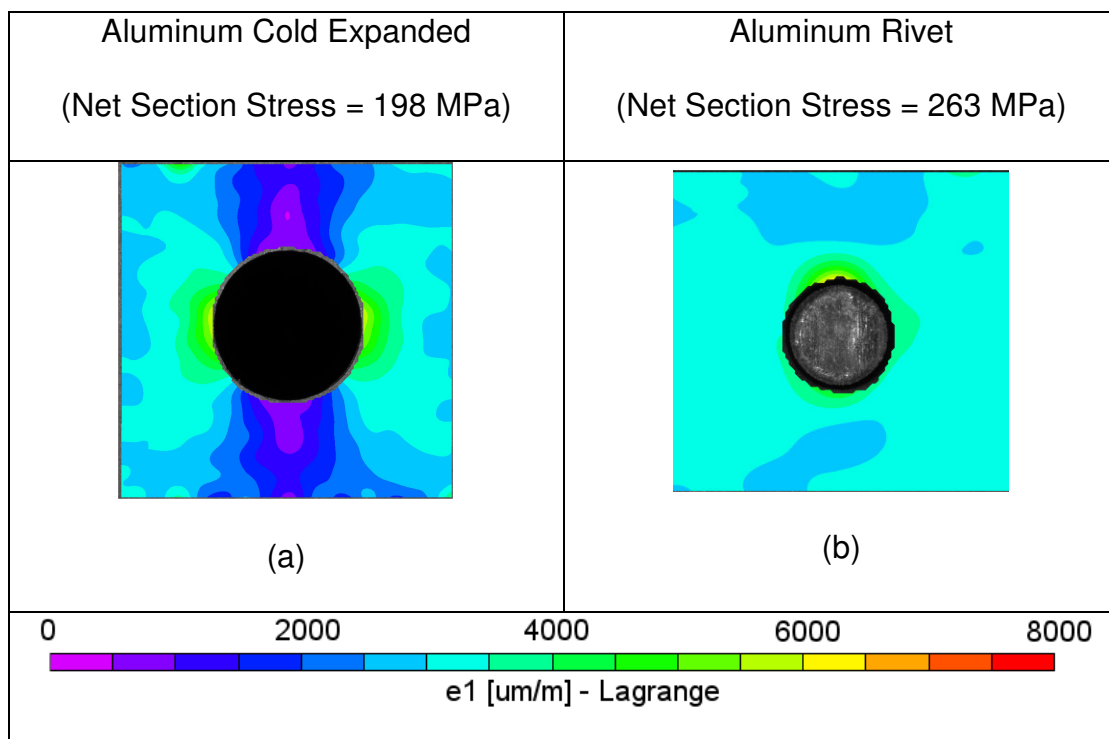
Figure 165: Comparison of maximum principal strains between (a) cold expanded
aluminum (specimen AL-L-27) and riveted aluminum (AL-L-9)

To verify Keshavanrayna et al's[92] hypothesis, horizontal strain profiles along lines

perpendicular to the load were obtained from the image correlation measurements

during fatigue loading for both a riveted and a cold expanded coupon. The strain

information was extracted at both the minimum and maximum of the load cycles and the

strain measurements were converted to hoop stress (σ_1) using Hookes law and

assuming linear-elastic isotropic behaviour:

$$\sigma_1 = \frac{E}{(1+v)(1-2v)} \cdot \left[(1-v)\varepsilon_1 + v\varepsilon_2 \right] \qquad \text{11.3.4a}$$

Clearly, a linear elastic stress-strain conversion is not completely valid for the cold

expansion results due to plasticity close to the hole, so the Von Mises failure criteria

(Equation 7.1.13) was used to determine the elastic-plastic boundary. The hoop stress

results for both cold expansion and riveting are shown in Figure 166 with the dotted line

representing the elastic-plastic boundary. At the elastic-plastic boundary both the mean

stress (Equation 11.3.5) and the stress amplitude (Equation 11.3.6) were determined for

the cold expanded and riveted coupon and the results presented in Table 15.
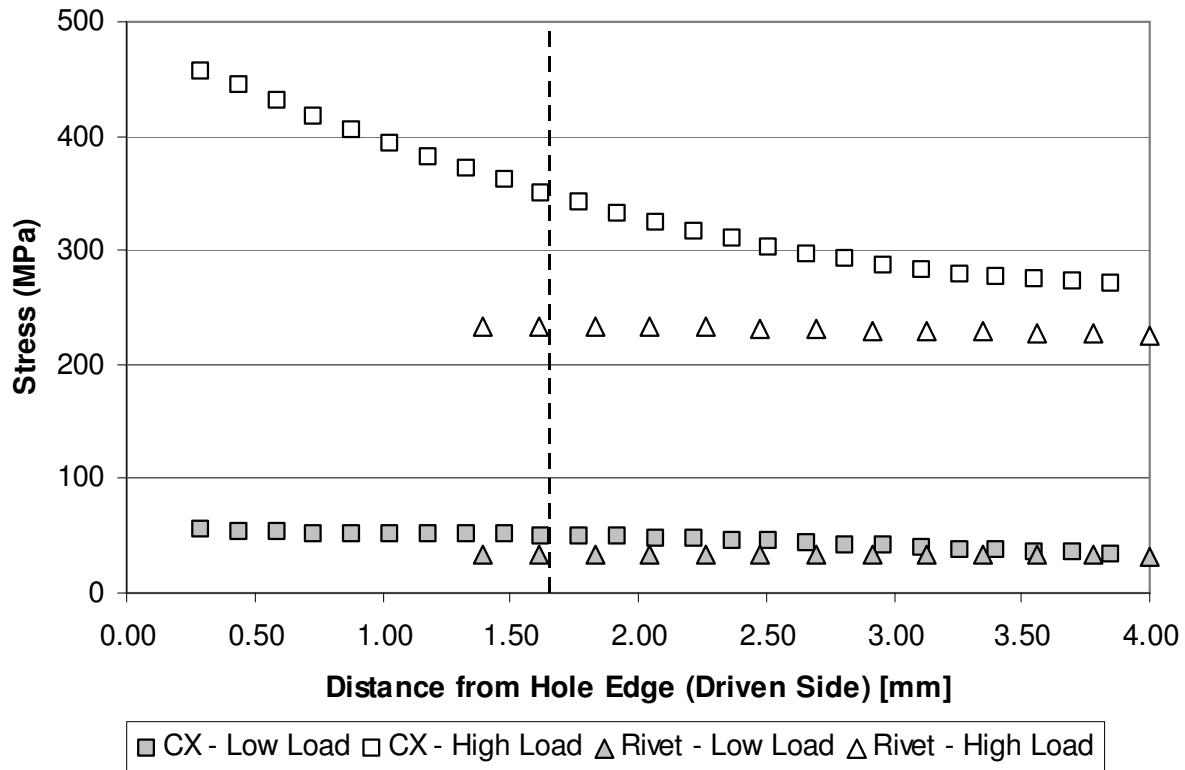
Figure 166: Cold expansion (specimen AL-L-27) and rivet strains (specimen AL-L-41) at high load (10 kN) and at low load (1 kN). Note: Dotted line denotes elastic-plastic boundary for cold expansion only

$$\sigma_{mean} = \frac{\sigma_{\max} - \sigma_{\min}}{2}$$ 11.3.5

$$\sigma_{amplitude} = \sigma_{\max} - \sigma_{\min}$$ 11.3.6

Table 15: Comparison between cold expansion and riveting stress values during fatigue loading

	Cold Expansion	Riveting
Mean Stress (σ_{mean})	150 MPa	100 MPa
Stress Amplitude (σ_{amp})	299 MPa	199 MPa
Stress Ratio (R_{eff})	0.14	0.15

These results clearly confirm Keshavanarayna et al's[92] hypothesis, showing that both the mean stress, and more importantly the stress amplitude, are significantly reduced in the riveting case. Interestingly, the effective stress ratio ($R_{eff}=\sigma_{max}/\sigma_{min}$) is very similar in both cases, but according to Schijve[16] it is the reduction in stress amplitude that plays the largest role in determining fatigue life.

It appears clear that two possible factors play a role in the enhanced fatigue performance seen with the riveted coupons. The first is the interference from the rivet shank and the second is due to the compression created by the formation of the driven head. Our previous measurements and analysis have shown that the residual strains due to the riveting process are lower than those from cold expansion so a closer investigation of the role of the rivet head is in order.

Given the uniformly high rivet squeeze force of approximately 13.3 kN it is reasonable to assume that the manufactured head of the rivet, which is in direct contact with the coupon body, not only compresses the material under the manufactured head but also provides resistance to the extensional load being applied to the coupon during fatigue and as a result reduces any potential crack opening displacements.

One means of quantifying this is to estimate the change in the net section stress due to hole filling and due to friction between the rivet manufactured head and the coupon. From the pressure distribution shown in Figure 163, the average normal stress (σ_n) under the rivet head was estimated to be approximately 87 MPa.
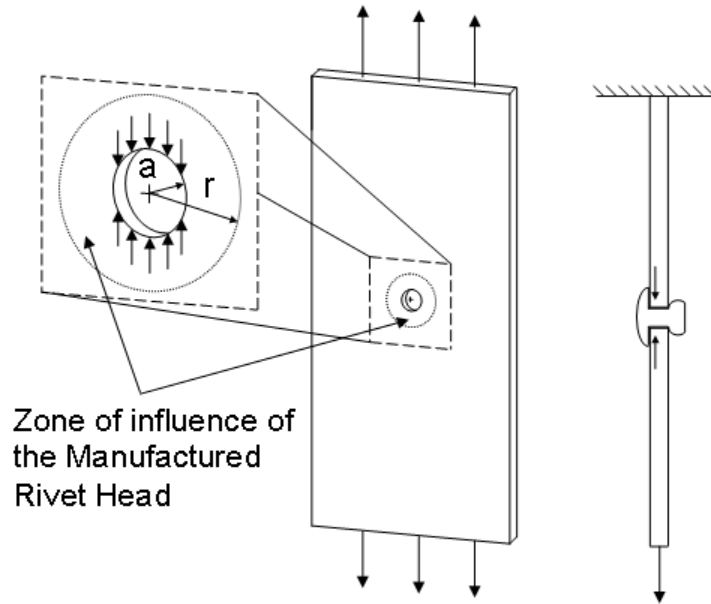
Figure 167: (a) Front view of riveted coupon highlighting pressure affected zone and (b) side view of rivet showing line of action of frictional force

The average area (A_{avg}) over which the normal stress from the rivet head acts, is

shown graphically in Figure 167, with the actual average area measured directly from

the pressure film stain and determined to be approximately 3.22×10^{-5} m^2. The

average normal force (F_N) could then be estimated from $F_N = \sigma_n A_{avg}$ which gave an

average force of 2801 N. The coefficient of kinetic friction (μ_k) between the aluminum

head and the rivet, assuming no lubrication between the surfaces, is $\mu_k = 1.4$ and thus

the frictional force (F_f) can be determined from $F_f = \mu_k F_N$ which gives a frictional force

acting opposite the applied load of approximately 3.9 kN. Given that the applied load to

the coupons is 14.2 kN, simple superposition of the forces shows that in the local area

under the rivet the net applied load would be reduced to 10.3 kN. If one uses the

original net section area of the riveted coupon (taken through the center of the rivet hole) equal to 5.4 x 10^{-5} m^2 then the local net section stress has been reduced to

($\sigma_{net}=F_{net}/A=10.3kN/5.4x10^{-5}$ m^2) to 191 MPa (27% reduction) and if one assumes perfect hole filling from the rivet, the net section area increases to 5.79 x 10^{-5} m^2, which reduces the local net section stress to 178 MPa (32% reduction), further supporting the hypothesis that the clamping force of the rivet and the frictional force it generates, is the root mechanism behind the increased fatigue life of the riveted coupons.

11.4 Effectiveness of New FML 4 [-60/0/60] variant

It is interesting that so few papers in the open literature deal with property optimization of fiber metal laminates. Van Rooijen et al[141] approached the topic of property optimization in FML by focusing mainly on improvements in the constituent components; determining the effects that changes to the aluminum or glass fibers would have on material properties, without addressing the conventionally accepted layup sequence of the various FML grades. More recent work Nam et al[142] looked at optimizing the stacking sequence in FML 3 by combining a classical laminated plate approach for determining material properties with a finite element method, using a Tsai-Hill failure criterion to determine material failure, and a genetic algorithm to predict the optimum ply sequence. As an outcome Nam et al[142] presented several possible stacking sequences, each optimized for a specific type of loading, emphasizing the importance of having several grades of FML to choose from depending on the application.

One possible reason that more isotropic FML laminates have not been pursued is the reluctance of composite engineers to produce quasi-isotropic materials. The quasi-isotropic approach for standard carbon fiber reinforced polymers (CFRP) is a design philosophy that is typically used as a last resort when there is a lack of information regarding a component's loading history. More modern design practice with composite materials relies on having some information regarding the applied loads and the design stresses so that the stacking sequence of the CFRP can be designed accordingly. A typical example would be a monocoque composite bike frame where each joint will typically have a specific layup based on typical rider loads and the design intent of the frame (i.e. optimized for weight or stiffness). Although fiber metal laminates are a class of composite, they are often referred to as hybrid materials, since they are hybrids of monolithic metal and glass fibers. As a hybrid material, FML do not have the same degree of customization as typical CFRP's, and the results of this study would certainly support the adoption of a new grade of quasi-isotropic FML 4 based on the [-60/0/60] stacking sequence.

Comparisons between the FML 4 variant and FML 4 [90/0/90] are complicated by the orthotropic nature of FML 4 [90/0/90]. Although the elastic modulus of the FML 4 variant is approximately 13% lower than FML 4 [90/0/90] in the transverse direction, a comparison of the off-axis properties of both materials shows a significantly better performance for the quasi-isotropic FML 4 variant, both of in terms of modulus and yield strength in the longitudinal and 45º degree orientation. From a fatigue perspective, the quasi-isotropic FML 4 variant also has superior fatigue life in the longitudinal and

45º degree orientations, but has a lower fatigue life in the transverse direction. Although

the difference in fatigue life may preclude immediate use in aerospace, the isotropy of

this new layup would certainly be suitable for static applications or applications involving

low cycle fatigue.

11.5 Error Analysis

The potential errors in various aspects of this research are assessed and discussed in

this section.

11.5.1 Static Testing and Measurements

Static strain measurements were made using digital image correlation and any error

analysis needs to focus on the potential errors associated with this measurement

technique. For the 3D image correlation measurement, the system sensitivity was

determined by taking multiple reference images and processing these images to

determine the level of strain below which measurements were difficult to discern from

noise in the system (CCD, variations in lighting, vibration etc). As mentioned previously

in all cases, the strain sensitivity for the 3D DIC setup was better than ±50 µε and the

out of plane displacement (w) sensitivity was better than ±0.0015 mm. Given that our

camera setup met the parameters stated in Chapter 2.5.2.2, the typical uncertainty for

in-plane displacement was estimated from the ratio D/10,000, where D is the in-plane

dimension of the object being measured. Uncertainty in the out-of-plane displacement

was estimated from the ratio Z/50 000 where Z is the distance from the object to the

CCD[30]. For the current, setup D was approximately 66 mm and Z was approximately

112 mm, giving an out of plane uncertainty on the order of 0.6% and an in-plane

displacement error on the order of 0.2%

For 2D image correlation, one of the largest sources of error is out-of-plane displacement. Since 2D DIC was used only for the fatigue testing, a digital dial gauge (Mitutyo Inc) was used to determine the average out-of-plane displacement during a fatigue cycle, which measured approximately 0.02 mm. The ratio ($\Delta z/z$) where Δz is the out of plane displacement and z is the distance from the CCD to the coupon face can be used to provide an estimate for the uncertainty in the measured strain results. With a CCD to coupon distance of 250 mm the effect of out of plane displacement is approximately 8.0×10^{-5} mm/mm which is more than two orders of magnitude smaller than the peak strains measured on these coupons.

11.5.2 Closed Form Solution

Although the chosen approach for modeling the rivet strains was similar to that used by Muller[23], in that he also only considered expansion of the shank and did not take into account compressive stresses from the rivet head, results from the fatigue test suggest that for zero load transfer rivets, the compression from the driven head is an important variable and this was discussed in detail in Chapter 11.3. Although the analytical model used did not take this variable into account,the calculated strains still corroborated well with the measured strains. This was not surprising since the strains that were measured were in the region outside of the driven and manufactured head, and it is likely that the strains in this region were predominately due to the interference from the rivet shank and not due compression from the rivet head. The strain due to compression from the rivet head appeared to be lower and more localized than that due to expansion of the rivet shank, and it is likely that that a more sophisticated model may be required to attain a more accurate strain solution close to the rivet hole.

In addition, the fidelity of the closed form model was limited by the available material

property data. For this work, a materials handbook[129] was consulted for aluminum

material properties in both the longitudinal and transverse orientation. These material

values are average values from many material batches and may not provide an exact

match to the material that was used here. For modeling FML, material properties were

obtained from an earlier test performed at NRC on various FML grades which provided

elastic modulus and yield strength information at 15º degree increments. The same

prepreg batch was used in our initial test coupons, ensuring fairly good accuracy for the

material information.

11.5.3 Fatigue Testing

The largest source of uncertainty in the fatigue testing was the relatively small sample

size available, which precluded determining the statistical significance of the differences

seen among the test groups. To compensate to some degree for the small number of

specimens, additional effort was made to reduce experimental variability.

Cold-expansion of the coupons was done in-situ in the load frame, using a precision

alignment jig to ensure that the mandrel was orthogonal to the coupon. For riveting, a

precision support fixture was designed to support the coupon, and rivets were milled to

size for each coupon, so that the amount of shank protruding was identical. The

instrumented arbor press also helped assure that consistent compressive loads were

applied to the rivet. The test plan required static loads identical to the fatigue loads be

applied to all coupons before the start of fatigue testing and this generated a benchmark

strain field that could be used to independently verify that the fatigue test machine was

applying the correct loads during the fatigue cycle and that the image capture system was capturing images at maximum load during the fatigue cycle.

The displacement limit of 0.89 mm, that was used to define fatigue failure, is adequate for coupons of the same material, cut in the same orientation. However, when comparing coupons of different orientations or different grades of FML some uncertainty will be introduced since displacement for a given load is a function of the material modulus. For the final phase of testing, the fatigue life comparison between the FML 4 [90/0/90] and the FML 4 variant was redefined on the basis of crack growth to remove this small bias.

11.6 Innovation and Contribution to Scientific Knowledge

Several innovations were developed as part of this research program. The largest innovation was the development and testing of a new quasi-isotropic FML 4 variant. Another innovation was the use of digital image correlation to measure cure induced residual stress in FML panels. Measuring surface strain during the cold expansion process had never been attempted using DIC, and both the static and fatigue strain measurements revealed information to better help understand this process in FML.

11.6.1 Scientific publications and conference proceedings

As part of this research program, several scientific publications and conference proceedings have been prepared and presented. The following is a list of the published and submitted scientific publications:

Journal Articles Accepted

1. Backman D, Liao M, Crichlow L, and Patterson EA *The use of digital image correlation in a parametric study on the effect of edge distance and thickness on residual strains after hole cold expansion*. Journal of Strain Analysis for Engineering Design, vol 43, number 8, 2008.

2. Backman D, Cowal C, and Patterson EA. *Analysis of the effects of cold expansion of holes using thermoelasticity and image correlation*. Fatigue and Fracture of Engineering Materials and Structures, In-press.

Conference Proceedings Accepted

1. Backman D and Patterson EA. *Measuring residual strains in aluminum and fiber metal laminate materials during cold expansion and riveting*, 2008 Society of Experimental Mechanics Annual Conference, Orlando, Florida.

2. Backman D and Patterson EA. *Fatigue life enhancement of fiber metal laminate materials as a result of hole cold expansion*, 2009 Society of Experimental Mechanics Annual Conference, Albequrque, New Mexico.

3. Backman D and Patterson EA. *Fatigue cracks in fibre metal laminates in the presences of rivets and cold expanded holes*, 2010 Society of Experimental Mechanics Annual Conference, Indianapolis, Indiana.

4. Backman D, Sears T, and Patterson EA. *Development of a new fiber metal laminate variant optimized for cold expansion and riveting*, 2011 International Conference on Aeronautical Fatigue, Montreal, Quebec.

12.0   RECOMMENDATIONS AND FUTURE WORK

The results from these tests suggest several avenues of investigation for future work in

this area. These areas can be broadly categorized as cold expansion process changes,

FML material changes, and new avenues of investigation.

12.1 Cold Expansion Process Changes

The results of both the static and fatigue portion of this research show that aluminum

and FML could benefit from an improved cold expansion process. Although there is no

doubt that the current split sleeve cold expansion process is effective in extending

fatigue life of both 2024-T3 and FML materials, the TSA data from the exit face shows

that the current cold expansion process is more effective at extending life in the early

stage of the fatigue process on the exit face. Crack growth information from the entry

face shows that, for cracks of less than approximately 1 mm, the number of cycles

required is only minimally decreased. Differences in the strain field between the two

faces, also show up on the static coupons and the current hypothesis for this

phenomenon is that a difference in geometric constraint exists between the material on

the entry and on the exit face.

As mentioned in the literature survey, the idea that the cold expansion process results in

an asymmetrical three dimensional strain field through the thickness of a specimen has

been noticed by other researchers. Although no research has looked at whether

specimen thickness plays a role in this phenomenon, there is no doubt that there is a

difference in residual strain between the entry and exit faces of the coupon, even for the

thin 1.42-1.70 mm coupons used and that this difference plays a role in limiting the

fatigue life of a cold expanded coupon. One interesting approach to this problem has been "double cold expansion" which involves performing cold expansion twice, but changing the direction of the mandrel so that each face of the coupon has been both an exit and an entry face. This type of procedure was modeled analytically by Jang and Kim[143] and used experimentally by both Bernard et al[144] and Stefanescu[45] to extend the fatigue life of open hole coupons. This "double cold expansion" is not that practical in a production environment and cannot be used where only one face of a structure is accessible. The fact that it does improve fatigue life supports the need to develop a viable modification to the cold expansion process that could achieve this in a more efficient manner.

One possible avenue of research would be to examine if the split sleeve cold expansion mandrel could be modified to reduce the additional geometric constraint on the entry face and thereby provide a more three dimensionally uniform cold expansion process. This approach was examined briefly by O'Brien[96], who investigated reducing the degree of taper at the mandrel head from 30º to 15º (Figure 159) as way of reducing the strain rate during the cold expansion process. Although he did not directly compare the effect that this modification had on the exit strains from a standard mandrel, a review of his data indicated that this modification reduced the exit strains and may have a positive effect on fatigue life[96]. Chakherlou and Vogwell[145] tried a similar approach, modifying the mandrel more significantly and reducing the taper to just over 1º. Although no corroborating strain measurements were presented, Chakherlou and Vogwell[145]

presented FEA and fatigue results that demonstrated a more even strain field around the entry and exit faces, as well as fatigue crack nucleation occurring away from the central hole.

Another possible approach would be to look at cold expansion methods that eliminate the split sleeve. The strain measurements clearly showed that the split sleeve and the material deformation resulting from it (Figure 168) have an effect on the residual strain field. Although modifying the cold expansion process to remove the split has been the subject of research by Karabin et al[146], who showed some potential improvements with a modified "split sleeve-less" method, in the current research, the strain concentration at the location of the split did not appear to influence crack nucleation during fatigue loading.

(a)   (b)
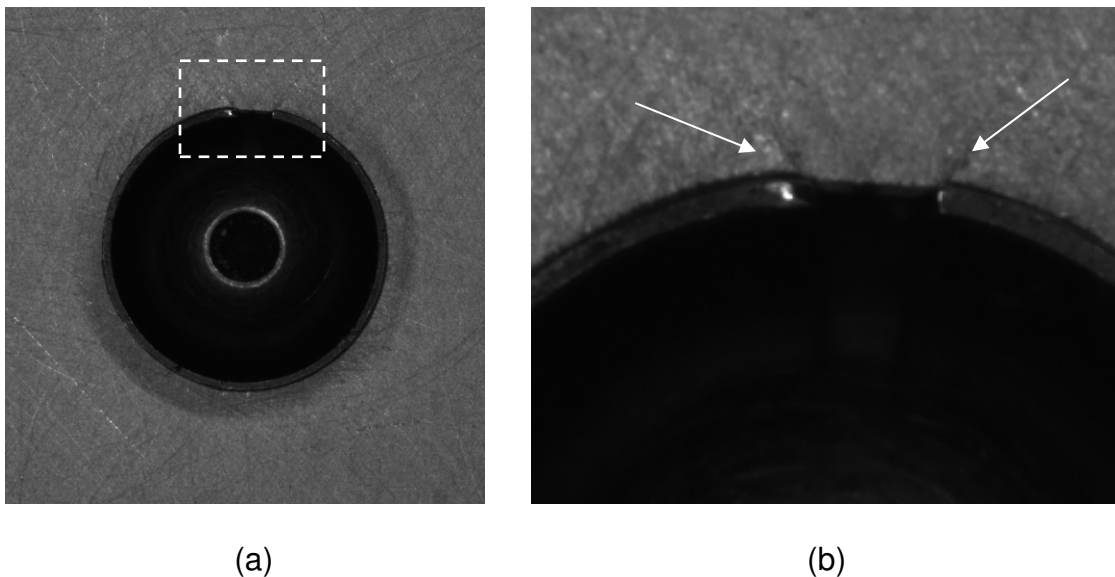
Figure 168: (a) Overview of open hole at the end of the cold expansion process. Location of the split sleeve highlighted in white box. (b) Close up view of split sleeve region with arrows highlighting deformation caused by the sleeve

The static setup used in this research program to make strain measurements during cold expansion would be ideally suited to determining the effectiveness of new mandrel designs. Using the same laser profilometer, the shape of the new mandrel could be measured and through the use of that information, the resulting strain on the entry face could be recorded and correlated to the effective interference of the mandrel as it displaces through the coupon. Using a mirror setup, it might also be possible to make concurrent measurements of the strain on the exit face as well. Investigation of a chemical etching capability would also be complementary to many of the investigations above, as this method could quantitatively address the issue of how much disbond occurs on the entry and exit face after cold expansion.

12.2 FML Process Changes

During the manufacturing process, fiber metal laminate materials are particularly susceptible to residual stress effects due to the mismatch in the coefficients of thermal expansion between the 2024-T3 aluminum and the S2 glass prepregs.   The proof of concept work that was performed to measure these residual stresses using image correlation showed that the new FML 4 variant has tensile residual stresses approximately equal to those of FML 3 or FML 4. Lowering the tensile residual stresses in the aluminum layer of the new FML 4 variant would be a simple way of improving its fatigue performance compared to standard grade FML 3 or FML 4. A new lower temperature cure process has been developed at NRC, specifically for FML and other hybrid-like materials, and the residual stress measurement method mentioned above would be ideal to quantify the change in residual stress resulting from this or other cure cycles.

A more advanced possibility would be to look at new prepreg systems that could be bonded to the aluminum without the need for a high temperature cure cycle. Combining this with new more fatigue resistant grades of aluminum might allow for a more fatigue resistant quasi-isotropic FML 4 variant, one that could perhaps be used in fatigue rated applications.

12.3 Future work

One possible area for future investigation would be to examine non-destructive evaluation technologies that would allow for real-time determination of the delamination state in the outer and inner aluminum plies during fatigue cycling. Of special interest would be an inspection process that could reveal the condition of the inner aluminum ply in FML 4. Currently no non-destructive technology exists to do this, and researchers who have examined the middle plies have had to rely on chemical etching of the aluminum and mechanical abrasion of the prepreg[147]. One possible candidate technology for looking at delamination in the outer aluminum plies would be lock-in thermography or a variant thereof which might be capable of real time disbond measurement.

Another area of investigation was inspired by an observation from the fatigue testing of FML 4 [90/0/90] in various material orientations and the difference in fatigue life between coupons from each of the orientations. This observation regarding the off-axis fatigue life of FML was supported by the results of the ultrasonic inspection which showed a significantly different area of disbond between coupons from the different material orientations. However, relatively little regarding this phenomenon has been

discussed in the literature with the most comprehensive work to date done by

Kawai et al[148,149] who focused solely on FML 2 in addition to a paper by

Chang et al[147], who focused on notched FML 4 and FML 4 with starter cracks. Chang

et al[147] made the observation that for off-axis laminates, the applied stress level in the

aluminum is increased leading to earlier "crack initiation". From an engineering design

perspective, determining the stress in the aluminum layer of an FML is relatively

straightforward, using the analytical solution presented in Chapter 7.6. If a relationship

could be determined between the effective stress in the aluminum layers and the

corresponding fatigue life, then it might be possible to use this as a generic method to

predict the fatigue life of other FML 4 variants

13.0   CONCLUSIONS

The aim of this thesis was to produce a new FML variant optimized for both cold expansion and riveting. To achieve this aim, three research objectives were proposed:

1. Experimentally measuring the strains in fiber metal laminates due to both the cold expansion and riveting process and establishing the effect of these processes on structural performance.

2. Developing a theoretical model that could be used to analytically predict the strains resulting from the hole cold expansion and riveting process.

3. Develop and test new variants of FML, optimized with regards to standard manufacturing processes such as cold expansion and riveting.

The broader conclusions from this research program have been grouped according to each of the objectives and detailed below:

13.1 Experimental Measurements

The full-field strains resulting from cold-expansion and from riveting on various grades of FML were measured using the digital image correlation technique. The cold-expansion results showed how the residual strain field was dependent on the split sleeve direction relative to the material orientation. These static strain measurements showed that changing the direction of the split sleeve could significantly reduce the magnitude of the residual strains, especially if the split was oriented at 45º degrees to the longitudinal axis, which in FML 3 and FML 4, corresponded to the orientation with lowest elastic modulus and lowest yield strength.   It was this observation that

suggested that designing a more isotropic fiber metal laminate material would improve performance after cold expansion and riveting.

An explanation for the mechanism behind the cold expansion process in FML was provided by observing cross-sectioned micrographs of the interior plies in FML after cold expansion. Indications of disbond close to the edge of the cold expanded hole suggested that it was the introduction of compressive residual stresses into the aluminum layers by the oversized mandrel that played the dominant role in extending fatigue life, as it appeared that the glass fibers in the immediate vicinity of the cold expanded hole disbonded due to the cold-expansion process.

13.2 Development of a Theoretical Model

An effective closed form solution for modeling stresses and strains in both aluminum and FML 3 was presented. Reasonable corroboration was shown between the analytical and experimental results for aluminum, while the best was corroboration was achieved for FML 3.

Classical laminated plate theory was used to analytically predict the elastic modulus of various grades of FML 4, each with a different prepreg layup. A comparison between the results calculated using CLP and the experimental measurements showed that the CLP derivation provided excellent estimates of the elastic modulus in all material orientations. CLP theory was also used to estimate the residual strength of the panels post-test and comparing the analytical results to those determined experimentally provided valuable evidence to suggest that the inner aluminum was largely intact after "fatigue failure".

13.3 Development and Testing of New FML Variants

13.3.1 Fatigue Testing

The fatigue test results conclusively showed that the cold expansion process is effective for all grades of FML tested, including the new FML 4 variant. Detailed correlation of TSA and DIC data to fractography was used to elucidate crack development after both cold expansion and riveting and proved that cold expansion extended life in the early stage of the fatigue process more effectively on the exit face than on the entry face, especially in aluminum.

For riveting, the combination of in-plane strains from the expansion of the rivet shank and the compression from the rivet head was shown to be very effective at delaying crack nucleation and shifting the nucleation location away from the central rivet hole.

Static tensile testing, post "fatigue failure", showed that the compliance basis for determining failure left all coupons with a significant amount of residual strength, with all coupons showing a residual elastic modulus of at least 35% of their original value.

Analysis of the crack growth curves showed that, while cold expansion was effective at reducing crack propagation rates, it was only minimally effective extending life in the early stage of fatigue crack growth (defined as a crack growth to 1 mm). One possible explanation for this was that the cold expansion process may result in delamination of the aluminum in the annular region next to the cold expanded hole. As a result, while the compressive residual stresses induced by cold expansion are quite effective at

reducing crack propagation for longer cracks, crack nucleation is only minimally affected.

13.3.2 Effectiveness of Quasi-Isotropic FML 4 [60/0/-60]

Static tensile testing showed that the FML 4 variant with a quasi-isotropic layup had an elastic modulus similar to that predicted by the closed form solution. Strain measurements after cold expansion and riveting showed that this FML 4 variant had a much more uniform residual strain field after cold expansion than either standard FML 3 or FML 4. Fatigue testing results showed that the fatigue life of the FML 4 variant was relatively constant, independent of material orientation, and that it held significant residual strength and stiffness after complete fatigue crack growth on both coupon faces. Although a quasi-isotropic FML may not be ideal in high-cycle fatigue applications, such as in an airplane fuselage, for static design applications or applications with multiaxial loading and or unknown loading, this FML 4 [-60/0/60] may prove to be extremely useful.

13.4 Summary

The aim of this research program, laid out in the introduction was met. Based on experimental measurements of the strain field during cold expansion and riveting, several new candidate FML variants were analyzed, manufactured, and tested. Of these, a quasi-isotropic FML 4 variant [-60/0/60] showed promising results and was subjected to additional testing. Comprehensive static and fatigue testing of this FML 4 [-60/0/60] variant demonstrated that it did indeed show quasi-isotropic behaviour. Although the modulus and fatigue life were lower than FML 4 [90/0/90] in the transverse orientation, the static and fatigue properties were similar or better in all other orientations. Overall, the FML 4 [-60/0/60] variant developed proved to be better suited

for cold expansion and riveting and would be an excellent addition to the standard

grades of FML that exist currently.

REFERENCES

REFERENCES

1. Alderliesten R and Homan J (2006) Fatigue and Damage Tolerance Issues of Glare in Aircraft Structures. International Journal of Fatigue 28:1116-1123.

2. Alderliesten R, Hagenbeek M, Homan J, Hooijmeijer P, de Vries T, and Vermeeren C (2003) Fatigue and Damage Tolerance of Glare. Applied Composite Materials 10:223-242.

3. Homan J (2006) Fatigue Initiation in Fibre Metal Laminates. International Journal of Fatigue 28:366-374.

4. Kaufman J (1967) Fracture Toughness of 7076-T6 and T651, Sheet, Plate and Multilayered Adhesive Bonded Panels. Journal of Basic Engineering 89:503-507.

5. Krishnakumar S (1994) Fiber Metal Laminates - Matching the Best in Composites and Metals. Materials Technology 9:114-119.

6. Krishnakumar S (1994) Fiber Metal Laminates - The Synthesis of Metals and Composites. Materials and Manufacturing Processes 9:295-354.

7. Vermeeren C (2003) An Historic Overview of the Development of Fibre Metal Laminates. Applied Composite Materials 10:189-205.

8. Asundi A and Choi A (1997) Fiber Metal Laminates: an Advanced Material for Future Aircraft. Journal of Materials Processing Technology 63:384-394.

9. Vlot A and Gunnink JW (2001) Fibre Metal Laminates: An Introduction. Kluwer Academic Publishers, Delft, The Netherlands.

10. Lawcock G, Ye L, and Mai Y (1995) Novel Fiber Reinforced Metal Laminates for Aerospace Applications - A Review: Part 1-Background and General Mechanical Properties. SAMPE Journal 31:23-31.

11. Laliberte J and Poon CJ (2004) Static Tensile Testing of Glare-3 and Glare-4. LM-SMPL-2004-0030.

12. Wu H, Wu L, Slagter W, and Verolme J (1994) Pilot Study of Metal Volume Fraction Approach for Fiber/Metal Laminates. Journal of Aircraft 32:663-671.

13. Wu G and Yang J (2005) The Mechanical Behavior of GLARE Laminates for Aircraft Structures. Journal of the Minerals, Metals and Materials Society 57:72-79.

14. Marissen R (1984) Flight Simulation Behaviour of Aramid Reinforced Aluminium Laminates (ARALL). Engineering Fracture Mechanics 19:261-277.

15. Alderliesten R (2005) Fatigue Crack Propagation and Delamination Growth in Glare. Thesis, Delft Technical University.

16. Schijve J (2001) Fatigue of Structures and Materials. Kluwer Academic Publishers, Dordrecht, The Netherlands.

17. Young J, Landry G, and Cavoulacos V (1994) Crack Growth and Residual Strength Characteristics of Two Grades of Glass Reinforced Aluminium 'GLARE'. Composite Structures 27:457-469.

18. Vasek A, Polak J, and Kozak V (1997) Fatigue Crack Initiation in Fibre-Metal Laminate GLARE 2. Material Science and Engineering A234-236:621-624.

19. Bradshaw R and Gutierrez S (2007) Characterization of Fatigue Crack Initiation and Growth in Hybrid Al-Graphite Fibre Composite Using Image Analysis. Fatigue and fracture of engineering materials and structures 30:766-781.

20. Chandawanich N and Sharpe WN (1979) An Experimental Study of Fatigue Crack Initiation and Growth From Coldworked Holes. Engineering Fracture Mechanics 11:609-620.

21. Kokaly M, Ransom J, Jude B, Restis H, and Reid L (2005) Predicting Fatigue Crack Growth in the Residual Stress Field of a Cold Worked Hole. Journal of ASTM International 2:119-131.

22. FTI Process Specification 8101D: Cold Expansion of Holes Using the Standard Split Sleeve System and Countersink Cold Expansion (CsCx). 2002. Fatigue Technology Inc.

23. Muller R (1995) An Experimental and Analytical Investigation on the Fatigue Behaviour of Fuselage Riveted Lap Joints. Thesis, DELFT University of Technology.

24. Dulieu-Barton J and Stanley P (1998) Development and Applications of Thermoelastic Stress Analysis. Journal of Strain Analysis 33:93-104.

25. Dulieu-Barton J (1999) Introduction to Thermoelastic Stress Analysis. Strain 35:35-38.

26. Stanley P and Chan W (1988) The Application of Thermoelastic Stress Analysis Techniques to Composite Materials. Journal of Strain Analysis 23:137-143.

27. Thomson W (1853) On the Dynamical Theory of Heat. Transactions of the Royal Society 20:261-283.

28. Boyce B (2007) Deltatherm User Manual. Stress Photonics Inc, Version 6C.

29. Chu A, Ranson A, Sutton M, and Peters A (1985) Applications of Digital Image Correlation Techniques to Experimental Mechanics. Experimental Mechanics 25:232-244.

30. Sutton M, Mcneill S, Helm J, and Chao Y (2000) Advances in Two-Dimensional and Three-Dimensional Computer Vision. Topics in Applied Physics 77:323-372.

31. Sutton M, Wolters W, Peters W, Ranson W, and Mcneill S (1983) Determination of Displacements Using an Improved Digital Correlation Method. Image and Vision Computing 1:133-139.

32. Sutton M, Orteu J, and Schreier H (2009) Image Correlation for Shape, Motion and Deformation Measurements. Springer Science, New York.

33. Champoux R (1986) An Overview of Cold Expansion Methods, Fatigue Prevention and Design. Chamelon press, London.

34. Poolsuk S and Sharpe W (1978) Measurement of the Elastic-Plastic Boundary Around Cold Worked Fastener Holes. Journal of Applied Mechanics 45:515-520.

35. Cloud G (1980) Measurement of Strain Fields Near Coldworked Holes. Experimental Mechanics 20:9-16.

36. Lai MO, Oh JT, and Nee YC (1993) Fatigue Properties of Holes With Residual Stresses. Engineering Fracture Mechanics 45:551-557.

37. Lai MO and Siew YH (1995) Fatigue Properties of Cold Worked Holes. Journal of Materials Processing Technology 48:533-540.

38. Leon A (1998) Benefits of Split Mandrel Coldworking. International Journal of Fatigue 20:1-8.

39. de Matos P, Moreira P, Pina J, Dias A, and de Castro P (2004) Residual Stress Effect on Fatigue Striation Spacing in a Cold-Worked Rivet Hole. Theoretical and Applied Fracture Mechanics 42:139-148.

40. Lacarac V, Smith D, and Pavier M (2004) Residual Stress Creep Relaxation Around Cold Expanded Holes in an Aluminium Alloy. AIAA Journal 42:1444-1449.

41. Link R and Sanford R (1990) Residual Strains Surrounding Split Sleeve Cold Expanded Holes in 7075-T651 Aluminium. Journal of Aircraft 27:599-604.

42. Ball D and Lowry D (1998) Experimental Investigation on the Effects of Cold Expansion of Fastener Holes. Fatigue and fracture of engineering materials and structures 21:17-34.

43. Beaver P, Mann J, and Sparrow J (1986) Grid Technique for the Measurements of Strains Close to Cold-Expanded Holes. Measurement and Fatigue - Engineering Integrity Society 1986, Bournemouth, England, 491-505.

44. O'Brien E (2000) Beneficial Residual Stress From the Cold Expansion of Large Holes in Thick Light Alloy Plate. Journal of Strain Analysis 35:261-276.

45. Stefanescu D (2003) Experimental Study of Double Cold Expansion of Holes. Journal of Strain Analysis 38:339-347.

46. Stefanescu D, Santiseban J, Edwards L, and Fitzpatrick M (2004) Residual Stress Measurement and Fatigue Crack Growth Prediction After Cold Expansion of Cracked Fastener Holes. Journal of Aerospace Engineering 91-97.

47. Stefanescu D, Steuwer A, Owen RA, Nadri B, Edwards L, Fitzpatrick ME, and Withers PJ (2004) Elastic Strains Around Cracked Cold Expanded Fastener Holes Measured Using Synchrotron X-Ray Diffraction Technique. Journal of Strain Analysis for Engineering Design 39:459-469.

48. Stefanescu D, Dutta M, Wang DQ, Edwards L, and Fitzpatrick ME (2003) The Effect of High Compressive Loading on Residual Stresses and Fatigue Crack Growth at Cold Expanded Holes. Journal of Strain Analysis for Engineering Design 38:419-427.

49. Petrak G and Stewart R (1974) Retardation of Cracks Emanating From Fastener Holes. Engineering Fracture Mechanics 6:275-282.

50. Wagner R, Reid L, Easterbrook E, and Ruffin A (1992) Beneficial Effects of Split Sleeve Cold Expansion on the Fatigue Lives of Pre-Cycled Cold Expanded Structures. Fatigue Technology Inc.

51. Beaver P, Mann J, and Sparrow J (1986) Fatigue Life Enhancement by the Cold Expansion of Holes - Research and Case Study. Fatigue: Prevention and Design: Proceedings of an International Conference, London, 11-21-1986123-138.

52. Zhang X and Wang Z (2003) Fatigue Life Improvement in Fatigue Aged Fastener Holes Using the Cold Expansion Technique. International Journal of Fatigue 25:1249-1257.

53. Chao L and Xiulin Z (1992) Effects of Cold Expansion of a Hole on Fatigue Crack Initiation Location and Life of an LY12CZ Alloy. Fatigue and fracture of engineering materials and structures 15:241-247.

54. Lacarac V, Smith DJ, Pavier MJ, and Priest M (2000) Fatigue Crack Growth From Plain and Cold Expanded Holes in Aluminium Alloys. International Journal of Fatigue 22:189-203.

55. Arora PR, Dattaguru B, and Subramanya Hande HS (1992) A Method for Estimation of the Radius of Elastic-Plastic Boundary Around Cold-Worked Holes. Journal of Testing and Evaluation 369-375.

56. Heller M, Jones R, and Williams JF (1991) Analysis of Cold Expansion for Cracked and Uncracked Fastener Holes. Engineering Fracture Mechanics 39:195-212.

57. Nadai A (1943) Theory of the Expanding of Boiler and Condenser Tube Joints Through Rolling. Transactions of the ASME 65:865-880.

58. Rich D and Impellizzeri F (1977) Fatigue Analysis of Cold-Worked and Interference Fit Fastener Holes. ASTM Special Technical Publication 153-175.

59. Jessop H, Snell C, and Holister G (1956) Photoelastic Investigation on Plates With Single Interference Fit Pins With Load Applied to Plate Only. The Aeronautical Quarterly 297-314.

60. Ozdemir A and Hermann R (1999) Effect of Expansion Technique and Plate Thickness on Near-Hole Residual Stresses and Fatigue Life of Cold Expanded Holes. Journal of Materials Science 34:1243-1252.

61. Ozdemir A and Edwards L (1996) Measurement of the Three-Dimensional Residual Stress Distribution Around Split Sleeve Cold Expanded Holes. Journal of Strain Analysis 31:413-421.

62. Ozdemir A and Edwards L (1997) Relaxation of Residual Stresses at Cold-Worked Fastener Holes Due to Fatigue Loading. Fatigue and fracture of engineering materials and structures 20:1443-1451.

63. Stefanescu D (2004) Measurement and Prediction of Fatigue Crack Growth From Cold Expanded Holes. Part 1: the Effect of Fatigue Crack Growth on Cold Expansion Residual Stresses. Journal of Strain Analysis for Engineering Design 39:25-39.

64. Pell RA, Beaver P, Mann J, and Sparrow J (1989) Fatigue of Thick Section Cold Expanded Holes With and Without Cracks. Fatigue and fracture of engineering materials and structures 12:553-567.

65. Forgues S, Bernard M, and Bui-Quoc C (1993) 3-d Axisymmetric Numerical Analysis and Experimental Study of the Fastener Hole Coldworking Process, Computer Methods and Experimental Measurements for Surface Treatement Effects. Wessex Institute of Technology, Wessex.

66. Babu N, Jagadish T, Ramachandra K, and Sridhara S (2007) A Simplified 3-D Finite Element Simulation of Cold Expansion of a Circular Hole to Capture Through Thickness Variation of Residual Stresses. Engineering Failure Analysis 15:339-348.

67. Lacarac V, Smith D, and Pavier M (2001) The Effect of Cold Expansion on Fatigue Crack Growth From Open Holes at Room and High Temperature. International Journal of Fatigue 23:S161-S170.

68. Pina J, Dias A, de Matos P, Moreira P, and de Castro P (2004) Residual Stress Analysis Near a Cold Expanded Hole in a Textured Alclad Sheet Using X-Ray Diffraction. Experimental Mechanics 45:83-88.

69. Stefanescu D (2004) Measurement and Prediction of Fatigue Crack Growth From Cold Expanded Holes. Part 2: Prediction of Fatigue Crack Growth From Cold Expanded Holes. Journal of Strain Analysis for Engineering Design 39:41-53.

70. Ozdemir A and Edwards L (2004) Through Thickness Residual Stress Distribution After the Cold Expansion of Fastener Holes and Its Effect on Fracturing. Journal of Engineering Materials and Technology 126:129-135.

71. Hsu Y and Forman R (1975) Elastic-Plastic Analysis of an Infinite Sheet Having a Circular Hole Under Pressure. Journal of Applied Mechanics 42:347-352.

72. Coker EA and Scoble WA (1913) The Distribution of Stress Due to a Rivet in a Plate. Transactions of the Institute of Naval Architecture 439-442.

73. Fox ME and Withers PJ (2007) Residual Stresses in and Around Electromagnetically Installed Rivets Measured Using Synchrotron and Neutron Diffraction. Journal of Neutron Research 15:215-223.

74. Fox ME and Withers PJ (2006) Relaxation of Residual Stresses in and Around Mechanical Fasteners Due to Fatigue Loading. Materials Science Forum 524-525:153-158.

75. Fitzgerald T and Cohen J (1994) Residual Stresses in and Around Rivets in Clad Aluminum Alloy Plates. Material Science and Engineering A188:51-58.

76. Fox M and Withers P (2006) Relaxation of Residual Stresses in and Round Electromagnetically Installed Rivets During Fatigue Loading. European Synchrotron Radiation Facility, ME-1036.

77. Li G and Shi G (2004) Effect of the Riveting Process on the Residual Stress in Fuselage Lap Joints. Canadian Aeronautics and Space Journal 50:91-105.

78. Langrand B, Patronelli L, Deletombe E, Markiewicz E, and Drazetic P (2002) Full Scale Experimental Characterisation for Riveted Joint Design. Aerospace Science and Technology 6:333-342.

79. Markiewicz E, Langrand B, Deletombe E, Drazetic P, and Patronelli L (1998) Analysis of the Riveting Process Forming Mechanisms. International Journal of Materials and Product technology 13:123-145.

80. Deng X and Hutchinson J (1998) The Clamping Stress in a Cold Driven Rivet. International Journal of Mechanical Science 40:683-694.

81. Szolwinski M and Farris T (2000) Linking Riveting Process Parameters to the Fatigue Performance of Riveted Aircraft Structures. Journal of Aircraft 37:130-137.

82. Atre A and Johnson W (2006) 3D FEA Simulations to Assess Residual Stresses in Riveting Processes. Journal of ASTM International 3:1-10.

83. Szymczyk E, Jachimowicz J, Slawinkski G, and Derewonko A (2009) Influence of Technological Imperfections on Residual Stress Fields in Riveted Joints. Procedia Engineering 59-62.

84. Rans C and Straznicky P (2007) Riveting Process Induced Residual Stresses Around Solid Rivets in Mechanical Joints. Journal of Aircraft 44:323-329.

85. Ryan L and Monaghan J (2000) Failure Mechanism of Riveted Joint in Fibre Metal Laminates. Journal of Materials Processing Technology 103:36-43.

86. Rans C, Alderliesten R, and Straznicky P (2005) Modelling of the Rivet Forming Process in Aluminum and GLARE for Design Against Fatigue. International Committee on Aeronautical Fatigue, Hamburg, Germany, 20051-17.

87. Rans C and Straznicky P (2005) Avoiding Knife-Edge Countersinks in GLARE Through Dimpling. Fatigue Fract Engng Mater Struct 28:633-640.

88. Lazzeri L (2001) Fatigue Behavior of Riveted Glare Lap Joints. Fatigue and fracture of engineering materials and structures 2001:579-589.

89. van der Kuip EMAH (2002) Fatigue Crack Initiation and Crack Growth in GLARE With Coldworked Holes. Thesis, Delft University of Technology.

90. Rans C, Alderliesten R, and Straznicky P (2006) Residual Stress in GLARE Laminates Due to the Cold Expansion Process. 1-15.

91. Lanciotti A and Polese C (2005) The Effect of Interference-Fit Fasteners on the Fatigue Life of Central Hole Specimens. Fatigue and fracture of engineering materials and structures 28:587-597.

92. Keshavanarayana S, Smith BL, Gomez C, and Caido F (2010) Fatigue Based Severity Factors for Shear Loaded Fastener Joints. Journal of Aircraft 41:181-191.

93. Olden E and Patterson EA (2000) A Rational Decision Making Model for Experimental Mechanics. Experimental Techniques 24:26-32.

94. Cannon D, Sinclair J, and Sharpe K (1985) Improving the Fatigue Performance of Bolt Holes in Railway Rails by Cold Expansion. Fatigue Life: Analysis and Prediction, 1985:353-369.

95. Li G, Shi G, and Bellinger N (2008) Study of the Residual Strain in Lap Joints. Journal of Aircraft 43:1145-1151.

96. O'Brien E (1997) Cold Expansion of Large Holes in Thick 7010 Light Alloy Aircraft Material - Strains in the Time Domain. Thesis, The University of Sheffield.

97. Sinke J and de Jong TW (1998) Formability and Machining of Fibre-Metal Laminates. 30th International SAMPE Technical Conference, 10-20-1998.

98. Kratz J, Djokic D, Laliberte J, and Mahendran M (2007) Fiber Metal Laminate Panel Manufacturing. National Research Council, LM-SMPL-2007-0102.

99. Chang P and Yang J (2008) Modeling of Fatigue Crack Growth in Notched Fiber Metal Laminates. International Journal of Fatigue 30:2165-2174.

100. Hofslagare P (2003) Residual Stress Measurement on Fibre-Metal-Laminates. Journal of Neutron Research 11:215-220.

101. Hofslagare P (2006) Investigation of Residual Stress in Fiber Reinforced Metal Laminates by Neutron Diffraction. The studsvik neutron research laboratory, 555.

102. Krimbalis P, Poon C, Behdinan K, and Fawaz Z (2009) On the Calculation and Simulation of Thermally Induced Residual Stresses in GLARE Fibre Metal Laminate. Canadian Aeronautics and Space Institute Conference.

103. Laliberte J, Mahendran M, Djokic D, Li C, and Kratz J (2007) Effect of Process Induced Residual Stresses on Mechanical Properties and Fatigue Crack Initiaiton in Fibre Metal Laminates. 24th International Conference on Aeronautical Fatigue, Naples, Italy.

104. Ayatollahi MR and Arian Nik M (2009) Edge Distance Effects on Residual Stress Distribution Around a Cold Expanded Hole in Al 2024 Alloy. Computational Materials Science 45:1134-1141.

105. Mendelson A (1983) Plasticity: Theory and Applications. Robert Krieger Publishing, Malabar, Florida.

106. Riley W and Zachary L (1989) Introduction to Mechanics of Materials.

107. Bridgman PW (1946) The Effect of Hydrostatic Pressure on Plastic Flow Under Shearing Stress. Journal of Applied Physics 17:692-698.

108. Bridgman PW (1937) Flow Phenomena in Heavily Stressed Metals. Journal of Applied Physics 8:328-336.

109. Dowling NE (1999) Mechanical Behavior of Materials. Prentice-Hall, Canada.

110. Popov EP (1998) Engineering Mechanics of Solids. Pearson Education.

111. Tsai S and Wu E (1971) A General Theory of Strength for Anisotropic Materials. Journal of Composite Materials 5:58-80.

112. Cortes P and Cantwell W (2006) The Prediction of Tensile Failure in Titanium Based Thermoplastic Fibre Metal Laminates. Composites Science and Technology 66:2306-2316.

113. Azzi V and Tsai S (1995) Anisotropic Strength of Composites. Experimental Mechanics 5:283-288.

114. Kawai M, Morishita S, Tomura S, and Takumida K (1998) Inelastic Behavior and Strength of Fiber Metal Hybrid Composite: GLARE. International Journal of Mechanical Science 40:183-198.

115. Iaccarino P, Langella A, and Caprino G (2007) A Simplified Model to Predict the Tensile and Shear Stress Strain Behaviour of FML. Composites Science and Technology 67:1784-1793.

116. Hill R (1948) A Theory of the Yielding and Plastic Flow of Anisotropic Metals. Proceedings of the Royal Society of London - Series A 193:281-297.

117. Staab G (1999) Laminar Composites. Butterworth and Heinemann, Woburn, MA.

118. Ramberg W and Osgood W (1943) Description of Stress Strain Curves by Three Parameters. National Advisory Committee for Aeronautics, NACA-TN-902.

119. Budiansky B (1971) An Exact Solution to an Elastic-Plastic Stress Concentration Problem. Journal of Applied Mathematics and Mechanics 35:40-48.

120. Hill R (1985) The Mathematical Theory of Plasticity. Oxford University Press.

121. Budiansky B (1959) A Reassessment of Deformation Theories of Plasticity. Journal of Applied Mechanics 259-264.

122. Ball D (1995) Elastic-Plastic Stress Analysis of Cold Expanded Fastener Holes. Fatigue and fracture of engineering materials and structures 18:47-63.

123. Guo W (1993) Elastic-Plastic Analysis of a Finite Sheet With a Cold-Worked Fastener Hole. Engineering Fracture Mechanics 45:857-864.

124. Zhang Y, Fitzpatrick M, and Edwards J (2005) Analysis of the Residual Stress Around a Cold-Expanded Fastener Hole in a Finite Plate. Strain 41:59-70.

125. Timoshenko S (1970) Theory of Elasticity.

126. Kobayashi A (1993) Handbook of Experimental Mechanics. VCH Publishers, New York, New York.

127. Hyer M (2008) Laminated Plate and Shell Theory, Comprehensive Composite Materials.

128. Reddy JN (1997) Mechanics of Laminated Composite Plates. CRC Press.

129. US Department of Defence (2008) Military Handbook. Metallic Materials and Elements for Aerospace Vehicle Structures.

130. Smith D, Poussard C, and Pavier M (1998) An Assessment of the Sachs Method for Measuring Residual Stresses in Cold Worked Fastener Holes. Journal of Strain Analysis 33:263-274.

131. Amrouche A, Mesmacque G, Garcia S, and Talha A (2003) Cold Expansion Effect on the Initiation and the Propagation of the Fatigue Crack. International Journal of Fatigue 25:949-954.

132. Backman D and Patterson EA (2008) Measuring Residual Strains in Aluminum and Fiber Metal Laminate Materials During Cold Expansion and Riveting. Society for Experimental Mechanics - 11th International Congress and Exhibition on Experimental and Applied Mechanics 2008, Bethel, CT, 1:217-223.

133. Patki A and Patterson EA (2010) Thermoelastics Stress Analysis of Fatigue Cracks Subject to Overloads. Fatigue and fracture of engineering materials and structures 00:1-13.

134. Alderliesten R and Homan J (2003) Fatigue Crack Growth Behaviour of Surface Cracks in GLARE. Advances in Damage Mechanics, Toronto, 5:213-222.

135. Backman D, Patterson EA, and Cowal C (2010) Analysis of the Effects of Cold Expansion of Holes Using Thermoelasticity and Image Correlation. Fatigue and fracture of engineering materials and structures 00:1-12.

136. de Rijck J, Homan J, Schijve J, and Benedictus R (2007) The Driven Rivet Head Dimensions As an Indication of the Fatigue Performance of Aircraft Lap Joints. International Journal of Fatigue 2208-2218.

137. Krimbalis P, Poon C, Behdinan K, and Fawaz Z (2008) On the Pin Bearing Behaviour of Orthotropic Fiber Metal Laminates. Journal of Composite Materials 42:1547-1566.

138. Alderliesten RC and Benedictus R (2007) Fiber/Metal Composite Technology for Future Primary Aircraft Structures. 40th AIAA/ASME Structures, Structural Dynamics and Materials Conference, Honolulu, Hawaii, 1-12.

139. Lanciotti A and Lazzeri L (2009) Fatigue Resistance and Residual Strength of Riveted Joints in FML. Fatigue and fracture of engineering materials and structures 32:837-846.

140. Backman DS, Taremi F, Marincak T, Bellinger NC, and Li G (2004) Experimental Measurement of the Pressure Distribution in a Simple Rivetted Lap Joint for Use in Modelling Fretting Fatigue. ICEM12 - 12th International Conference on Experimental Mechanics, Politecnico di Bari, Italy.

141. van Rooijen R, Sinke J, de Vries T, and van der Zwaag S (2004) Property Optimisation in Fibre Metal Laminates. Applied Composite Materials 11:63-76.

142. Nam H, Hwang W, and Han K (2000) Stacking Sequence Design of Fiber-Metal Laminate for Maximum Strength. Journal of Composite Materials 35:1654-1683.

143. Kim D and Jang J (2008) Re-Cold Expansion Process Simulation to Impart the Residual Stresses Around Fastener Holes in 6061 A-T6 Aluminium Alloy. Proc. ImechE. , Part B: J. Engineering Manufacture 222:1325-1332.

144. Bernard M, Bui-Quoc T, and Burlat M (1995) Effect of Re-Cold Working on Fatigue Life Enhancement of a Fastener Holw. Fatigue and fracture of engineering materials and structures 18:765-775.

145. Chakherlou T and Vogwell J (2004) A Novel Method of Cold Expansion Which Creates Near-Uniform Compressive Tangential Residual Stress Around a Fastener Hole. Fatigue and fracture of engineering materials and structures 27:343-351.

146. Karabin M, Barlat F, and Schultz R (2007) Numerical and Experimental Study of the Cold Expansion Process in 7085 Plate Using a Modified Split Sleeve. Journal of Materials Processing Technology 189:45-57.

147. Chang P, Yang J, Seo H, and Hahn H (2007) Off-Axis Fatigue Cracking Behaviour in Notched Fibre Metal Laminates. Fatigue Fracture Engineering of Material Structures 30:1158-1171.

148. Kawai M, Hachinohe A, Takumida K, and Kawase Y (2001) Off-Axis Fatigue Behaviour and Its Damage Mechanics Modelling for Unidirectional Fibre-Metal Hybrid Composite: GLARE 2. Composites: Part A 32:13-23.

149. Kawai M and Kato K (2006) Effects of R-Ratio on the Off-Axis Fatigue Behavior of Unidirectional Hybrid GFRP/AL Laminates at Room Temperature. International Journal of Fatigue 28:1226-1238.